Intermontane valley fills: recorders of climate, tectonics and landscape evolution

Jürgen Mey

Kumulative Dissertation
zur Erlangung des akademischen Grades
Doktor der Naturwissenschaften (Dr. rer. nat.)
in der Wissenschaftsdisziplin Geologie

eingereicht an der
Mathematisch-Naturwissenschaftlichen Fakultät
der Universität Potsdam

Potsdam, 20. Juni 2016

Published online at the
Institutional Repository of the University of Potsdam:
URN urn:nbn:de:kobv:517-opus4-103158
http://nbn-resolving.de/urn:nbn:de:kobv:517-opus4-103158

Für Hanna und Horst

Abstract

Sedimentary valley fills are a widespread characteristic of mountain belts around the world. They transiently store material over time spans ranging from thousands to millions of years and therefore play an important role in modulating the sediment flux from the orogen to the foreland and to oceanic depocenters. In most cases, their formation can be attributed to specific fluvial conditions, which are closely related to climatic and tectonic processes. Hence, valley-fill deposits constitute valuable archives that offer fundamental insight into landscape evolution, and their study may help to assess the impact of future climate change on sediment dynamics.

In this thesis I analyzed intermontane valley-fill deposits to constrain different aspects of the climatic and tectonic history of mountain belts over multiple timescales. First, I developed a method to estimate the thickness distribution of valley fills using artificial neural networks (ANNs). Based on the assumption of geometrical similarity between exposed and buried parts of the landscape, this novel and highly automated technique allows reconstructing fill thickness and bedrock topography on the scale of catchments to entire mountain belts.

Second, I used the new method for estimating the spatial distribution of post-glacial sediments that are stored in the entire European Alps. A comparison with data from exploratory drillings and from geophysical surveys revealed that the model reproduces the measurements with a root mean squared error (RMSE) of 70 m and a coefficient of determination (R^2) of 0.81. I used the derived sediment thickness estimates in combination with a model of the Last Glacial Maximum (LGM) icecap to infer the lithospheric response to deglaciation, erosion and deposition, and deduce their relative contribution to the present-day rock-uplift rate. For a range of different lithospheric and upper mantle-material properties, the results suggest that the long-wavelength uplift signal can be explained by glacial isostatic adjustment with a small erosional contribution and a substantial but localized tectonic component exceeding 50% in parts of the Eastern Alps and in the Swiss Rhône Valley. Furthermore, this study reveals the particular importance of deconvolving the potential components of rock uplift when interpreting recent movements along active orogens and how this can be used to constrain physical properties of the Earth's interior.

In a third study, I used the ANN approach to estimate the sediment thickness of alluviated reaches of the Yarlung Tsangpo River, upstream of the rapidly uplifting Namche Barwa massif. This allowed my colleagues and me to reconstruct the ancient river profile of the Yarlung Tsangpo, and to show that in the past, the river had already been deeply incised into the eastern margin of the Tibetan Plateau. Dating of basal sediments from drill cores that reached the paleo-river bed to 2–2.5 Ma are consistent with mineral cooling ages from the Namche Barwa massif, which indicate initiation of rapid uplift at ~4 Ma. Hence, formation of the Tsangpo gorge and aggradation of the voluminous valley fill was most probably a consequence of rapid uplift of the Namche Barwa massif and thus tectonic activity.

The fourth and last study focuses on the interaction of fluvial and glacial processes at the southeastern edge of the Karakoram. Paleo-ice-extent indicators and remnants of a more than 400-m-thick fluvio-lacustrine valley fill point to blockage of the Shyok River, a main tributary of the upper Indus, by the Siachen Glacier, which is the largest glacier in the Karakoram Range. Field observations and ^{10}Be exposure dating attest to a period of recurring lake formation and outburst flooding during the penultimate glaciation prior to ~110 ka. The interaction of Rivers and Glaciers all along the Karakorum is considered a key factor in landscape evolution and presumably promoted headward erosion of the Indus-Shyok drainage system into the western margin of the Tibetan Plateau.

The results of this thesis highlight the strong influence of glaciation and tectonics on valley-fill formation and how this has affected the evolution of different mountain belts. In the Alps valley-fill deposition influenced the magnitude and pattern of rock uplift since ice retreat approximately 17,000 years ago. Conversely, the analyzed valley fills in the Himalaya are much older and reflect environmental conditions that prevailed at ~110 ka and ~2.5 Ma, respectively. Thus, the newly developed method has proven useful for inferring the role of sedimentary valley-fill deposits in landscape evolution on timescales ranging from 10^3 to 10^7 years.

Zusammenfassung

Sedimentäre Talverfüllungen sind ein häufiges Merkmal von Gebirgen auf der ganzen Welt. Sie speichern Abtragungsprodukte über Zeiträume von Tausenden bis Millionen von Jahren und beeinflussen den Sedimenttransport vom Gebirge in das Vorland und in die ozeanischen Becken. Die Bildung solcher Sedimentspeicher geht oft auf Zustände im fluvialen System zurück, welche mit bestimmten klimatischen und tektonischen Prozessen in Verbindung gebracht werden können. Talverfüllungen stellen daher wertvolle Archive dar, die über fundamentale Zusammenhänge in der Landschaftsgenese Aufschluss geben und deren Untersuchung dazu beiträgt, die Auswirkungen des Klimawandels auf die Sedimentdynamik im Gebirge zu prognostizieren.

In dieser Arbeit untersuchte ich intermontane Talverfüllungen, um die klimatische und tektonische Geschichte von Gebirgszügen über mehrere Zeitskalen hinweg zu ermitteln. Zuerst entwickelte ich eine Methode zur Abschätzung von Sedimentmächtigkeiten mit Hilfe von künstlichen neuralen Netzen, die auf der Annahme basiert, dass sich die zugeschütteten und die freiliegenden Bereiche der Landschaft geometrisch ähneln. Diese neuartige und hochautomatisierte Methode macht es möglich, Sedimentmächtigkeiten und Untergrundtopographien für einzelne Einzugsgebiete bis hin zu ganzen Gebirgen abzuschätzen.

Als zweites benutzte ich die neue Methode, um die Mächtigkeitsverteilung der postglazialen Sedimentspeicher in den Europäischen Alpen zu rekonstruieren. Ein Vergleich mit Daten aus Bohrlochmessungen und geophysikalischen Explorationen zeigte, dass das Modell die gemessenen Mächtigkeiten mit einem quadratischen Mittelwert des Fehlers (RMSE) von 70 m und einem Bestimmtheitsmaß (R^2) von 0.81 reproduziert. Ich verwendete diese Sedimentverteilung in Kombination mit einem Modell der alpinen Eiskappe des letzten glazialen Maximums (LGM), um die Reaktion der Lithosphäre auf Abschmelzen, Erosion und Ablagerung zu berechnen und deren Beiträge zur derzeitigen Gesteinshebung abzuleiten. Unter Berücksichtigung einer Reihe verschiedener Eigenschaften der Lithosphäre und des oberen Erdmantels zeigten die Resultate, dass das langwellige Hebungsmuster im Wesentlichen durch Glazialisostasie erklärt werden kann und dass die Entlastung durch Erosion eine untergeordnete Rolle spielt. Darüber hinaus postulierte ich eine tektonische Komponente von über 50% in Teilen der Ostalpen und im Schweizer Rhône Tal. Die Studie verdeutlicht, dass die Entflechtung der Prozesse, die zur Gesteinshebung beitragen, eine entscheidende Rolle spielt bei der Interpretation rezenter Bewegungen entlang aktiver Orogene und bei der Abschätzung von physikalischen Eigenschaften des Erdinneren.

Im dritten Teil berechnete ich die Mächtigkeitsverteilung der sedimentären Talverfüllung des Yarlung Tsangpo Tales oberhalb des Namche Barwa Massivs am östlichen Rand des Tibet Plateaus. Dies ermöglichte meinen Kollegen und mir das ehemalige Flusslängsprofil zu rekonstruieren und zu zeigen, dass sich der Yarlung Tsangpo in der Vergangenheit bereits tief in den östlichen Rand des Tibet Plateaus einschnitt. Die Basis der Sedimente wurde erbohrt und beprobt und deren Ablagerung auf 2–2.5 Ma datiert was konsistent mit Abkühlungsaltern von Mineralen des Namche Barwa Massivs ist, die auf den Beginn einer beschleunigten Hebung vor ~4 Ma hindeuten. Dies führte zu der Schlussfolgerung, dass die Bildung der Tsangpo Schlucht und die Aggradation der Talsedimente höchstwahrscheinlich in Folge der schnellen Hebung des Namche Barwa Massivs geschah, welche letztendlich auf tektonische Aktivität zurück geht.

Der vierte und letzte Teil behandelt die Interaktion fluvialer und glazialer Prozesse am südöstlichen Rand des Karakorums. Indikatoren für die frühere Eisausdehnung und die Überreste einer bis zu 400 m mächtigen fluvio-lakustrinen Talverfüllung weisen auf eine Blockade des Shyok, eines Hauptzuflusses des Oberen Indus, durch den Siachen Gletscher, den größten Gletscher des Karakorums, hin. Weitere Geländebefunde und Oberflächendatierungen mittels kosmogenem ^{10}Be bezeugen, dass es während des vorletzten Glaziales zu einem mehrfachen Aufstauen des Shyok und damit assoziierten Seeausbrüchen

gekommen ist. Das Zusammenwirken von Flüssen und Gletschern entlang des Karakorums war maßgeblich für die Landschaftsentwicklung und führte möglicherweise zum Einschneiden von Tälern in den westlichen Rand des Tibet Plateaus.

Die vorliegende Arbeit unterstreicht die Bedeutung von Vergletscherung und Tektonik bei der Bildung von intermontanen Sedimentspeichern und deren Einwirken auf die Entwicklung zweier Gebirge. In den Alpen beeinflusst die Ablagerung von Talfüllungen die Raten und das Muster der Gesteinshebung seit Rückzug des Eises vor ca. 17,000 Jahren. Demgegenüber sind die in dieser Arbeit betrachteten Talfüllungen des Himalayas weit älter und geben Aufschluss über die Umweltbedingungen vor jeweils 110 ka und 2.5 Ma. Es zeigt sich, dass die neue Methode zur Abschätzung von Mächtigkeiten und Volumina intermontaner Talverfüllungen dazu beiträgt, die Landschaftsentwicklung über Zeiträume von 10^3 bis 10^7 Jahren zu rekonstruieren.

Contents

List of Figures

List of Tables

Acknowledgements

This PhD project started out with a 6-month-stipend from the DFG (Deutsche Forschungsgemeinschaft) Graduate School GRK 1364 “Interactions between Tectonics, Climate & the Biosphere in the African-Asian Monsoonal Region” and later became part of the Potsdam Research Cluster for Georisk Analysis, Environmental Change and Sustainability (PROGRESS) financed by the German Federal Ministry of Education and Research (BMBF). Additional funding was received from the DFG through Emmy Noether grant SCHI 1241/1-1 awarded to Taylor Schildgen.

I am particularly indebted to my advisor Dirk Scherler, who sparked my interest in glaciology and glacial geomorphology, and who was available for discussion on a weekly basis even during his stay at Caltech. He guided and supported me in every possible way and his deep dedication to our scientific field inspired me and was key for the accomplishments of this project. I am grateful to Manfred R. Strecker for the confidence he bestowed upon me and for his helpful feedback and constructive criticism. I thank Taylor Schildgen for her financial support, David Egholm for inviting me to Aarhus and allowing me to work with his iSOSIA code, and Andy Wickert for everything he taught me about glacial isostasy. I am thankful to Rasmus Thiede for his support during field work in Ladakh, and to Esther Hintersberger, Henry Wichura, Christian Wolff and the participants of the Field School “Tectonics and Climate in the Indian Himalaya”, which was a great experience. Gerold Zeilinger, Martin Timmerman, Michael Szurlies, Erik Düsterhöfft and Franziska Scheffler are acknowledged for their company during the student field trips to the Harz Mountains. I thank Ed Sobel for introducing me to the procedures of crushing, sieving and magnetical separation and Patricia Eugster for processing our samples in the clean-lab. I am grateful to my office mate Saptarshi Dey, with whom I could always discuss questions regarding ^{10}Be exposure-age dating and tectonic geomorphology and all the other colleagues who make Golm a wonderful place to work.

Finally, I wish to express my deepest gratitude to my family for their love and encouragement during the past 5 years; to my parents, who paved my way from the very beginning and whose confidence and guidance played an extraordinary role for the accomplishment of this scientific task. I would not have been able to finish this work without my loving, caring and supportive wife, Claudia and the heartwarming smile of my daughter Elisabeth.

Chapter 1

Introduction

Crustal shortening, thickening and uplift expose rocks at the Earth's surface that are subject to climate-driven weathering and erosion processes. The eroded sediments get transported by water, wind and ice to sedimentary basins where they are ultimately buried and diagenetically altered to become rocks again. Influenced by plate-tectonic processes and the superposed effects of climate and climate change, these processes constitute the rock cycle. Exhumation of rock and sediment burial are rather slow processes, typically with rates of mm kyr^{-1}, while the transport of sediments on the Earth's surface is rather fast. Today and throughout Earth's history, these sedimentary sinks have included ocean basins, rifts, foreland basins straddling tectonically active mountain belts, or slowly subsiding cratonic interiors. However, within mountain belts with temporarily severed fluvial connectivity with the adjacent forelands sediments may be transiently stored in intermontane valleys for prolonged time spans, often forming thick valley fills. Such severed fluvial conditions may be caused by valley impoundment by voluminous mass movements or glacial activity, lowered stream power resulting from orographic barrier uplift and aridification or an increase in tectonic rates. Accordingly, the resulting intermontane deposits may be preserved on timescales spanning several millennia to several millions of years, and they are therefore a common phenomenon in many mountain belts around the world. As such the sedimentary fills represent important archives that offer valuable insights into past climatic and erosional conditions, and thus, landscape evolution. Understanding these sedimentary fills thus helps to assess the impact of present and future climate change and tectonic processes on Earth surface dynamics. In this study I focus on the formation of valley-fill deposits in orogenic settings and analyze their complex relationship with glaciation and tectonics.

1.1 The formation of valley fills

In the following the term "valley fill" is a generic term that refers to all kinds of unconsolidated terrestrial sediments residing on the floor of topographic depressions within mountain belts. Hence, for the creation of valley fills, topography, relief and a sediment source are required. Irrespective of the process, which is responsible for the emergence of topography, subaerially exposed rocks are subject to erosion, which is eventually focused by the combined effects of streams or glaciers and the degree of tectonic activity creating valleys and ridges. Erosion itself is a function of weathering and transport, which both are sensitive to climate and tectonics (Gilbert, 1877). Combined, these processes constitute denudation, which over long timescales, is responsible for the complete downwearing of mountain belts. The eroded material, constituting the potential valley fill, is usually transported by water, wind or glaciers from higher to lower elevations until it is deposited in the intermontane basins, thereby depriving the foreland and ocean basins of sediment. In general, deposition occurs when the transport capacity of the moving medium is exceeded by the supply of eroded material (Gilbert and Murphy, 1914). In the case of rivers the transport capacity is strongly dependent on the slope of the river (S) and its discharge (Q_w, Fig. 1.1). Considering a graded river, which has a slope that is everywhere adjusted to allow the supplied sediment to be transported (Mackin, 1948), valley-fill formation would not be possible unless the base level of the river (*sensu* Davis, 1902, p. 84), is located within the mountains or at their margin.

Figure 1.1 illustrates the relation of controlling factors for aggradation and incision, i.e., for perturbations of the equilibrium river profile. From this relation it can be easily recognized that a decrease in discharge or

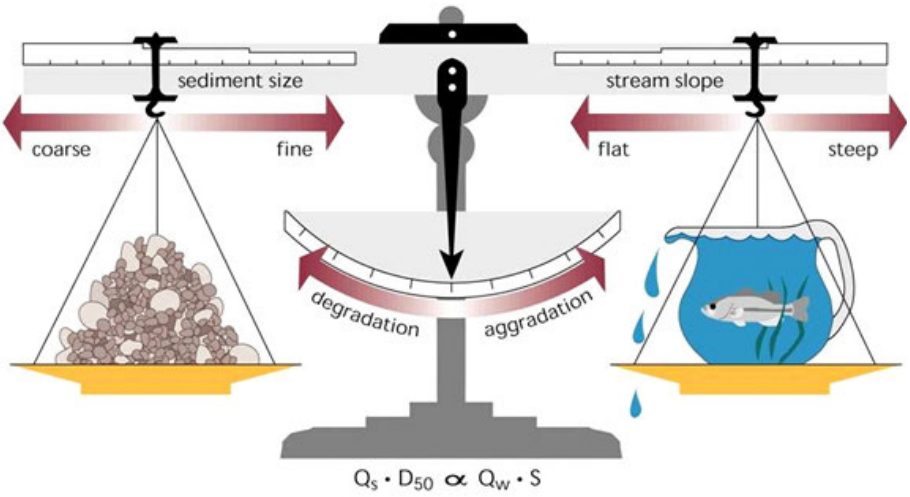

Figure 1.1: Schematic relationship of competing factors determining the state of a river taken from Rosgen and Silvey (1996) modified after Lane (1955). Increases in discharge (Q_w) or stream slope (S) would shift the balance towards incision, whereas increases of sediment supply (Q_s) or grain size (D_{50}) would act in the opposite direction, i.e. towards aggradation, hence valley-fill formation.

slope as well as an increase in sediment supply (Q_s) or median grain size (D_{50}) would shift the balance of the system towards a state of aggradation. Because S, Q_w, Q_s and D_{50} are themselves functions of tectonics, climate and lithology, a wide spectrum of mechanisms may be responsible for the formation of valley fills of which the most important are briefly outlined below.

Differential uplift/subsidence. Tectonic movements along faults can directly impact the slope and the course of a stream. In extreme cases this may lead to an inversion of the flow direction, drainage reorganization and the formation of endorheic basins. Tectonically controlled valley fills typically have a preservation potential on the order of $10^6 - 10^7$ yr (Burbank and Johnson, 1982; Cronin et al., 1989; Hain et al., 2011; Wang et al., 2014). Apart from their tectonic origin, uplift and subsidence can also be driven by flow within the mantle (Becker et al., 2015) or by mass redistribution on the Earth's surface related to glaciation or erosion/deposition which can lead to large scale reorganization of river networks (e.g., Wickert et al., 2013; Calais et al., 2010).

River damming. The blockage of a river course is often accompanied by the formation of a lake, whose size and longevity is determined by the process responsible for the damming (Korup and Schlunegger, 2007). In the longitudinal river profile a lake causes an abrupt decrease in slope and transport capacity, which forces even very fine grains to settle, making lakes efficient sediment traps (Hinderer, 2001). The most important causes for river damming are landslides and glaciers (Baker, 2002; O'Connor and Costa, 2004). While damming caused by landslides is followed by aggradation, erosion of the dam and re-incision (Costa and Schuster, 1988), blockage by glaciers is more complicated (Tweed and Russell, 1999). Because of the low density of ice compared to water, ice dams are inherently unstable as they tend to float when the lake level reaches a certain threshold, leading to drainage of the lake until dam stability is reestablished. Apart from this short term ($10^2 - 10^3$ yr) pattern of recurring lake drainage and backfilling, the climate dependency of glacier size, i.e. the potential for river damming, introduces a long term ($10^4 - 10^5$ yr) and potentially global control on the formation of ice-dam related valley fills. Therefore we may expect cyclicity in the remnants of these deposits reflecting fluctuating lake levels and multiple phases of aggradation and incision (Bretz, 1969; Barber et al., 1999; Scherler et al., 2014).

Glacial overdeepening. In contrast to rivers, whose erosional power dissipates when they approach their base level, glaciers can erode their beds below the local fluvial base level or even below sea level creating subglacial basins, called overdeepenings (e.g., Gutenberg et al., 1956; Linton, 1963; Frank, 1979; van Husen, 1979; Van Husen, 1987; Van Der Beek and Bourbon, 2008; Cook and Swift, 2012). Because ice transmits

longitudinal and transverse stresses there is a non-local control on basal sliding, which determines erosion rates (Harbor, 1989; Cuffey and Paterson, 2010). Therefore, glacial valley profiles depart considerably from their fluvial, smooth and concave-up, counterparts. Besides overdeepenings, the glacial valley profile displays cirques, steps, flats, and hanging valleys (e.g. Penck, 1905; Iverson, 2002; Evans, 2008). After ice retreat, overdeepenings usually host lakes which act as sediment traps (see previous Paragraph). Depending on the size of the overdeepening, retention of sediment can lead to the formation of very large valley fills with thicknesses of $100 - 1000$ m and volumes in excess of $100\,km^3$ (e.g., Pfiffner et al., 1997; Hinderer, 2001; Brückl et al., 2010b; Jordan, 2010; Preusser et al., 2010; Mey et al., 2015). Due to the fact that fluvial erosion cannot remove sediment out of overdeepenings that go deeper than the corresponding base level, these valley-fills have a preservation potential equivalent to at least the duration of one interglacial interval (10^4 yr; Scherler et al., 2014).

Climate change Because climate exerts a strong control on weathering rates and mass wasting processes (e.g., Büdel, 1981; Bull, 1991; Tucker and Slingerland, 1997) it affects the amount of material that is available to the fluvial system. Transport of this material depends on the shear stress at the river bed (Bagnold, 1966), which is a function of slope and discharge with the latter being directly linked to precipitation (e.g., Bookhagen and Burbank, 2010). Thus, an increase in temperature and moisture availability may increase sediment supply through enhanced weathering and mass wasting but at the same time higher precipitation will lead to more runoff and an increase in transport capacity (Lane, 1955). How the fluvial system eventually responds to climate perturbations is largely determined by the landscape preconditions, e.g. soil mantled or threshold hillslopes, the amount of available sediment, the degree of glacial overprint or vegetation cover (e.g., Langbein and Schumm, 1958; Burbank et al., 1993; Tucker and Slingerland, 1997; Bookhagen et al., 2005; Hu et al., 2012; Torres Acosta et al., 2015; Scherler et al., 2015) and might exhibit non-linear behavior (Godard et al., 2013; Simpson and Castelltort, 2012; Tucker and Slingerland, 1997). Valley-fills that were formed by river aggradation in the course of climate change are typically regionally distributed (Bull, 1991) and can therefore be distinguished from dam-related valley fills (e.g., Scherler et al., 2016). Because rivers are sensitive to fluctuations in sediment supply and runoff, they often alternate between states of incision and aggradation, which might result in the formation of fluvial terraces (e.g., Pazzaglia et al., 1998; Schildgen et al., 2002). Dating the terrace surfaces provides the age of onset of incision, which is typically on the order of $10^3 - 10^4$ years (e.g., Repka et al., 1997; Schaller et al., 2002; Bookhagen et al., 2006; Steffen et al., 2010; Scherler et al., 2015; Schildgen et al., 2016; Dey et al., in revision). Comparison with paleoclimate proxy records from e.g., pollen or $\delta^{18}O$ from speleothems, ice- or sediment cores, eventually allows for inferring the impact of climate change on landscape evolution.

Because the above controlling factors can be assumed to interfere with each other to various degrees (e.g., Suresh et al., 2007), valley-fill deposits might be polygenetic (e.g., Scherler et al., 2014; Dey et al., in revision), which complicates their interpretation. Here I focus on the description of valley-fills in terms of their geometry. Because valley fills constitute a substantial component of transiently stored material in the intermontane sediment cascade, knowing their thickness distribution helps to assess the long-term mass budgets of mountain belts (e.g., Straumann and Korup, 2009; Hain et al., 2011). Previous studies, which attempted to determine fill thicknesses and volumes by using geophysical methods were rather limited to individual valleys (e.g., Hoffmann and Schrott, 2002; Schrott et al., 2003; Otto et al., 2009; Götz et al., 2013) and therefore also limited in furnishing models regarding entire mountain belts. A similar issue arises with the scaling of area-volume relationships (Straumann and Korup, 2009), which assumes a self-similar landscape, not accounting for differences in e.g., lithology, structural fabric and erosional mechanism. Conventional morphometric methods on the other hand that rely on the extrapolation of slope angles into the subsurface, require significant amounts of manual digitization, which is hardly reproducible and simply not feasible for catchment- or orogen-wide studies. In light of these problems and a lacuna in reliable methodological approaches suitable for assessing sediment thicknesses at the scale of mountain belts, the first part of this PhD project was devoted to the development of an efficient methodology to determine the spatial distribution of intermontane valley-fill sediments using readily available topographic data. The second step involved the identification of suitable applications of this new method and the following research questions guided me in this process:

1. What is the role of intermontane valley-fills in modulating the isostatic response to deglaciation and erosional unloading in the European Alps?

2. How can the relatively simple metrics of thickness and volume of valley-fill deposits be used to decipher the climatic and/or tectonic history of mountain belts? What kind of additional data is required?

3. What are the factors controlling valley-fill deposition and removal in the high, semi-arid environment of the Eastern Karakoram? What are the implications for long-term landscape evolution?

I have addressed these questions in several chapters that constitute manuscripts that have either been published or that are currently in review/revision. Chapter 2 introduces an approach that uses artificial neural networks (ANNs) to quantify intermontane valley fills in terms of their thickness and hence, volume. I investigated the potential of this novel technique by conducting experiments on synthetic, semi-synthetic, and finally real-world valley fills, where results can be compared with data from geophysical measurements.

The method's applicability to large spatial scales is exemplified in Chapter 3 where I made an assessment of the volume of intermontane sedimentary valley fills for the entire European Alps. These deposits are inferred to reflect a large fraction of the material which has been eroded and stored since ice-retreat at the end of the Last Glacial Maximum (LGM; Hinderer, 2001; Dürst Stucki et al., 2010; Preusser et al., 2010; Jordan, 2010). In combination with estimates of postglacially exported material volumes (Hinderer et al., 2013), this allows to infer a mean post-LGM denudation rate of the Alpine mountain belt of ~0.7 mm yr^{-1}. The derived map of bedrock elevations was then used in a multi-model approach to answer the question of how much of the measured present-day rock uplift in the European Alps can be attributed to the Earth's isostatic adjustment to glacial and erosional unloading since the LGM. I suggest that the uplift signal is dominated by the response to ice-melting rather than erosional unloading, which contradicts current hypotheses. This study highlights the connection between surface- and upper mantle-processes, which is manifested on relatively short timescales of $10^3 - 10^4$ years. Moreover, the changing loads may affect the crustal stress field, which might trigger considerable intraplate seismicity (e.g., Grollimund and Zoback, 2001; Møller, 1993; Stewart et al., 2000; Calais et al., 2010) and thus have to be taken into account in seismic hazard assessment.

Chapter 4 analyzes the eastern margin of the Tibetan plateau where the Yarlung Tsangpo River has cut an exceptionally steep gorge through the young massifs of the eastern Himalayan syntaxis. Upstream of this gorge the river flows for ~300 km within a wide alluvial valley, where exploratory drilling reached bedrock at consistently greater depths when approaching the confluence with the Nyang River. I used the ANN approach developed in Chapter 2 to create a map of valley-fill thicknesses for the alluvial reaches of the Yarlung Tsangpo and Nyang rivers upstream of the Namche Barwa massif. The very good correlation of estimated and measured fill thicknesses helped reconstructing the longitudinal profile of the paleo Yarlung Tsangpo River. In combination with cosmogenic nuclide burial dating of material from the base of the deepest drill core using *in situ*-produced ^{10}Be and ^{26}Al, it was shown that at ~2.5 Ma the Yarlung Tsangpo River had achieved a nearly graded profile, and eroded back into the Tibetan plateau. Furthermore, the onset of aggradation just before ~2.5 Ma is consistent with the young mineral cooling ages from the Namche Barwa and Gyala Peri massifs indicating initiation of rapid exhumation after ~4 Ma, which points to a tectonically controlled formation of the Yarlung Tsangpo gorge. Thus, the formation of intermontane valley fill is a direct consequence of this tectonic uplift, which largely affected the gradient and transport capacity of the fluvial system.

Chapter 5 focuses on the interaction between glaciers, rivers and sediments in the remote eastern Karakoram mountains. Surface-exposure dating of glacial deposits and fluvial fill terraces using cosmogenic ^{10}Be allowed for a reconstruction of the aggradation and incision history of the Shyok River, which is located at the western margin of the Tibetan Plateau. The distribution of lateral moraines and lacustrine sediments indicates a former impoundment of the Shyok River by the Siachen Glacier, one of the largest glaciers of the Karakoram. A pronounced cyclicity in the lake deposits, consisting of more than 25 fining upward sequences can be observed. These probably reflect oscillating lake levels, which in turn are interpreted to be related to individual flood events that initiated farther upstream and were blocked by the Siachen Glacier dam. The study further suggests that glacial erosion outpaced fluvial incision in setting the base level for many of the tributaries draining the Karakoram. Glacial damming and associated outburst flooding thus were important, and rather frequent processes in the Quaternary evolution of these valleys and possibly have promoted headward incision into the western margin of the Tibetan Plateau.

1.2 Author contribution

Chapters 2 to 4 represent studies that were submitted to peer-reviewed journals. Chapter 2 ("Estimating the fill thickness and bedrock topography in intermontane valleys using artificial neural networks" by Jürgen Mey, Dirk Scherler, Gerold Zeilinger and Manfred R. Strecker) was published in the *Journal of Geophysical Research–Earth Surface* (Mey et al., 2015). I developed the computer code and conducted the model experiments. Chapter 3 ("Glacial isostatic uplift of the European Alps" by Jürgen Mey, Dirk Scherler, Andrew D. Wickert, David L. Egholm, Magdala Tesauro, Taylor F. Schildgen and Manfred R. Strecker) was accepted for peer review in *Nature Communications* on March 16, 2016. I co-designed the study, performed the modelling and wrote the manuscript. Chapter 4 ("Tectonic control of Yarlung Tsangpo Gorge revealed by a buried canyon in Southern Tibet" by Ping Wang, Dirk Scherler, Jing Liu-Zeng, Jürgen Mey, Jean-Philippe Avouac, Yunda Zhang and Dingguo Shi) was published in *Science* (Wang et al., 2014). I created the map of valley-fill thicknesses and contributed to writing the manuscript. Chapter 5 ("Ice dams, outburst floods, and glacial incision at the western margin of the Tibetan Plateau: A >100 k.y. chronology from the Shyok Valley, Karakoram" by Dirk Scherler, Henry Munack, Jürgen Mey, Patricia Eugster, Hella Wittmann, Alexandru T. Codilean, Peter Kubik and Manfred R. Strecker) was published in the *Bulletin of the Geological Society of America* (Scherler et al., 2014). I participated in the field work and helped with the sampling of material for exposure age dating, measured glacial striations and mapped lateral moraines. Moreover, I carried out the mechanical and magnetic separation of samples WP014, WP016 and WP020, and conducted the grain size analysis of the lake sediments.

Chapter 2

Estimating the fill thickness and bedrock topography in intermontane valleys using artificial neural networks

Abstract

Thick sedimentary fills in intermontane valleys are common in formerly glaciated mountain ranges but difficult to quantify. Yet knowledge of the fill-thickness distribution could help to estimate sediment budgets of mountain belts and to decipher the role of stored material in modulating sediment flux from the orogen to the foreland. Here we present a new approach to estimate valley-fill thickness and bedrock topography based on the geometric properties of a landscape using artificial neural networks. We test the potential of this approach following a four-tiered procedure. First, experiments with synthetic, idealized landscapes show that increasing variability in surface slopes requires successively more complex network configurations. Second, in experiments with artificially filled natural landscapes, we find that fill volumes can be estimated with an error below 20%. Third, in natural examples with valley-fill surfaces that have steeply inclined slopes, such as the Unteraar and the Rhône Glaciers in the Swiss Alps, for example, the average deviation of cross-sectional area between the measured and the modeled valley fill is 26% and 27%, respectively. Finally, application of the method to the Rhône Valley, an overdeepened glacial valley in the Swiss Alps, yields a total estimated sediment volume of 97 ± 11 km^3 and an average deviation of cross-sectional area between measurements and model estimates of 21.5%. Our new method allows for rapid assessment of sediment volumes in intermontane valleys while eliminating most of the subjectivity that is typically inherent in other methods where bedrock reconstructions are based on digital elevation models.

2.1 Introduction

The sedimentary fills of intermontane basins and adjacent forelands have been considered underutilized archives (DeCelles, 2012) that potentially yield information on the interaction between tectonic, erosive, and depositional processes and on economically relevant deposits. In addition, human population centers in mountainous regions are usually located on the floor of intermontane valleys, with sedimentary fills of spatially variable thickness. These sedimentary fills usually host aquifers that are important for human water consumption, agriculture, and geothermal energy production (Margat and der Gun, 2013). The thickness of unconsolidated valley fills also influences seismic wave propagation, with greater thicknesses promoting higher surface-wave amplitudes, hence increasing earthquake hazards associated with liquefaction and landsliding in tectonically active mountain belts (e.g., Aki and Richards, 2002; Allen and Wald, 2009; Mugnier et al., 2013). Intense shaking of soils and unconsolidated terrace deposits in the intermontane basin close to the epicenter of the 2015 M7.8 earthquake of Nepal is dramatic example of the relationships between valley fills and increased seismic hazards (http://earthquake.usgs.gov/earthquakes/shakemap/global/shake/20002926/).

Finally, knowing the distribution of sediment thicknesses in intermontane valleys further helps to assess the long-term sediment budgets of mountain belts (e.g., Straumann and Korup, 2009; Hain et al., 2011) and to understand the role of stored material in the sediment cascade from the orogen to foreland basins and beyond (e.g., Caine and Swanson, 1989; Ingersoll, 2011; Scherler, 2014; Wang et al., 2014).

However, direct measurements of sediment thicknesses are complex and time consuming and typically require sophisticated geophysical tools, infrastructure, and logistics that are often not available. This is the reason for a general scarcity of sediment-thickness data,, especially in remote areas of mountain belts such as the intermontane valleys of the Eastern Cordillera of the Andes, the Pamir of Central Asia, or the Himalaya-Karakoram orogen. Moreover, direct measurements are always restricted to a limited number of points or profiles that require significant interpolation to achieve more complete coverage. Unlike in the case of valley glaciers, where a number of reasonably well performing, ice physics-based methods for estimating ice thicknesses exist (Huss et al., 2008; Farinotti et al., 2009; Li et al., 2012; Linsbauer et al., 2012; Clarke et al., 2013), no corresponding approach for estimating sediment thicknesses is available. Therefore, previous studies that attempted to determine sediment volumes in intermontane valleys have largely used empirically based volume-area scaling, a method that is readily applicable to entire mountain belts (Straumann and Korup, 2009; Blöthe and Korup, 2013) but does not yield the spatial distribution of sediment thicknesses. Furthermore, this approach assumes universal self-similarity that is most certainly an oversimplification of natural systems, particularly when considering differences in lithology or geomorphic history, e.g., fluvial versus glacial sculpting or combinations thereof. Studies that explicitly address the distribution of valley-fill thicknesses or bedrock elevations have mainly used morphometric methods combined with geophysical measurements and are therefore spatially restricted to areas where such data are available (e.g., Hinderer, 2001; Schrott and Adams, 2002; Schrott et al., 2003; Otto et al., 2009).

Alternative approaches that do not depend on geophysical constraints involve, for instance, a simple geometric projection of hillslopes into the subsurface along cross-valley profiles (e.g., Brooks, 1992; Hinderer, 2001) or surface interpolation using splines (Smith and Wessel, 1990). The former method requires users to make a number of rather arbitrary decisions concerning profile locations, the distance over which hillslope angles are determined, and the method that is used for interpolation. The latter method on the other hand tends to result in smooth, minimum curvature surfaces and makes the reconstruction of a V-shaped valley morphology virtually impossible (e.g., Sulebak and Hjelle, 2003). Similarly, the sloping local base-level method (Jaboyedoff and Derron, 2005) was specifically developed to estimate the fill thickness in glacial U-shaped valleys, assuming parabolic cross sections. The aim of this study is to develop a method that allows predicting the bedrock topography beneath valley fills, eliminates the subjectivity as much as possible, and can be applied to glacial as well as to fluvial valleys from catchment to mountain-belt scale. Inspired by the work of Clarke et al. (2009), who used artificial neural networks (ANNs) to estimate glacier-bed topography and ice volumes, we present a modified version of this approach, which is based on the assumption of morphological similarity between exposed and buried parts of the landscape.

In the remainder of this study, we first provide a brief introduction to the principles of ANNs before we describe our approach in detail. To explore the general functionality of ANNs with respect to our research question, we first run experiments with four synthetic landscapes of different complexity, followed by tests on five natural valley sites that were artificially filled. Subsequently, we apply the method to the Unteraar and the Rhône Glaciers in the European Alps, which we consider as special cases of valley fills with steeply inclined surfaces. The available ground-penetrating radar measurements of ice thicknesses (Funk et al., 1994; Bauder et al., 2003, 2007) allow for an analysis of the predictive performance under natural conditions. In a third case study, we estimate the sediment-fill thickness in the Rhône Valley, one of the largest intermontane valleys in the Central Alps, and use seismic reflection data (Finckh and Frei, 1991; Pfiffner et al., 1997) to assess the method's performance on a large spatial scale. Finally, we discuss limits, uncertainties, advantages, and promising applications of our method.

2.2 Methods

2.2.1 Principles of ANNs

ANNs are mathematical models that can perform supervised learning. They comprise artificial neurons called nodes, which are organized in layers as shown in Fig. 2.1a. The nodes of adjacent layers receive and

transmit signals through a number of weighted connections, ultimately leading to a response of the entire system, the desired output. The layer between inputs and output is called hidden layer, and the corresponding nodes are called hidden nodes (Bishop, 1995). The actual processing (Equation 2.1) takes place at the hidden nodes and the output node. Each processing node is assigned a layer-specific activation function f, which takes the weighted sum of the inputs plus a bias and produces the node's response or activation value y_j, according to:

$$y_j = f\left(\sum_i w_{ij} x_i + \theta_j\right) = f\left(s_j\right) \tag{2.1}$$

where x_i is the i-th input, w_{ij} is the weight for the connection from the i-th input to the j-th node, and θ_i is a bias for node j. The activation values of hidden nodes represent the inputs for the node of the output layer (Fig. 2.1a). It has been shown (Hornik et al., 1989) that an ANN that consists of one hidden layer with a nonlinear activation function (f) is able to approximate any continuous function to arbitrary precision, provided that the number of hidden nodes is sufficiently large. One of the most common choices for f is the hyperbolic tangent $f(s_j) = \tanh(s_j)$ (Bishop, 1995; LeCun et al., 1998). In this study, we only investigated ANNs using a hyperbolic tangent activation function, at a single hidden layer, a linear activation function, $f(s_j) = s_j$ at the output layer, and a scaled conjugate gradient learning algorithm (Møller, 1993).

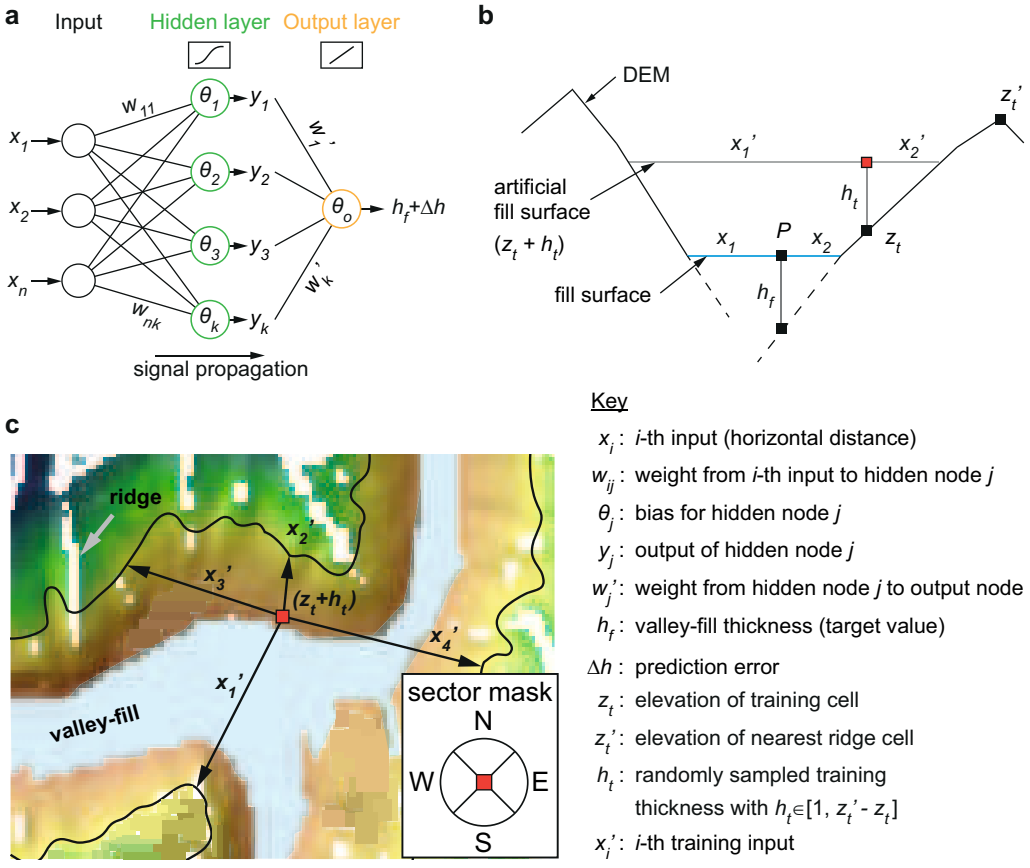

Figure 2.1: Schematic illustration of the presented method. (**a**) Example of a two-layer feed forward artificial neural network with three inputs, four hidden nodes, and one output node. The type of activation function for the active layers is indicated by the pictograms, hyperbolic tangent for the hidden layer, and linear for the output layer. The color of the nodes refers to the respective layer in which they are organized. (**b**) Idealized valley cross section illustrating the variables used in (**a**) and in the text. The training data are obtained by using an artificial fill surface (see text for details). Dashed lines represent the valley fill-bedrock interface. (**c**) Map view of (**b**) and the corresponding sector mask with four sectors. Thin black line is the elevation contour $z_t + h_t$. In (b) x_3' and x_4' have been omitted for clarity. DEM = digital elevation model.

The ability to learn and generalize from training data is the central property of ANNs. In the training phase, the ANN processes a number of independently constrained input-output examples and iteratively

adjusts the weights to minimize the residual error between observed and predicted output of the training data. This recursive procedure, the learning, is continued until a predefined stop criterion is met. The resulting training error is influenced by the learning algorithm, the number of iterations or training cycles, and the number of training examples and hidden nodes. The number of training examples determines how well the underlying function, which relates inputs to outputs, is represented during the learning, whereas the number of hidden nodes controls the network's ability to approximate functions of different "complexity". More hidden nodes are needed for fluctuating functions than for smooth functions. A crucial requirement for ANN-based predictions is that the training data form a representative subset of all the cases we wish to predict. Predictions that fall outside the ranges of input and output values defined by the training data require extrapolation and hence are unreliable (Haley and Soloway, 1992). We used the ANN implementation provided by the free MATLAB toolbox NETLAB (Nabney, 2002).

2.2.2 Input data

For successful predictions with an ANN, the identification of appropriate inputs is essential (Wolpert, 1994, 1996b,a); i.e., there has to be a functional relationship between the input variables and the prediction target or output. In our case, the output is the thickness of the valley fill or, when subtracted from the elevation of the fill surface, the bedrock topography beneath the valley fill. For the choice of input data we followed Clarke et al. (2009), who found that the distance to the nearest hillslope above the valley fill, calculated for different directions by applying an angular sector mask (Fig. 2.1c), provides the most useful geometric information for the ANN. This choice can be based on the geometrical argument that the width of the valley floor is positively correlated with the valley-fill thickness (Wang et al., 2014). For a given point, P, in the center of the valley floor, an increase of the distance to the nearest hillslope is accompanied by an increase in the valley-fill thickness at P, provided that constant hillslope angles exist (Fig. 2.1b). If we consider only one distance, the prediction will likely result in rather symmetrical valley cross sections. Therefore, we need to include at least one additional distance input to better account for the asymmetry of natural valleys. The relationship between these distances and the valley-fill thickness can be learned and generalized by an ANN, provided that a sufficiently large pool of training examples can be acquired. Obviously, the perfect training data set would consist of a large number of valley-fill thickness measurements, e.g., obtained by drilling, which cover the entire range of valley morphologies. Every possible combination of input and output would have an optimal representation in a subset of this data set, which could be used for the training process. Unfortunately, direct observations are rare and spatially discontinuous, as mentioned earlier, so we cannot recruit our training data from field measurements. However, if there exists morphological similarity between hillslopes above the valley fill and the bedrock surface beneath the valley fill, we can use a digital elevation model (DEM) to create a large number of training examples. This morphological similarity could be assumed if we argue that the entire landscape was once subjected to the same surface-shaping processes prior to the deposition of the valley fills as in the case of the European Alps (e.g., Kelly et al., 2004) and presumably other mountain belts that were affected by Pleistocene glaciations (see Discussion Section 2.5). We consider the effect of a deviation of subaerial and subsurface morphologies on the prediction at the end of Section 2.3.

To test the validity of our approach under ideal conditions, i.e., with preset morphological similarity, we carried out experiments using synthetic landscapes of different complexity (see Section 2.3). We created our training data according to the following procedure (Figs. 2.1b, 2.1c).

1. First, we create a mask of the valley fill by manually digitizing the valley-floor deposits using a geological map. In regions for which no or only synoptic geological maps are available, the creation of the mask can be done based on aerial images combined with a shaded relief map. Alternatively, in steep landscapes, one may use a slope threshold and further processing to automatically detect valley-fill surfaces (e.g., Blöthe and Korup, 2013). All unmasked cells constitute a pool of potential training cells.

2. A predefined number (N) of cells are randomly chosen from the training pool and constitute the actual training cells.

3. For each training cell, located at an elevation z_t, a randomly chosen value, h_t, is added and the entire DEM is artificially filled to the elevation $z_t + h_t$. Pixels below this fill are masked out. The

value h_t is restricted to lie within the interval [1 m, $z'_t - z_t$], where z'_t is the elevation of the nearest ridge cell satisfying the condition $z'_t > z_t$. This constraint ensures that a sufficient fraction of the topography remains exposed after artificially filling the DEM. Ridge cells are defined as all cells that are characterized by a flow accumulation of zero; that is, there exist no cells in the DEM that belong to the contributing area of the ridge cells. This zero-flow accumulation condition is satisfied not only by cells representing ridge crests but also by isolated cells on the hillslopes. We consider these scattered cells as noise and remove them with a 3×3 median filter. The value h_t represents the training output.

4. The training inputs are assembled by calculating the Euclidean distances to the valley walls for n directions, using an angular sector mask (Fig. 2.1c) as proposed by Clarke et al. (2009).

The above procedure results in N vectors that consist of the input and output data, which are used for training the network. DEM cells, which were not selected in Step 2, are used to generate a validation data set (again by applying Steps 2 to 4) that is used to estimate the generalization error. Besides modifying the initial mask (Step 1) and thereby limiting the training data to a particular range of variable values, the parameters that can be varied to explore network performance are the number of inputs (sectors, n), hidden nodes (p), and training examples (N) and the number of training cycles. The hidden nodes represent small processors that perform the calculation defined in Equation (2.1). As such they do not have a representation on the map and their number can arbitrarily be chosen. Before we apply our ANN to real landscapes, we first systematically benchmark different network configurations in terms of the number of inputs, hidden nodes, and training examples by using synthetic data sets, which provide insight into the input-output relationship. By following the above split-sample approach, where the data are divided into a training set and a validation set that are both based on the same landscape above the valley fill, we can automatically and objectively determine the optimal network configuration (Weiss and Kulikowski, 1991).

In our experiments on natural landscapes we used a 30-m-resolution DEM that was generated by J. de Ferranti (http://www.viewfinderpanoramas.org) by digitizing the elevation contours of local topographic maps from the year 1997, with scales of 1:25,000 and 1:50,000. In the case of the Rhône Valley, we resampled the DEM to 90-m-resolution to increase computational efficiency. For processing the digital elevation data we used the MATLAB-based TopoToolbox 2 (Schwanghart and Scherler, 2014).

2.3 Synthetic landscapes

We created four different synthetic landscapes that have radial symmetric shapes, as we want to exclude effects that arise from valley asymmetry. The first two of these landscapes have V-shaped and U-shaped idealized cross sections resembling those of fluvial and glacial valleys, respectively (Fig. 2.2).We additionally prepared a third landscape that has a smooth sinusoidal cross section, similar to that expected for a composite valley. To explore the effect of random deviations from ideal shapes, we included another landscape where we added noise to the U-shaped example, which we refer to as U-noise hereafter. In each of these landscapes a valley fill is created that separates the data into two subsets. All cells that lie above the fill surface are used to generate the training and validation data sets, and the cells below the fill surface are used to generate the test data set. To avoid extrapolation, we chose the elevation of the valley fill so that the maximum fill thickness lies well within the elevation range of the training data. The difference between the estimated and the observed valley-fill thicknesses is used to calculate the root-mean-square error (RMSE):

$$RMSE = \sqrt{\frac{1}{M}\sum_{1}^{M}\left(h_f - h_e\right)^2} \tag{2.2}$$

where h_f is the observed valley-fill thickness, h_e is the estimated valley-fill thickness, and M is the total number of predictions, i.e., the number of fill cells. To facilitate comparison between different experiments and landscapes, we normalized the RMSE by the range of observed thicknesses (h_f) according to:

$$NRMSE = \frac{RMSE}{h_{max} - h_{min}} \tag{2.3}$$

where h_{min} is the minimum and h_{max} the maximum observed valley-fill thickness. In the following, the NRMSE of the validation and the test data sets are simply termed E_v and E, respectively. In principle, we

can sample very large numbers of training examples (N) from the pool of potential training cells, i.e., from the landscape above the valley fill. However, the computation time increases with $\sim 0.75N$, and therefore, we tested the behavior of our ANN as we systematically increase N. We chose the number of training examples N depending on the number of predictions (M). In a first series of runs we keep N at approximately 0.01 times the number of predictions and systematically increase the number of hidden nodes and sectors from 1 to 20. Each of the resulting 400 different network architectures passes through 100 training cycles and is applied to the validation set. To obtain statistically more reliable results, we perform four of these parameter tests for each synthetic landscape and use the mean of the corresponding minimum error on the validation set, $\bar{E}_{v,min}$, as an estimate for the generalization error for each network configuration (Bishop, 1995). This procedure is repeated as we increase N to 0.1, 0.5, 1, and 2 times the number of predictions. The following results can be observed. All landscapes show a decrease of $\bar{E}_{v,min}$ when N/M is raised from 0.01 to 0.1 (Fig. 2.3a). Any further increase of N/M has only minor effects on $\bar{E}_{v,min}$. Because N only needs to be high enough to represent the variation in the data, any further increase of N leads to higher redundancy in the inputs and does not significantly improve the estimates.

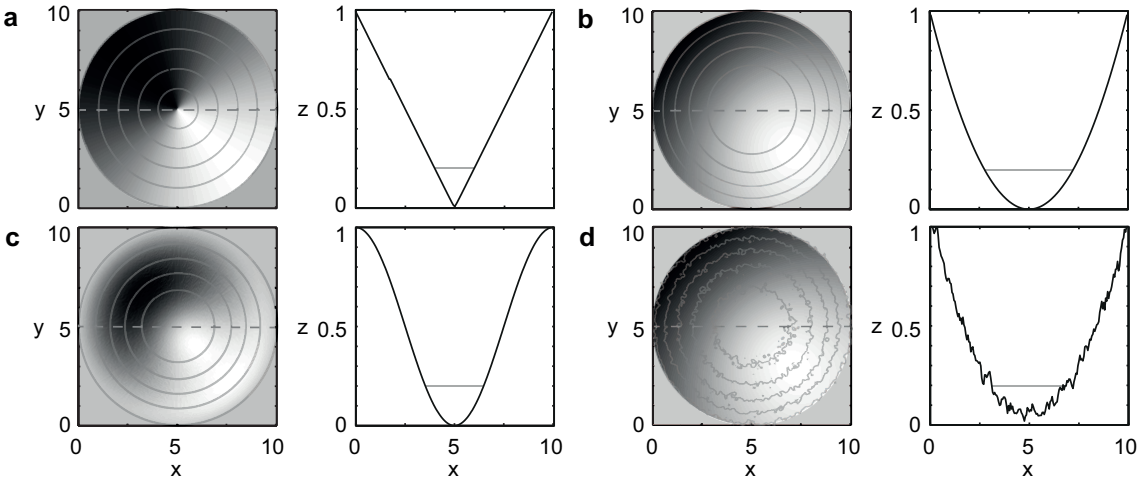

Figure 2.2: Synthetic landscapes used to investigate the general network functionality. Each example is shown in map view and in the corresponding cross-sectional view, respectively. (**a**) V-shape, (**b**) U-shape, (**c**) a sinusoidal landscape, and (**d**) U-shape with added noise. Contours in map view are drawn at intervals of 0.2. The thin horizontal line in the cross-sectional view indicates the artificial fill level which is chosen to be constant and at an elevation of 0.2 units for all synthetic examples.

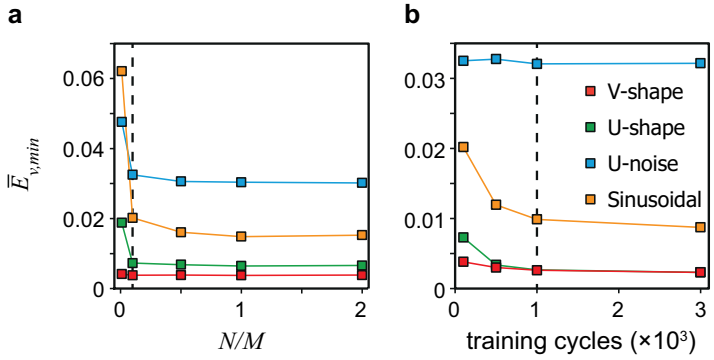

Figure 2.3: Sensitivity of minimum validation error ($\bar{E}_{v,min}$) to network architecture. (**a**) Influence of number of training cells relative to number of test cells. The number of training cycles is fixed at 100. (**b**) Influence of number of training cycles. The N/M ratio is fixed at 0.1. Vertical dashed lines indicate N/M ratio and number of training cycles used for all subsequent experiments. Legend in (**b**) refers to the synthetic data sets shown in Fig. 2.2.

Next, we kept the N/M ratio equal to 0.1 and increased the number of training cycles stepwise from 100 to 500, 1000, and 3000. In case of the sinusoidal and the U-shaped landscapes $\bar{E}_{v,min}$ is reduced by half at

1000 training cycles, whereas increasing the number of training cycles to more than 100 has no effect on $\bar{E}_{v,min}$ for the other two landscapes (Fig. 2.3b). We conclude that with $N/M = 0.1$ and with 1000 training cycles, we have reached a good compromise between prediction accuracy and computational effort.

With the number of training examples and training cycles fixed, we next determined which combination of hidden nodes and sectors results in the lowest validation error and we used this combination for the prediction phase (Fig. 2.4). Based on our assumption of morphological similarity between the landscape above and below the valley fill, we expect that errors on the training/validation data set and the test data set follow a similar trend; i.e., network configurations that yield low validation errors should also lead to low test errors. This expectation is generally confirmed for all the synthetic landscapes, and for each, a distinctive pattern in the distributions of $\bar{E}$ and $\bar{E}_v$ (averaged over four model runs) is apparent. For the V-shaped landscape the errors are more sensitive to changes in the number of sectors than to changes in the number of hidden nodes, with more sectors resulting in higher errors. All network configurations that use only one sector (one input), including the simplest configuration of one sector and one hidden node, result in virtually perfect predictions. This can be attributed to the radial symmetry and straight slopes.

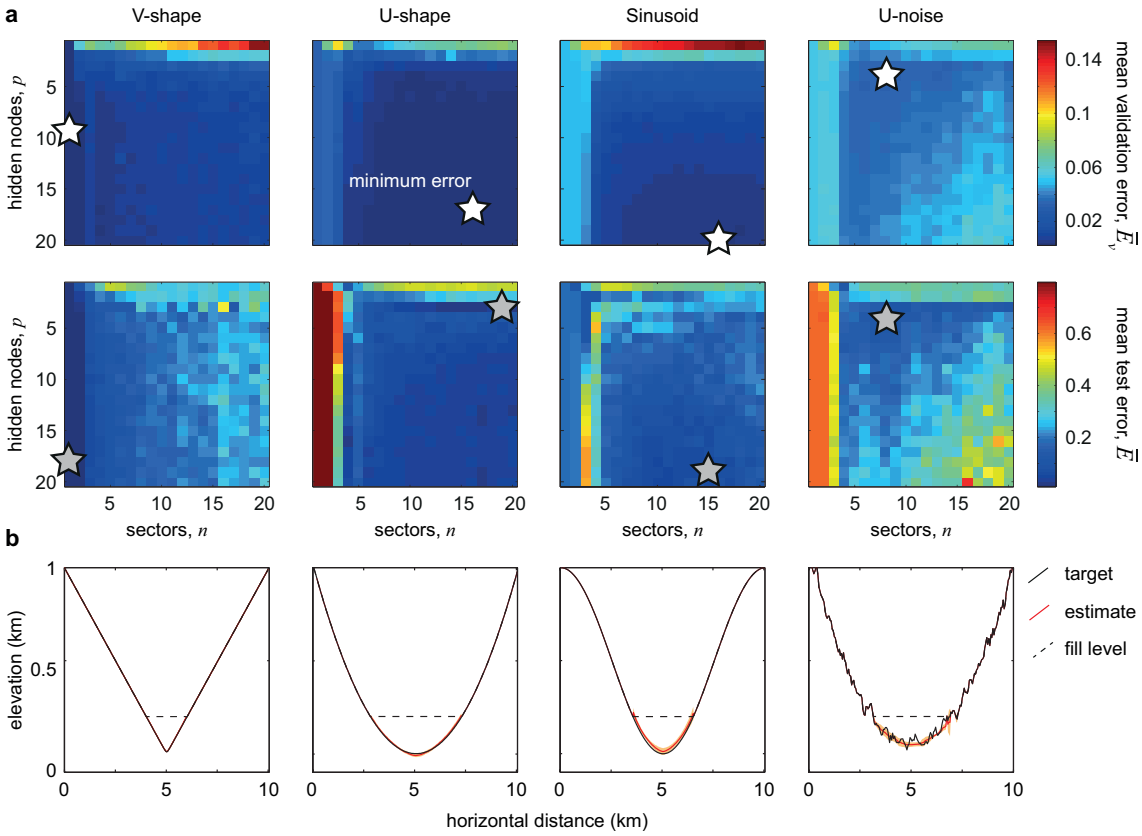

Figure 2.4: Synthetic data model results. (**a**) Mean validation error ($\bar{E}_v$) and mean test error ($\bar{E}$) as a function of the network configuration in terms of the number of sectors (n) and hidden nodes (p) for the four synthetic landscapes. Stars indicate the minimum error network configurations, i.e., number of sectors—number of hidden nodes for the validation data set (V-shape: 1–9, U shape: 16–17, sinusoidal: 16–20, and U noise: 8–4, (top row)) and the test data set (V shape: 1–18, U shape: 19–3, sinusoid: 15–19, and U noise: 8–4, (bottom row)). Zones of low $\bar{E}_v$ coincide with depressions in $\bar{E}$ for all cases. (**b**) Cross sections showing the observed and the estimated thicknesses when minimum $\bar{E}_v$ configuration is used for prediction. Orange regions represent the 2σ envelope. Statistics are calculated from four runs with N/M= 0.1 and 1000 training cycles.

In contrast, the U-shaped and sinusoidal landscapes reach their minimum validation errors at considerably higher numbers of sectors and hidden nodes and have also higher corresponding test errors. Network configurations with only one to two hidden nodes result in relatively high validation errors, and at least four sectors are required to adequately account for the input-output relationship. We note that for both of these landscapes it is possible that even better results could be obtained by further increasing the number of hidden nodes and/or sectors. However, the prediction accuracy already reached is sufficiently high and does not

seem to warrant extra computation time. The pattern of $\bar{E}$ in the U-noise landscape is more complex, with both errors increasing with the number of sectors and hidden nodes. Minimum errors are achieved with eight sectors and four nodes. It is important to note that the predicted topography beneath the valley fill is smooth and reflects projection of the U-shaped topography, without the added noise (Fig. 2.4b). We furthermore observe a higher variation in the output of the individual networks, as indicated by the 2σ envelope of the predicted valley beneath the fill in Fig. 2.4b.

In summary, our experiments have shown that it is in principle possible to train an ANN for predicting valley-fill thicknesses if a morphological relationship between the training and test data sets exists. With an independent validation data set, the validation error can be used to constrain the optimal network configuration. Furthermore, if short-wavelength undulations in the training data can be considered noise, the method will predict rather smooth surfaces, devoid of this noise. However, if the geometries of the training and test data sets depart from each other due to, for instance, breaks in the slope angle below the fill surface, larger errors might be encountered. Theoretically, an abrupt increase of the slope angle beneath the valley fill would lead to an underestimation, whereas an abrupt decrease would lead to an overestimation of the valley-fill thickness. In our synthetic landscapes, the relative magnitude of this error depends on the magnitude of the break in slope angle and the depth below the fill surface at which this break occurs. Figure 2.5 shows the functional relationship between the difference in slope angle, γ, between hillslope angles in the training (α) and test region (β) and the resulting deviation in cross-sectional area, ΔA, and maximum fill thickness, ΔH, for a V-shaped landscape. For a given γ, both ΔA and ΔH decrease with increasing slope angles in the training region. If we consider hillslope angles of 20–40° and breaks in slope of -20° to +20° as reasonable values in mountainous terrain, ΔA would range between -100% and +130% and ΔH between -2000% and +70%. However, these errors only reflect the worst case in which the break in slope occurs directly at the elevation of the valley fill surface. With increasing depth of the break in slope below the fill surface, the magnitudes of ΔA and ΔH decrease further.

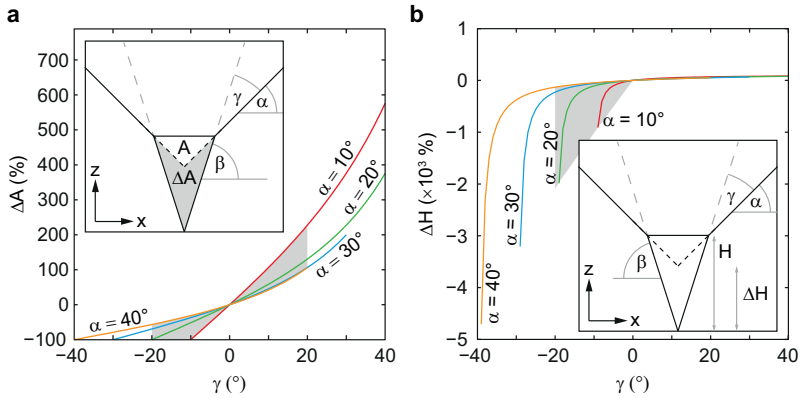

Figure 2.5: The effect of a violation of the main assumption of morphological similarity between exposed and buried parts of the landscape. (**a**) The deviation in cross-sectional area (ΔA), as a function of the difference in slope angle (γ) between hillslopes above (α) and below (β) the valley fill surface with $\gamma = \beta - \alpha$. (**b**) Deviation of the maximum fill thickness (ΔH) as a function of γ. The grey shaded area in (**a**) and (**b**) represents likely combinations of α and β in high mountain environments. Positive and negative (ΔA) and (ΔH) indicate underestimation and overestimation, respectively.

2.4 Natural landscapes

2.4.1 Natural landscapes with artificial fills

To test the method's performance in natural settings, we next applied it to three glacial (U1–U3) and two fluvial (V1 and V2) valleys in the Central European Alps that contain no visual, morphologic, or geologic evidence for substantial sediment infill (Fig. 2.6). The sizes of the corresponding catchments range between 10 km^2 and 150 km^2 (see Table 2.1). We followed the same procedures as in the case of the synthetic landscapes and defined the training/validation and test data sets by artificially filling each valley to a constant elevation. Again, to avoid extrapolation, the fill elevation was chosen so that the maximum valley-fill

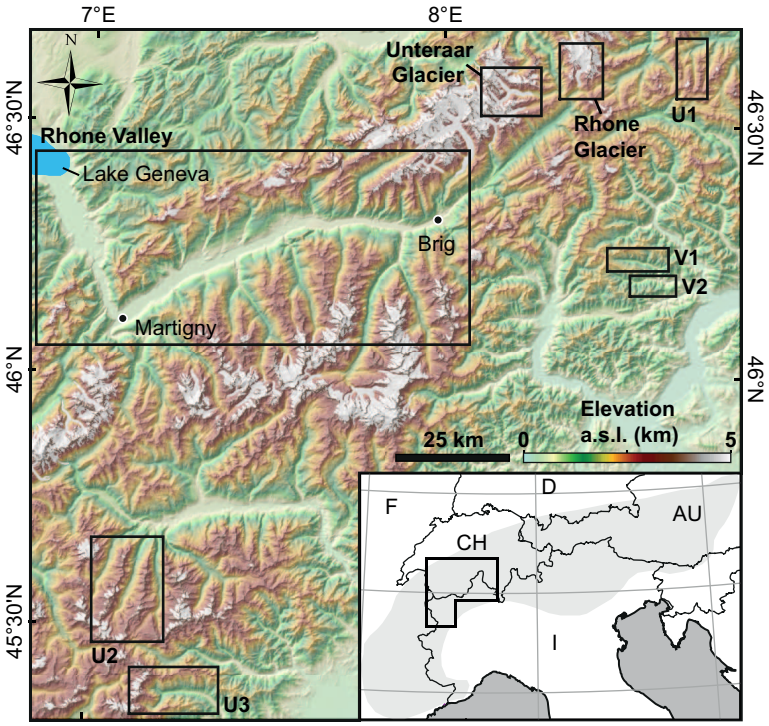

Figure 2.6: Overview of study areas in the Central European Alps. Our method was tested on artificially filled fluvial (V1 and V2) and glacial (U1–U3) valleys. Experiments on natural fills were carried out for the Unteraar Glacier, the Rhône Glacier, and the Rhône Valley. White areas are present-day glaciers after Arendt et al. (2012).

Table 2.1: Experiment Results for Natural Valleys with Artificial Fills[a]

			Area (km^2)		Volume (km^3)				Mean Thickness (m)		Best Configuration[d]	
ID[b]	Type	h* (m)	Catchment	Fill	Observed	Estimated	ΔV^c (%)	$\bar{E}$ ($\times 10^{-2}$)	Fill	Training	Validation	Test
V1	fluvial	20	65 7	2 6	0 205	0.193 (0.210)	5.8 (-2.3)	8.1 (10.2)	79	71 (83)	2/5 (4/10)	1/1 (1/1)
V2	fluvial	100	52 6	3 4	0 325	0.319 (0.332)	2.0 (-2.1)	7.0 (7.3)	95	61 (96)	1/1 (2/10)	1/1 (1/1)
U1	glacial	20	11 4	1 2	0 115	0.104 (0.113)	9.0 (1.3)	7.6 (5.5)	100	91 (102)	7/6 (6/3)	6/4 (6/3)
U2	glacial	50	152 1	6 3	0 810	0.726 (0.771)	10.3 (4.8)	8.6 (8.2)	128	104 (124)	8/15 (5/12)	8/5 (8/11)
U3	glacial	150	95 6	8 1	1 365	1.389 (1.403)	-1.8 (-2.8)	11.3 (10.9)	169	122 (173)	5/16 (7/18)	6/5 (6/5)

[a] Experiments were carried out with N/M= 0.1 and 1000 training cycles; values in parentheses refer to experiments where threshold h* was applied to the training/validation set (see text for details).
[b] For location of valleys V1, V2, and U1–U3, see Fig. 2.6.
[c] Negative sign indicates an overestimation of the observed fill volume.
[d] Best configuration with respect to the number of sectors/hidden nodes.

thicknesses fell into the range of the possible training thicknesses. In contrast to the synthetic landscapes, the artificial valley fill of the natural landscapes is in direct contact with the DEM boundaries on at least one side, and for some DEM cells, the distance to unmasked hillslopes is not defined within certain sectors. Cells in the training data set for which this is the case were excluded from the training. In consequence, the maximum number of training cells decreases, as the number of sectors n increases. The same applies to the number of cells in the valley fill for which predictions are possible: with progressively more sectors, the area of the test data set shrinks from the DEM boundaries inward. We thus constrained n to be not greater than eight, as otherwise the size of the test data set would be too small and there would be too few training cells to provide a good spatial representation of the surrounding hillslopes. Using a larger DEM is a way to minimize the impact of the above-described edge effects. However, due to the higher computational costs, we preferred to use rather small test scenarios at this stage of our investigation.

We used the same number of training examples ($N/M = 0.1$) and training cycles (1000) as in our experiments with synthetic landscapes, and for each of the valleys the network configuration with the lowest mean error in the validation phase ($\bar{E}_v$) was chosen for the prediction of the test data set. In addition to the mean test error $\bar{E}$, we also included the volume difference ΔV of the valley fill as another prediction criterion.

The results show that for all valleys the mean prediction error $\bar{E}$ is close to 0.1, that is, 10% of the maximum fill thickness, and the volume difference ranges from approximately -2% to +10% (Table 2.1). Due to the fact that we underestimated the true valley-fill volumes in four out of five valleys and that in each of these cases the mean fill thickness in the training data was smaller than the corresponding mean fill thickness in the test data, we investigated the effect of adjusting the sampling range of training cells so that the mean training thickness is similar to the mean fill thickness. To do so, we introduced a threshold h^* to limit the training/validation data set to those cells, which meet the condition $(z_i' - z_i) > h^*$. Effectively, we constrain the samples in the training/validation data set to meet a certain thickness criterion. In this case, we provide a lower bound for the possible training thicknesses h_t. Although this modification is somewhat ambiguous, a consistent lowering of ΔV can be observed and leads to a slight overestimation of the total volumes in three of the five valleys (numbers in parentheses in Table 2.1). The entire error distribution in the numbers of sectors and hidden nodes space and comparison between estimated and observed thicknesses are provided in Figs. A.1–A.5 in the supporting information. Although *a priori* knowledge of the mean valley-fill thickness is unlikely, there may exist ways of inferring the magnitude of h^*, which we address in the discussion below (see Section 2.5.4). For now, we refer to the results without any threshold imposed and show that the best network configuration appears to be affected by valley type. The optimal network configuration from the validation phase consists of only one or two sectors in the case of V-shaped valleys (V1 and V2), which is consistent with the respective optimal network configuration in the test phase and with our results from the synthetic landscapes. In contrast to this, the best network configurations in the glacially sculpted, U-shaped valleys consist of more sectors, in both the validation and the test phase. This is in general agreement with our results from the synthetic landscapes.

The main findings from our experiments with natural valleys and artificial fills are as follows. First, our main assumption that we can use existing morphological similarities between training and target regions to reconstruct the bedrock topography remains valid. The results suggest that we can estimate fill volumes with an error well below 20%. Second, if we can tune our sampling of training examples to account for the frequency distribution of the valley-fill thicknesses, our estimates improve. This represents a possibility to incorporate *a priori* knowledge about the valley fill of interest (e.g., from borehole data or seismic profiling) into the model. Third, for spatially extensive valley fills that stretch beyond the region of interest defined by the DEM boundaries, the possibility that one or more of the sectors remain undefined increases with the number of sectors. This can be accounted for by either limiting the number of sectors, as we did above, or by simply increasing the spatial dimension of the DEM to ensure that edge effects do not affect the region of interest. The latter, however, requires that the surrounding mountains are sufficiently high, which may be difficult to achieve for valley fills that grade into foreland basins. Finally, we acknowledge that natural valley fills are not perfectly horizontal but rather exhibit gently sloping surfaces, unless they are located in intramontane orogenic plateaus that have been subjected to protracted internal drainage conditions, such as in the Andes (e.g., Strecker et al., 2009) or parts of the Anatolian Plateau (e.g., Schildgen et al., 2014). We address the question of how the model outcome is influenced by the inclination of the fill surface in the following section.

2.4.2 Glaciers

From the somewhat unrealistic horizontal fills of the last section, we proceeded in our investigation of natural landscapes to present-day glaciers, which represent another type of valley fill, usually associated with more steeply inclined surfaces. We apply our method to the Unteraar and the Rhône Glaciers in the European Alps (Fig. 2.6). Both are moderately large valley glaciers with surface areas of 23 km^2 and 15 km^2, respectively (see Table 2.2), and were chosen due to their distinct shapes (Fig. 2.7). The Unteraar Glacier has three main branches and is confined by very steep hillslopes (mean slope angle ~38°), whereas the Rhône Glacier has a more compact geometry and the surrounding hillslopes are less steep (mean slope angle ~31°). The glaciers themselves have highly variable surface slopes of 0–65° (mean 11°) for the Unteraar Glacier and 0–46° (mean 13°) for the Rhône Glacier. Furthermore, there exist several ice-thickness measurements, based on ground-penetrating radar (GPR) data that we used for ground control. These measurements have yielded a maximum ice thickness of approximately 440 m for both glaciers. Borehole studies on the rheological properties of the substratum beneath the lower part of Unteraar Glacier show that at least partly, the ice rests on a layer of unconsolidated material (Fischer et al., 2001). While the thickness and extent of subglacial

Table 2.2: Ice Volume Estimates and Deviation in Cross-Sectional Areas (ΔA)

		ΔA[a]		Volume (km^3)			Best Configuration[c]	
Name	Area (km^2)	m^2 ($\times 10^4$)	%	Volume-Area Scaling[b]	Farinotti et al. (2009)	ANN	Validation	Test
Unteraar Glacier	22.7	5.8	26	2.3	4.00	3.6 ± 0.4	6/20	14/19
Rhône Glacier	15.1	4.1	27	1.3	1.97	2.6 ± 0.5	6/17	8/17

[a] Mean absolute deviation in cross-sectional areas between measurements and ANN estimates.
[b] Taken from Table 4 in Farinotti et al. (2009).
[c] Best configuration with respect to the number of sectors/hidden nodes.

sediments remain speculative (Röthlisberger and Vögtli, 1967; Funk and Rothlisberger, 1989), similar investigations on other Alpine glaciers have shown that the thickness of basal till typically is in the range of meters (e.g., Kavanaugh and Clarke, 2006; Hart et al., 2011). The recent retreat of the Rhône Glacier exposes bedrock. Farinotti et al. (2009) estimated the total ice volume of the Unteraar Glacier to be ~4 km^3 and the volume of the Rhône Glacier to be ~1.97 km^3, using bedrock reconstructions based on mass-balance fields and ice-mechanical principles. In contrast, volume estimates derived from volume-area scaling (after Bahr et al., 1997) are much lower with 2.3 km^3 for the Unteraar Glacier and 1.3 km^3 for the Rhône Glacier (see Table 2.2).

For the ANN-based approach, we used the glacier outlines provided in Farinotti et al. (2009) to create our fill masks. On the Unteraar Glacier we tested network architectures encompassing 1–20 sectors and 1–20 hidden nodes, whereas on the Rhône Glacier we limited the number of sectors to eight because of the low number of potential training cells at higher numbers of sectors, which would also result in a low spatial extent of the training region. Because we do not know the true ice thickness for each DEM cell that is part of the ice fill, we determined the test error using the GPR data shown in Fig. 2.7 according to Equation 2.3 with h_{min} and h_{max} being the minimum and the maximum measured thickness, respectively.

As we are dealing with actively evolving subglacial terrain, we expect U-shaped valley cross sections beneath the ice, which is confirmed by GPR data. Thus, we also expect similarly complex optimal network configurations as for the U-shaped valleys in Section 2.4.1. Indeed, the minimum validation error for both glaciers is achieved with network configurations of six sectors and a relatively high number of hidden nodes (Unteraar Glacier: 20; Rhône Glacier: 17; Table 2.2). The magnitude of the mean errors for the validation and test data sets, as a function of numbers of sectors and hidden nodes, is shown in the supporting information Fig. A.6. Comparison of our estimates with measured ice thicknesses along the GPR profiles yields acceptable results (Fig. 2.7) with test errors of 0.21 (21%) for the Unteraar Glacier and 0.22 (22%) for the Rhône Glacier. In general, however, the ANN tends to underestimate the measured ice thicknesses (Fig. 2.8a). For both glaciers the mean misfit is approximately -40 m with a standard deviation of ~70 m (Fig. 2.8b). An explanation for this underestimation could be the presence of breaks in slope beneath the ice surface (e.g., profile vi in Fig. 2.7b) or gently sloping lateral moraines at the base of hillslopes in the ablation area (e.g., profile v in Fig. 2.7b).

The mean absolute deviation of cross-sectional areas is 5.8×10^4 m^2 for the Unteraar Glacier and 4.1×10^4 m^2 for the Rhône Glacier which corresponds to 26% and 27% of the areas measured by GPR, respectively. The higher standard deviation of the individual network outputs for the Rhône Glacier (Fig. 2.7b) is most likely due to a relatively small training region compared to the ice-covered area. Larger discrepancies particularly occur in areas where the ice is steeply inclined (Unteraar Glacier: vi and vii; Rhône Glacier: i and ii). In general, ice thicknesses tend to be low where surface gradients are large (e.g., Paterson, 1994), but our network only considers horizontally measured distances as inputs, while any information on the slope of the fill cells is not considered. This could be overcome by invoking a physically based estimator that accounts for ice plasticity and the basal shear stress to approximate the thickness of steep ice, which has been done by Clarke et al. (2009). In the case of sedimentary deposits, however, there exists no physical basis to generalize that steeper surfaces correspond to shallower valley fills. In our study, we aim at estimating the thickness of sedimentary deposits on the floors of large valleys and for now explicitly exclude steep storage landforms such as talus slopes or debris cones, which are volumetrically less significant. Nevertheless, we provide a possible solution on how to include these landforms into the prediction in Section 2.5 below.

Concerning the estimation of glacier-ice thicknesses, there exist several methods, based on ice-mechanical principles that are superior to the ANN approach (Huss et al., 2008; Farinotti et al., 2009; Li et al., 2012;

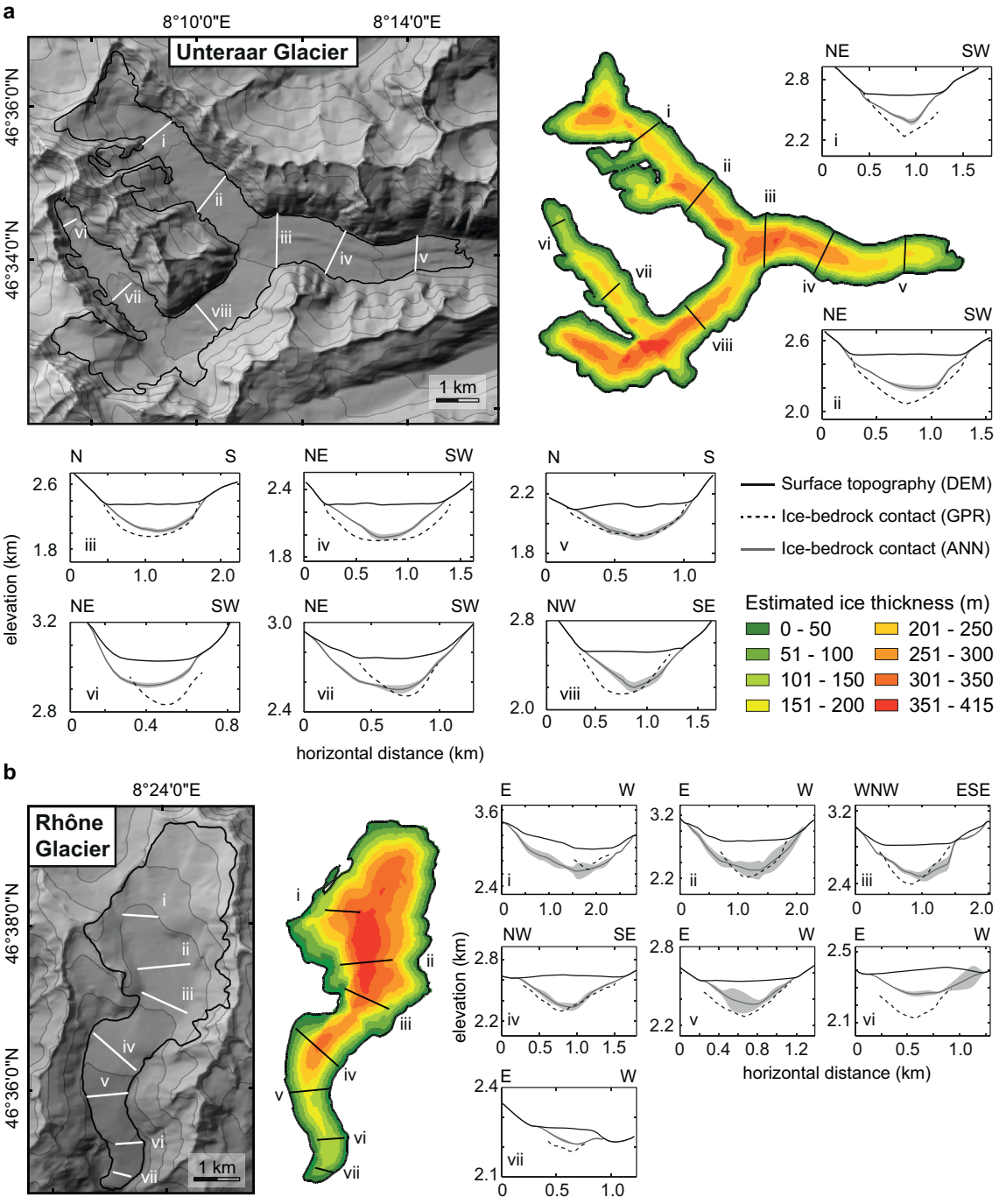

Figure 2.7: Model results for (**a**) the Unteraar Glacier and (**b**) the Rhône Glacier in the Swiss Alps (see Fig. 2.6 for location) showing shaded relief maps of both glaciers with the respective ice extents after Farinotti et al. (2009) and the locations of the available ice thickness measurements (small roman numerals). Elevation contours are drawn in 100 m intervals illustrating the variable ice surface inclination. Model-derived ice thickness maps for network configuration 6/20 (Unteraar Glacier) and 6/17 (Rhône Glacier) are shown in color. Cross sections show a comparison of estimated (grey solid lines) and measured (black dashed lines) ice thicknesses along profiles i–viii and i–vii, respectively. Grey shadings indicate 1σ intervals calculated from four model runs with identical network configuration. Ice thickness measurements are based on ground-penetrating radar (GPR) surveys (Funk et al., 1994; Bauder et al., 2003, 2007) and digitized from Figs. 6 and 9 in Farinotti et al. (2009).

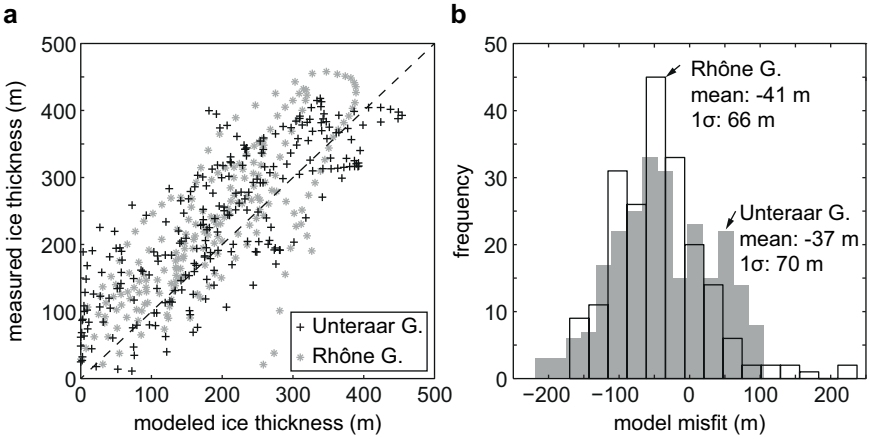

Figure 2.8: (**a**) Modeled versus measured ice thicknesses for the Unteraar Glacier and the Rhône Glacier. (**b**) Frequency distribution of the model misfit showing that the ANN tends to underestimate the measured ice thicknesses by ~ 40 m on average. G. = Glacier.

Linsbauer et al., 2012; Clarke et al., 2013). In our final experiment we deal with the estimation of the sediment thickness of a large intermontane valley fill, where no corresponding method is available.

2.4.3 Rhône Valley

The Rhône Valley is one of the largest intermontane valleys of the Central Alps, extending for ~150 km from the terminus of the Rhône Glacier at ~2250 m above sea level (asl) to Lake Geneva at ~380 m asl. The Rhône River first flows southwestward, along regional tectonic structures, before it abruptly turns ~90°, near the city of Martigny, and follows a northwesterly course. From the ensemble of landforms (e.g., hanging valleys and cirques) and the sedimentary record of the valley fill, it has been proposed that during the Last Glacial Maximum and presumably also earlier, the Rhône Valley was occupied by glacial ice with a thickness exceeding 1000 m (Florineth, 1998; Kelly et al., 2004). After deglaciation, a strong but short-lived sedimentary pulse (Hinderer, 2001) resulted in partial burial of the glacially sculpted valley. The present-day valley floor has a mean surface gradient of ~2°. Previous volume estimates of the sedimentary fill in the Rhône Valley were based on seismic (Besson et al., 1991; Finckh and Frei, 1991; Pfiffner et al., 1997), gravimetric (Rosselli and Raymond, 2003), and borehole measurements (Wildi, 1984; Pugin, 1988). Estimated sediment volumes range from 80–100 km^3 (Rosselli and Raymond, 2003) to ~106 km^3 (Hinderer, 2001), with the latter based on the existing geophysical data in conjunction with a geomorphological approach that involved the extrapolation of hillslope angles into the subsurface. Based on the assumption of parabolic valley-cross sections, Jaboyedoff and Derron (2005) proposed a volume of 118 km^3. In our study we focus on a ~120-km-long section that extends from the city of Brig (700 m asl) to Lake Geneva and features a continuous alluvial plain with an area >260 km^2 and a maximum width of approximately 6 km at its downstream end (Fig. 2.6).

For generating the valley-fill mask we first applied a slope threshold to the DEM and assigned all cells with a slope angle below 10° to the valley fill. The slope threshold was iteratively determined by comparing the extent of the resulting fill mask with that of mapped alluvium in a 1:500,000 geological map of Switzerland (Swisstopo, 2005). Subsequently, we manually refined the valley-fill mask using the same map. During the training phase we excluded all cells with a distance of more than 5 km to the valley fill to maintain spatial coherence between the training data set and the seismic profiles, which we used as our test data set. To avoid edge effects, we limited the number of sectors to six and varied the number of hidden nodes between 1 and 20. Prediction of the validation data set yielded an optimal network configuration of three sectors and 20 hidden nodes, which is close to the optimal network configuration of five sectors and 19 hidden nodes as determined from the test data set. Our model predicts a maximum sediment thickness of approximately 1400 m near Lake Geneva (Fig. 2.9a), which probably is an overestimation when considering nearby geophysical measurements that indicate a depth to bedrock of ~700 m below the lake level (Vernet et al., 1974). This overestimation can be attributed to the fact that at the margin of the orogen the valley

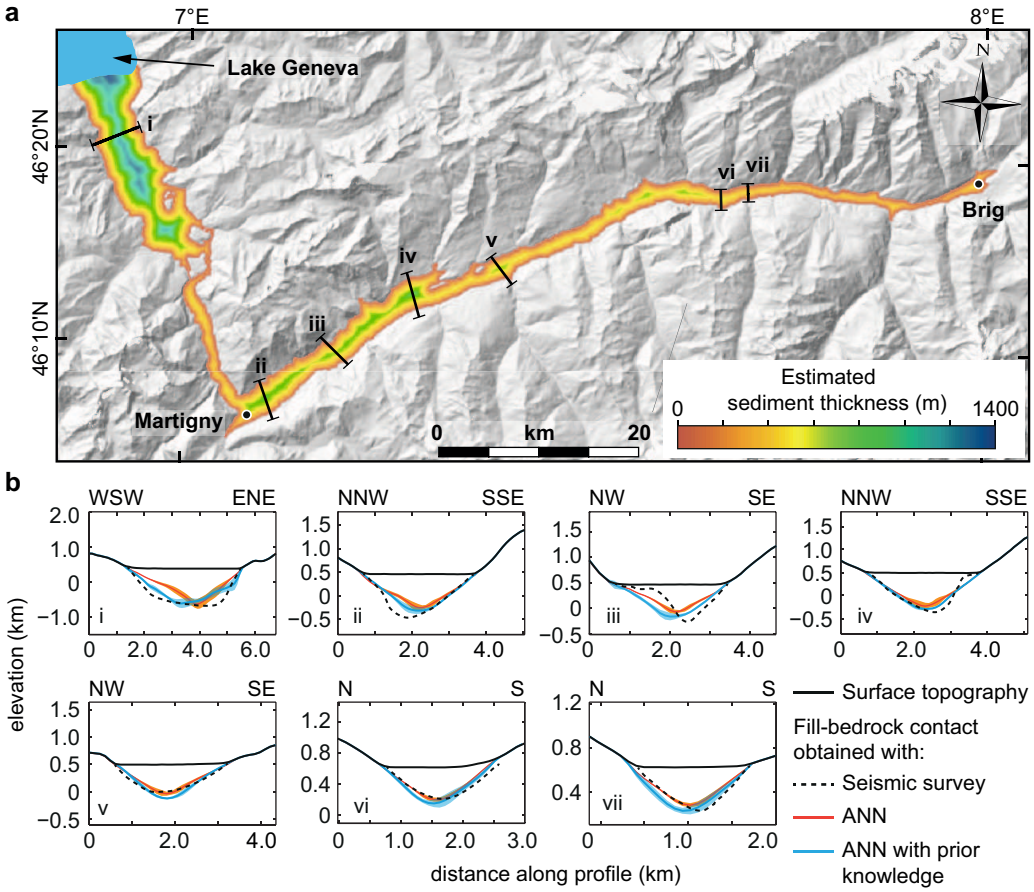

Figure 2.9: Model results for the Rhône Valley, Switzerland. (**a**) Sediment thickness distribution as predicted by the ANN superimposed on a shaded relief map of the region. (**b**) Comparison between the model output (red line) and seismic interpretation (dashed line) (Finckh and Frei, 1991; Pfiffner et al., 1997). In addition, results from a model run using prior knowledge about the fill thickness are indicated with blue lines (see text for details). The ANN using prior knowledge produces more U-shaped valley cross sections at the downstream part of the valley thus resulting in a slightly better fit to the measurements especially for profiles "i" and "ii". Total estimated sediment volumes are $97 \pm 11\,\mathrm{km}^3$ (1σ) for the ANN and $106 \pm 15\,\mathrm{km}^3$ (1σ) for the ANN using prior knowledge.

fill transitions into the foreland basin and the valley width can no longer be used to estimate the valley-fill thickness. Our estimated bedrock topography at the position of profile i has a rather V-shaped morphology and clearly departs from the seismic interpretation, which has steep flanks and a flat valley bottom. This leads to a maximum error along profile i of around 500 m. Profile iii is another example for abrupt changes in slope beneath the valley floor that lead to higher errors in the prediction (Fig. 2.5). Most other profiles (iv–vii) are in very good agreement with the geophysical observations. Our total estimated valley-fill volume is $97 \pm 11\,\mathrm{km}^3$ and falls in the range of previously published values (see above). The uncertainty represents the standard deviation calculated from four model runs with identical network configurations.

In a second run, we attempted to incorporate prior constraints on the fill thickness as briefly introduced in Section 2.4.1. By averaging the seismically derived thicknesses, we estimated the mean fill thickness to be ~360 m. Compared to this number, the mean training thickness of 100 m in our first estimation appears too low. Therefore, we arbitrarily imposed a sampling threshold of $h^* = 500\,\mathrm{m}$. which resulted in an increase of the mean training thickness to 320 m. At yet higher thresholds, the number and the spatial coverage of the potential training cells decrease rapidly. The resulting valley-fill thickness of this run shows a better fit to the seismic interpretation (Fig. 2.9b) and yields a higher estimated sediment volume of $106 \pm 15\,\mathrm{km}^3$. The mean absolute deviation in cross-sectional area is $2.6 \times 10^5\,\mathrm{m}^2$ in our first estimate and $1.9 \times 10^5\,\mathrm{m}^2$ in our second estimate, which corresponds to 21.5% and 15.2%, respectively. The mean errors in the validation and test data sets, as a function of the numbers of sectors and hidden nodes, are shown in the supporting information Fig. A.7.

2.5 Discussion

2.5.1 Optimal network configuration

Despite the fact that in most of our experiments the optimal network configurations for the validation and test data sets are different, there exists general similarity between the error distributions in the validation and test data sets. Thus, network configurations that yield low validation errors also tend to result in low test errors (Fig. 2.10a). In most of the above experiments the optimal number of sectors was lower than the maximum tested number of sectors, respectively. Moreover, we could observe an increase of edge effects with larger numbers of sectors, which poses a limit to the possible number of sectors in the network. The maximum number of hidden nodes on the other hand is theoretically only limited by the computational cost. Practically, however, we found that the additional gain in the prediction accuracy for more than 20 hidden nodes is rather limited. Figure 2.10b shows the relative average sensitivity of the prediction error, $\bar{E}$, on both parameters. Considering all of the tested landscapes, a higher sensitivity of $\bar{E}$ to changes in the number of sectors can be observed in two thirds of the experiments. For the natural landscapes with artificial fills and the Rhône Valley, however, variations in the number of hidden nodes have about the same effect on $\bar{E}$ as variations in the number of sectors (Fig. 2.10b). In the case of the studied glaciers, $\bar{E}$ is twice as sensitive to changes in the numbers of hidden nodes as compared to changes in the number of sectors. Although our experiments with natural landscapes certainly do not encompass all possible valley morphologies, we suggest that typical network configurations with low errors consist of 6–8 sectors and 4–16 hidden nodes for glacial valleys and one to two sectors and one to five hidden nodes for fluvial valleys.

To give a rough estimate of the computational demands, testing network configurations encompassing 1–8 sectors and 1–10 hidden nodes, 4000 training examples (N), 40,000 predictions (M), and 1000 training cycles takes ~25 h on an Intel Core i7-4770 processor with 3.4 GHz, running on four cores simultaneously.

2.5.2 Uncertainties

For a given network configuration, that is, a given number of training examples, training cycles, hidden nodes, and sectors, the method's inherent uncertainty depends on the degree of overlap between the ranges of training and prediction inputs, i.e., the horizontal distance to unmasked cells within each sector. Hence, the variation in the outputs of consecutively applied networks increases with the number of prediction inputs that fall outside the training-data range. For the volume estimates of the Unteraar Glacier, the Rhône Glacier, and the Rhône Valley this uncertainty is approximately 11%, 19%, and 11%, respectively. For an assessment of the absolute uncertainty with respect to the geophysical data we used the averaged absolute differences in cross-sectional area between the measurements and mean estimates. This uncertainty adds up to 5.8×10^4 m^2, 4.1×10^4 m^2, and 2.6×10^5 m^2, which equals 26%, 27%, and 21.5% of the total cross-sectional areas, respectively.

2.5.3 Advantages of the method and its application

Compared to previous methods for inferring sediment thicknesses (e.g., extrapolation of hillslopes along cross-valley profiles), the only manual input in the ANN approach is the generation of the valley-fill mask. If sufficiently detailed digital geological maps are available, no extra effort may be involved. Because the algorithm is specifically designed to automatically detect the best out of a pool of different network configurations using an independent validation-data set, the objectivity of the method is maintained and it can be applied to fluvial as well as glacial valleys. Together with the required minimum input of a DEM and the mask of the valley fill, the results are easy to reproduce. Furthermore, the method results in a continuous output of valley-fill thicknesses that can be easily transformed into a map of bedrock elevations.

The achieved accuracy of the results with respect to the geophysical data encourages us to propose using the model to derive the bedrock topography as a boundary condition in numerical landscape evolution models. For example, an increasing number of studies use ice-flow models to reconstruct paleoclimatic conditions based on glacier extents (e.g., Anderson and Mackintosh, 2006; Golledge et al., 2012; Rowan et al., 2014). So far, these necessarily disregarded the effect of potentially thick valley-fill deposits on glacier-bed elevation and hence on glacier-mass balances. Quantitative estimates of the sediment-thickness distribution can therefore be used to include and quantify these effects. Moreover, the postglacial formation of thick

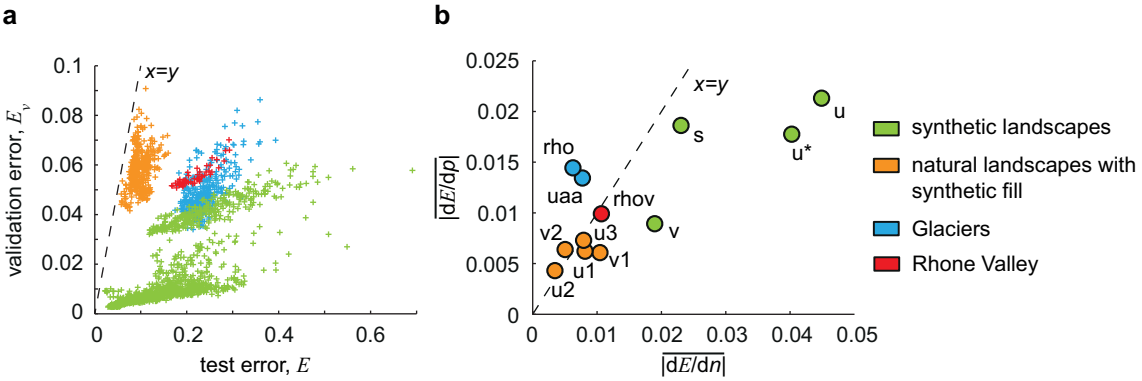

Figure 2.10: Relationship between validation and test errors and sensitivity of the results to the number of sectors and hidden nodes.(**a**) Relationship between validation and test errors for all experiments. Validation errors are consistently lower than the test errors in all cases. (**b**) Mean absolute error gradients along sector and hidden node dimensions. Point locations above (below) the x = y line indicate higher test error sensitivity to changes in the number of hidden nodes (sectors). v = V shape, u = U-shape, s = sinusoid, u* = U-noise, uaa = Unteraar Glacier, rho = Rhône Glacier, and rhov = Rhône Valley.

sedimentary fills, like that of the Rhône Valley, for example, might have modulated the flexural response of the lithosphere due to the ice unloading after deglaciation, and the replacement of ice by sediments could have attenuated the glacial isostatic adjustment (Champagnac et al., 2009). When knowing the distribution of the sedimentary load, this effect could be quantified. In combination with constraints on the timing of deposition, denudation rates in the sediment-source areas (Hinderer, 2001), as well as spatial and temporal patterns of mass redistribution in the orogen, can be studied. In a recent application of our method by Wang et al. (2014), the reconstruction of the bedrock topography beneath a thick sedimentary fill in the Yarlung Tsangpo Valley helped to constrain the tectonic history in the eastern Himalayan syntaxis.

Quantitative estimates on the distribution of intermontane sediments can also help to understand the feedbacks between crustal loading and seismicity. On timescales of several 10^5 years, for example, the deposition and removal of sedimentary fills may impact the tectonic activity of fault arrays that bound intermontane basins, leading to out-of-sequence thrusting, when sedimentary fills are removed (Dahlen, 1984; Hilley and Strecker, 2005). Conversely, faulting may be suppressed when lithostatic stresses increase due to the formation of voluminous valley fills (Sobel et al., 2003; Pingel et al., 2013). Knowledge about the involved sedimentary loads could be useful for quantifying these lithostatic stresses and might reveal potential thresholds for the activity of the associated faults. For a detailed analysis of earthquake hazards in a valley-fill setting, however, additional information on, e.g., fill density, grain size, or pore-fluid pressure are required (e.g., Wald and Allen, 2007) to be of use on shorter timescales. Nevertheless, in this context, our new method could provide first-order thickness estimates that can be used for planning field measurements or as complementary information to the spatially restricted primary data.

2.5.4 Limitations of the method

Estimating bedrock beneath valley fills with ANNs relies on the assumption that landscapes below and above valley fills are morphologically similar. This may not be the case if the surface-shaping processes that were once acting on the landscape changed after the infilling of valleys. Whereas the sedimentary fills are subsequently shielding the bedrock from further modification, the subaerial hillslopes continue to evolve and may gradually adjust to changed conditions (Norton et al., 2010). Thus, we would expect differences between the morphology of the buried and exposed parts of the landscape to increase with time. The European Alps have acquired their distinct surface morphology over the course of several glacial cycles during the Quaternary (e.g., Kelly et al., 2004). At least in some places, sediment-filled, U-shaped valleys and overdeepenings are thought to have been repeatedly excavated and enhanced during glacial advances, followed by backfilling upon glacial recessions (Dürst Stucki et al., 2010; Jordan, 2010; Preusser et al., 2010). Compared to this long-lasting period of glacial sculpting and given millennial-scale Holocene erosion rates of ~1 mm yr^{-1} (Wittmann et al., 2007), the period of deglaciation and paraglacial adjustment after the Last

Glacial Maximum (e.g., Schlüchter, 1988; Reitner, 2007) did not erase the inherited glacial imprint on the landscape. Buried valleys in the European Alps are therefore morphologically similar to nonburied ones, and this condition probably applies to other mountain belts that were affected by significant valley glaciations during the Quaternary. Unless arguments exist that indicate no change in process, or if erosion rates are very low, estimating the thickness of older valley fills involves higher uncertainties that are not entailed in the results.

For generating the training-data set we use a horizontal artificial fill surface to sample horizontal distances and corresponding thicknesses (Step 3 in Section 2.2.2), although real valley-floor deposits are generally not perfectly horizontal. However, if we consider a distance of 5000 m on an alluvial plain inclined with 1°, the projection on the horizontal would only be 0.75 m shorter. We therefore conclude that errors due to our use of a horizontal artificial fill surface for sampling the training data are negligible. Due to the method's shortcoming with respect to steeply inclined valley-fill surfaces, estimates of sediment-storage volumes are primarily focused on the valley floors. However, on medium to large spatial scales valley-floor deposits represent the bulk amount of total stored material in the landscape (Otto et al., 2008, 2009). In small catchments, where sediments that are stored in talus slopes can dominate (Schrott et al., 2003), in its current form, the proposed method will most likely fail to provide reasonable estimates. Nevertheless, a possible approach to enable the model to adequately deal with steep storage landforms could be to create an artificial fill surface that lies above the talus deposits. After the application of the method to this artificial fill, subtraction of the added height from the resulting prediction would give an estimate of the real fill thickness including steep storage landforms as illustrated in Fig. 2.11.

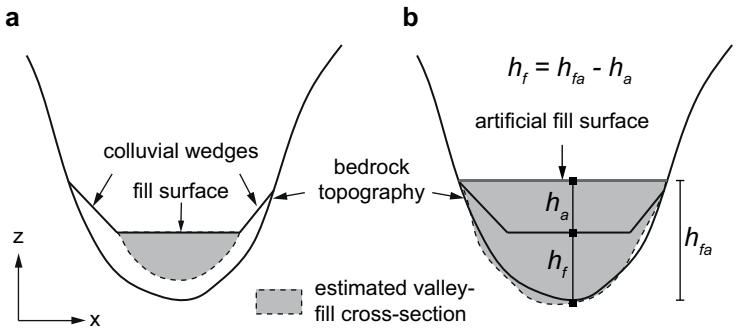

Figure 2.11: Approach to estimate the thickness of steep storage landforms with the presented method. (**a**) In valleys with extensive colluvial wedges, valley fill thicknesses can be underestimated. (**b**) Creating an artificial fill surface above the colluvial wedges may allow to recover the true bedrock surface.

The requirement that the training data are a representative subset of all the cases that we wish to predict (Section 2.2.1) implies that exposed hillslopes, where the training is based on, need to have larger horizontal and vertical dimensions than their subfill continuations. Hence, if the relief of the buried topography exceeds that of the above-fill topography, there will be an increased need for extrapolation, which leads to higher uncertainties. But even under optimal conditions where all predictions fall within the range of the training data, and with given similarity between buried and exposed topography, our method is not able to predict complex subfill topography and tends to smooth out any existing small-wavelength bedrock undulations (Fig. 2.4).

Because the outcome of any prediction strongly depends on the extent and accuracy of the fill mask, the precision with which the valley-fill boundaries can be mapped represents a fundamental limitation to the method. Preferably, delineation of valley fills should be done manually and supported by as many observations as possible, e.g., from geological maps. At larger spatial scales, however, it may be more practical to use DEM-based approaches like the one proposed by Straumann and Purves (2008) who used a region-growing algorithm that is based on thresholds in gradients to map flat areas in the vicinity of stream cells. The latter has been shown to yield results that are in good agreement with independently constrained areas of sediment storage in the European Alps (Straumann and Korup, 2009).

In its current form our method integrates over potentially existing lithological, structural, and geomorphic differences in the training data, and therefore, it has no ability to resolve spatial heterogeneity in composite landscapes. In principal, however, additional inputs can be easily introduced to account for spatial

heterogeneity as long as they can be linked to numerical values. Potential geomorphic differences between glacially influenced areas at higher elevations and relatively lower regions with fluvial signatures, for example, could be accounted for by incorporating the absolute elevation as an additional input into the model. Initial tests we performed show that in the European Alps, doing so does not significantly affect the results, which we think may be related to negligible altitudinal differences in the geomorphic character. Similarly, morphologic differences that are caused by variations in lithology and/or structural properties could potentially be accounted for by including geographic coordinates or metrics of erosional resistance as given by geological strength indices (Kühni and Pfiffner, 2001; Korup and Schlunegger, 2009; Dürst Stucki and Schlunegger, 2013). The key is that the additional input has to convey the morphologic similarity between training and target areas. When applying the method on a regional scale, like an entire mountain belt, for instance, these modifications could allow processing the data altogether rather than dividing it into distinct subsets. However, the maximum size of the data set that can be processed at once is limited by the available primary memory of the computer.

A priori knowledge about the fill thickness is not required for a successful application of our method. However, as shown in Sections 2.4.1 and 2.4.3, the incorporation of such constraints potentially leads to more accurate valley reconstructions (Fig. 2.9b) and thus storage-volume estimates (Table 2.1). In the above examples we simply used an iteratively determined sampling threshold to adjust the mean training thickness to the mean fill thickness, which, in the case of the Rhône Valley, was inferred from the seismic profiles. In cases where only point measurements are available, a mean thickness could be inferred based on a presumed frequency distribution of thicknesses, which ought to be related to the valley morphology. For example, if the maximum fill thickness h_{max} is known from borehole measurements, the approximate mean fill thickness would be $h_{max}/2$ for a V-shaped valley and $2h_{max}/3$ for a U-shaped valley.

2.6 Conclusion

We have explored the potential of artificial neural networks to estimate the thickness of valley fills and the bedrock topography, based on the assumption of morphological similarity between the bedrock topography below and above a valley fill. Our experiments suggest that the optimal network configuration is controlled by the bedrock morphology and that differences in this configuration exist between different landscapes and fills. We used a split-sample approach that allows automatically and objectively estimating the optimal network configuration (Weiss and Kulikowski, 1991). With tests on artificially filled valleys we demonstrated the validity of this approach and achieved errors in the estimated fill volumes that are consistently below 20%. Our predictions of the ice thickness of the Unteraar Glacier and the Rhône Glacier are in reasonable agreement with independent measurements but inferior to methods, which are based on ice-mechanical principles (Farinotti et al., 2009). Moreover, these predictions revealed limitations concerning steeply inclined fills, and we find that the method performs best when estimating the thickness of valley-floor deposits. For the sedimentary fill of the Rhône Valley in Switzerland, our new method predicts bedrock elevations, which are consistent with independent ground measurements, and yields a total fill volume of $97 \pm 11\,\mathrm{km}^3$ that is in the range of previously published values. Our approach eliminates most of the subjectivity that is typically associated with methods where bedrock reconstructions are based on digital elevation models. The minimal input consists of a digital elevation model and a mask of the valley fill, which makes the method easily applicable and a useful contribution for quantifying sediment storage on the scale of catchments to entire mountain belts.

Chapter 3

Glacial isostatic uplift of the European Alps

Abstract

The demise of large continental ice sheets at the end of the last glacial period induced crustal rebound in tectonically stable regions of North America and Scandinavia that is still ongoing. Unlike the ice sheets, the Alpine icecap developed on a relatively young mountain belt where the measured uplift is potentially a composite signal of tectonic shortening (Brückl et al., 2010a), lithospheric delamination (Lippitsch et al., 2003), and unloading due to deglaciation and erosion (Champagnac et al., 2009). Here we show that virtually all of the geodetically measured surface uplift in the European Alps can be explained by the Earth's viscoelastic response to ice unloading after the last glacial maximum (LGM), provided an upper mantle viscosity of $\sim 10^{20}$ Pa s. We reconstructed the geometry of the Alpine LGM icecap with a numerical ice-flow model, taking into account post-glacial erosion and sediment redeposition within the mountain belt, and spatial variations in lithospheric flexural rigidity. We observe residual uplift in the Swiss Rhône Valley, where seismicity and fault scarps indicate recent tectonic activity. In the Eastern Alps residual uplift as well as subsidence are likely due to ongoing eastward lateral extrusion of fault-bounded blocks (Grenerczy, 2005).

3.1 Introduction

Recent vertical movements of the Earth's crust are mostly due to tectonic deformation, volcanism, and changes in crustal loading from water, ice and sediments (Watts, 2001). The decay of large continental ice masses was the primary cause for the Holocene eustatic sea level rise, and is one of the main concerns of the impacts of global warming on coastal communities worldwide (IPCC, 2014). Changes in the ice load of tectonically active mountain ranges, such as the Alps, Alaska, or the Himalaya, although much smaller, nevertheless trigger an isostatic response. The resulting stress changes in the Earth's crust can influence crustal deformation and seismicity (Stein et al., 2009) and are thought to have caused changes in fluvial networks and some of the largest intraplate earthquakes following LGM deglaciation (Stewart et al., 2000). The key controls on how the Earth responds to changes in crustal loading are the viscosity of the upper mantle and the lithospheric effective elastic thickness (EET) — a geometric measure of the flexural rigidity of the lithosphere, which describes the resistance to bending under the application of vertical loads (Watts, 2001). Most previous estimates of mantle viscosity come from old and tectonically stable continents, where the vertical motion can almost entirely be attributed to post-glacial rebound (Mitrovica, 1996). In contrast, the complexity of the uplift signal in tectonically active mountain belts requires the relative contribution of different potential driving mechanisms to be disentangled.

For half a century, the cause for recent uplift of the European Alps has been debated. Possible drivers of uplift include post-glacial rebound (Gudmundsson, 1994), erosional unloading (Champagnac et al., 2009), tectonic deformation (Persaud and Pfiffner, 2004), lithospheric slab dynamics (Lippitsch et al., 2003), and combinations thereof (Fig. 3.1). Some of these processes, such as lithospheric delamination, manifest themselves on timescales of $\sim 10^6 - 10^7$ yr, whereas others, such as post-glacial rebound, occur relatively rapidly ($\sim 10^3$ yr). New approaches to modelling orogen-scale sediment storage (Mey et al., 2015), glaciation

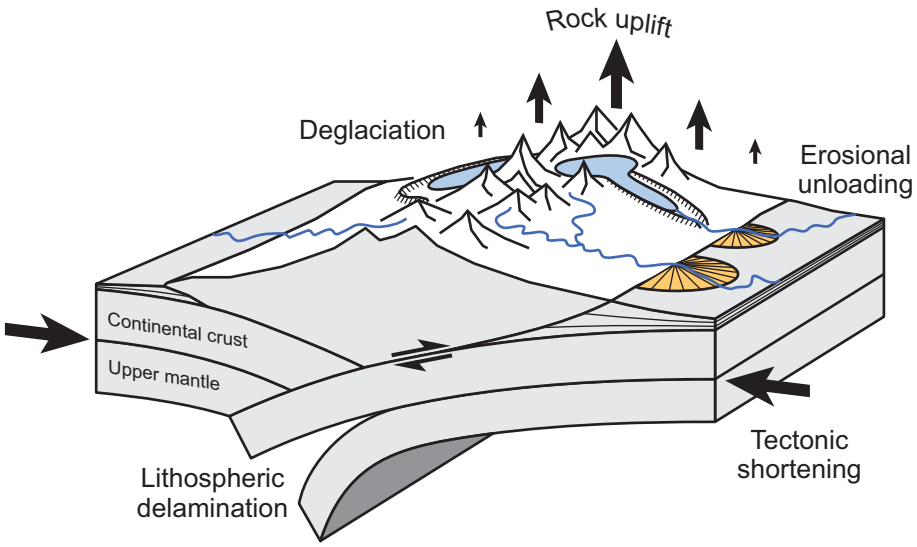

Figure 3.1: Processes contributing to rock uplift. The individual components are interdependent and their relative contribution to the rock uplift changes over time.

(Egholm et al., 2011), and spatial variations in EET (Tesauro et al., 2009) provide new constraints for estimating the contribution of glacial isostatic adjustment (GIA) to present-day uplift rates in the European Alps.

3.2 Study area

Mountain building in the European Alps is due to the convergence of Africa and Eurasia beginning in the Mesozoic with continental collision culminating in the Eo-Oligocene, and a late phase of outward tectonic growth in the Early Miocene, creating the Jura Mountains and thrusting of the Swiss Plateau (Schmid et al., 1996) (Fig. 3.2a). Further tectonic shortening was accompanied by eastward extrusion of the Eastern Alps and exhumation of metamorphic domes in the Central Alps (Ratschbacher et al., 1991). The cessation of outward tectonic expansion of the Western and Central Alps during the Late Miocene likely reflects an increase in the ratio of erosional to accretionary material flux and the onset of orogenic decay (Willett et al., 2006). During the Pleistocene, the Alps were repeatedly glaciated with icecaps that covered almost the entire mountain belt and substantial parts of the northern foreland (Ehlers and Gibbard, 2004).

3.3 Results

Among the most prominent features of the Alpine landscape are overdeepened valleys that were carved by glaciers and are now partially buried by thick sedimentary deposits. The isostatic adjustment to deglaciation was likely attenuated by the postglacial accumulation of sediments in these valleys (Champagnac et al., 2009). We used an artificial neural network algorithm (Mey et al., 2015) to estimate the sediment thickness within all Alpine valleys (see Methods; Fig. 3.2a). Our estimates agree well with fill thicknesses observed in boreholes or estimated from seismic and gravimetric surveys (Table 3.2), and they yield consistently similar or higher thicknesses where boreholes did not reach bedrock (Fig. 3.2b). Very shallow valley fills (<200 m) show the largest relative discrepancies, which can be attributed to distances between observation sites and valley walls that are smaller than the spatial resolution of the model. According to our estimate, the total volume of valley-filling sediments is $1{,}800 \pm 202\,\mathrm{km}^3$. A large fraction of this volume was trapped in a closed system of overdeepened valleys and marginal lake basins, where only small amounts of material were efficiently exported (Hinderer, 2001). To account for catchments that were only temporarily closed, we added another 10% to our volume estimate (Hinderer, 2001), resulting in $1{,}980 \pm 222\,\mathrm{km}^3$. By distributing this volume evenly over the Alps (~123,000 km^2, excluding valley fill area) and assuming a mean density of 2,000 $\mathrm{kg\,m}^{-3}$ for unconsolidated sediments and 2,700 $\mathrm{kg\,m}^{-3}$ for bedrock, we compute a total surface

lowering of 11.9 ± 1.3 m. As the valley fill must have formed following ice retreat ~17 kyr BP (Hinderer, 2001), this corresponds to a mean postglacial denudation rate of 0.7 ± 0.08 mm yr^{-1}. To create a mass conserving topographic basis for modelling the Alpine icecap, we redistributed the calculated sediment volume catchment-wise and as a power-law function of local relief (Montgomery and Brandon, 2002) back onto the hillslopes.

Based on mapped ice extent and thickness indicators, such as terminal moraines (Ehlers and Gibbard, 2004) and trimline elevations (Kelly et al., 2004; Florineth, 1998; Florineth and Schlüchter, 1998), we reconstructed the LGM ice cover using a numerical ice-flow model (Egholm et al., 2011). Because it is not our aim to derive paleoclimatic conditions during the LGM, we used modern precipitation maps and an Alpine-wide average glacial mass balance profile together with an iteratively adjusted equilibrium line altitude (ELA) to fit the observations (see Methods). The steady-state icecap, which best fits ice extent indicators (Fig. 3.2c, 3.2d) has a mean and a maximum ice thickness of 423 m and 2,448 m, respectively. The maximum ice thickness is higher than previously reported values of ~2,000 m (Florineth and Schlüchter, 1998; Kelly et al., 2004) due to our removal of thick post-LGM valley fills from the underlying topography. The total ice mass is 65×10^3 Gt, which is ~16 times the mass of the eroded sediments.

The LGM Alpine ice cap started growing before 30 kyr BP and reached its maximum ~21 kyr BP, followed by rapid deglaciation with ~80% ice loss over the course of 3 kyr (Ivy-Ochs et al., 2008). This chronology is consistent with the dated onset of marginal lake formation, which indicates ice retreat to the mountain interior at 16–18 kyr BP (Hinderer, 2001). In our rebound modelling, we therefore assume that the LGM ice mass rapidly shrunk to a much smaller size by 17 ± 2 kyr BP. Because durations of ice-cap growth are long (>10 kyr) compared to maximum expected viscoelastic relaxation times of 3–6 kyr (Mitrovica, 1996), we assume that the Alpine icecap reached full isostatic compensation. We calculated the lithospheric equilibrium deflection (Wickert, 2015), by combining ice loading, sediment loading, and erosional unloading, while accounting for a variable EET (Tesauro et al., 2009). Although relative spatial variations in EET are well constrained (Tesauro et al., 2009), the absolute values are not, since they strongly depend on the assumed rheology and geothermal gradient. For the Alps, a range of 10–50 km has been reported (Watts, 2001). Therefore, we solve for a range of possible average EETs while maintaining the spatial pattern (see Methods). An increase of the EET results in a smaller amplitude but a larger wavelength of the deflection. Whereas the ice invokes an additional loading of the crust, the redistribution of sediments induces spatially variable loading and unloading. The deflection of the crust approximately follows the ice extent with a maximum depression of 143–223 m near the centre of the icecap and an elevated forebulge of 5–6 m, depending on the assumed EET (Fig. 3.5). The effect of spatial variations of EET decreases with an increasing average EET. Compared to the flexural pattern that results from a constant EET of 50 km, the deflection using a variable EET of 39–58 km is up to 6 m higher in the centre, and 3 m lower at the periphery (Fig. 3.6).

Because of the relatively small dimensions of the Alpine icecap, the upper mantle viscosity determines isostatic uplift and relaxation rates. For a range of mantle viscosities of 10^{19}–10^{21} Pa s, we calculated the corresponding uplift rates and compared them with measurements obtained from precise levelling (Schlatter et al., 2005; Ruess and Mitterschiffthaler, 2015), which were adjusted to a common reference frame using data from permanent GPS stations (Bruyninx, 2004) (see Methods). Using an average EET of 50 km and an upper mantle viscosity of $2.2 \pm 0.5 \times 10^{20}$ Pa s, we are able to reproduce virtually all of the geodetically measured uplift (Fig. 3.2f). This viscosity value is reasonable, as it is lower than that estimated for an old craton ($3–10 \times 10^{20}$ Pa s, Fennoscandia), but higher than that for a region with recent crustal thinning (0.18×10^{20} Pa s, Basin and Range province, Table 3.1).

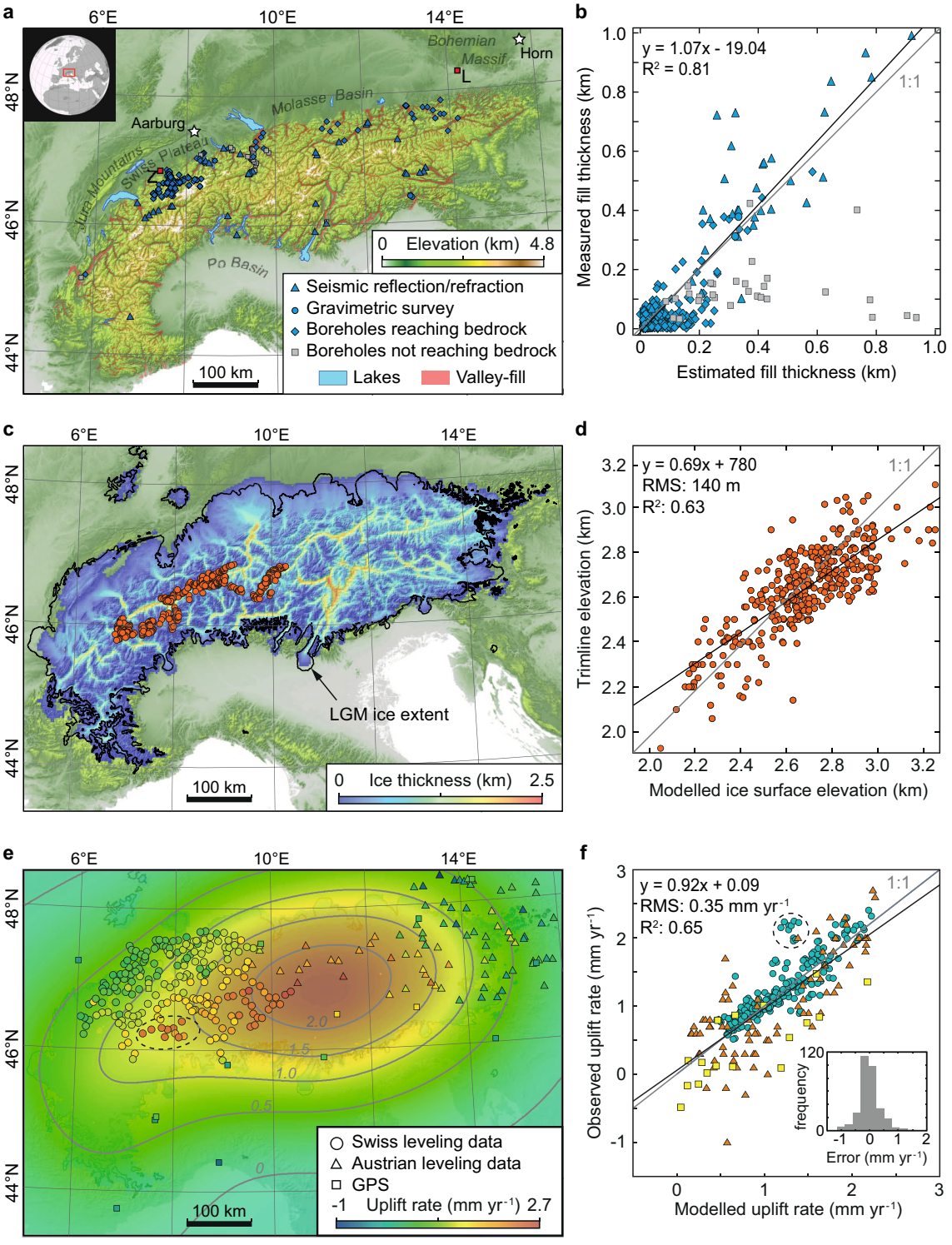

Figure 3.2: Effect of deglaciation and sediment redeposition on rock uplift rates. (**a**) Present-day topography of the Alps, ice cover (white), and distribution of sedimentary valley-fills. Stars indicate locations of the reference points for the Swiss and Austrian precise levelling data, respectively. "L" and "Z" are the locations of the permanent GPS stations used to adjust the levelling data to the global reference frame IGb08. (**b**), Comparison of estimated and measured valley-fill thicknesses. See Table 3.2 for data sources. (**c**, **d**), Steady-state ice geometry and comparison of trimline elevations (Kelly et al., 2004; Florineth, 1998; Florineth and Schlüchter, 1998) with modelled ice surface elevations. (**e**, **f**), Inferred and measured (Schlatter et al., 2005; Ruess and Mitterschiffthaler, 2015; Bruyninx, 2004) uplift pattern assuming instantaneous deglaciation at 17 ± 2 kyr and an upper mantle viscosity of $2.2 \pm 0.5 \times 10^{20}$ Pa s.

3.4 Discussion and conclusion

It has previously been argued that the geodetically measured uplift of the Alps is dominated by its isostatic response to erosional unloading (Champagnac et al., 2009) that is supposed to have increased threefold from Pliocene to Quaternary times (Kuhlemann et al., 2002), although some of this increase may be an artefact of incomplete preservation (Willenbring and von Blanckenburg, 2010). Our models show that the LGM ice load (~65×10^3 Gt) was much larger than post-glacially eroded sediments (~4×10^3 Gt) and suggest the dominance of ice melting over erosional unloading in contributing to the total recent uplift rate, even if sub-glacial erosion rates had been several times higher than post-glacial erosion rates.

Table 3.1: Estimates of upper mantle viscosity (μ).

Region	μ ($\times 10^{20}$ Pa s)	Reference
Antarctica	5	(Argus et al., 2014)
Hudson Bay	4	(Mitrovica and Forte, 2004)
Fennoscandia	3–10	(Nordman et al., 2015)
Great Britain	3–4	(Lambeck et al., 1998)
European Alps	1.5–3	this study
Australian coastline	2	(Nakada and Lambeck, 1989)
Basin and Range	0.18	(Bills et al., 1994a)
Central Andes	0.01–1	(Bills et al., 1994b)
Japan	0.5	(Okuno and Nakada, 1998)
Cascadia margin	0.05–0.5	(James et al., 2000)
Iceland	0.01–0.5	(Sigmundsson and Einarsson, 1992)

The most sensitive parameter in our modelling that is not well constrained is the average EET. A lower average EET does not change the best-fit viscosity by much ($1.8–2.2 \times 10^{20}$ Pa s), but leads to systematically lower modelled uplift rates in the northwest periphery of the Alps (Fig. 3.7b). However, active tectonic shortening across that region is less than 1 mm yr^{-1}, which would result in only small rock uplift (<0.2 mm yr^{-1}, Champagnac et al., 2009). If other processes, such as lithospheric delamination (Lippitsch et al., 2003) or ongoing tectonic shortening (Persaud and Pfiffner, 2004) were to account for some of the observed uplift in the periphery of the Alps, these would have to generate the same uplift pattern as the ice unloading, which is unlikely. Nonetheless, we observe a conspicuous cluster of residual uplift in the Swiss Rhône Valley, which is close to a zone of enhanced seismicity and may thus have a tectonic origin (Fig. 3.3). Furthermore, the mismatch of our model with respect to parts of the Austrian levelling data could be explained by the ongoing eastward extrusion of the Eastern Alps involving strike-slip tectonics with a complex pattern of transtensional and transpressional zones (Grenerczy, 2005; Ratschbacher et al., 1991). Therefore we suggest that the recent uplift rate is predominantly determined by glacial isostatic adjustment and that any residuals are due to local tectonic activity.

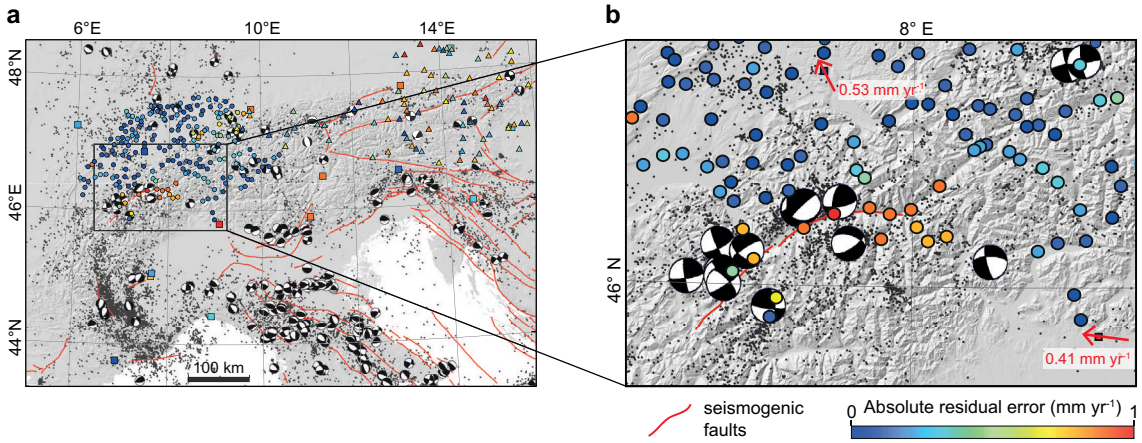

Figure 3.3: Model error in a seismotectonic context. (**a**) Seismogenic faults (red solid lines, http://diss.rm.ingv.it/share-edsf/), seismicity (grey dots, NEIC, 1973–2008) and focal plane solutions from the global Centroid-Moment-Tensor catalogue (Ekström et al., 2012) superimposed on a hillshade map of the study area. (**b**) Inset focusing on the cluster of excess uplift in the Swiss Rhône Valley. Red arrows show horizontal motion of permanent GPS stations relative to a fixed Eurasian Plate (Bruyninx, 2004).

3.5 Methods

3.5.1 Estimation of valley-fill thicknesses

Based on the assumption of geometric similarity between the exposed and the buried parts of the landscape, we used an artificial neural network (ANN) algorithm (Mey et al., 2015) and a 90-m-resolution digital elevation model (DEM) to explicitly estimate the depth to bedrock for grid cells that include valley fill. We expect geometric similarity of the bedrock surface, because the entire landscape was subject to glacial erosion prior to deposition of the valley fill. For each cell in the DEM that is part of a valley fill, the depth to bedrock is estimated from the horizontal distance to the nearest hillslope, calculated for different directions. Training and validation of the ANN was initially performed on the presently exposed topography using synthetic fills. We created a mask of all valley fills by a combination of slope thresholds and manual digitization using geological maps with a scale of 1:25,000 (https://map.geo.admin.ch) and 1:50,000 (https://www.geologie.ac.at, http://infoterre.brgm.fr, http://www.geoviewer.isprambiente.it).

Table 3.2: Data sources for measurements of valley-fill thicknesses.

River catchment	Reference	Method
Aare	(GEOSOND, 2014)	drilling
Adige	(Faccioli and Vanini, 2003; Bassetti and Borsato, 2005)	drilling, seismic
Drau	(Brückl et al., 2010b; Heinz and Walach, 1979)	drilling, seismic
Inn	(Aric and Steinhauser, 1976; Preusser et al., 2010; Steinbrener, 2011)	drilling, seismic
Isar, Loisach, Lech	(Frank, 1979)	drilling
l'Isère	(Nicoud et al., 2002)	drilling
Reuss, Seez, Linth	(Wildi, 1984)	drilling, seismic
Rhine	(Eberle, 1987; Wildi, 1984; Pfiffner et al., 1997)	drilling, seismic
Rhône	(Finckh and Frei, 1991; Pfiffner et al., 1997)	seismic
Salzach	(Bleibinhaus et al., 2010; van Husen, 1979)	drilling, seismic
Sarca	(Faccioli and Vanini, 2003)	seismic
Tagliamento	(Barnaba et al., 2010)	drilling, gravimetric
Ticino	(Pfiffner et al., 1997)	seismic
Traun, Ens	(van Husen, 1979)	drilling
Ubaye	(Jongmans and Campillo, 1993)	seismic

3.5.2 Icecap reconstruction

To reconstruct the Alpine icecap during the LGM, we employed a numerical ice flow model (Egholm et al., 2011) to solve the shallow ice approximation (Hutter, 1983), which simplifies ice dynamics but allows for computational efficiency at sufficiently high spatial resolution (3 km). The ice rheology is thereby governed by Glen's flow law, $\epsilon_{ij} = A\tau_e^2\tau_{ij}$, where ϵ_{ij} are the components of the strain rate tensor, and τ_{ij} are the components of the deviatoric stress tensor. τ_e is the effective stress and $A = 1 \times 10^{-16}\,\mathrm{Pa}^{-3}\,\mathrm{yr}^{-1}$. The sliding velocity is assumed to be proportional to the basal shear stress, τ_s, and of magnitude given by: $u_s = A_s\tau_s^2 N^{-1}$. Here A_s is a sliding coefficient depending inversely on the bed roughness, and N is the effective pressure at the base of the ice set to 40% of the ice overburden pressure. The surface mass balance is modelled with an accumulation/ablation gradient of 0.7 m snow-water equivalent yr^{-1} $(100\,\mathrm{m})^{-1}$ (Dyurgerov et al., 2002) and a spatially variable maximum accumulation rate, using the recent pattern of mean annual precipitation (Isotta et al., 2014) (Fig. 3.4a). To reach the best match between modelled and mapped ice extent and thickness, we iteratively adjusted equilibrium line altitudes (ELAs) for each catchment that drains the Alps according to the areal misfit determined after each model run (Fig. 3.4b). This adjustment was repeated for As = 25, 75, 100, 150, and $200 \times 10^{-10}\,\mathrm{m\,yr}^{-1}\,\mathrm{Pa}^{-2}$. The best agreement between mapped trimline elevations and the modelled ice-surface was reached with $A_s = 100 \times 10^{-10}\,\mathrm{m\,yr}^{-1}\,\mathrm{Pa}^{-2}$. Furthermore, we increased A_s stepwise within the foreland to prevent Alpine ice from overtopping the Jura Mountains. Field observations clearly document that two branches of ice were flowing to the northeast and to the southwest of the Jura Mountains (Jäckli, 1962). This pattern was reproduced when A_s in the foreland was increased by a factor of 15. We attribute differences in the sliding coefficient between the foreland and mountain interior to deformable sediments (Kamb, 2001) and higher amounts of meltwater (Herman et al., 2011), which both are likely associated with higher sliding velocities.

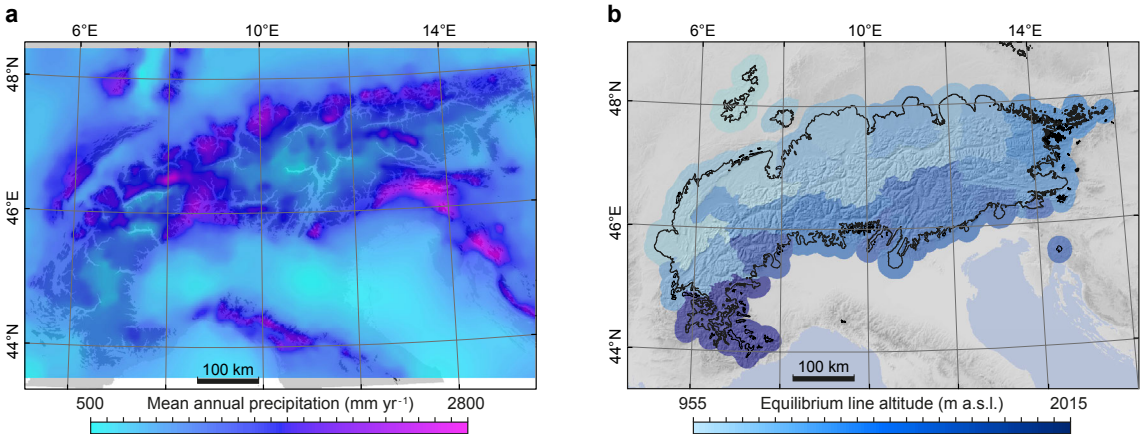

Figure 3.4: Mean annual precipitation and equilibrium altitudes. (**a**) Mean annual precipitation was determined from rain gauge measurements from 1971–2008 (Isotta et al., 2014), which were used to impose spatially variable maximum accumulation rates in the ice model. (**b**) Distribution of equilibrium line altitudes for the ice model, which best fits LGM ice geometry indicators, i.e., moraines (Ehlers and Gibbard, 2004) and trimlines (Kelly et al., 2004; Florineth, 1998; Florineth and Schlüchter, 1998).

3.5.3 Flexure of the lithosphere

Because the lithospheric deflection due to glacier growth has a direct effect on the slope and elevation of the ice-surface and hence on the ice-flow and mass balance, we reconstructed the icecap for uniform EETs of 20, 30, 40 and 50 km, respectively. We calculated the flexural isostatic adjustment, $W_f(x, y)$, for every 10 model time steps (~30 days) using the two dimensional elastic thin-plate equation:

$$\frac{\partial^4 W_f}{\partial x^4} + 2\frac{\partial^4 W_f}{\partial x^2 \partial y^2} + \frac{\partial^4 W_f}{\partial y^4} = \frac{L(x, y)}{D_f}. \tag{3.1}$$

Here $D_f = YEET^3/12(1 - \nu)$ denotes the flexural rigidity, where EET is the effective elastic thickness of the lithosphere, $Y = 100\,\mathrm{GPa}$ is the Young's modulus and $\nu = 0.25$ is the Poisson ratio. $L(x, y) =$

$\rho_i g H(x,y) - \rho_a g W_f(x,y)$ is the vertical load where $\rho_i = 917\,\mathrm{kg\,m^{-3}}$ is the density of ice, $H(x,y)$ is the ice thickness in each model cell and $\rho_a = 3{,}300\,\mathrm{kg\,m^{-3}}$ is the density of the compensating asthenosphere. The variation in total ice volume and maximum ice thickness due to an increase of the EET from 20 to 50 km is less than 5%. To further investigate the effect of a laterally heterogeneous lithosphere, we introduced variations in EET (Tesauro et al., 2009), and calculated the isostatic depression due to the combined loads of the steady-state icecap and the sediments using the algorithm gFlex (Wickert, 2015), which uses finite difference solutions for the problem of elastic plate bending under arbitrarily shaped surface loads. To account for the effect of the differences in the resulting flexural patterns on the ice geometry, we adjusted the glacier bed according to the results from gFlex and continued running the ice model to find the new steady-state ice geometry (Fig. 2c). Imposing a variable EET results in $1 \times 10^3\,\mathrm{km^3}$ more ice, which is small when compared to the total ice volume of $70 \times 10^3\,\mathrm{km^3}$. The larger ice volume can be attributed to thicker ice (up to 160 m) in the foreland lobes.

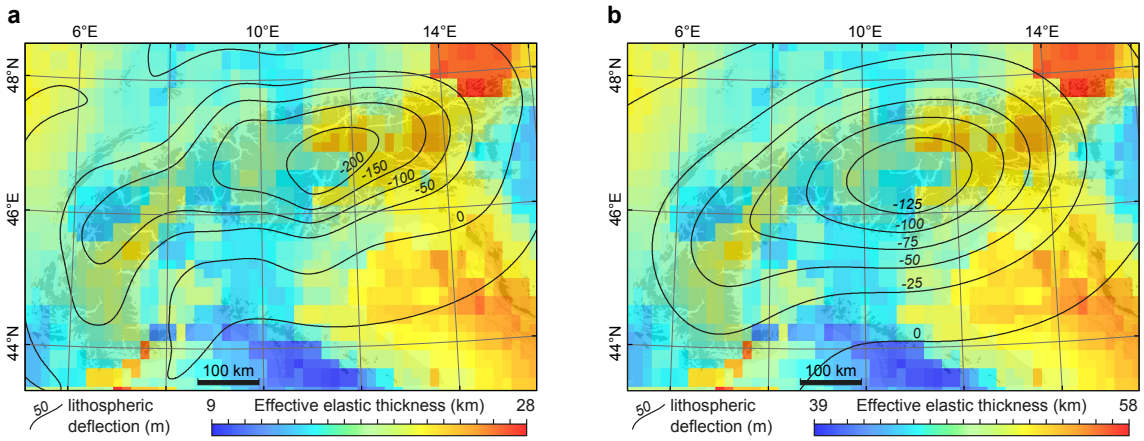

Figure 3.5: Deflection of a heterogeneous Alpine lithosphere. Subsidence due to the load of the LGM icecap and redeposited sediments for (**a**), a low rigidity (Tesauro et al., 2009) and (**b**), a high rigidity lithosphere.

3.5.4 Effective elastic thickness

The effective elastic thickness of the lithosphere exerts a primary control on the plate's flexural rigidity, which in turn determines the magnitude and pattern of the isostatic response. Reflecting the long-term and often complex history of the continental plate, the EET depends mostly on the combined effects of rheological and thermal heterogeneity. In this study we use EET estimates (Tesauro et al., 2009) obtained by following the approach of Burov and Diament (1995). The crustal rheology, corresponding to quartzite in the upper crust and diorite in the lower crust (Tesauro et al., 2013), was thereby assigned using the velocity distribution of the crustal model EuCRUST-07, which is based on integration of several hundred seismic profiles and receiver-function data (Tesauro et al., 2008). For the mantle lithosphere, a "dry" olivine rheology was used. Lithospheric temperatures were derived from the inversion of a seismic velocities tomographic model of Europe (Koulakov et al., 2009). The EET ranges from 14 to 27 km in the Alpine region, with overall higher values in the Eastern Alps compared to the Central and Western Alps (Fig. 3.5a). However, these values reflect only a lower bound endmember, assuming a high geothermal gradient and a "soft" rheology ("dry" quartzite and "wet" diorite) (Tesauro et al., 2009). Therefore, we modified the corresponding EET by adding 10, 20, 30, 40 and 50 km to the absolute values, respectively, to account for lower geothermal gradients and harder rheologies.

3.5.5 Rebound model

The viscoelastic decay of the lithospheric deflection after removal of the surface load results in uplift at a rate u, which we calculated using the exponential function:

$$u = -w_0/\tau * e^{-t/\tau} \tag{3.2}$$

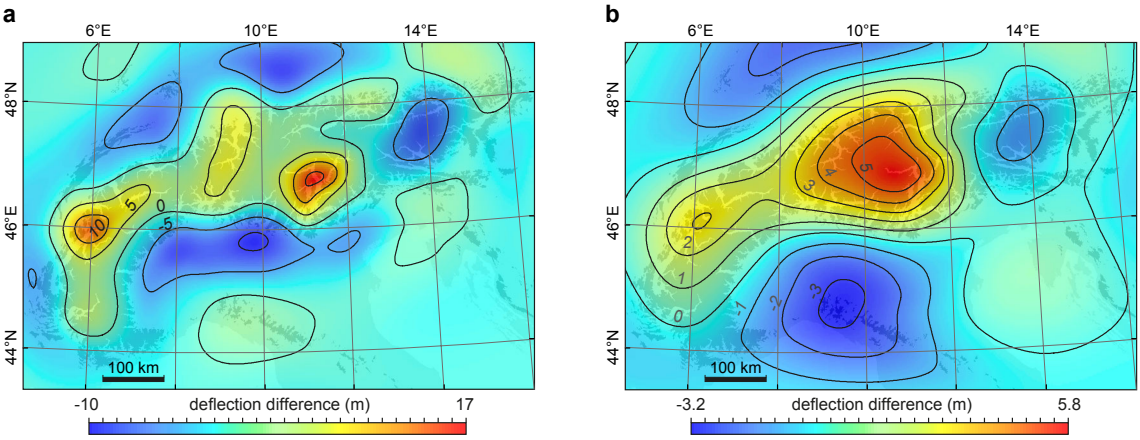

Figure 3.6: Effect of variations in EET (Tesauro et al., 2009). Deflection difference relative to a lithosphere with a uniform EET of (**a**), 20 km and (**b**), 50 km.

where w_0 is the equilibrium deflection, τ is a characteristic timescale of relaxation, and t is the time since unloading (Turcotte and Schubert, 2002). The timescale of relaxation is defined as:

$$\tau = 4\pi\mu/\rho g\lambda \tag{3.3}$$

where μ is the mantle viscosity, $\rho = 3{,}300\,\mathrm{kg\,m^{-3}}$ is the mantle density, g is the gravitational acceleration, and $\lambda = 320\,\mathrm{km}$ is the wavelength of the load, which we calculated from the average transverse extent of the LGM icecap. We used uplift rates determined by precise levelling in Switzerland (Schlatter et al., 2005; Kahle et al., 1997) and Austria (Ruess and Mitterschiffthaler, 2015), obtained from repeated measurements of benchmarks since the beginning and the middle of the 20$^{\mathrm{th}}$ century, respectively. Thus, they represent vertical velocities in relation to arbitrarily chosen reference points. The reference point for the Swiss data is located near the city of Aarburg on the Swiss Plateau and the Austrian data refer to a point near the city of Horn ~70 km northwest of Vienna (Fig. 3.2a). Direct comparison of both datasets requires that the vertical velocities of the respective reference points can be determined. For this purpose, we used data from the permanent GPS stations Zimmerwald (Z) and Linz (L), which are located on the Swiss Plateau and the Bohemian Massif, respectively. Both stations provide continuous time series of ground motion from 1998–2015 (17 yr) and from 2005–2013 (8 yr), with vertical velocities of $1 \pm 0.08\,\mathrm{mm\,yr^{-1}}$ (Z) and $0.8 \pm 0.15\,\mathrm{mm\,yr^{-1}}$ (L) in the global reference frame IGb08 (Bruyninx, 2004). To adjust the measurements to a common reference frame we subtracted the GPS-rates with the uplift rates of the nearest levelling benchmarks, which resulted in uplift of $0.94 \pm 0.08\,\mathrm{mm\,yr^{-1}}$ for the Swiss reference point and $1 \pm 0.15\,\mathrm{mm\,yr^{-1}}$ for the Austrian reference point. We inverted the adjusted uplift rates for the mantle viscosity using Equation (3.2) with $t = 17 \pm 2\,\mathrm{kyr}$, resulting in a viscosity of $1.8\text{–}2.8 \pm 0.5 \times 10^{20}\,\mathrm{Pa\,s}$, depending on the assumed EET, with larger EETs leading to higher viscosities (Fig. 3.7c).

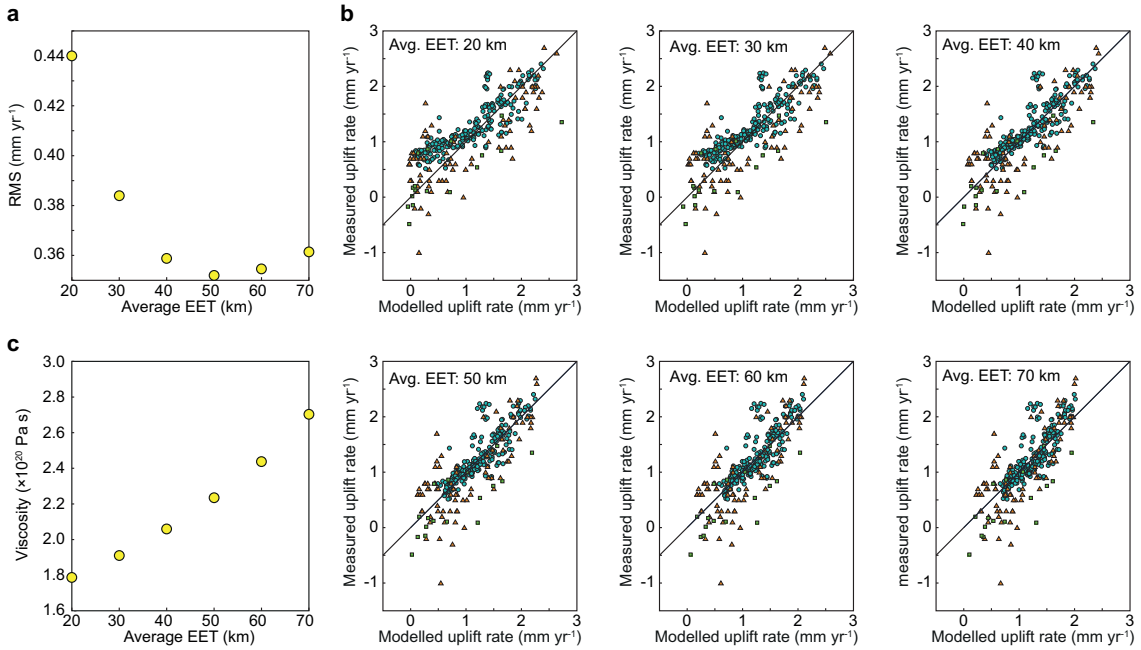

Figure 3.7: Sensitivity of viscosity and modelled uplift rates to changes in EET. (**a**) Mean absolute error as a function of the average EET. A minimum error occurs with an EET of 50 km. (**b**) Modelled versus measured uplift rates for 20, 30, 40, 50, 60, and 70 km of EET. Blue circles = Swiss levelling data (Schlatter et al., 2005; Kahle et al., 1997). Orange triangles = Austrian levelling data (Ruess and Mitterschiffthaler, 2015). Green rectangles = permanent GPS data (Bruyninx, 2004). Avg. = average. (**c**) Estimated viscosity as a function of the average EET.

Chapter 4

Tectonic control of Yarlung Tsangpo Gorge revealed by a buried canyon in Southern Tibet

Abstract

The Himalayan mountains are dissected by some of the deepest and most impressive gorges on Earth. Constraining the interplay between river incision and rock uplift is important for understanding tectonic deformation in this region. We report here the discovery of a deeply incised canyon of the Yarlung Tsangpo River, at the eastern end of the Himalaya, which is now buried under more than 500 meters of sediments. By reconstructing the former valley bottom and dating sediments at the base of the valley fill, we show that steepening of the Tsangpo Gorge started at about 2 million to 2.5 million years ago as a consequence of an increase in rock uplift rates. The high erosion rates within the gorge are therefore a direct consequence of rapid rock uplift.

4.1 Introduction

The topographic evolution of mountain ranges results from the competition between tectonic and erosive forces (Tapponnier et al., 2001; Sobel et al., 2003; Liu-Zeng et al., 2008) and controls the organization of drainage and atmospheric-circulation systems (Brookfield, 1998; Clark et al., 2004; Molnar et al., 2010). Although tectonics and erosion act in opposing directions, there may be feedbacks that couple the two (England and Molnar, 1990; Avouac and Burov, 1996). Prominent candidates for such coupling comprise the syntaxes regions (Zeitler et al., 2001; Koons et al., 2013), at either end of the Himalaya, where the two biggest rivers draining Tibet, the Indus and Yarlung Tsangpo, have cut deep gorges into very young metamorphic massifs (Fig. 4.1a) (Burbank et al., 1996; Burg et al., 1998; Finnegan et al., 2008; Seward and Burg, 2008; Crowley et al., 2009; Enkelmann et al., 2011; Larsen and Montgomery, 2012). In the so-called tectonic aneurysm model, it has been proposed that rapid incision within these gorges has thermally weakened the crust and now sustains a positive feedback between uplift and erosion (Zeitler et al., 2001; Koons et al., 2013), but how and when this happened remains elusive.

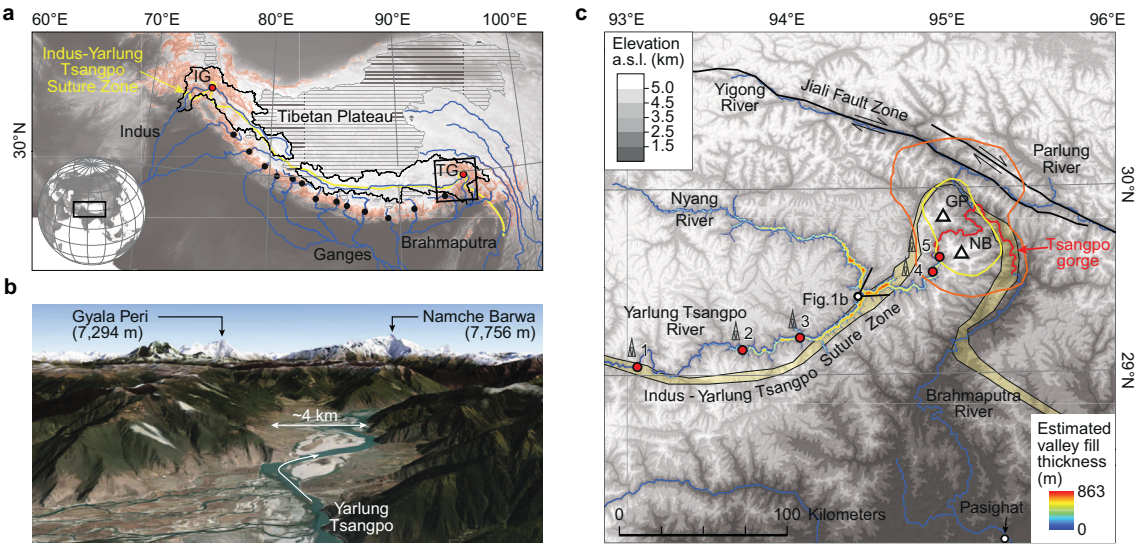

Figure 4.1: River gorges in the Himalaya. (**a**) Geographical overview of Tibet and the Himalaya, with internally drained areas (horizontally hatched), major rivers, and gorges (red and black points) located within steep mountainous areas—i.e.,where 5-km-radius local relief is >2 km (red). Black polygons show the mountainous drainage basins of the Indus River in the west and the Yarlung Tsangpo-Brahmaputra River in the east. The Indus-Yarlung Tsangpo Suture Zone separates the Eurasian (north) from the Indian plate (south) and is strongly distorted in the Indus Gorge (IG) and Tsangpo Gorge (TG). (**b**) Oblique northeastward aerial view of the Yarlung Tsangpo upstream of the Tsangpo Gorge (from Google Earth, www.google.com/earth). (**c**) Map of the eastern Himalayan syntaxis with the studied valley fill and drill core locations (red points). Contour lines show rapidly exhuming areas with young (<2 Ma) Zircon U/Th-He (orange), and Biotite $^{40}Ar/^{39}Ar$ ages (yellow) centered on the Tsangpo Gorge (Enkelmann et al., 2011), which is marked by a red line.

4.2 Study area

Deeply incised gorges exist along the entire Himalaya and always coincide with very steep river gradients that have been related to zones of rapid rock uplift and incision (Seeber and Gornitz, 1983; Hodges et al., 2001; Lavé and Avouac, 2001). The most spectacular and emblematic gorge in the Himalaya, and probably on Earth, is the Tsangpo Gorge, where the Yarlung Tsangpo drops by 2 km in elevation as it cuts through the ~50-km-wide eastern Himalayan syntaxis where erosion rates are exceptionally high (Fig. 4.2b). The contorted and generally steep course of the gorge is often considered evidence for relatively young capture of the Yarlung Tsangpo by the headward incising Brahmaputra River, from a former course connecting it to the Parlung and Yigong rivers, which themselves might have been connected to rivers farther to the east (Seeber and Gornitz, 1983; Brookfield, 1998; Zeitler et al., 2001; Clark et al., 2004). Provenance studies from the Himalayan foreland, however, indicate that a connection between the Yarlung Tsangpo and Brahmaputra River was already established before the Middle Miocene (Cina et al., 2009; Chirouze et al., 2013; Lang and Huntington, 2014), emphasizing the stability of the gorge. More recently, the discovery of extensive lake deposits that have accumulated behind a river-blocking glacial dam upstream of the Tsangpo Gorge (Montgomery et al., 2004) has spurred the idea that glacial damming during the Quaternary inhibited headward incision of the Brahmaputra River and might have contributed to initiating rapid rock uplift (Korup and Montgomery, 2008).

Before entering its narrow gorge, the Yarlung Tsangpo flows for ~300 km across a broad alluvial plain that increases gradually in width toward the confluence with the Nyang River (Fig. 4.2a). Such downstream widening is typical for lakes that have drowned valleys upstream of dams. Five drillings recently conducted along the Yarlung Tsangpo (Fig. 4.1c) provide evidence of a thick sedimentary valley fill upstream of the gorge. The drillings were located near the valley center and reached bedrock at depths that increase from 70 m at the most upstream site (no. 1), to a maximum depth of 567 m (no. 3) at ~80 km upstream from the Nyang River confluence. Two more sites at distances of ~40 and 20 km upstream from the gorge yielded depths to bedrock of 510 (no. 4) and 230 m (no. 5), respectively.

Hillslopes bordering the valley floor are generally steep, with uniform slope angles of ~30°, comparable to hillslopes downstream of the Tsangpo Gorge (Fig. 4.2b) and suggestive of threshold hillslopes that are at

their critical angle of stability (Burbank et al., 1996). Simple projection of hillslopes into the subsurface predicts a depth to bedrock of ~1000 m near the Yarlung Tsangpo-Nyang River confluence (Fig. 4.2a), where the valley floor is widest. Based on the assumption that hillslopes below and above the valley fill are similar, we reconstructed the depth to bedrock (Figs. 4.1c and 4.2a) using an artificial neural network approach (Clarke et al., 2009). Close correspondence of estimated and observed depths in drill cores provide us with confidence in the reconstruction, which confirms our initial notion of a steadily decreasing elevation of the former valley floor toward the Yarlung Tsangpo-Nyang River confluence. Downstream of the confluence, the valley floor remains ~4 km wide and deeply filled with sediments (Fig. 4.2a) until the river leaves the Indus-Yarlung Tsangpo Suture Zone and abruptly narrows to <2.5 km. Because no obvious spill-over toward other valleys exists near the deepest reach of the valley fill, we argue that the former Yarlung Tsangpo was following its present-day course and that uplift of the Namche Barwa and Gyala Peri massifs resulted in steepening of the river where it crosses the gorge and concurrent backfilling of upstream reaches (Fig. 4.6).

4.3 Results

Valley-fill sediments from the three sites closest to the Tsangpo Gorge (no. 3 to no. 5) (Figs. 4.1c and 4.2a) consist of clastic, mainly fluvial deposits that are dominated by pebbly gravel and sand (figs. 4.3 to 4.5). The cores from sites no. 3 and no. 4 both have coarse grain sizes in the lower half, including boulders up to 50 cm in diameter, and fine grain sizes in the upper half, including silt and clay that probably stems from lake periods (Fig. 4.2A and table S1). This fining upward sequence indicates a decrease in stream competency, consistent with lowered river gradients during backfilling upstream of the Tsangpo Gorge. The lack of upward fining in drill core no. 5, which is closer to the gorge and located ~120 m lower, may be related to erosion of its upper part during uplift and incision of the gorge (Fig. 4.6). We collected three samples from near the base of drill core no. 3 for cosmogenic nuclide burial dating with in situ–produced ^{10}Be and ^{26}Al (see Material and Methods). Our samples yield consistent results that overlap within uncertainties (table S2) and indicate that deposition at this site initiated between ~2 and 2.5 million years ago (Ma) (Figs. 4.7 and 4.8). Because site no. 3 is ~150 km upstream of the gorge and deposition may not have started immediately, it is likely that uplift and steepening of the gorge was initiated somewhat earlier.

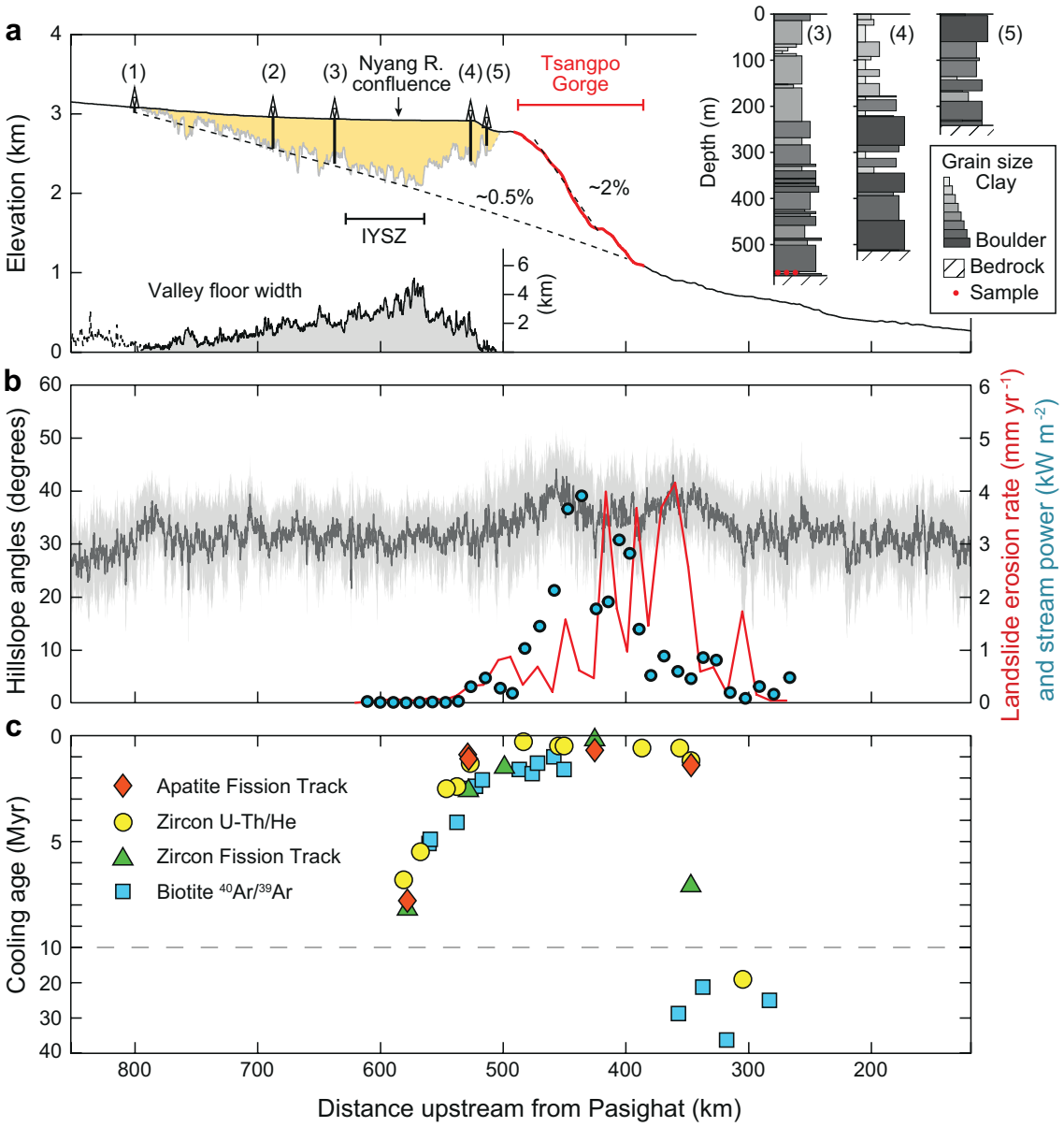

Figure 4.2: Tsangpo Gorge and valley fill. (**a**) Longitudinal river profile showing present-day elevation (black; red where passing through Tsangpo Gorge), location of drill cores with observed depth to bedrock (vertical black bars), estimated depth to bedrock from artificial neural network (yellow area), and reconstructed valley bottom before uplift of Tsangpo Gorge (dashed line). IYSZ, Indus-Yarlung Tsangpo Suture Zone. Inset figures show present-day valley bottom width (lower left) and simplified drill core stratigraphy (upper right), with grain size variations (see Fig. 4.3 for details) and sample locations (red points). (**b**) Hillslope angles within a 10-km-distance from the river (mean $\pm$ 1σ), specific stream power (Finnegan et al., 2008), and landslide erosion rates (Larsen and Montgomery, 2012). (**c**) Mineral cooling ages (Burg et al., 1998; Finnegan et al., 2008; Seward and Burg, 2008) within a 10-km-distance from the river. See Fig. 4.9 for spatial distribution of cooling ages.

4.4 Discussion and conclusion

Steepening of the Tsangpo Gorge requires either an increase in rock uplift rate or a decrease in erosional efficiency. Young crystallization and mineral cooling ages from bedrock within the gorge are consistent with an increase in rock uplift rates after ~4 Ma (Fig. 4.2c) (Burg et al., 1998; Finnegan et al., 2008; Seward and Burg, 2008). If rock uplift rates were constant and all surface uplift was due to changes in specific stream power (product of gravity, water density, channel slope, and discharge per unit width; (Finnegan et al., 2008)), discharge would have to have decreased by more than a factor of four as channel slopes increased in the gorge (Fig. 4.2a). No observations exist to support discharge reductions of this magnitude, either due to climate change or drainage capture. River-blocking glacial dams (Korup and Montgomery, 2008) can also be excluded as causes of lowered erosional efficiency because the uplifted river reach was below ~2 km elevation, far from any glacial influence. Further- more, the presence of >200 m of sediments beneath the moraines considered responsible for glacial damming (Montgomery et al., 2004) is incompatible with the reduced bedrock incision proposed previously (Korup and Montgomery, 2008).

Our results clearly show that ~2.5 Ma the Yarlung Tsangpo was able to erode back into the Tibetan Plateau and develop a nearly graded profile (Fig. 4.2a), which is consistent with provenance data from Miocene to Quaternary sediments in the Himalayan foreland of the Tsangpo Gorge (Lang and Huntington, 2014). The reported increase of Eurasian-plate detritus in deposits of the Brahmaputra River between 7 and 3 Ma (Chirouze et al., 2013) could reflect the headward incision of the Yarlung Tsangpo into Tibet until uplift of the Namche Barwa and Gyala Peri massifs focused erosion to Indian-plate rocks within the Tsangpo Gorge (Finnegan et al., 2008). This scenario is consistent with an independently estimated onset of accelerated incision of the adjoining Parlung River at 4 to 9 Ma, based on detrital cooling ages (Duvall et al., 2012), which most likely occurred as a result of capture by the Yarlung Tsangpo-Brahmaputra.

Striking similarities between the Indus and Tsangpo gorges have been noted previously (Burg et al., 1998; Zeitler et al., 2001; Koons et al., 2013) and suggest that the tectonic framework of the Himalayan syntaxes sets the stage for the exceptionally high rates of rock uplift (Burg et al., 1998; Seeber and Pêcher, 1998). Even if positive feedbacks between erosion and uplift nowadays help to maintain these gorges in their current location (Zeitler et al., 2001; Koons et al., 2013), our results suggest that rapid incision within the Tsangpo Gorge is the result rather than the cause of rock uplift. A similar evolution could have taken place in the Indus Gorge, where mineral cooling and metamorphic ages (Burbank et al., 1996; Zeitler et al., 2001; Koons et al., 2013) suggest equally high erosion rates, with some evidence for order-of-magnitude acceleration in exhumation by ~1.7 Ma (Crowley et al., 2009). Notably, ponding of the Indus River up-stream of the gorge and deposition of ~1200 m of fluvial and glacial deposits (Cronin et al., 1989) apparently started before ~2.6 Ma (Seong et al., 2007) and might also reflect an increase in rock uplift in the western Himalayan syntaxis. Because new data are warranted, we leave it to future studies to test the suggested similarity and investigate the cause for synchronous initiation of rapid rock uplift of both Himalayan syntaxes.

4.5 Material and methods

4.5.1 Yarlung Tsangpo shallow drilling

To investigate the nature and amount of trapped sediments along the Yarlung Tsangpo, a series of exploratory shallow drillings were undertaken along the trunk river on point bars, riverbanks, and high terraces. The drillings (Fig. 4.3) were located on modern riverbanks, no more than 20 m above the current river level. Each site consisted of an array of drillings, tens of meters apart, which reached bedrock (Figs. 4.4, 4.5) and from which the deepest drill core was selected for analysis. However, there is no guarantee that the deepest position has been reached and thus the measured depth to bedrock should be considered a minimum estimate of the true depth to bedrock. Grain size data for cores #3–5, which were accessible for scientific analysis, is based on estimation during on-site visual inspection of the drill cores (Fig. 4.3). A stratigraphic division of the deposits in the drill core from site #3 is provided in Table S1.

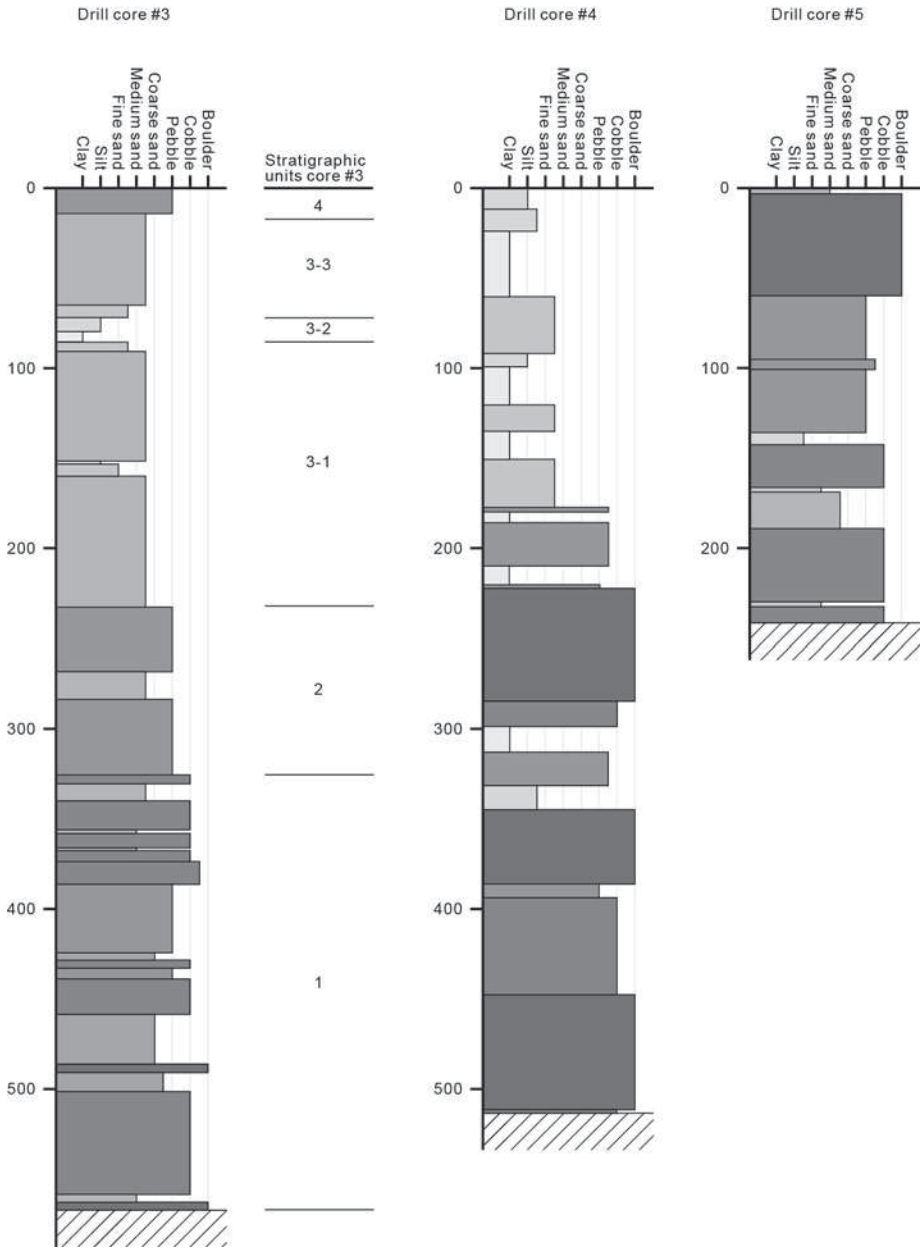

Figure 4.3: Simplified stratigraphic columns of the drill cores at sites #3–#5.

Figure 4.4: Drill core recovered from drilling site #5 at a depth of 235.5–241.2 m. This section consists mainly of unconsolidated sand, gravel, and pebbles. Rounded pebbles near the bottom indicate fluvial transport. These deposits constitute the base of the valley fill at this site. The width of the box is ~ 1 m.

4.5.2 Depth to bedrock

Ground-truth point measurements of the depth to bedrock are given by the drill cores. We obtained a first estimate of the depth to bedrock between the core locations by projecting hillslopes into the subsurface at a constant angle of 30°, which corresponds to the average hillslope angle within the Yarlung Tsangpo Valley (Fig. 4.2b). Reasonable agreement with the drill core data motivated us to reconstruct the bedrock beneath the valley fill using an artificial neural network (ANN), based on the approach in Clarke et al. (2009). We used a 2-layer ANN with 10 hidden nodes and estimated the depth to bedrock at each valley-fill pixel in a 180-m-resolution digital elevation model (DEM) based on the distance to hillslopes within 2 different sectors. The ANN was initially trained on hillslopes above the valley fill and within a maximum distance of 5 km from the valley floor. The valley-fill mask was based on manual digitization using Google Earth and local slope angles. We extended our depth to bedrock estimation not farther upstream than core location #1, where the depth to bedrock is 70 m and where the channel width equals the valley floor width.

4.5.3 Cosmogenic nuclide sample preparation

Three samples, each of 2–3 kg sand, were collected from the drill core at a depth of 561–564 m directly overlying a 2-m-thick cobble layer that rests on bedrock. After washing and cleaning, the sand was sieved and the grain size fraction of 250–500 μm was used for further analysis. Subsequent procedures for purifying quartz separates are based on the methods described in Kohl and Nishiizumi (1992): First, the samples were soaked overnight in HCl/H_2O_2 to remove carbonate, iron oxide coating and organic matter. The samples were then leached for at least 9 hours at a constant temperature of 80°C in diluted HF/HNO_3 solution in an ultrasonic bath to remove meteoric ^{10}Be and other minerals except for quartz. The leaching and subsequent drying was repeated five times. Residual impurities were removed by heavy-liquid and hand separation under the microscope and the samples were once more treated with diluted HF/HNO_3 solution and dried. Aliquots of two grams were taken from each sample, dissolved in concentrated HF/HNO_3 and analyzed by Inductively Coupled Plasma Optical Emission Spectrometer (ICP-OES) measurements for ^{27}Al and other elements to assure purity. The remaining quartz was spiked with 0.25 mg of ^{9}Be in a weak HNO_3 carrier solution, and then heated and dissolved. Fluorides were removed by fuming with $HNO_3/HClO_4$. The

Figure 4.5: Drill core recovered from drilling site #5 at a depth of 241.2–246.7 m. This section consists of gneissic bedrock. The width of the box is ~ 1 m..

resulting samples were dissolved in pure water and $HClO_4$, heated and dried two times, then rinsed out with HCl. Al^{3+} and Be^{2+} were isolated using ion exchange resin, and neutralized by ammonia water to yield $Al(OH)_3$ and $Be(OH)_2$. The oxides were separated gravitationally, transferred to quartz crucibles, and dried. The samples were baked at 750°C, yielding powder of Al_2O_3 and BeO. These samples were sent to the Cosmogenic Nuclide Laboratory of the European Center for Earth Sciences, Environment Research and Education (CEREGE) in France for target preparation and measurement of the $^{10}Be/^{9}Be$ and $^{26}Al/^{27}Al$ ratios (Table S2). The ratios were measured relative to the standard NIST4325 with a nominal $^{10}Be/^{9}Be$ ratio of 2.79×10^{-11}, and SM-Al-11, with a nominal $^{26}Al/^{27}Al$ ratio of 7.401×10^{-12}. Our process blank $^{10}Be/^{9}Be$ ratio was 2.7×10^{-15} and the corresponding ^{10}Be atoms were subtracted from the reported sample results. Analytical uncertainties as well as uncertainties in the carrier and blanks were propagated using standard error-propagation methods. The lab-specific standard uncertainty (standard deviation) of the ICP-OES measurement of Al, regularly calibrated using standard blanks, is 5%.

4.5.4 Burial dating

In steadily eroding landscapes, rocks are moving towards the Earth's surface with time and accumulate both ^{10}Be and ^{26}Al at rate that depends on the depth below the surface, the density of the overlying material and the geographic position (Lal, 1991). For ^{10}Be and ^{26}Al, three main production mechanisms exist. At shallow depths, most of the production occurs by spallation, but the production rate decreases rather rapidly with depth. At greater depths (>several meters in most materials), the production of cosmogenic nuclides is dominated by negative and fast muons, with the production rates being much lower compared to spallation and decreasing with depth at a slower rate (Gosse and Phillips, 2001). Because transport on hillslopes and in rivers is usually fast compared to exhumation on hillslopes, the cosmogenic nuclide concentration of river sediment can be used to calculate catchment-averaged hillslope erosion rates (Granger et al., 1996). When river sediment is deposited and gets successively buried to greater depths, at first, cosmogenic nuclides will continue to build up at a rate that depends, similar to hillslope erosion, on the rate of burial and the density of the deposited sediment. At sufficiently large depths, production rates are negligible and as time proceeds, the ^{10}Be and ^{26}Al atoms in the sediment will decay at a rate defined by the radioactive half-life (Granger and Muzikar, 2001). The half-life of ^{10}Be is 1.387 ± 0.012 Ma (Chmeleff et al., 2010; Korschinek et al., 2010) while the half-life of ^{26}Al is 0.705 ± 0.024 Ma (Norris et al., 1983). Burial dating with ^{10}Be and ^{26}Al relies

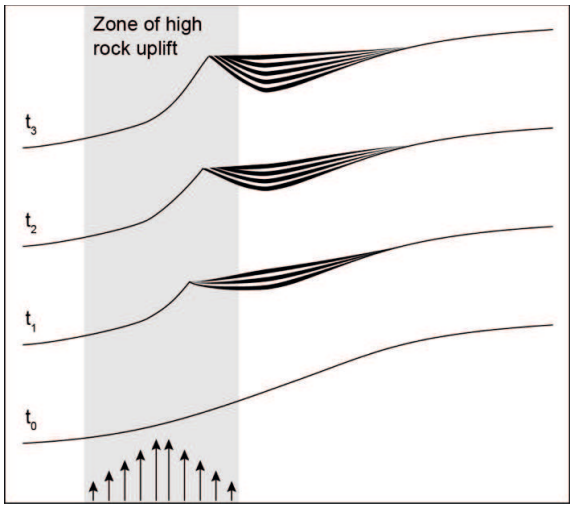

Figure 4.6: Schematic illustration showing the response of a nearly graded river to localized uplift. t_0 at bottom shows initial state, prior to uplift, and t_3 at the top shows final state with steep river reach centred on zone of high rock uplift. During river steepening, sediments accumulated upstream of the zone of high rock uplift.

on the fact that both, the production rates and the half-lives of ^{10}Be and ^{26}Al are known, so that deviations from the steady exposure ^{26}Al/^{10}Be ratio of ~7:1 can be converted to a burial age.

We modelled the concentration of cosmogenic nuclides, N (atoms g^{-1}), as a function of depth below the surface, z, which we made to be a function of time since deposition, t, according to (Granger and Smith, 2000):

$$N(z,t) = N_{inh}e^{-\lambda t} + \int_0^t \left[P_n(z(t')) + P_\mu(z(t'))\right] e^{-\lambda t} dt' \tag{4.1}$$

where, N_{inh} is the inherited concentration, λ is the decay constant, and P_n and P_μ are the depth-dependent production rates by neutrons and muons, respectively. The decline of cosmogenic nuclide production by neutrons with depth depends on the material density, ρ, and follows an exponential decline with an attenuation length scale, Λ, of ~160 g cm^{-2} (Gosse and Phillips, 2001)

$$P(z) = P_0 e^{-z\rho/\Lambda}. \tag{4.2}$$

The depth-dependency of cosmogenic nuclide production by muons is more complicated and we use the formulation of Heisinger et al. (2002a,b), as adopted by Balco et al. (2008), and provided in the numerical functions of the CRONUS Earth online calculator[1]. Different analytical approximations exist to capture the depth-dependency of cosmogenic nuclide production by muons with a series of exponentials. We use the formulation of Granger and Smith (2000) to account for the inherited component in Equation 4.1 (N_{inh}), which corresponds to the cosmogenic nuclides that were produced during hillslope exhumation. At steady state, the concentration of cosmogenic nuclides at the Earth's surface is a function of the erosion rate, ϵ (Granger and Riebe, 2007):

$$N(\epsilon) = \sum_{i=0}^{3} \frac{P_i(0)}{\lambda + \frac{\epsilon\rho}{\Lambda_i}} \tag{4.3}$$

where $P_i(0)$ are the surface production rates due to neutrons ($i = 0$), negative muons ($i = 1, 2$) and fast muons ($i = 3$), and Λ_i are the effective attenuation length scales (Λ_0 = 160 g cm^{-2}, Λ_1 = 738.6 g cm^{-2}, Λ_2 = 2688 g cm^{-2}, and Λ_3 = 4360 g cm^{-2}). Using the MATLAB® functions of the CRONUS-Earth online calculator (v. 2.2, Balco et al., 2008), we calculated site specific surface production rates due to spallation based on a time-dependent version of the scaling model by Lal (1991) and Stone (2000), which is denoted "Lm" in the CRONUS-Earth online calculator (Balco et al., 2008). Muogenic production rates are compensated for local air pressure following Stone (2000).

For calculating the cosmogenic nuclide concentrations acquired during hillslope exhumation using Equation 4.3, we computed average surface production rates for areas that are upstream of the sampling

[1] http://hess.ess.washington.edu/math/al_be_v22/functionlist.html

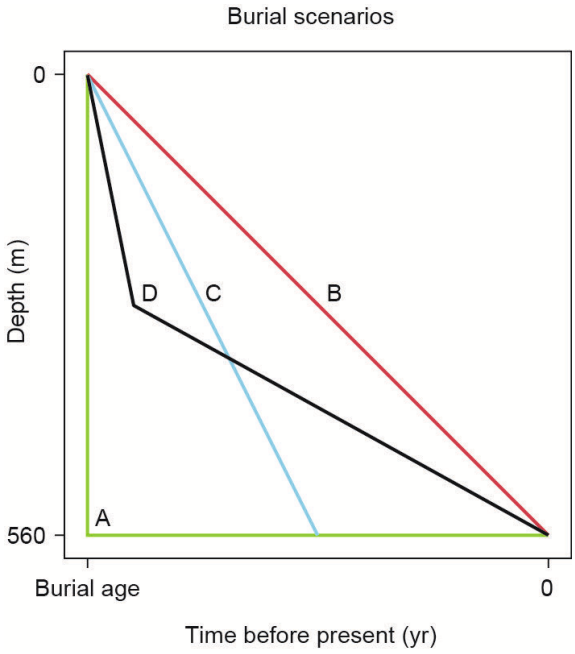

Figure 4.7: Burial scenarios used for converting measured ^{10}Be and ^{26}Al concentrations to burial ages.

site. As these areas are very large and it may well be that different parts of this area did not contribute to our sample at all, we tested the influence of different upstream areas on average production rates. For upstream areas of ~300-1900 km^2 that successively entail larger areas upstream from the sampling point (drill core #3), average surface production rates vary between 10.3 and 12.3 atoms (g qz)$^{-1}$ yr^{-1}, and are thus relatively insensitive to the exact extent of the contributing areas. However, our uncertainty in the extent of the contributing area means that we cannot use the paleo-erosion rates to estimate sediment fluxes from upstream. For the pre-burial production, we assume a rock density of 2.7 g cm^{-3}.

One requirement for burial dating is that the pre-burial ^{26}Al/^{10}Be ratio is known. For samples that have been continuously exposed to cosmic radiation this ratio reflects the differences in the production rates of ^{26}Al and ^{10}Be. However, if the grains in our samples have experienced burial and exhumation prior to deposition in the valley fill, the ^{26}Al/^{10}Be ratio may be lower than for continuous exposure. This would result in an overestimated burial age. However, we don't think that this effect is particularly important for the following reasons. First, significant shifts in the ^{26}Al/^{10}Be ratio requires rather long (>10^5 yrs) burial at sufficiently great depths (>~10 m). Although temporary storage may be quite common, for longer and deeper burial histories, it is less likely that the sediment is remobilized. In other words, the number of grains with low ^{26}Al/^{10}Be ratios to start with is likely small relative to the number of grains that have not undergone deep prior burial. Second, remobilizing deeply buried grains requires that they get exhumed to the surface, during which they will again accumulate cosmogenic nuclides that shift the ratios to higher values. For example, if our samples had been buried with a starting ^{26}Al/^{10}Be ratio of ~7:1 to their current depth at a constant rate for 2 Myr, the ^{26}Al/^{10}Be ratio would be ~2.7:1. If they would then exhume again at the same rate over the next 2 Myr, the ^{26}Al/^{10}Be ratio would be ~5.3:1 when they reach the surface, yielding an apparent burial age of ~0.5 Ma. Third, although the upstream area of the Yarlung Tsangpo near the gorge is huge, the areas contributing material to the sediment transported by the river is most likely much smaller. By definition, depositional areas do not contribute any material. Eroding hillslopes contribute relatively more for increasing hillslope angles. Hence, it can be expected that the areas close to the sampling location, where hillslopes are steep (Fig. 4.2b), had been contributing relatively more material compared to the many flat areas farther upstream. Therefore, we think that recycled, previously buried material with ^{26}Al/^{10}Be ratios lower than ~7:1 is not a significant source of uncertainty.

Because we don't exactly know the burial history, i.e., the time-depth history of our samples, we explored different burial scenarios (Figs. 4.7, 4.8). In all scenarios, we assume a wet bulk density of the sediment of 2.1 g cm^{-3}, which corresponds to sediment with a particle density of 2.7 g cm^{-3} and 35% saturated pore space. The first scenario serves for illustrative purposes and assumes instantaneous burial to depths where no

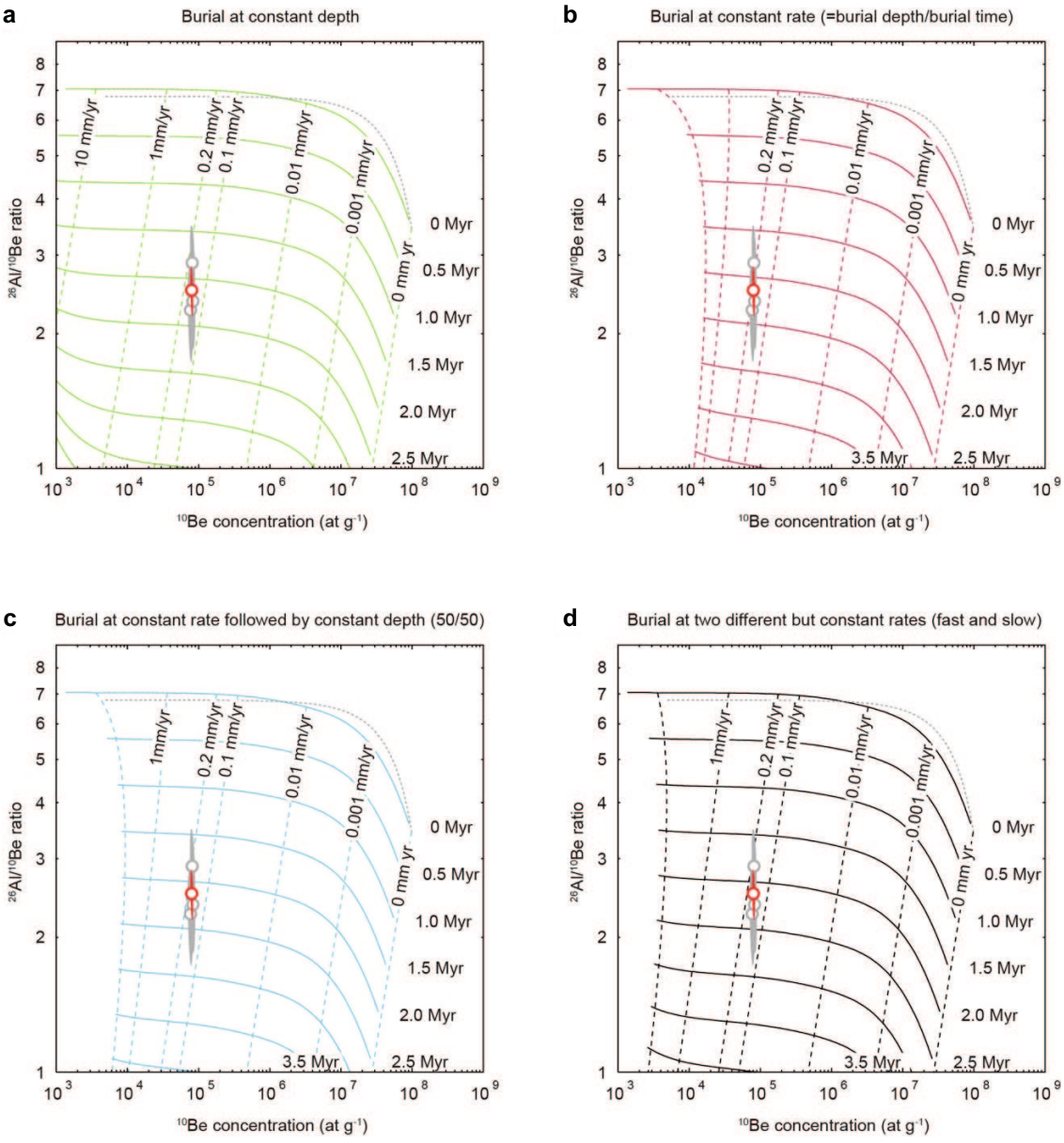

Figure 4.8: Predicted combinations of burial age and paleo-erosion rate for the four burial scenarios shown in Fig. 4.6. Note that the concentrations correspond to the measured concentrations, that is, they have not been normalized by the site-specific scaling factors.

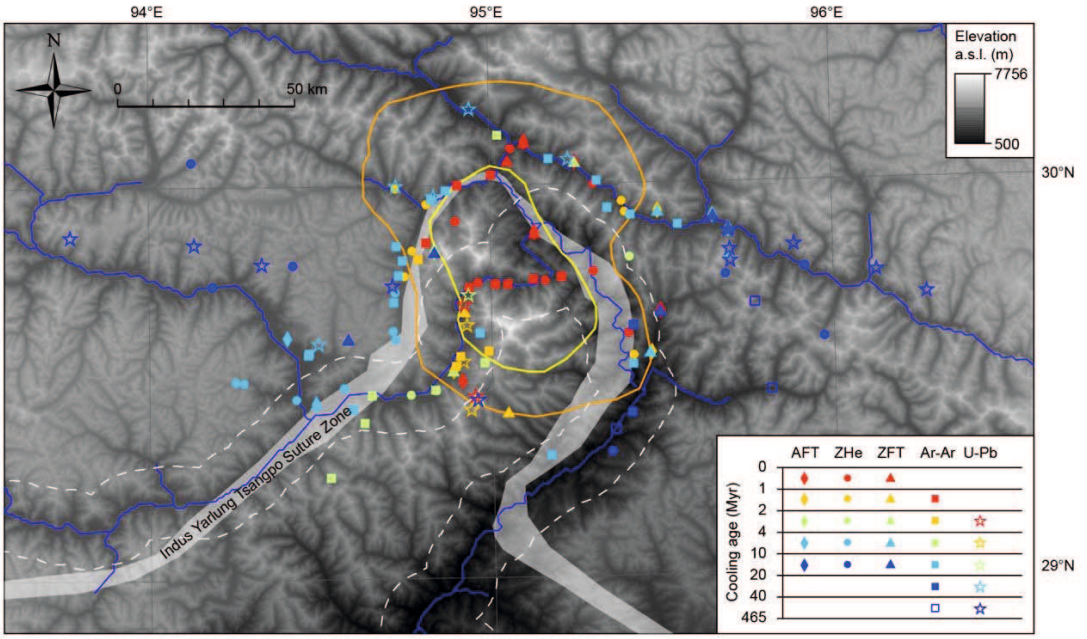

Figure 4.9: Published bedrock cooling and crystallization ages. AFT = Apatite Fission Track (Burbank et al., 1996; Crowley et al., 2009);ZHe = Zircon U/Th-He (Malloy, 2004); ZFT = Zircon Fission Track (Burbank et al., 1996; Crowley et al., 2009); Ar-Ar = $^{40}Ar/^{39}Ar$ (Ding et al., 2001; Quanru et al., 2006; Zeitler et al., 2006); U-Pb = Zircon Uranium-Lead (Crowley et al., 2009; Booth et al., 2004). Contour lines show rapidly exhuming areas with young (<2 Ma) Zircon U/Th-He (orange), and Biotite Ar-Ar ages (yellow) centered on the Tsangpo Gorge (Seeber and Gornitz, 1983). Dashed white line extents 10 km to either side of Yarlung Tsangpo River and marks boundary for measuring hillslope angles shown in Fig. 4.2b and sampling cooling ages shown in Fig. 4.2c.

more production of cosmogenic nuclides occurs ("A" in Figure 4.7, Fig. 4.8a). In this case, the burial age lies between ~2 and 2.5 Ma and the corresponding cosmogenic nuclide-derived erosion rate is ~0.1-0.2 mm yr^{-1}. In the second scenario we assume that burial occurred at a constant rate throughout the entire burial history ("B" in Fig. 4.7, Fig. 4.8b). This scenario is also rather unlikely, as we would assume that surface uplift rates and thus burial rates decreased with time as the Tsangpo Gorge was uplifted and river incision rates increased due to steepening of river gradients. Obviously, the additional production of cosmogenic nuclides during burial affects the total concentration of the sample. However, because most of the additional cosmogenic nuclide accumulation takes place in the upper few meters, that is, during the initial stages of the burial history, it mostly affects the inferred paleo-erosion rate but has only minor effect on the burial ages. The additional cosmogenic nuclide accumulation becomes important only for rather high paleo-erosion rates (>0.2 mm yr^{-1}), that is, when the inherited cosmogenic nuclide concentration is rather low. In the remaining two scenarios, we assumed burial rates that started out faster and slowed down with time ("C" and "D" in Fig. 4.7, Fig. 4.8c and d). Both scenarios predict concentrations that lie in between the first two scenarios, but have only little effect on the burial ages of our samples. Thus, we conclude that for a range of burial scenarios, our samples yield consistent results, with burial ages of ~2-2.5 Ma and paleo-erosion rates of ~0.1-0.2 mm yr^{-1}. Because our three samples stem from the same 3-m-thick sand unit, we treat them as different estimates of the same depositional age and refer to the weighted mean concentration for our best estimate of the depositional age.

Chapter 5

Ice dams, outburst floods, and glacial incision at the western margin of the Tibetan Plateau: A >100 k.y. chronology from the Shyok Valley, Karakoram

Abstract

Some of the largest and most erosive floods on Earth result from the failure of glacial dams. While potentially cataclysmic ice dams are recognized to have repeatedly formed along ice-sheet margins, much less is known about the frequency and longevity of ice dams caused by mountain glaciers, and their impact on landscape evolution. Here we present field observations and results from cosmogenic nuclide dating that allow reconstructing a >100-kyr-long history of glacial damming in the Shyok Valley, eastern Karakoram (South Asia). Our field observations provide evidence that Asia's second-longest glacier, the Siachen, once extended for over 180 km and blocked the Shyok River during the penultimate glacial period, leading to upstream deposition of a more than 400-m-thick fluvio-lacustrine valley fill. ^{10}Be-depth profile modeling indicates that glacial damming ended with the onset of the Eemian interglacial and that the Shyok River subsequently incised the valley fill at an average rate of ~4–7 m kyr^{-1}. Comparison with contemporary ice-dammed lakes in the Karakoram and elsewhere suggests recurring outburst floods during the aggradation period, while over 25 cycles of fining-upward lake deposits within the valley fill indicate impounding of floods from farther upstream. Despite prolonged damming, the net effect of this and probably earlier damming episodes by the Siachen Glacier is dominated by glacial erosion in excess of fluvial incision, as evidenced by a pronounced overdeepening that follows the glaciated valley reach. Strikingly similar overdeepened valleys at all major confluences of the Shyok and Indus Rivers with Karakoram tributaries indicate that glacial dams and subsequent outburst floods have been widespread and frequent in this region during the Quaternary. Our study suggests that the interaction of Karakoram glaciers with the Shyok and Indus Rivers promoted valley incision and headward erosion into the western margin of the Tibetan Plateau.

5.1 Introduction

The significance of rare but catastrophic events in Earth's history relative to steady but uniform processes is an important topic in the Earth sciences [e.g., Wolman and Miller, 1960]. Amongst the most impressive examples of catastrophic landscape-shaping events are dam-related megafloods, many of which appear to be intimately related to glacial climates and environments (e.g., Baker, 2002; O'Connor and Costa, 2004). For example, the Missoula floods (northwestern U.S., Bretz, 1969) and the flood that emptied Lake Agassiz (north-central North America, Barber et al., 1999) were due to failure of ice dams at the margins of the Laurentide ice sheet, and had far-reaching environmental consequences (e.g., Clarke et al., 2003). In mountainous landscapes, and

in response to present-day warming, moraine-dammed lakes frequently develop in front of retreating glaciers, and their catastrophic outbursts pose a significant hazard for downstream communities (e.g., Clague and Evans, 2000; Hewitt and Liu, 2010; Benn et al., 2012). In contrast to moraine-dammed lakes, ice-dammed lakes commonly form when a tributary glacier has detached from the main trunk glacier, and the resulting lakes commonly drain subglacially on a relatively frequent basis (Costa and Schuster, 1988). Merzbacher Lake, for example, is an ice-dammed lake associated with the Inylchek Glacier, Tien Shan (Central Asia), which drains almost every summer (Ng and Liu, 2009). More dangerous situations occur when the valley where damming occurs is largely ice free itself, so that a substantial amount of water can be impounded by the dam before failure (Costa and Schuster, 1988). Clearly, the higher and more stable the dam and the shallower the dammed valley, the greater the ice-dammed lake volume and the potential flood discharge. Examples from the European Alps (Haeberli, 1983), Alaska (Post and Mayo, 1971), the Karakoram (South Asia, Hewitt and Liu, 2010), and many other regions world-wide (Costa and Schuster, 1988) underscore the importance of glacial dams on modulating flood frequency and peak discharges. Because these factors could be of primary importance for the long-term efficiency of sediment transport and bedrock incision (e.g., Wolman and Miller, 1960; Snyder, 2003; Tucker, 2004; Lague, 2005), glacial dams may have a far greater impact on landscape evolution in mountainous regions than their areal footprint and representation in the depositional record would suggest.

Depositional evidence for very large (up to 2,835 km^2) glacially dammed Holocene lakes upstream of the Tsangpo River gorge, on the southeastern edge of the Tibetan Plateau, led Montgomery et al. (2004) to suggest that catastrophic failure of these lakes may have resulted in the most erosive events in recent Earth history. Furthermore, Korup and Montgomery (2008) argued that repeated glacial damming of major rivers in this region substantially impeded headward river incision into the Tibetan Plateau and has helped preserve a distinct plateau edge through protracted sediment accumulation and storage upstream from the barriers (e.g., Montgomery et al., 2004). These studies bring glacial dams to the forefront of processes shaping the edges of Cenozoic orogenic plateaus that are impacted by glacial climates. However, the longevity of glacier dams and the damming frequency are generally not well constrained (Korup and Tweed, 2007), which makes assessing their geomorphic relevance in the long term difficult. Although historically active glacier dams tend to fail frequently (Costa and Schuster, 1988), examples of larger glacier dams are rare and their hydrology may be more complex, potentially rendering them more stable. We address these issues in our study of one of the most impressive examples of Pleistocene glacial damming in the Karakoram and demonstrate that ice dams and associated outburst floods were likely frequent and important processes in the Quaternary evolution of the Shyok and Indus Valleys.

Glacier Dams in the Karakoram Mountains The Karakoram Mountains, at the north-western edge of the Tibetan Plateau, have the greatest concentration of glaciers in the Himalayas and feature some of the longest glaciers in Central Asia (Fig. 5.1). They also host one of the world's largest assemblages of presently or historically active glacier dams, many of which have failed catastrophically (Cunningham, 1854; Mason, 1929; Gunn et al., 1930; Hewitt, 1982; Korup et al., 2010). The historically most devastating floods were related to lakes that formed in valleys blocked by glaciers coming from tributaries (Hewitt and Liu, 2010). At present, there are more than 90 reports of ice dam-related outburst floods that occurred during the past 200 years in rivers draining the Karakoram Mountains (Hewitt and Liu, 2010). The Kyagar Glacier, for example, is blocking the upper Shaksgam River (Fig. 5.1), a tributary of the Yarkand River that repeatedly forms an up to 7-km-long lake (Fig. 5.2). During the past 50 years, this lake drained at least 19 times catastrophically, resulting in 7 major or destructive floods. Two times, peak discharges measured at Kaqun, China, located some 500 km downstream from the ice dam, exceeded 6,000 $m^3\ s^{-1}$ (Hewitt and Liu, 2010). In other places without direct flood or lake reports, strandlines behind glaciers can be seen in satellite images (e.g., Google Earth http://www.google.com/earth/), and provide indirect evidence for the existence of ice-dammed lakes in the past.

Several Karakoram valleys stand out with an unusual abundance of active or historic glacier dams: the Shaksgam, Shimshal, Karambar, and uppermost Shyok. All of these valleys are parallel to mountain ranges that host several large, ice-covered tributaries. On a larger spatial and longer temporal scale, the same applies to the entire Karakoram and its main drainages. While the aforementioned valleys have been ice covered, glacial morphology and deposits in the Gilgit, Hunza, Shigar, and Nubra Valleys (Fig. 5.1)

indicate that Pleistocene glaciers reached the Indus and Shyok Valleys (Derbyshire et al., 1984; Shroder et al., 1989; Phillips et al., 2000; Owen et al., 2006; Seong et al., 2007; Dortch et al., 2010), where they probably formed ice-dammed lakes. However, distinguishing between fluvio-lacustrine deposits related to glacial or landslide processes can be difficult, and it has been argued that many previously identified moraines and ice dam-related lake deposits are due to large rock avalanches (Hewitt, 1999; Hewitt et al., 2011). Here, we report field observations that document one of the largest known glacier dams in the Karakoram. Cosmogenic nuclide exposure dating together with published data allow reconstruction of a >100-k.y.-long history of glacial damming, and associated upstream aggradation and subsequent incision in the upper Shyok River.

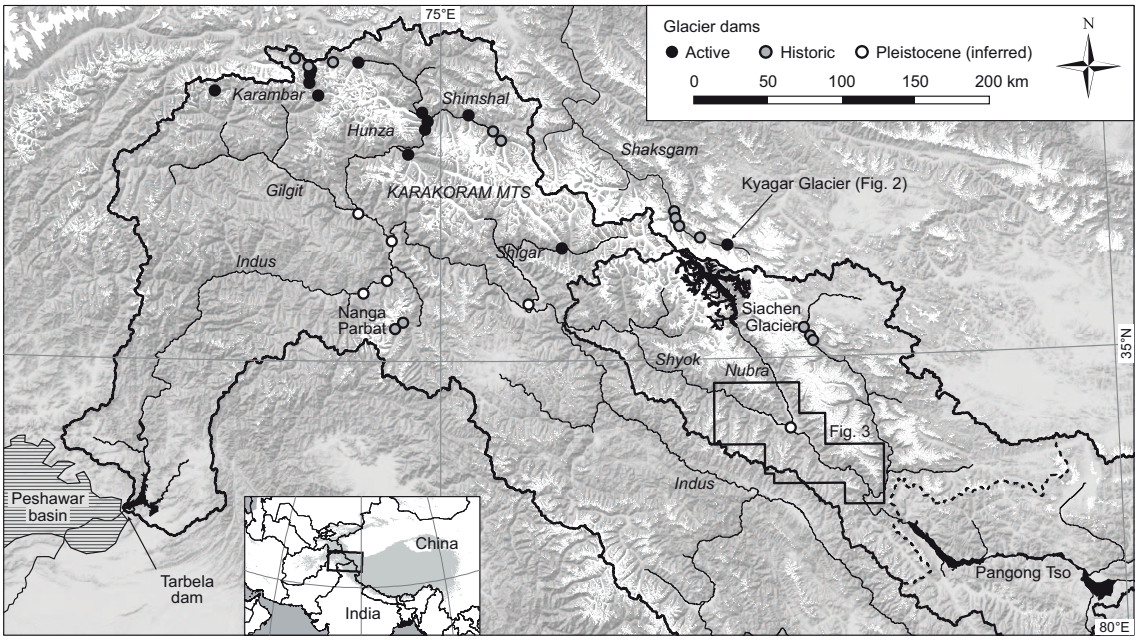

Figure 5.1: Study area in the eastern Karakoram Mountains (South Asia). Thick bold lines indicate the outline of the Shyok and Indus catchments. Dashed line in the Shyok catchment delimits the currently endorheic area, draining to Pangong Tso. River names are given in italic font. Glacier dams after Hewitt (1982), Dortch et al. (2010), Seong et al. (2007), Phillips et al. (2000), and inspection of satellite images. Active glacier dams are defined as places where a glacier confines the flood plain of a river to a width that is smaller than up- or downstream of the confinement. White areas are present-day glaciers after Arendt et al. (2012).

5.2 Study area

The Shyok River is the largest tributary of the upper Indus River and drains much of the high and rugged eastern Karakoram, the Transhimalaya, and low-relief areas on the western Tibetan Plateau (Fig. 5.1). Its drainage area is currently ~15,000 km^2, but may have been ~80,000 km^2 when Lake Pangong Tso spilled over its north-western edge and was hydrologically connected with the Shyok River in the early Holocene (Gasse et al., 1996) and probably during earlier times in the last glacial cycle (Shi et al., 2001). In the heart of the eastern Karakoram lies the presently 70-km-long Siachen Glacier. Its terminus is at 3,600 m above sea level (asl) and sources the Nubra River, which flows ~80 km southeast along the Karakoram fault before it enters the Shyok suture zone and joins the WNW-flowing Shyok River (Rolland et al., 2000). From the glacier terminus down to ~3,000 m asl, the Nubra and Shyok Valleys are wide and alluviated, with widths that reach >5 km at their confluence. At the mouths of most of their tributaries, large alluvial fans extend far into the valley and testify to a period of aggradation that appears to be still ongoing (Fig. 5.3a) (Drew, 1873). Active aggradation is also evident at the Shyok-Nubra confluence, where the Shyok River is currently building a fan that forces the Nubra River to the downstream side of the valley (Fig. 5.3a).

Near the Shyok-Nubra confluence, well preserved wave-cut lake shorelines occur up to ~150 m above the present-day valley bottom, and have been related to a lake that formed due to Siachen Glacier's damming of the Shyok River (Dortch et al., 2010). Although the shorelines have not been dated chronometrically, based

on regional stratigraphic and geomorphic relationships their formation has been bracketed by dated moraines to between 41 ± 2 ka and 81 ± 6 ka (Dortch et al., 2010). Furthermore, till-mantled hillslopes that occur up to ~900 m above the valley floor indicate that the Siachen Glacier may once have been much thicker, but these deposits have not been dated so far. In contrast, Phartiyal et al. (2005) assigned lake sediments at various elevations near the confluence to a phase when an extensive paleolake stretched for ~100 km along the Shyok Valley and ~30 km upstream into the Nubra Valley. Their interpretation, the stratigraphic relationship with dated moraines, and calibrated ^{14}C ages from these lake sediments of ca. 25–27 ka (Phartiyal and Sharma, 2009) are in conflict with the glacial-damming hypothesis and merit further investigation. We combine the previous results by Dortch et al. (2010) with our own field data and cosmogenic nuclide dating to decipher the glacial damming history at the Shyok-Nubra confluence.

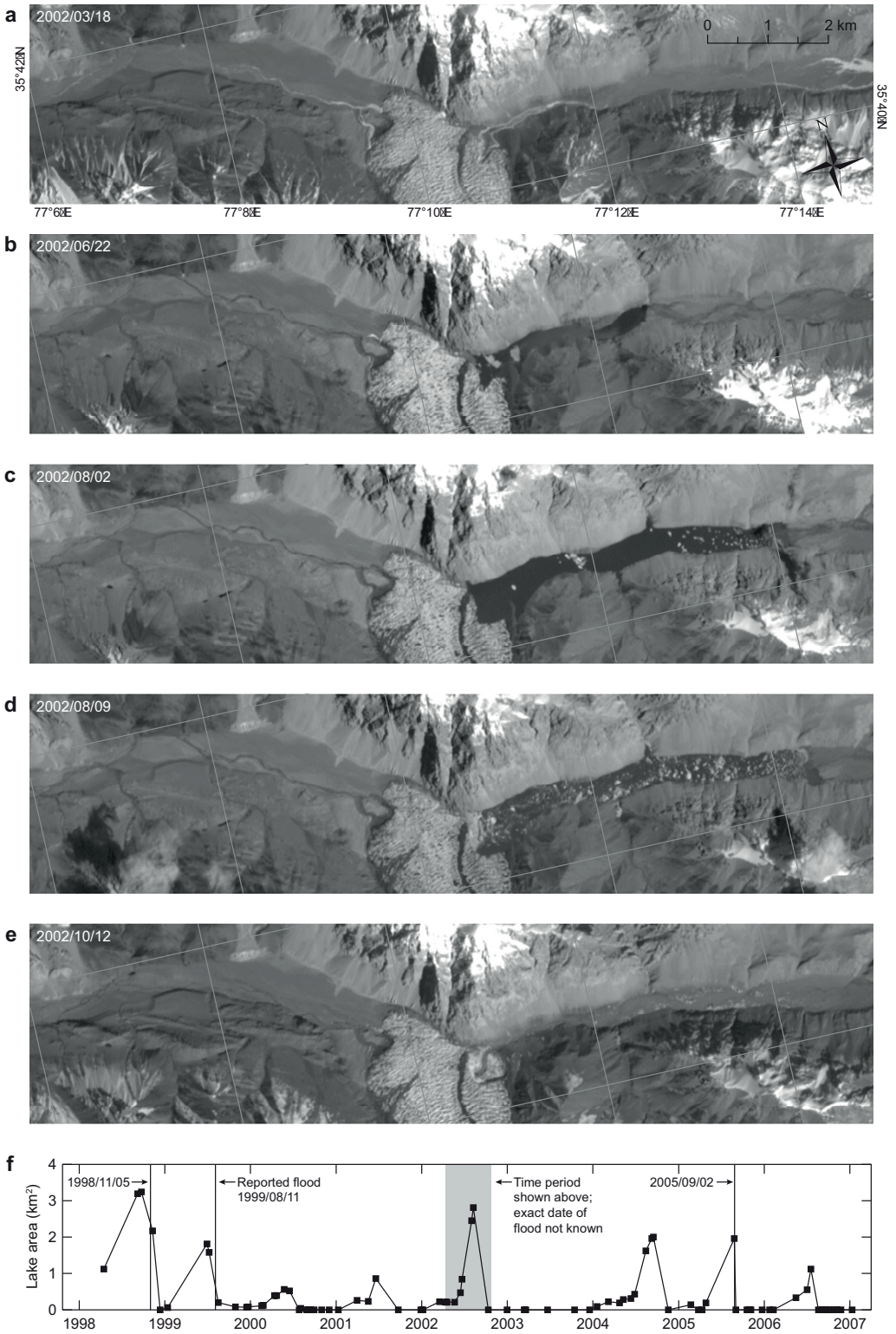

Figure 5.2: Kyagar Glacier terminus and lake in the upper Shaksgam River. (**a–e**) Landsat ETM+ satellite images (band 8), acquired March to October 2002. (**f**) Evolution of lake area obtained from Landsat TM and ETM+ satellite images, together with reported flood dates from Hewitt and Liu (2010). Estimated uncertainty in lake area is ~15%, and up to ~30% after 31 May 2003, when the scan line corrector instrument of the ETM+ sensor failed

5.3 Methods

5.3.1 Mapping and remote-sensing analysis

We conducted field work in the Shyok Valley between the villages of Chasthang and Agham, and in the Nubra Valley up to the village of Panamik, where we mapped Quaternary deposits and landforms and collected samples for cosmogenic nuclide surface-exposure dating. Because there have been controversies about inferred glacial origins of Quaternary deposits in several parts of the Karakoram (Hewitt, 1999; Hewitt et al., 2011), we employed a conservative approach of mapping glacial deposits and looked specifically for glacial striations and their association with lateral moraine ridges. Spatial references were obtained using a handheld GPS and topographic maps. We supplemented our field mapping with analysis of optical satellite imagery and 90-m-resolution Shuttle Radar Topography Mission digital elevation models (DEM). Specifically, we identified and mapped terraces and moraines in areas we could not access in the field, e.g., farther upstream from Agham and on steep hillslopes, based on surface morphology, extent, appearance in high-resolution optical imagery in Google Earth, and similarity with landforms that we mapped in the field. We again used the same cautious mapping approach in the sense that any landform identified in this way would have to be between landforms of the same type that we mapped in the field.

5.3.2 Surface-exposure dating

We dated aggradation surfaces in the study area using in situ-produced cosmogenic nuclides. Specifically, we measured ^{10}Be in amalgamated samples from two depth profiles and at one location from a surface sample alone. Each sample consisted of ~30–40 well-rounded, granitic and gneissic pebbles of ~5 cm diameter or equally sized chunks from slightly larger cobbles (<10 cm), which were taken from the same depth (± 5 cm) or the surface. After standard physical and chemical preparatory steps (e.g., Kohl and Nishiizumi, 1992; von Blanckenburg, 2004), we measured the in situ-produced ^{10}Be/^{9}Be ratios in our samples at the Ion Beam Facility of the ETH Zürich, Switzerland, and the Centre for Accelerator Mass Spectrometry of the University of Cologne (CologneAMS) (Dewald et al., 2013), Germany (Table 1).

We calculated exposure ages from ^{10}Be concentrations based on a time-dependent version of the production rate scaling model by Lal (1991), updated by Stone (2000), as provided in the CRONUS online calculator (v.2.2, Balco et al., 2008, denoted there by "Lm"), and using a ^{10}Be half-life of 1.387 ± 0.016 m.y. (Chmeleff et al., 2010; Korschinek et al., 2010). At two sites, we modeled the total in situ ^{10}Be production as due to the fractional production by neutron spallation (n, 97.85%), slow muons (m_1, 1.5%) and fast muons (m_2, 0.65%), with attenuation lengths of 160 g cm^{-2} (Λ_n), 1,500 g cm^{-2} (Λm_1), and 5,300 g cm^{-2} (Λm_2), respectively (Braucher et al., 2003, 2009):

$$\begin{aligned} C(x,t) = &\frac{P_0 n}{\epsilon/\Lambda_n + \lambda} e^{(-x/\Lambda_n)} \left[1 - e^{-t(\epsilon/\Lambda_n + \lambda}\right] + \\ &\frac{P_0 m_1}{\epsilon/\Lambda_{m1} + \lambda} e^{(-x/\Lambda_{m1})} \left[1 - e^{t(\epsilon/\Lambda_{m1} + \lambda}\right] + \\ &\frac{P_0 m_2}{\epsilon/\Lambda_{m2} + \lambda} e^{(-x/\Lambda_{m2})} \left[1 - e^{-t(\epsilon/\Lambda_{m2} + \lambda)}\right], \end{aligned} \tag{5.1}$$

where C is the ^{10}Be concentration (atoms g^{-1}), x is depth below the surface (cm), t is the exposure time (yr), P_0 is the surface production rate (atoms g^{-1} yr^{-1}), ϵ is the erosion rate (g cm^{-2} yr^{-1}), and λ is the decay constant. Note that ϵ used here reflects an erosion rate given in cm yr^{-1} multiplied by density, ρ (g cm^{-3}). We derived the scalar surface production rate, P_0, by averaging the decay-weighted, time-dependent instantaneous surface production rates, $P_{0,i}$, over the model time according to:

$$P_0 = \frac{\sum P_{0,i} e^{\lambda t_i}}{\sum e^{-\lambda t_i}} \tag{5.2}$$

where the subscript i refers to the discrete times for which production rates are calculated, typically at increments of 1 k.y. Following Braucher et al. (2009) we obtained best-fit results with an estimated uncertainty for our depth-profile data using a Monte Carlo inversion method. For each depth profile, we randomly sampled 200 concentration profiles from our n samples, which lie within the range defined by the measured

Table 5.1: Cosmogenic nuclide sample data

Sample name	Latitude (°N)	Longitude (°E)	Elevation above sea level (m)	Depth below surface (cm)	Topographic shielding	Sample weight (g)	^{10}Be concentration (atoms [g qz]$^{-1}$)[a]	^{10}Be concentration uncertainty (atoms [g qz]$^{-1}$)[b]
Shyk-1	34.3158	77.8185	3710	0	0.998	23.00	5.687E+06	1.804E+05
Shyk-6	34.3204	77.8187	3700	0	0.998	23.58	5.764E+06	1.828E+05
Shyk-7_40	34.3204	77.8187	3700	40	0.998	47.59	4.631E+06	1.467E+05
Shyk-7_60	34.3204	77.8187	3700	60	0.998	41.03	3.813E+06	1.209E+05
Shyk-7_80	34.3204	77.8187	3700	80	0.998	47.93	3.095E+06	9.815E+04
Shyk-7_100	34.3204	77.8187	3700	100	0.998	58.23	2.429E+06	7.702E+04
Shyk-7_120	34.3204	77.8187	3700	120	0.998	50.64	1.937E+06	6.152E+04
Shyk-7_140	34.3204	77.8187	3700	140	0.998	55.33	1.433E+06	4.556E+04
Shyk-7_160	34.3204	77.8187	3700	160	0.998	47.29	1.217E+06	3.875E+04
WP016-0cm	34.5699	77.6535	4048	0	0.997	28.31	6.475E+06	2.048E+05
WP016-20cm	34.5699	77.6535	4048	20	0.997	27.14	5.009E+06	1.590E+05
WP016-50cm	34.5699	77.6535	4048	50	0.997	30.19	3.929E+06	1.251E+05
WP016-75cm	34.5699	77.6535	4048	75	0.997	30.20	2.853E+06	9.081E+04
WP016-100cm	34.5699	77.6535	4048	100	0.997	30.45	1.903E+06	6.112E+04
WP014	34.5768	77.6307	3389	0	0.992	35.00	3.005E+06	9.535E+04
WP020	34.4853	77.7104	3483	0	0.992	29.42	4.565E+06	1.461E+05

[a] The subtracted average laboratory process blank ^{10}Be/^{9}Be ratios are 3.9×10^{-15} (Shyk-1 to Shyk-7; 0.02%–0.09% of the measured ^{10}Be/^{9}Be ratios) and 2.5×10^{-15} (WP014 to WP020; 0.02%–0.08% of the measured ^{10}Be/^{9}Be ratios). ^{10}Be/^{9}Be ratios were normalized to the ETH in-house standard S2007N (Shyk-1 to Shyk-7), and to the standard 07KNSTD that was used in Cologne (WP014 to WP020). Note that the two standards are equivalent within rounding error. qz = quartz.

[b] ^{10}Be concentration uncertainties reflect total analytical uncertainties at the 1σ level.

concentrations (C_i) plus/minus their uncertainties ($2\sigma_i$) and obtained the best-fit solution by minimizing the chi-squared misfit (χ^2) between the measured and modeled concentrations (Equation 5.1) for given exposure age-erosion rate or exposure age-density pairs, with the other parameters predefined, e.g., inheritance (C_0), density, erosion rate:

$$\chi^2 = \sum_{i=1}^{n} \left(\frac{C_i - C(x_i, t, \rho, \epsilon, C_0)}{2\sigma_i} \right)^2 . \tag{5.3}$$

We emphasize that ^{10}Be production rates are poorly constrained in the study area and that instantaneous production rates, calculated with different existing scaling models, vary by up to 60% during the past 100 k.y. (e.g., Balco et al., 2008). The absolute ages presented in this study are therefore subject to greater uncertainty, with respect to chronologies obtained with other dating methods, than indicated by the analytical and modeling uncertainties that we provide. To allow comparison with our new ages, we recalculated the exposure ages published by Dortch et al. (2010) based on the same production-rate scaling model used for our samples and refer to the recalculated ages from here on and in all of our figures. Additional details on the ^{10}Be-depth profile modeling, the recalculated published ^{10}Be exposure ages, and data on glacial striation measurements are located in the Supplementary Data (Appendix B).

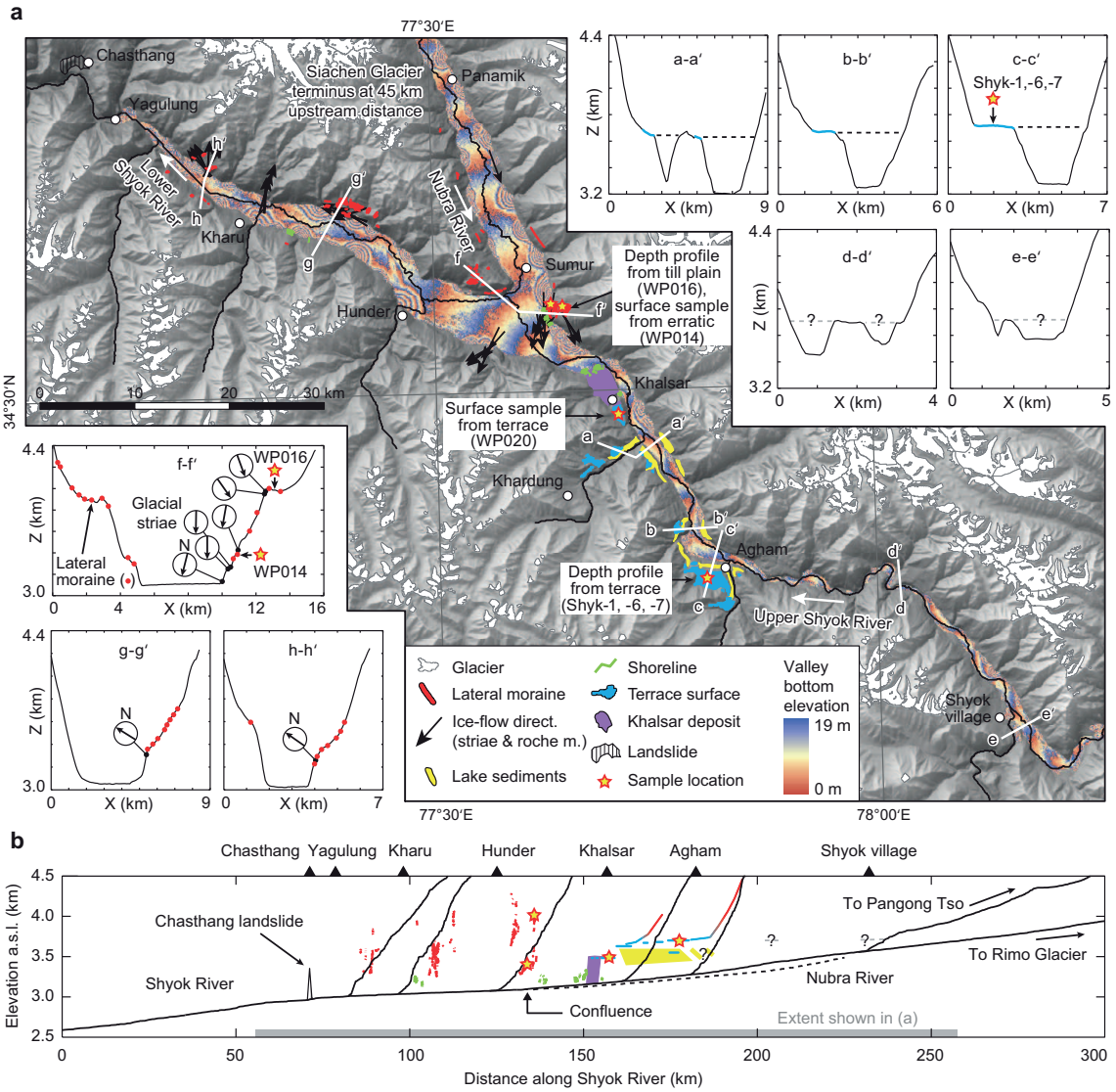

Figure 5.3: Geomorphology of the Shyok-Nubra confluence. (**a**) Hillshade image with glaciers (white), major depositional landforms (colored polygons), ice-flow directions from glacial striae and roches moutonnées (black arrows), sample locations (stars), and traces of surface elevation profiles (a–a' through h–h'). Dashed lines in profiles a–a' through e–e' give top of reconstructed valley fill. Elevations of Shyok and Nubra valley bottoms are colored, repeating every 20 m to highlight low gradients and alluvial fans. White arrows give flow direction of rivers. (**b**) Longitudinal profiles of the Shyok River and major tributaries (solid black lines); the Nubra River is dashed (a.s.l.–above sea level). Colored lines and polygons give moraine ridges (red), terrace surfaces (blue), shorelines (green), and lake deposits (yellow). Triangle near Chasthang indicates a landslide.

5.4 Results

5.4.1 Fluvial and lacustrine deposits in the Upper Shyok Valley

The upper Shyok River, i.e., upstream of the Nubra confluence, flows mostly on >1-km-wide alluviated valley bottoms, but approaches bedrock between the villages of Agham and Shyok, where the valley is more confined and steeper (Fig. 5.3). Where valley bottoms are wide, the valley is riddled with remnants of an up to ~400-m-thick sequence of fluvio-lacustrine deposits that are frequently topped by flat terrace surfaces. These terrace surfaces have top elevations between ~3600 and ~3700 m asl and can be traced >20 km along the upper Shyok Valley, and several kilometers into major tributaries (Figs. 5.4a, 5.4b). Between Khalsar and Agham the top elevation drops ~5.5 m per kilometer, which is similar to the present-day gradient of the Shyok River. We could not access areas much farther upstream from Agham, but sub-horizontal surfaces, which could correspond to fill or strath terraces, can be identified in the DEM (Fig. 5.3a).

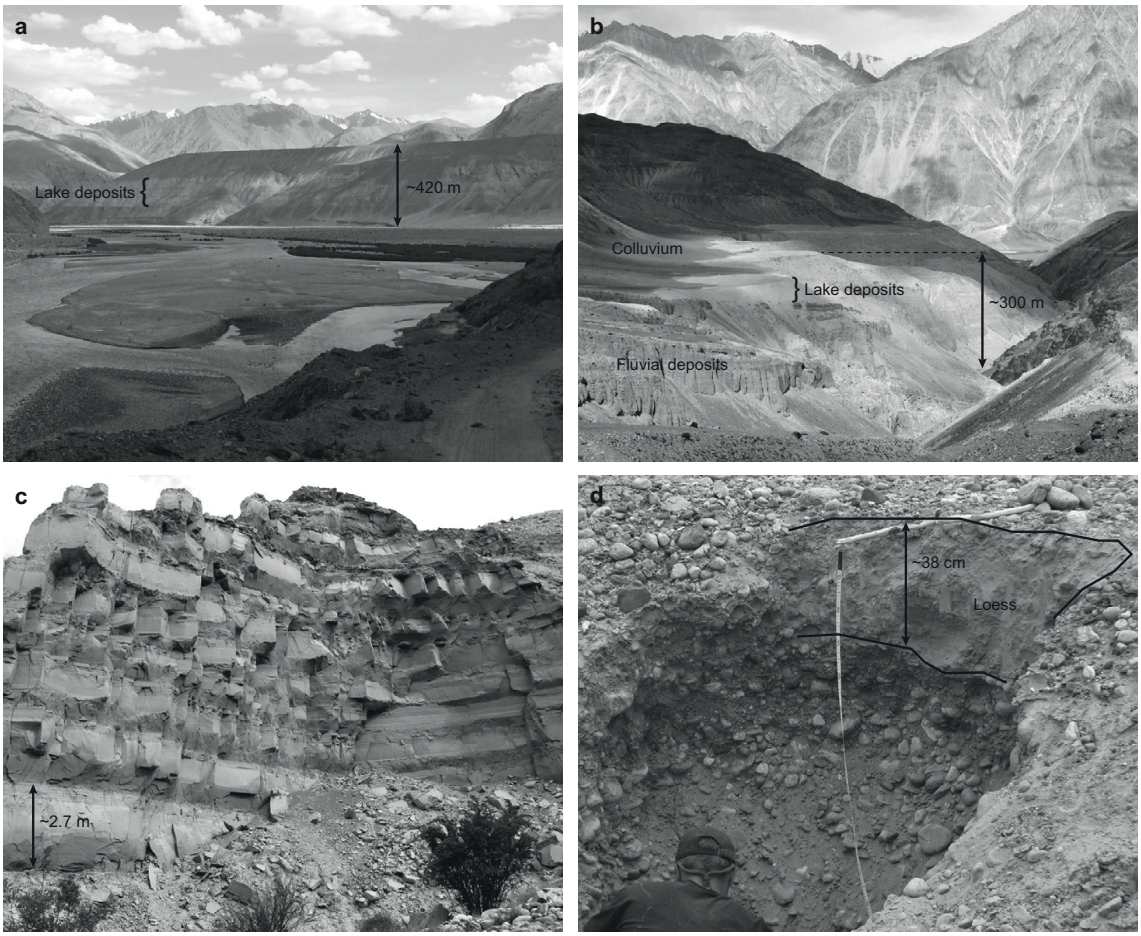

Figure 5.4: Field photographs of fluvial-lacustrine valley fill in the upper Shyok Valley. (**a**) Fill terrace near Agham village. Note bright-colored lake sediments. View is southeast, upstream the Shyok River. (**b**) Valley fill in a tributary near Khardung. View is north, toward confluence with the Shyok River. (**c**) Lake sediments exposed at a terrace near Agham. Height of outcrop is ~16 m. Note cyclic repetition of dark to light-colored sediments. (**d**) Pit for sampling ^{10}Be-depth profile on a terrace near Agham. Note fine-grained loess deposits between desert pavement and fluvial cobbles.

Where accessible, the upper and lower parts of the valley fill are dominated by relatively homogenous cobble and gravel deposits with occasional boulders and sand lenses typical for a braided-river depositional environment (Fig. 5.4a). The middle part comprises a ~150–200-m-thick lacustrine unit (Fig. 5.4b) that is exposed between Agham (~3450–3600 m asl) and Khalsar (~3400–3600 m asl) and easily visible on satellite images. No comparable lake-sediment outcrops were seen farther upstream in satellite images or farther downstream in the field (Fig. 5.3a). Within the tributary joining the Shyok at profile a-a' in Fig. 5.3a, the lake

deposits pinch out at a distance of ~4.5 km from the Shyok, whereas their extent appears to be more restricted in the tributary near Agham. In these two tributaries, the fluvio-lacustrine valley fills grade upstream into glacial facies at a distance of ~10 and 7 km from the Shyok, respectively. At a well-exposed lake-sediment outcrop near Agham, we observed 25 upward-fining units, with a few more obscured by colluvium (Fig. 5.4c). In this location, each unit is ~1–5 m thick and starts with rippled fine sands at the base that grade into massive silts, and finally laminated silty clays at the top. Throughout these deposits, isolated small dropstones can be found. Samples that were taken from these lake sediments (Figs. 5.4c, 5.6) are devoid of any ostracods (S. Mischke, 2012, personal commun.), and unfortunately not suitable for optically stimulated luminescence (OSL) dating due to signal saturation (J. Bloethe, 2012, personal commun.).

5.4.2 The Khalsar deposit

A conspicuous deposit occupies ~10 km^2 in the upper Shyok Valley near Khalsar village, close to the Shyok-Nubra confluence (Fig. 5.5; termed here the Khalsar deposit). At the down-stream end of this deposit, well-developed lake shorelines that have been related to glacial damming at the Shyok-Nubra confluence occur up to an elevation of 3250 m asl, that is, ~100 m above the present-day river, and less well developed shorelines occur up to ~200 m above the present-day river (Dortch et al., 2010). The origin and timing of deposition is important because of this stratigraphic relationship, but has been debated in previous studies. Pant et al. (2005) and Dortch et al. (2010) interpreted the Khalsar deposit as a moraine and therefore as evidence for glaciers in the upper Shyok Valley reaching all the way to the confluence. We agree with Phartiyal et al. (2005), interpreting it as a landslide deposit, based on several criteria. Although most of the deposit is currently inaccessible for civilians, accessible outcrops near its downstream limit, and close to the present valley bottom, reveal a disturbed contact between monomict, intensely fragmented granitic material and convoluted fluvial cobble beds below, which resemble present-day Shyok cobbles (Fig. 5.5, inset).

A rock avalanche is furthermore corroborated by a large (~4 m) boulder with extension fractures that radiate from a point on its upper end and create a jigsaw pattern (Fig. 5.5, inset), suggesting a large and sudden in situ loading, as well as clastic dikes of sand and pebbles that intrude several meters into the overlying material (Shreve, 1987; Owen et al., 2008). The tributary coming from the south makes a 1.8 km southeast, i.e., upstream, detour around most of the deposit before it flows northeast again and joins the northwest-flowing Shyok (Fig. 5.5). The tributary dissects the deposit at Khalsar village and exposes a sharp basal contact with an up to 300-m-thick section of underlying fluvial cobbles that are identical to those previously described and in continuity with a terrace surface extending another ~1 km upstream at an elevation of ~3480 m asl. On the southwestern edge of the terrace surface, perched between the southern hillslopes and the monomict granitic deposits, are a few meters of exposed lake sediments. Our observations suggest that at least part of the deposit, if not all, is related to a rock avalanche that originated from the northern granitic valley walls and fell partly onto a fluvial terrace, causing upstream deflection and ponding of the tributary. We note that we found no indicators in the field or on satellite images that the ~1.5 km offset of the tributary could be due to movement on a previously unrecognized strand of the Karakoram fault, which traces the northern side of the upper Shyok Valley in this location (Phillips, 2008).

5.4.3 Glacial marks and deposits in the Nubra and Lower Shyok Valleys

In the lower Shyok Valley, i.e., downstream of the Nubra confluence, terraces associated with fluvio-lacustrine deposits are absent. Instead, like in the adjoining Nubra Valley (Dortch et al., 2010), hillslopes are commonly mantled with glacial deposits that mostly consist of rounded to sub-angular, unsorted allochthonous boulders in a sand-silt matrix (Fig. 5.7). These deposits are commonly capped with long, valley-parallel lateral moraines that occur on both sides of the Nubra confluence up to >4000 m asl (Figs. 5.3a, 5.7). At three locations in the lower Shyok Valley, where hillslope angles are relatively gentle, abundant and closely spaced lateral moraines can be observed (Fig. 5.3a, profiles f–f', g–g', h–h'). The elevation of lateral moraines in the lower Shyok Valley systematically decreases downstream, for both individual moraines as well as sets of moraines (Fig. 5.3b). Glacial striations and roches moutonnées are widespread in the Nubra and lower Shyok Valleys and consistently indicate down-valley ice movement (Fig. 5.3a). On some bedrock ridges in front of confluences in the lower Shyok Valley we found striations documenting ice transport toward the tributaries.

Yet, within these tributaries, close to their mouths, we also observed remnants of valley fills that appear to be of fluvial origin. Farther up in these tributaries, tills and moraines are widespread.

At the lower end of our study area, near the village of Yagulung, two large and smooth whaleback-shaped bedrock bumps protrude up to 200 m over the valley floor. These features closely resemble roches moutonnées, but we did not find any glacial striations on them. Yet farther downstream, at the village of Chastang (34.822°N, 77.081°E), a landslide deposit with surface elevations between 3200 and 3500 m asl abuts the river (Fig. 5.3). The northern hillslope above this landslide deposit appears to be still in motion. Apart from the well-developed shore-lines near the confluence (Fig. 5.7) (Dortch et al., 2010), we also found shorelines between Kharu and Hunder, occurring up to an elevation of ~3250 m asl, that is, ~200 m above the present-day river (Fig. 5.8). These shorelines and those at the confluence are characterized by staircase morphologies with rhythmic downhill variations in slope angle and grain size that can be laterally traced and appear perfectly horizontal.

5.4.4 Surface-exposure dating

We collected five samples along a depth profile that extends from the surface to a depth of 100 cm that we obtained from a relatively flat till plain found at ~4000 m asl at the Nubra-Shyok confluence (Fig. 5.3a, site WP016). Because we were not able to measure densities in the field, and because density can vary spatially in tills over very short distances depending on the presence of boulders or fines, we applied Equations 5.1 and 5.2 and the previously described model with erosion rate and exposure age as free parameters and tested results for average densities of 1.9, 2.0, and 2.1 g cm^{-3} (Fig. B.2). These densities are within the range of dry bulk densities (average ~2.0 g cm^{-3}) that have been measured in tills from the UK (Fülöp, 2012) and Minnesota, South Dakota, and Iowa (http://depts.washington.edu/cosmolab/projects/summary_density.html) (Balco, 2004). We refer to dry bulk densities, instead of wet bulk densities, because the environment in the Shyok Valley is arid and the sample location is located on a diffluent surface, rendering it unlikely that water stays in the uppermost 1 m of the ground for a long time period. Despite insufficient data to accurately model the exposure age or the amount of surface erosion, our results suggest a minimum exposure age of ca. 100 ka, assuming a dry bulk till density of 2.0 g cm^{-3} and no erosion (Fig. 5.9a). For more likely erosion rates of 2–6 mm k.y.$^{-1}$, best-fit exposure ages are between 124 and 200 ka. At erosion rates of ~7 mm k.y.$^{-1}$, the modeled concentrations approach steady state and yield good fits with our measurements only for higher assumed densities (Fig. B.2).

We further obtained ^{10}Be concentrations from two surface samples (>1 km apart) and seven samples along a 160-cm deep profile at an extensive terrace (~4–5 km^2) near the village of Agham (Fig. 5.3, samples Shyk-1 to Shyk-7). On this terrace, dark-coated pebbles of the surficial desert pavement overlie a fine-grained layer, 38 cm thick at the sampling location, which we infer to be inflated loess (aeolian dust) that has buried the samples at depth while the surface samples were passively uplifted and continuously exposed (e.g., McFadden et al., 1987; Wells et al., 1995; Hancock et al., 1999). We therefore included loess accumulation in our depth-profile modeling, while exposure age, density, and inheritance are free parameters. Because we have no constraints on loess-accumulation rates apart from its final thickness, we explore several scenarios. Assuming that no erosion has taken place before loess accumulation, the end-member scenarios are instant accumulation of the entire loess deposit either right after deposition of our samples, or just before our sampling. Both scenarios are unlikely and yield ^{10}Be concentration profiles that do not match the entire profile. In particular, the ^{10}Be concentrations of the surface samples are too low for an early rapid loess deposition, and too high for a late-stage rapid deposition.

The simplest reasonable scenario is continuous and constant loess accumulation, i.e., a negative erosion rate that is set by the exposure time divided by the thickness of the loess layer. The model results are in good agreement with our measurements (Fig. 5.9b) and yield 107–116 ka surface-exposure ages, with an inheritance of 50,000 atom g^{-1} and for densities of 1.85–2.0 g cm^{-3} (best fit: 112 ka and 1.9 g cm^{-3}). Tests with higher inherited concentrations show that best-fit densities vary within reasonable ranges (~1.9–2.1 g cm^{-3}) for inherited concentrations <700,000 atom g^{-1}, whereas exposure age is relatively insensitive (107–117 ka; Fig. B.3). We explored other, more variable loess-accumulation scenarios, by modeling the ^{10}Be accumulation (Equation 5.1) numerically (Fig. 5.10). In these cases, we did not perform Monte Carlo experiments to estimate the uncertainties. We furthermore assumed 50,000 atoms g^{-1} inheritance and a fixed density equal to our best-fit density from the first scenario (1.9 g cm^{-3}), and varied the exposure duration manually until

a visually good fit was obtained. We do not expect that a full parameter search would add any accuracy at this stage, because an unlimited number of possible dust-accumulation scenarios exist. While many scenarios yield model results that fit the samples at depth reasonably well, reproducing the surface-sample concentrations requires that accumulation of dust occurred mostly during the glacial period. Furthermore, variable loess-accumulation scenarios that yield good fits with our data indicate an exposure age that is similar to the simple model of constant and continuous dust accumulation during the duration of exposure (~110 k.y.).

We also collected one amalgamated surface sample from a terrace near the village of Khalsar (sample WP020; cf. Fig. 5.5). Because loess underlies the desert pavement on this flat terrace surface too, we assume a formation similar to the terrace surface at Agham, and obtained a maximum exposure age based on simple continuous exposure of the surface sample and zero inheritance. The resulting maximum exposure age, calculated with the CRONUS online calculator (v. 2.2, Balco et al., 2008), is 100.3 ± 9.3 ka. For an assumed inheritance of 50,000 atoms g^{-1}, the exposure age would reduce to 99.3 ± 9.2 ka. Finally, we collected one sample (WP014) from an erratic granitic boulder located on a moraine at an elevation of 3389 m asl at the confluence, which yielded an exposure age of 69.6 ± 6.4 ka, assuming no surface erosion.

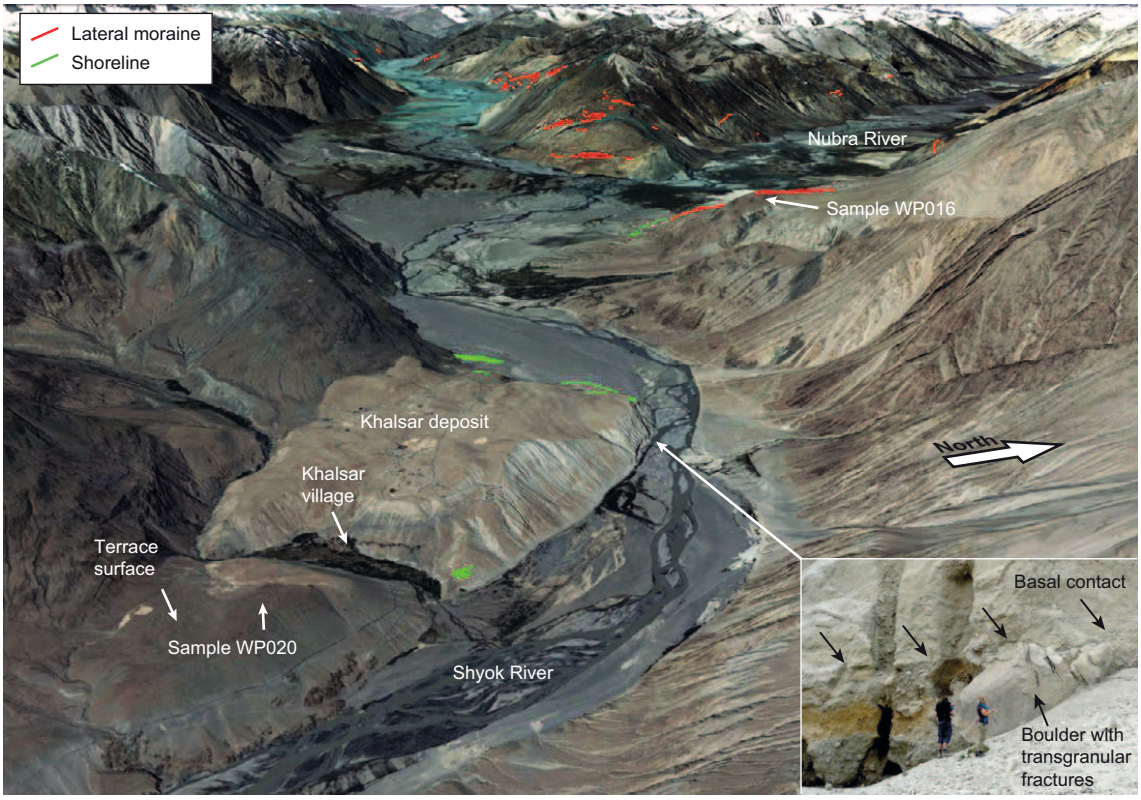

Figure 5.5: Perspective aerial view of the Shyok Valley near Khalsar (Google Earth, http://www.google.com /earth/). View to the northwest, downstream the Shyok Valley. Nubra Valley joins from the upper right corner. Field of view at the bottom of the figure is ~5 km. Inset photo shows basal contact of granitic fragmented material (top) with fluvial cobbles and boulders (below). Note the >4-m-tall boulder with transgranular extension fractures radiating from a point on its upper end.

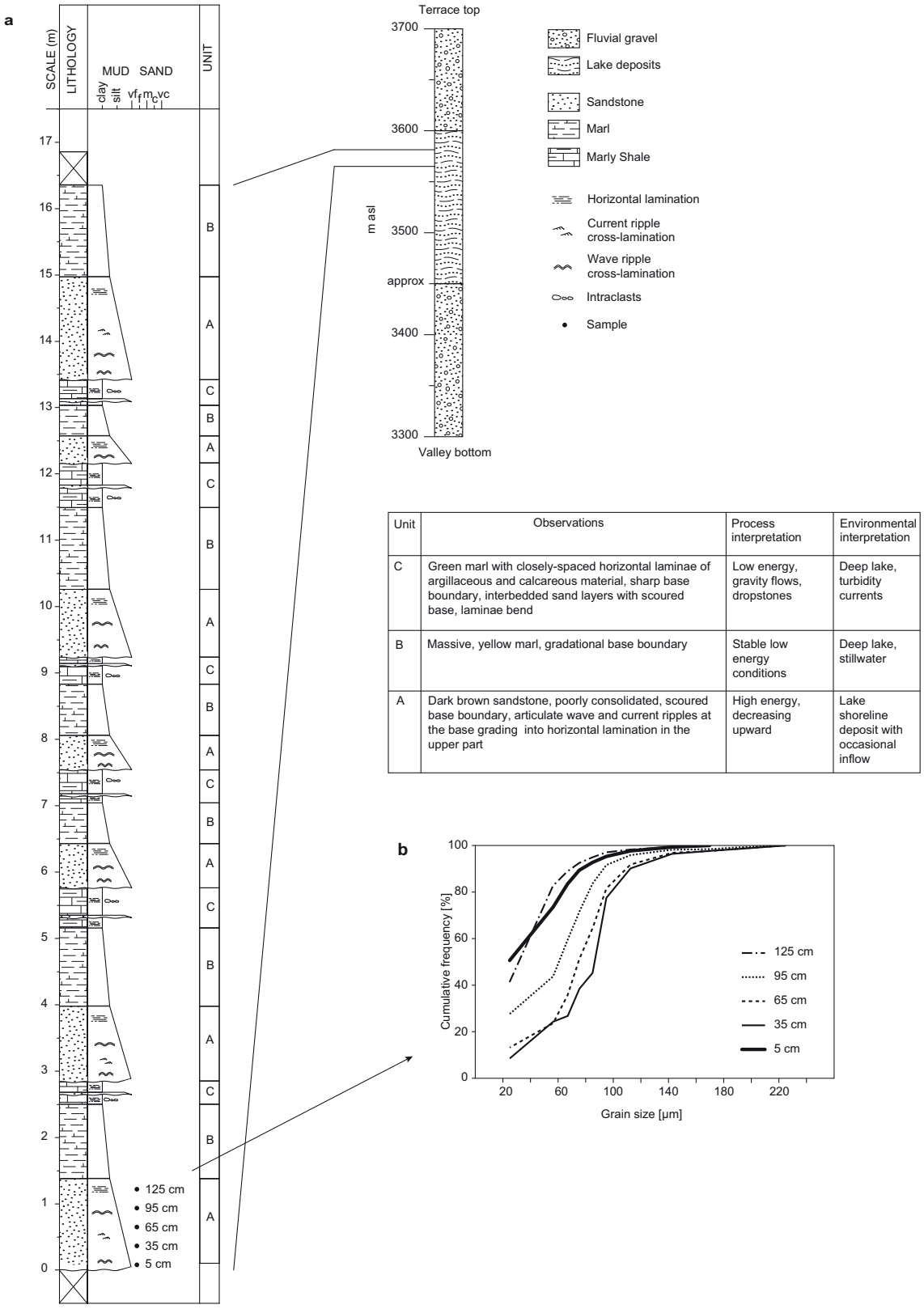

Unit	Observations	Process interpretation	Environmental interpretation
C	Green marl with closely-spaced horizontal laminae of argillaceous and calcareous material, sharp base boundary, interbedded sand layers with scoured base, laminae bend	Low energy, gravity flows, dropstones	Deep lake, turbidity currents
B	Massive, yellow marl, gradational base boundary	Stable low energy conditions	Deep lake, stillwater
A	Dark brown sandstone, poorly consolidated, scoured base boundary, articulate wave and current ripples at the base grading into horizontal lamination in the upper part	High energy, decreasing upward	Lake shoreline deposit with occasional inflow

Figure 5.6: Stratigraphic column of valley fill exposed at the terrace near Agham village (asl–above sea level). Lower-right plot shows cumulative grain-size distributions from lake sediment samples indicated at the lower end of the stratigraphic column.

5.5 Discussion

5.5.1 Timing and extent of glacial damming

The distribution of glacial striations and deposits in the lower Shyok Valley indicate glacial coverage over a length of at least 45 km. When considering the highest occurrence of moraine ridges and extrapolating their downstream decrease in elevation, the ice may even have extended much farther. Although U-shaped valley morphologies suggest ice reaching farther downstream, we currently lack direct evidence based on striations and unequivocal deposits. Because glacial marks and deposits are highest near the confluence and extend down-valley but not up-valley, it appears most reasonable to connect this ice cover to the Siachen Glacier in the Nubra Valley, which would have extended over a total length of >180 km, that is, >120 km from its present-day terminus.

The fluvio-lacustrine deposits in the upper Shyok Valley adjoining the glacial marks and deposits in the lower Shyok Valley provide compelling evidence that the Siachen Glacier blocked the Shyok River at its confluence with the Nubra River, resulting in extensive upstream aggradation and lacustrine deposition. The mapped succession of fluvial and lacustrine deposits is similar to a 450-m-thick sequence of fluvial and lacustrine deposits in the French Alps, which have been related to aggradation behind glacial dams during the last glacial cycle (Brocard et al., 2003). We found no direct contacts between glacial and fluvio-lacustrine deposits, but the highest glacial striations at the confluence suggest that the Siachen Glacier would have flowed a short distance up into the upper Shyok Valley (Fig. 5.3a, profile f-f'), although certainly not farther than where the lacustrine deposits are found. The spatial distribution of our mapped deposits indicates that a continuous valley fill extended at least to the village of Agham. Horizontal, low-relief surfaces, which slightly increase in elevation farther upstream from the extensive fill terrace near Agham, indicate a possible extent close to the village of Shyok. However, this greater extent must not have prevailed throughout the entire aggradation period. Instead, given the extensive ice coverage in the headwaters of the Shyok today (Fig. 5.1), it appears more plausible that these glaciers advanced farther downstream and temporarily occupied the more distal parts of the upper Shyok Valley.

Our ^{10}Be-depth profile data from the till plain above the Shyok-Nubra confluence suggest that the Siachen Glacier retreated from an elevation of more than 900 m above the present-day river (Fig. 5.3b) most likely no later than ca. 124 ka, and probably at the beginning of the Eemian/Sangamon interglacial. Such an elevation is sufficient for the glacier to have blocked the Shyok River and to account for the observed valley fill. Furthermore, the timing is in accordance with cessation of damming and an onset of fluvial incision into the valley fill by ca. 107–116 ka, constrained by the terrace surface near Agham. However, for higher inferred erosion rates, it is possible that the till plain we dated is older than 124 ka and even unrelated to the valley fill. We note, however, that morphostratigraphically younger moraine ridges occurring at lower elevations at the confluence indicate ice elevations that would have been high enough (>3600 m asl) to block the Shyok and account for the observed valley fill (Figs. 5.3, 5.7). These moraines must be older than the ca. 75 ± 3 ka moraines that occur at elevations of ~3250–3400 m asl ([Dortch et al., 2010]; and our sample WP014). The ca. 100 ± 9 ka maximum surface-exposure age of the terrace that hosts the Khalsar deposit and which is at an elevation of ~3480 m asl is also compatible with an incision of the valley fill that started ca. 107–116 ka.

Our interpretation contrasts with that of Dortch et al. (2010) who inferred that glaciers occupied the upper Shyok Valley down to the Shyok-Nubra confluence during the suggested aggradation period. Their argument for ice coverage is based on inferred roches moutonnées in the upper Shyok and a glacial origin of the Khalsar deposit, for which we do not find any supporting evidence. First, we could not find any glacial striations on bedrock in the area of the valley fill, and no observations to this extent are provided by Dortch et al. (2010). This is in stark contrast to the many striated bedrock surfaces in the lower Shyok and at the Shyok-Nubra confluence. Second, as outlined above, we interpret the Khalsar deposit to have formed by a rock avalanche, which occurred after formation of the ca. 100 ± 9 ka terrace that hosts part of the deposit. Third, the age constraints for ice cover-age provided by Dortch et al. (2010) are based on exposure ages from cobbles, boulders, and a bedrock surface, located just upstream of the terrace near Khalsar, and range from ca. 100 to 140 ka. Because these samples stem from elevations (3534–3557 m asl) that would have been buried by the valley fill (top elevation >3600 m asl) and because we did not find any convincing evidence for a former glacier in this part of the upper Shyok Valley during the time of aggradation, we suggest that these

ages most likely reflect a complex exposure history related to the time before burial and after excavation of the valley fill.

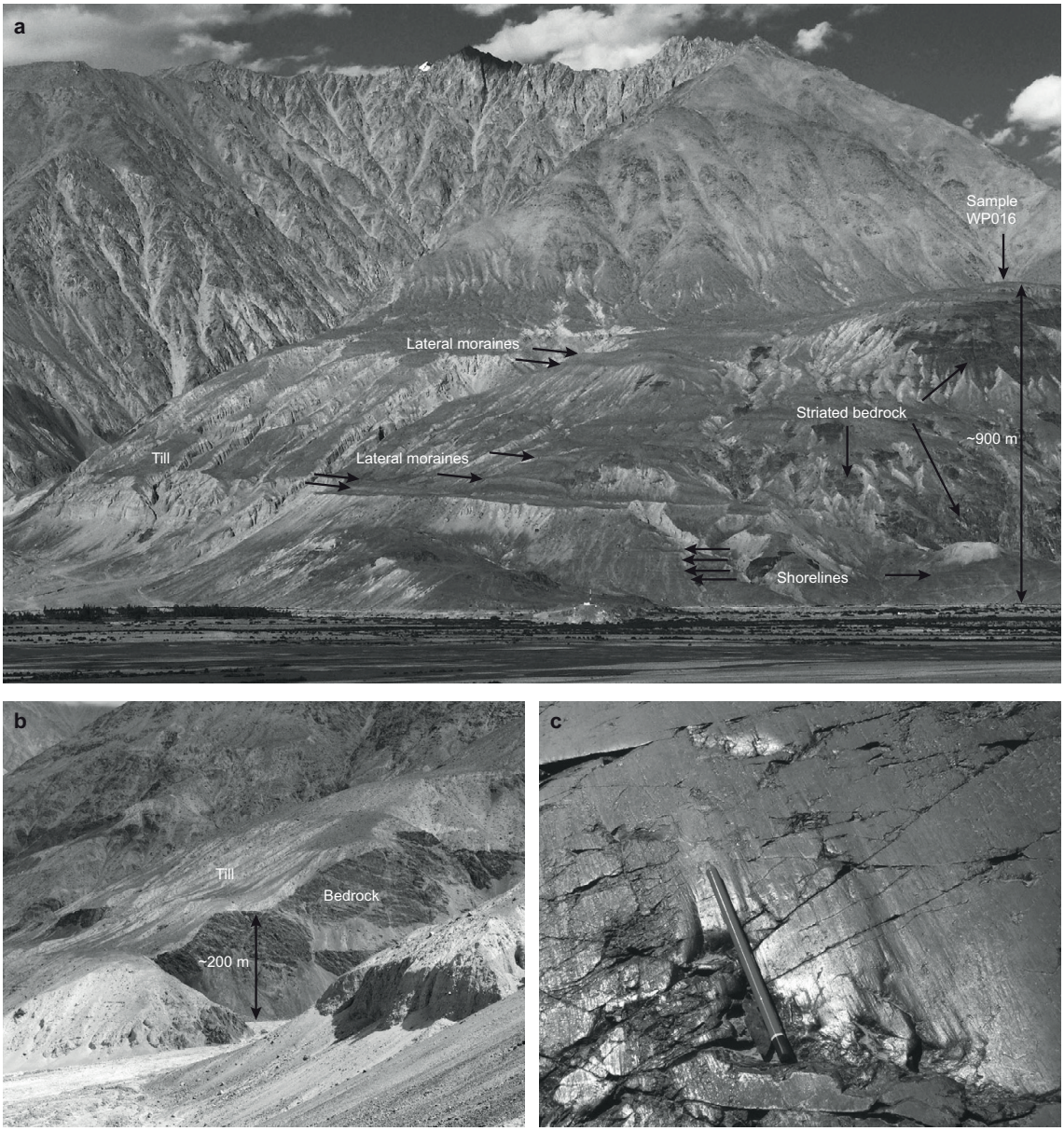

Figure 5.7: Field photographs of glacial deposits and marks. (**a**) Lateral moraines, till, and ice-polished bedrock at the Shyok-Nubra confluence. Note dissected, light-colored till covering dark-colored (striated) bedrock, with sub-horizontal lateral moraine ridges dipping from left to right. Note also horizontal shorelines near the valley bottom. Depth-profile samples (WP016) were collected from the till plain near the vertical arrow, ~900 m above the valley bottom. View to the northeast. (**b**) Till-mantled hillslope near the Nubra-Shyok confluence, dissected by a tributary. Note light-colored tills on staircase-cut bedrock. View to the north. (**c**) Glacial striations on the upglacier side of a roche moutonnée in Nubra Valley.

5.5.2 Aggradation and incision history

The thick and extensive valley fill in the upper Shyok Valley testifies to a period of protracted upstream sediment deposition. Unfortunately, we were not able to date the onset or duration of the aggradation period, but with the geometry of the valley fill and published erosion-rate estimates, we can derive first-order estimates of the time scales of aggradation. From the DEM and the topmost valley-fill surface, we calculated the minimum volume removed by erosion to be 30.7 km^3, corresponding to an extent of the valley fill just beyond Agham. Approximately 10 km^3 of this valley fill are lake sediments. Estimates of subglacial erosion

rates beneath the Siachen Glacier that are based on proglacial river-gauging data span 0.11–0.46 mm yr^{-1} (Bhutiyani, 2000), whereas cosmogenic nuclide–derived catchment-wide erosion rates from Shyok tributaries draining the Ladakh batholith range from ~0.05 to 0.07 mm yr^{-1} (Dortch et al., 2011b). Hence, assuming erosion rates of 0.1–0.5 mm yr^{-1} across all areas upstream of the confluence but downstream of Pangong Tso (Fig. 5.1), and acknowledging a lower density of sediment (2.0 g cm^{-3}) as compared to bedrock (2.7 g cm^{-3}), yields aggradation times of 6–27 k.y. This is based on the assumption that all incoming material is retained behind the dam. If we consider that the fluvial deposits reflect only the bedload, which is typically ~10% (e.g., Hinderer, 2001) but could be as high as ~33% (Pratt-Sitaula et al., 2007) of the eroded material upstream, these numbers increase to ~13–196 k.y., and include ~2–9 k.y. of lacustrine deposition, during which trapping of all the bed and suspended load occurred.

Given these estimates and considering that they pertain only to the valley fill that has been eroded since incision, it is reasonable to assume that the aggradation of the valley fill occurred over several tens of thousands of years, most likely starting during the previous glacial period when glaciers south of the Ladakh Range (Owen et al., 2006), in Zanskar (Hedrick et al., 2010), and in the central Karakoram (Seong et al., 2007) were also more extensive than subsequently. The aggradation period was likely accompanied by concurrent changes in Siachen Glacier's length and thickness and thus the ice-dam height, which probably affected the depositional environments (Figs. 5.12a–5.12c). The apparent lack of lake deposits upstream of Agham, along with the recognition of terrace-like surfaces at elevations near 3700 m asl between Agham and the Shyok village (see Fig. 5.3, profiles d–d' and e–e'), suggest that higher parts of the upper Shyok Valley had been ice covered during deposition of the lacustrine units, but may have been ice free thereafter (Fig. 5.12b).

Our data show that the aggradation period ended at ca. 107–116 ka, when the Shyok River started to incise the valley fill. The ca. 100 ± 9 ka exposure age of the terrace near Khalsar is statistically indistinguishable from this age, but its lower position argues that it is truly younger, possibly related to a period of lateral planation, which shaped this terrace and another cut terrace near Agham (Fig. 5.3b). Such stalling of incision could be due to readvance of the Siachen Glacier and associated damming at the beginning of the last glacial period (Fig. 5.12d). Further dissection of the valley fill might have halted again for some time during readvance of the Siachen Glacier that terminated at ca. 75 ± 3 ka (Fig. 5.12e) at the confluence (Dortch et al., 2010), but there is no indication in form of cut terraces.

The Khalsar deposit, which is stratigraphically younger than the ca. 100 ± 9 ka terrace surface it partly rests on, is in contact with fluvial gravels 20 m above the present-day valley bottom (3180 m asl), and hosts well-developed shorelines at its northern edge (Fig. 5.3). Dated nearby moraines with and without shorelines at the same elevation apparently constrain their formation to between ca. 41 ± 2 and ca. 75 ± 3 ka (Dortch et al., 2010), indicating that the Shyok had already incised to near its present-day level by this time (Fig. 5.12f). Although the formation of these shorelines by a glacier-dammed lake appears reasonable (Dortch et al., 2010), the shorelines near Kharu (Fig. 5.8) that also occur up to an elevation of 3250 m asl could be related to the same lake. In this case, the Siachen Glacier could not have impounded the lake. An alternative explanation links lake formation to the landslide near Chasthang, which may once have blocked the Shyok River (Fig. 5.3), but this hypothesis needs further investigation. In any case, this lake period appears to have been brief, as no associated lacustrine deposits were found. Another readvance of the Siachen Glacier that ended at ca. 41 ± 2 ka (Dortch et al., 2010) had the potential for further damming of the Shyok River, while thereafter the confluence appears to have been mostly ice free (Figs. 5.12g, 5.12h).

The currently available age constraints therefore suggest that the Shyok River incised the valley fill with an average rate of ~4–7 m $k.y.^{-1}$ and reached its present level between ca. 41 ± 2 and ca. 75 ± 3 ka (Fig. 5.11). Postglacial incision rates of a similarly thick glacially dammed valley fill in the French Alps were initially about an order of magnitude higher (>60 m $k.y.^{-1}$) but dropped to ~10 m $k.y.^{-1}$ after 5 ka (Brocard et al., 2003). Because retreat of the Siachen Glacier would have exposed a steep knickpoint in the profile of the Shyok River, we expect that incision rates were also much higher initially, but were slowing down as the step in the profile got progressively leveled. Given the extent of damming before incision and the apparently incomplete dissection during the interglacial, it is quite likely that readvances of the Siachen Glacier during the earlier part of the last glacial period, e.g., ca. 75 ± 3 ka, slowed or temporarily stopped incision of the valley fill.

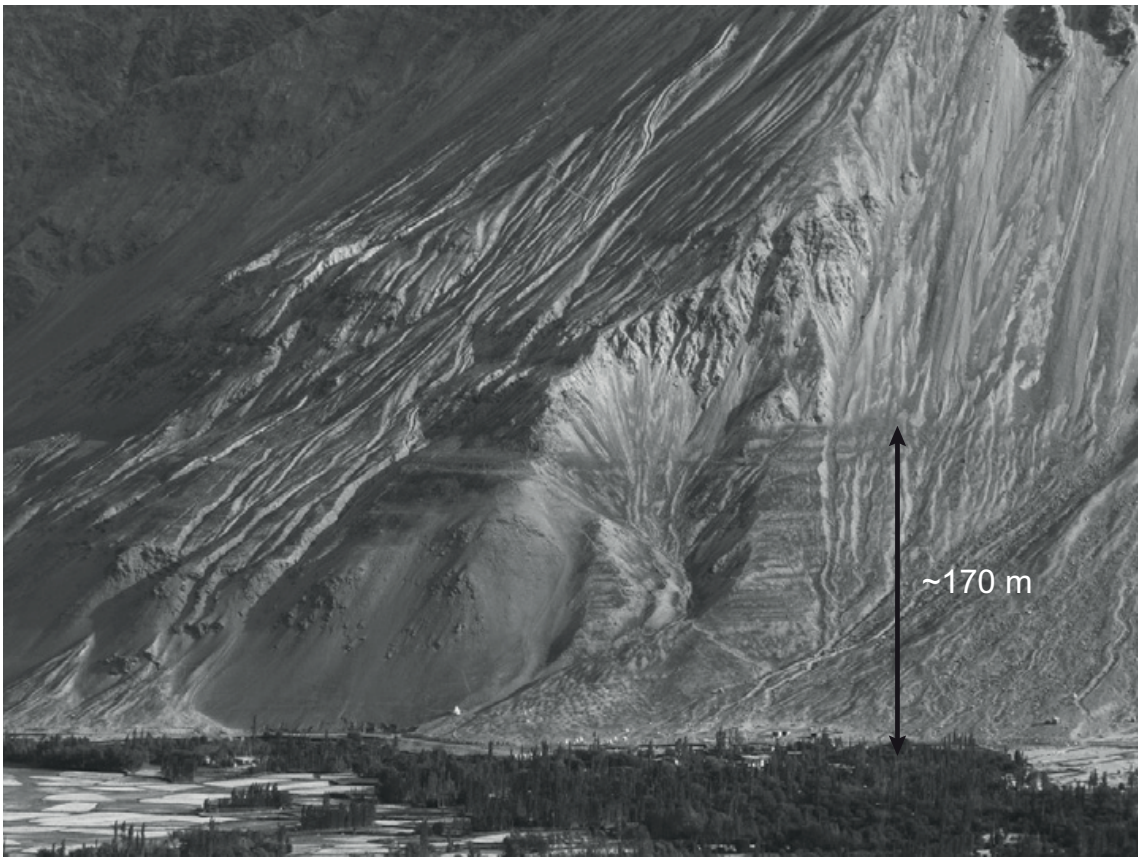

Figure 5.8: Field photograph of shorelines near Kharu. View to the south.

5.5.3 Catastrophic outburst floods from ice-dammed lakes

Aggradation of the fluvial deposits in the Shyok valley fill was likely accompanied by frequent formation and drainage of an ice-dammed lake, perhaps resembling the lake that repeatedly forms and drains behind the Kyagar Glacier dam (Fig. 5.2). Alternatively, the Shyok River could have passed by the ice laterally, without any ponding, similar to the Shimshal River, which currently passes the Khurdopin Glacier over a length of ~3 km, in the eastern Hunza watershed (Fig. 5.1). We do not know how the Shyok eventually discharged its waters past the ice-covered confluence, but lateral passage is more conceivable when the glacier's extent downstream from the confluence was short and the up-glacier supply of ice low, so that the Shyok could have maintained connectivity with downstream areas. When the glacier stretched far beyond the confluence, however, and the upstream supply of ice was much higher due to thicker ice with higher velocities, keeping a passage open would have been more difficult, especially during winter when discharge is low.

In analogy to the dynamics of historically active glacier dams in the Karakoram (Fig. 5.2) (Mason, 1929; Hewitt, 1982) and elsewhere (Roberts, 2005, and references therein), it therefore seems most likely that blocking of the Shyok River by the Siachen Glacier resulted in a hydraulically fragile system with high potential for frequent outburst flooding from ephemeral lakes. If lake drainage occurred through a subglacial tunnel, the discharge at the glacier terminus would be expected to increase exponentially over hours to days due to melt widening of the water-filled conduit (e.g., Nye, 1976), resulting in peak-flood discharges that greatly exceed regular discharges. Yet ice dams formed by tributary glaciers often fail by subaerial breaching, which usually results in more rapid discharge increases (Walder and Costa, 1996) and more catastrophic outburst floods (Haeberli, 1983). We note however that breaching of a very long ice dam would require greater work expenditure by the passing waters so that discharge increases may be slower, which would prolong flood duration at the expense of peak-flood discharges. We argue that the lake formation and most likely rapid lake drainage on an annual basis would not have provided conditions stable enough for continuous lacustrine deposition, while the resulting flood discharges upstream of the dam would still have allowed for transport and deposition of fluvial gravels up to the dam.

Table 5.2: Shyok River water discharge

Sample Location	Mean discharge ($m^3\ s^{-1}$)	Upstream area[a] (km^2)	Specific runoff ($mm\ yr^{-1}$)
Shyok-Indus confluence[b]	333	33,382	314
Shyok-Nubra confluence[c]	199	14,941	314

[a] Mean discharge values from Faran Ali and de Boer (2008).
[b] Mean discharge was back-calculated by assuming the same specific runoff as at the Shyok-Indus confluence.
[c] Upstream area excluding areas draining into Pangong Tso.

In contrast, the lacustrine deposits of the valley fill document the existence of a lake that must have stretched over at least 20 km, approximately between Khalsar and Agham. The cyclic fining-upward units are best explained by periodically changing water depths (Fig. 5.6). Because the units are relatively thick (~1–5 m), and for the same argument as above, it appears unlikely that deposition occurred during lake-level changes on a regular annual basis. On the other hand, the >25 units make a link with long-term climatic changes, e.g., due to orbital variations with 10^4–10^5-year periodicities, also unlikely. From the present-day discharge of the Shyok River at its confluence with the Indus River (Faran Ali and de Boer, 2008, Table 5.2) we estimate the Shyok discharge upstream of its confluence with the Nubra to be ~200 $m^3\ s^{-1}$, or ~6 $km^3\ yr^{-1}$. For this discharge, for lake bottoms between 3450 and 3600 m asl elevation, and for an assumed maximum water depth of 100–200 m. lake volumes estimated from the DEM are between 9 and 48 km^3, assuming the lake extended just beyond the village of Agham. Given these estimates, it would have required from about one to eight years for filling up the lake if all water from upstream areas were retained in the lake. Considering model-based estimates of annual evaporation from lake surfaces in the high and arid western part of Tibet (Avouac and Burov, 1996), we conclude that evaporation would have prolonged the infilling insignificantly, because of the relatively small area compared to the high inflow rate.

Despite our crude estimate, such short time periods for lake filling leave two basic alternatives of lake behavior. In the first scenario, lake sedimentation was relatively slow, perhaps occurring at rates of ~10 $mm\ yr^{-1}$, resulting in a ~15-k.y. lacustrine period. Deposition of the meter-thick lake units at gradually increasing water depths would thus have required a significant amount of leakage during lake-level rise in order to avoid flotation of the ice dam. Although we deem this scenario not very likely, we acknowledge that an ice dam rimmed by significant amounts of glacial sediments could have been more stable and allowed for a spill-way between lateral moraines and the adjacent hillslopes. In this scenario, periodic lake-level changes on centennial time scales could have occurred due to final dam flotation or possibly glacier surges, i.e., recurring periods of rapid basal sliding that are particularly common amongst Karakoram glaciers (Copland et al., 2011) and which have surge periods of several decades to >100 years (Hewitt, 1998).

In the second scenario, the lake was ephemeral and sedimentation was rapid. In this case, each cyclic lake unit may represent the deposits of an individual flood event that initiated farther upstream and got ponded by the Siachen Glacier dam at the Shyok-Nubra confluence. An analogy can be made with the well-studied glacial Lake Missoula outburst-flood deposits that accumulated in back-flooded valleys of Washington, USA, and which are commonly referred to as rhythmites (Waitt, 1985). These rhythmites are typically fining upwards, have thicknesses ranging from centimeters to several meters (Atwater, 1986), and were deposited at intervals spanning several decades (Waitt, 1985; Clague et al., 2003). In the upper Shyok Valley, potential sources of catastrophic floods are located in the headwaters of the Shyok River, where historic failures of tributary ice dams (Fig. 5.1) have repeatedly resulted in destructive catastrophic outburst floods (Mason, 1929). During glacial periods, however, the upper Shyok glaciers most likely advanced farther down in the trunk valley and potentially reached the Shyok village (Fig. 5.3), where they would have blocked the tributary that is coming from Pangong Tso. The ~2 km downstream displacement of the confluence of this tributary may actually be the vestige of such blocking. Dortch et al. (2011a) reported evidence for catastrophic partial drainage of Pangong Tso at ca. 11 ± 1 ka through this tributary, which they relate to lake spillover during a more humid period (Gasse et al., 1996). When Pangong Tso is hydrologically connected to the Shyok River, the drainage area of this tributary increases from ~2000 to 46,000 km^2. The resulting increase in discharge may very well increase the hydraulic pressure on any ice that blocks this tributary and initiate a period of

outburst flooding that is archived in the lacustrine deposits. In light of these considerations, the scenario of upstream flood-related lake deposition appears to provide better support of the current data and observations.

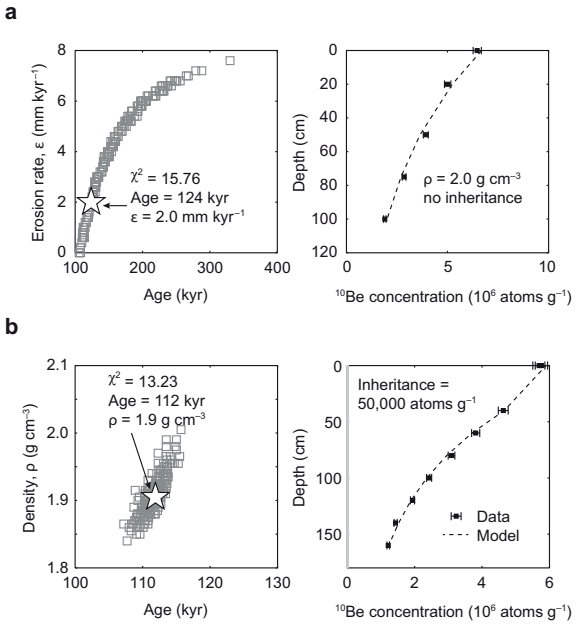

Figure 5.9: Best-fit ^{10}Be model results of depth-profile data. (**a**) Till plain at the Shyok-Nubra confluence. (**b**) Fill terrace near the village of Agham. Left panels show Monte Carlo best-fit results of exposure age–erosion rate (ϵ) (**a**) or exposure age–density (ρ) (**b**). Right panels show depth profiles of measured and best-fit modeled ^{10}Be concentrations. Error bars reflect 2σ analytical uncertainties.

5.5.4 Glacial damming and the Quaternary evolution of the Shyok Valley

The reconstructed period of glacial damming and associated upstream aggradation and incision occurred for several tens of thousands of years and directly affected ~100 km of the Shyok Valley. Yet, the current landscape and morphodynamics in the Shyok Valley appear to be largely controlled by the results of glacial erosion. Numerous alluvial fans along the previously glaciated, kilometer-wide valley floors (Fig. 5.3b) and active aggradation of the Shyok River at the confluence testify to the current incapacity of the Shyok and Nubra Rivers to evacuate the material that is supplied by their tributaries. The most obvious interpretation of this gentle-sloping valley reach is that of a glacial overdeepening that was carved by the Siachen Glacier and subsequently back-filled with alluvium (e.g., Penck, 1905; Gutenberg et al., 1956). This interpretation is supported by tributaries to the Shyok and Nubra, which are often seen hanging above the main stem rivers, suggesting differential incision as is typical for glacial valleys (e.g., Amundson and Iverson, 2006). Furthermore, simple backfilling behind a landslide dam (e.g., Hewitt et al., 2011) can be excluded, because no active dam exists near the downstream end of the alluviated valley reach, which is widest at the confluence as opposed to its downstream end. We also note that we found no evidence in the field or in published studies (Phillips, 2008; Taylor and Yin, 2009) that differential uplift along active tectonic structures contributes to this overdeepening, but it may be that the rocks in the lower Shyok and Nubra Valleys are more erodible than elsewhere, due to their proximity to the Shyok suture zone and Karakoram fault, respectively (Fig. 5.13a). In this context it is also worth mentioning that we have not seen any obvious signs of recent deformation, e.g., disrupted or displaced depositional surfaces, along the Karakoram fault in our study area.

Our results furthermore show that the Siachen Glacier had been much more extensive prior to the last interglacial as compared to the last glacial period. A similar pattern has been observed in the Ladakh Range to the south, leading Owen et al. (2006) to speculate about a long-term aridification of the region. It is also conceivable, however, that progressive glacial incision during more extensive periods successively forced the Siachen Glacier to smaller extents (e.g., Oerlemans, 1984; Kaplan et al., 2009), because any lowering of the bed that is not sufficiently compensated by uplift would have led to a successively lower ablation area, smaller accumulation area, and thus a shorter glacier with time (Anderson et al., 2012). This idea is

compatible with the valley overdeepening as a product of subglacial erosion. But even if this were not the case and rock uplift did at least balance valley incision, unless previous times had been significantly drier, for which there is currently no evidence (cf. Owen et al., 2006), we see no reason why similar damming episodes would not have occurred during earlier times and possibly throughout much of the Quaternary. We therefore suggest that extensive glacial damming and associated processes have not been extraordinary, rare events, but occurred rather frequently during earlier episodes during the Quaternary period.

It has been recently argued that repeated glacial damming of the Tsangpo-Brahmaputra River during the Quaternary might have stabilized the Tibetan Plateau edge by impeding headward fluvial incision (Korup and Montgomery, 2008). In the Shyok Valley, however, the inferred valley overdeepening suggests that incision by the Siachen Glacier has been higher than fluvial incision farther downstream, rendering the net effect of blocking fluvial incision not very important. It follows that the base level of the upper Shyok River is actually controlled by glacial erosion at the confluence and therefore decoupled from its downstream areas. This tributary control of local base level has prevailed for at least the last two glacial cycles, but likely much longer. Our reconstruction also suggests that the valley fill was not fully dissected before further, although minor, damming occurred, and that the upper Shyok River in our study area has probably not been flowing on bedrock for the same amount of time, i.e., the last two glacial cycles. However, no major knick zone is developed along the upper Shyok River, which could indicate either efficient glacial incision during periods when potentially the entire upper Shyok was ice covered or fluvial incision to below the current level whenever bedrock was exposed in between previous damming periods. In any case, our data suggest that the influence of glaciers in the Shyok Valley has been to promote rather than delay the incision of the plateau edge. Future studies should examine the apparent contrasting role of glaciers for the evolution of the Tibetan Plateau margins more closely.

5.5.5 Signatures of glacial damming and erosion along the Karakoram

The courses of the Indus and Shyok Rivers, both of which have vast catchment areas in low-relief regions of the Tibetan Plateau and run for hundreds of kilometers parallel to the Karakoram, make these rivers particularly prone to interacting with large glaciers that originate in the Karakoram. Indeed, signs of ice coverage have been identified at all major confluences of the Indus and Shyok with rivers draining the Karakoram (Burgisser et al., 1982; Derbyshire et al., 1984; Shroder et al., 1989; Cornwell, 1998; Phillips et al., 2000; Seong et al., 2007; Hewitt et al., 2011), which suggests that the formation of ice dams, upstream aggradation, and catastrophic outburst flooding have been widespread in this region and probably common during much of the Quaternary. However, ample evidence as found at the Shyok-Nubra confluence is often missing from farther downstream, and some of the deposits previously cited as evidence for glacial dams along the Indus River may actually be related to younger rock avalanches (Hewitt, 1999; Hewitt et al., 2011).

There exist several accounts of historical floods related to glacier or landslide dams in the Shyok and Indus Valleys that had devastating effects on local communities (e.g., Cunningham, 1854; Shroder, 1998; Hewitt and Liu, 2010). Cornwell and Hamidullah (1992) reported the distribution of boulder beds, plunge pools, and chutes along the middle Indus Valley (between Gilgit River and the Tarbela dam), which they interpret as geomorphic evidence of such floods. More evidence appears farther downstream in the Peshawar Basin, which is located just west of the Tarbela dam, where the Indus exits the mountains (Fig. 5.1). Throughout this basin, several tens of decimeter- to meter-scale rhythmites are interpreted to represent deposits of repeated catastrophic floods in the Indus Valley that occurred during the Bruhnes geomagnetic chron, i.e., <730 ka (Burbank and Tahirkheli, 1985). Cornwell (1998) suggested that ice-dammed lakes located along the middle Indus Valley, downstream of Nanga Parbat, were the likely sources of such floods, but this is difficult to test and at least some historical floods are clearly related to landslide dams (e.g., Shroder, 1998).

Based on our discussion about the origin of the lacustrine deposits in the upper Shyok, and because Karakoram glaciers appear to respond synchronously to climatic changes (Hewitt, 2005; Scherler et al., 2011b), we emphasize that glacier-dammed lakes along the Indus and Shyok Valleys could have acted as both sources of outburst floods as well as impounding basins for floods from farther upstream. In general, the farther downstream the ice or landslide dam, the higher the annual discharge and the greater the likelihood of catastrophic floods from farther upstream. Moreover, the volume of ephemeral lakes and therefore the potential flood magnitude increase as valley gradients upstream of the dam decrease, which is expected for farther downstream reaches. To what extent this partly explains fewer well-preserved valley fills farther

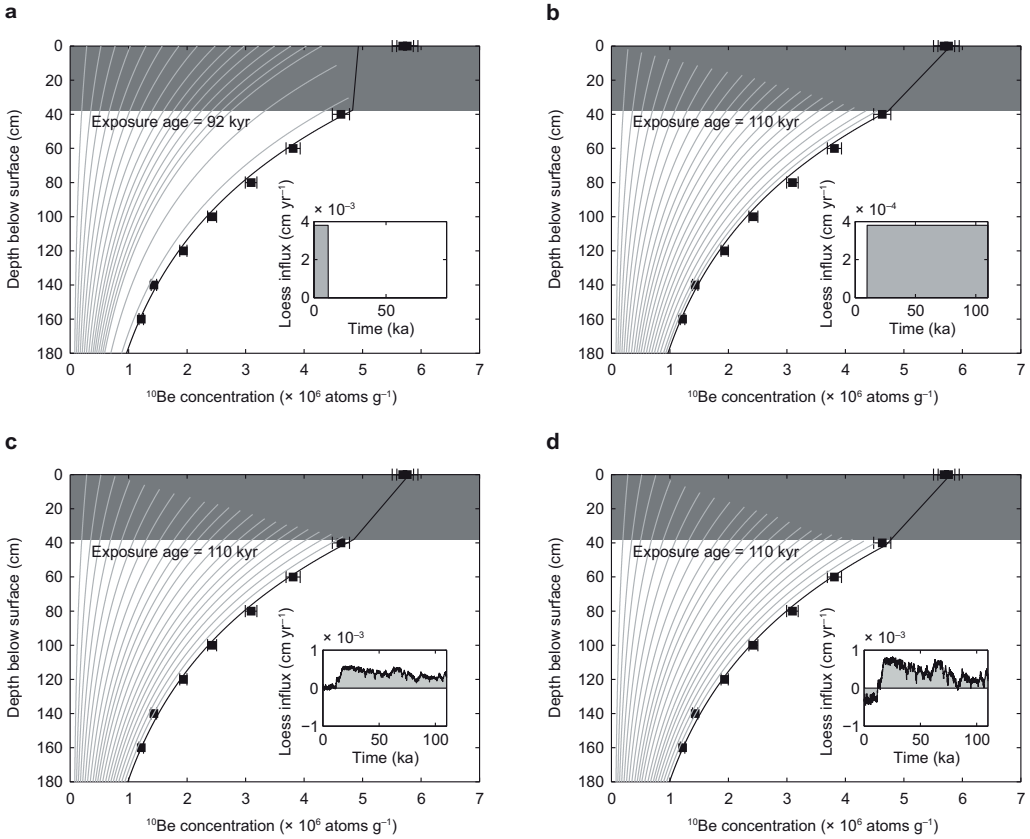

Figure 5.10: ^{10}Be depth-profile modeling results for different loess accumulation scenarios. (**a**) Constant accumulation during the interglacial. (**b**) Constant accumulation during the glacial. (**c**, **d**) Loess accumulation scaled by the Antarctic temperature record (Stenni et al., 2001). Loess accumulation in (**d**) is more negative during interglacial periods and more positive during glacial periods. Data points give measured concentrations; error bars the 2σ analytical uncertainties. Black thick lines connect modeled concentrations. Thin gray lines give concentrations during the model run in 5000 yr time steps. Inset figures give loess influx rates (positive: inflation, negative: deflation) during the model run. Dark gray box covering the top 38 cm indicates thickness of the loess layer with unknown concentration. All models use a density of 1.9 g cm^{-3} and an inheritance of 50,000 atoms g^{-3}.

downstream is currently, due to the limited amount of data, difficult to tell. But it is notable that historical floods in the Indus Valley have scoured valley walls up to several tens of meters above the valley floor (Cunningham, 1854). Instead of depositional evidence, we identify striking similarities between all other major confluences of the Indus and Shyok Rivers with Karakoram tributaries (i.e., Gilgit-Hunza-Indus, Shigar-Indus, Hushe-Shyok) and the Shyok-Nubra confluence that involve (Fig. 5.13): (1) a high degree of present-day ice coverage in the tributaries that serves to source far-reaching glacier advances, (2) alluviated valley reaches that are widest at the confluence and extend far into the tributaries where they are commonly more gently sloping than the Indus or Shyok trunk streams (Fig. 5.13b), and (3) a systematic pattern of valley gradients being low where the valleys are wide but the gradients gradually increase upstream of the confluences, concurrent with a valley narrowing. It is also worth noting that all major tributaries appear more deeply incised than the trunk Shyok or Indus valleys near the confluences, especially when considering that bedrock in these tributaries is most likely significantly lower than the alluviated valley floors. In addition, the fact that the alluviated reaches are gradually widening upstream, just to the confluences where they occur, argues against a single landslide origin, which would show the opposite pattern, i.e., widest at the barrier and narrowing upstream. Note, however, that this argument does not preclude landslides or rock avalanches from occurring within these reaches (e.g., Hewitt, 1999; Hewitt and Liu, 2010). In fact, the glacial preconditioning of the landscape may enhance both the susceptibility to large slope failures (Hewitt, 2009) as well as the preservation potential due to the shallow valley floors.

5.5.6 Implications for the Quaternary evolution of the Western Tibetan Plateau Margin

The glacial overdeepenings along the Shyok and Indus Valleys clearly testify to a greater long-term efficiency of glacial erosion compared to fluvial incision, which has been noted elsewhere (e.g., Brocklehurst and Whipple, 2002, 2006). Although damming-related upstream aggradation locally protects the bedrock from erosion (Korup and Montgomery, 2008), the long-term effects of such shielding appear to be subordinate in these valleys, compared to either glacial incision during periods of more extensive glaciation or fluvial incision whenever bedrock was exposed. Areas located downstream of glacial dams, on the other hand, have likely been subjected to repeated outburst floods, whose main effect is to concentrate the total discharge into a few high-magnitude events. In the presence of thresholds for sediment transport (e.g., Snyder, 2003; Tucker, 2004) and considering that sediment provides the tools for bedrock erosion (e.g., Sklar and Dietrich, 1998), such floods are most likely highly erosive events that have the potential to incise valley fills, or bedrock in areas of no valley fill, at a higher rate than under non-flood discharge conditions (cf. Wulf et al., 2010).

We therefore suggest that glacially controlled local base-level lowering together with catastrophic outburst flooding are important processes in the Quaternary evolution of these valleys, and possibly the margins of the Tibetan Plateau in general (cf. Montgomery et al., 2004; Lang et al., 2013). Variable glacial extents during the Quaternary could focus erosion along different segments of a glaciated catchment, thereby deepening the tributary valleys. Concurrently, the confluences with the Shyok and Indus Rivers would have alternated between periods of glacial incision and fluvial damming with associated outburst flooding, which would have promoted headward incision into the western margin of the Tibetan Plateau (van der Beek et al., 2009). During this process, concurrent changes in catchment morphology and supra-glacial debris cover (Scherler et al., 2011b) may influence glacial mass balances and extents such that flood-effective glacial dams could still occur long after a valley has been deeply incised. In the lower Indus Valley, for example, Nanga Parbat glaciers apparently reached the Indus at an altitude of ~1200 m asl during the last glacial cycle (Phillips et al., 2000). Similar processes may also operate along other orogenic plateaus, such as the Pamir Plateau with its deeply entrenched valley systems and extensive glaciers, glacial overprint of lower valley reaches, and stream captures along its western and northwestern flanks (v. Ficker and Rickmers, 1932; Strecker et al., 2003). These examples emphasize the potentially destructive role of glacial systems with respect to the preservation and longevity of orogenic plateau margins, particularly in environments where snowlines and precipitation allow for the formation of extensive and fast-moving glaciers, such as in the Karakoram (Scherler et al., 2011a). Where snowlines are higher and glaciers much smaller, as for instance along the eastern margin of Tibetan Plateau, the extent of glacial incision is certainly much lower, but the formation of glacial dams with associated outburst flooding may nevertheless be an important process (Lang et al., 2013).

5.5.7 Significance of glacial dams for mountainous landscape evolution

The thick valley fill at the Shyok-Nubra confluence clearly shows that large glacial dams can be efficient barriers for sediment transport (Korup and Tweed, 2007), probably over time scales that are mostly dictated by glacial dynamics and mass balances, and thus climate. Therefore, glacial dams can strongly modulate the sediment dispersal from partly glaciated mountainous regions, which will inevitably affect the rates and patterns of sediment accumulation in intermontane or foreland depositional basins. At the same time, however, their tendency to fail catastrophically leads to concentrating the upstream available discharge into highly erosive flood events downstream (e.g., Haeberli, 1983; Costa and Schuster, 1988; Walder and Costa, 1996; Tweed and Russell, 1999; Roberts, 2005), which lowers the preservation potential of previous glacigenic deposits. It is important to realize that unless the climatic or topographic boundary conditions change, glacial dams will reform after each failure, thus resulting in recurring annual to decadal flood events. Although more depositional evidence is needed, the available data and observations suggest that in the Shyok and Indus Rivers, catastrophic flood discharges may have been frequent rather than exceptional events throughout much of the Quaternary period.

The impact of glacial dams on modulating discharge is in contrast to that of landslide or moraine dams, which in most cases will fail only once or, as in the case of voluminous landslides, may have long recurrence intervals when they affect slopes repeatedly. In addition, a fraction of the ice itself can contribute to elevating the flood discharge, whereas the material of debris dams tends to be spread out downstream during and after

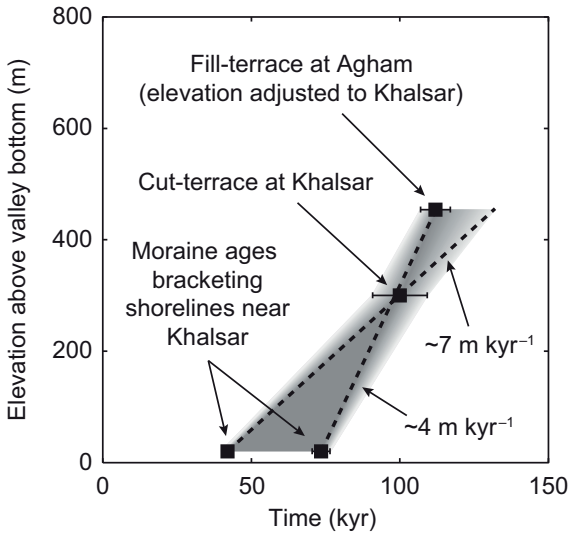

Figure 5.11: Incision history of the Shyok River into the valley fill. Error bars reflect Monte Carlo best-fit model results for the Agham terrace age and external uncertainties from CRONUS online calculator (Balco et al., 2008) for other ages. Shaded areas indicate likely incision paths. Dashed lines and numbers give possible average incision rates. See text for details.

dam failure, often leading to long-lasting valley floor aggradation (Korup, 2004; Korup and Tweed, 2007) on the order of several thousands of years (Trauth et al., 2000; Bookhagen et al., 2005; Ouimet et al., 2007). The coarse material, typical of many landslide dams, can subsequently also affect channel roughness and promote aggradation (Brummer and Montgomery, 2006). We note, however, that bedrock erosion during floods may delicately depend on the availability of tools, in the form of boulders, which are certainly more abundant in debris dams as compared to ice dams. Whether tools are in short supply at repeatedly failing glacier dams, or whether the supply of debris by the glacier and from ice-free downstream reaches is sufficient, needs to be tested. The above differences between ice and debris dams have in any case important consequences for the erosive impact of catastrophic floods from natural dams that are so far poorly understood.

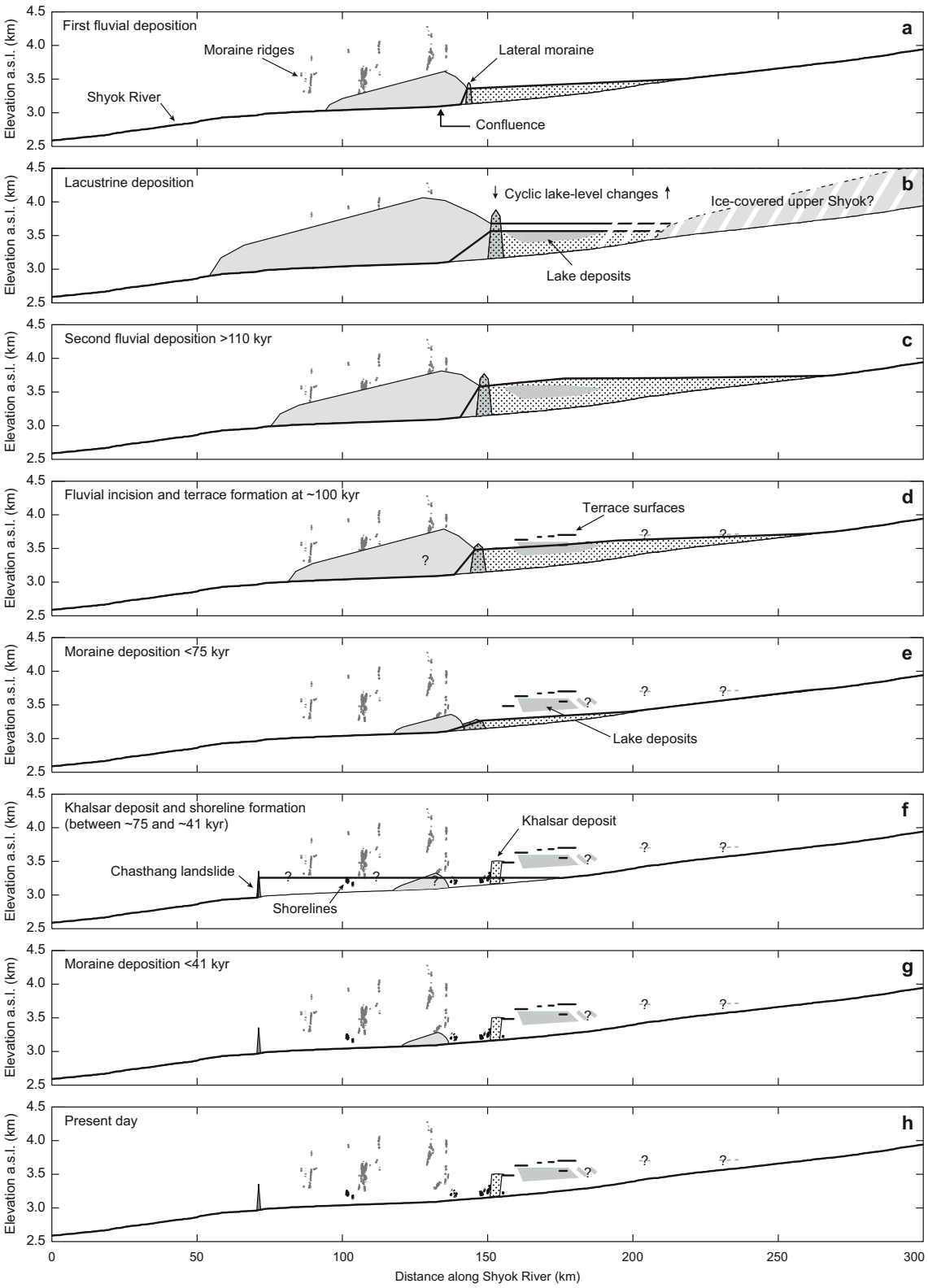

Figure 5.12: Conceptual model of the aggradation and incision history of the valley fill in the vicinity of the Shyok-Nubra confluence (a.s.l.–above sea level). See text for details and compare with Fig. 5.3.

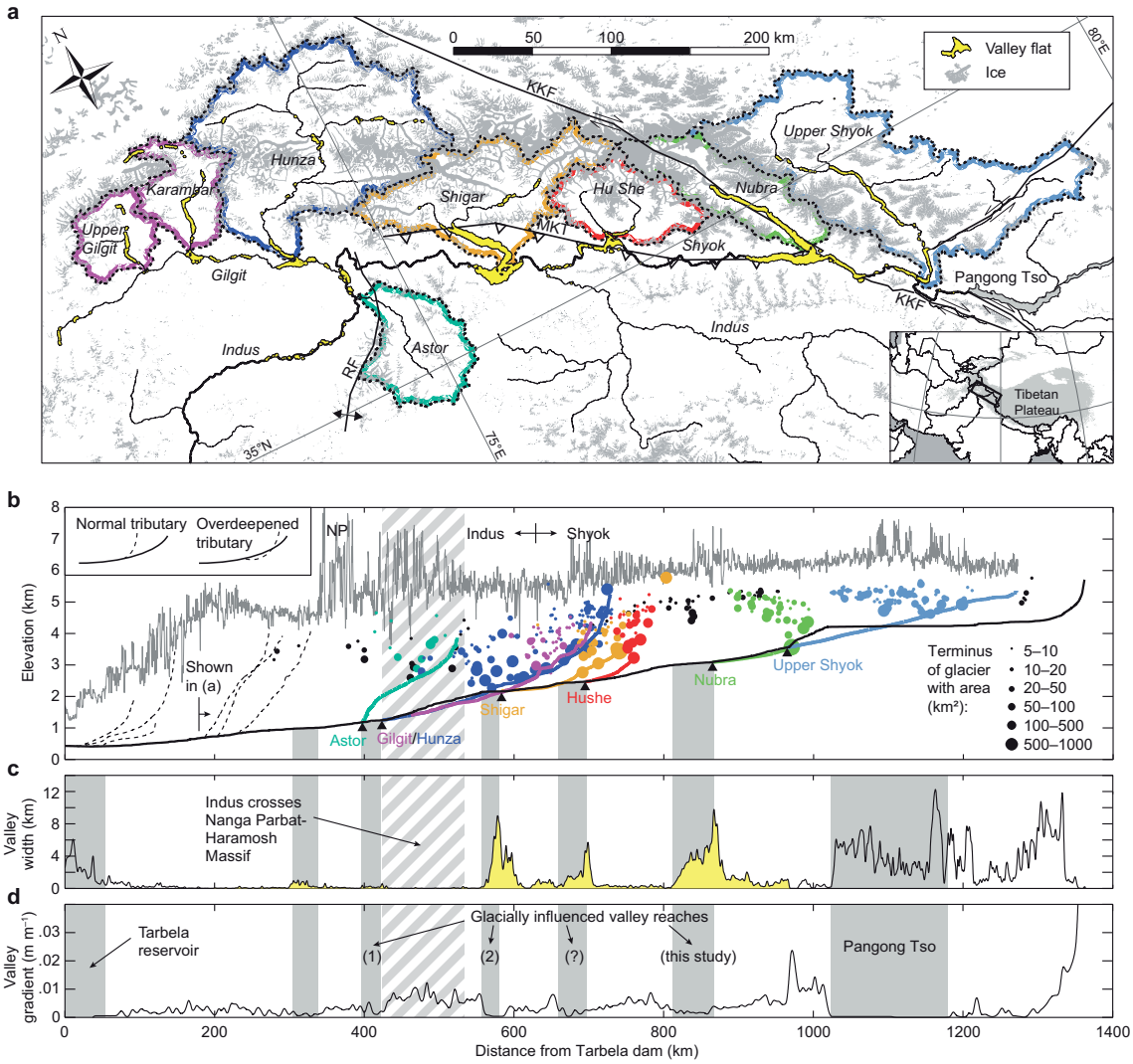

Figure 5.13: Morphologic characteristics of formerly glaciated confluences along the Shyok and Indus Rivers. (**a**) Catchments of major rivers that drain the Karakoram Mountains, along with the distribution of present-day glaciers (gray) and valley flats (yellow). RF–Raikhot fault; MKT–Main Karakoram thrust; KKF–Karakoram fault. (**b**) Longitudinal profiles following the Shyok and Indus Rivers (black line) where they are adjacent to the Karakoram and major Karakoram tributaries (colored lines) shown in A (NP–Nanga Parbat). Filled circles show termini of glaciers >5 km^2. Size of circle indicates glacier area and color whether it drains into a Karakoram tributary (colored) or directly into the Shyok or Indus (black). Gray line shows maximum elevation within a 80-km-wide swath profile that follows the Shyok and Indus Rivers adjacent to the Karakoram. All positions along the x-axis refer to the distance from the Tarbela dam along the channel network, even if the channel network is not shown, as in the case of the glacier termini. (**c**) Valley width and (**d**) valley gradient along the trunk stream profile shown in (**b**). Numbers in parenthesis refer to (1) Derbyshire et al. (1984), (2) Seong et al. (2007).

5.6 Conclusion

We presented evidence that the Siachen Glacier formed a long-lived glacier dam in the Shyok Valley, which resulted in aggradation of a thick valley fill. Cosmogenic nuclide dating constrains the damming episode to the penultimate glacial cycle with its incision starting during the last interglacial. Our new data allow refining the glacial chronology of the Shyok-Nubra confluence and demonstrate that the Siachen Glacier had been much more extensive during the penultimate glacial cycle compared to the last glacial cycle, while the Shyok Valley upstream of the confluence with the Nubra had been ice free over at least 20 km. Frequent formation and catastrophic drainage of ice-dammed lakes during the time of aggradation is likely, whereas lake deposits within the valley fill suggest that the ice dam might also have impounded floods from farther upstream. Subglacial erosion by the Siachen Glacier has produced a pronounced valley overdeepening and suggests a glacial control of local base level along the Shyok River.

Existing glacial reconstructions and chronologies from other parts of the Karakoram allude to similar ice dams along the Indus and Shyok Rivers at confluences with major Karakoram tributaries. As a result, the present-day longitudinal profile of the Shyok and Indus Rivers adjacent to the Karakoram resembles a staircase of filled-up, overdeepened valleys that are separated by narrower and steeper valley reaches. Whereas the overdeepenings and the previously glaciated tributaries show that glacial incision has been outpacing fluvial incision along the trunk streams, the lack of significant knick zones upstream of the damming sites suggests that the net result of glacial interaction with the Shyok and Indus Rivers was to promote incision of these valleys into the western margin of the Tibetan Plateau. Key factors in this process have probably been widespread and frequent catastrophic outburst floods from glacially dammed lakes throughout much of the Quaternary.

Chapter 6

Discussion

The primary aim of this thesis was to find an efficient way to estimate the thickness and distribution of intermontane valley-fill deposits and to demonstrate how such knowledge can be used to constrain the tectonic/climatic history of mountain belts. It was shown that valley-fill deposits play an important role in landscape evolution on various timescales. The Tsangpo study (Chapter 4) deals with a fill that formed in response to long-term tectonic forcing and whose stratigraphy and geometry reflect the uplift of the Namche Barwa and Gyala Peri massifs since at least 2.5 Ma. Intermontane valley fills in the European Alps (Chapter 3) substantially buffer the mass flux from the orogen on timescales of $\sim 10^4$ yr, which eventually inhibits erosional unloading. The work on the Shyok and Nubra rivers (Chapter 5) revealed that their large and widespread valley fills reflect the influence of glacial erosion on landscape evolution. Since sediment dynamics is strongly influenced by glacier fluctuations, it is sensitive to orbital forcing on the timescale of $\sim 10^4$–10^5 yr of Milankovic cycles. These short- to intermediate-term processes are superimposed by very short-term cycles, which involve the repeated catastrophic drainage of lakes. The first two studies show that retrieving the geometry of valley-fill deposits provides new possibilities for e.g. the reconstruction of paleo-streams or derivation of boundary conditions in landscape-evolution models. In the following I will discuss important aspects of the above studies and in particular of Chapter 3 that were only briefly addressed in the manuscripts due to journal-specific length limits, but which deserve further attention. This will be followed by a survey of the findings from the previous chapters in light of the main objective of this thesis and an outlook concerning potential future work.

6.1 Timing of valley-fill deposition

A fundamental contribution of Chapters 3 and 4 is the quantification of valley-fill thicknesses. However, this data would have been of little use without some kind of age control that ultimately allowed for the interpretation of the valley-fills in the spatiotemporal context of regional climate and tectonics. Timing of fill formation in the Alps has previously been indirectly constrained by radiocarbon dating of the Quaternary marginal lakes (Hinderer, 2001, and references therein). Accordingly, lake formation began 16–18 ky BP. Since this time, sediment export from the corresponding catchments was low in relation to the amount of material that was trapped, e.g. 8% and 5% in case of Rhine and Rhône valleys, respectively (Hinderer, 2001). In some places in the Alps (e.g., Rhône and Rhine valleys) the fill deposits are thought to be the result of one single glacial retreat. Regarding the very deep successions however, this is often based only on seismo-stratigraphic interpretation (Pfiffner et al., 1997) and direct observations from boreholes are scarce. A review of data from deep drilling in the Inn Valley on the other hand points to the possibility that there are pre-LGM and even Tertiary valley fills preserved (Preusser et al., 2010). However, in this specific case the reconstructed bedrock elevation used here is consistent with the top of these older fills and I assume that most of the derived volume reflects post-LGM deposition. While underestimation of the amount of older material within the estimate would reduce the proposed post-LGM mean erosion rate of 0.7 mm yr^{-1}, an underestimation of the exported material would lead to an increase of the erosion rate. To what degree both factors influence the final estimate is uncertain. In contrast to the indirect age constraints employed in Chapter 3, CRN burial- and exposure-age dating as in Chapters 4 and 5 provides direct age estimates for the onset of aggradation and incision, respectively.

6.2 Deconvolving factors that lead to rock uplift

The potential drivers of rock uplift in a contractional orogen are tectonics (e.g., Lavé and Avouac, 2001; Wang et al., 2014), erosional unloading (e.g., Small and Anderson, 1995; Champagnac et al., 2009), deglaciation (Gudmundsson, 1994) and deeper rooted processes like slab detachment (e.g., Davies and von Blanckenburg, 1995; Duretz et al., 2011), crustal/lithospheric delamination (e.g., Meissner and Mooney, 1998; Göğüş and Pysklywec, 2008) or mantle upwelling (Fig. 3.1, Lyon-Caen and Molnar, 1989). Since data on the latter processes are scarce, Chapter 3 focused on tectonics, erosion and glacial isostasy. By modeling the LGM ice cover and the post-LGM sediment budget of the Alps I determined their relative contribution to the recent rock uplift and interpreted the residuals in terms of tectonics.

Erosion can lead to isostatic uplift if the eroded material is transported far enough away from the source (Watts, 2001). How far this must be is strongly governed by lithospheric strength. Considering a zero-strength lithosphere, i.e. assuming local isostasy (Airy, 1855; Pratt, 1855), redistribution of mass from the ridges to the neighboring valleys would trigger isostatic uplift of the ridges and subsidence of the valleys according to the density contrast between crustal rocks and the mantle. With an increasingly stronger lithosphere however, changes of lithospheric loading can be supported and the isostatic response becomes non-local (Vening Meinesz, 1931). Under these conditions the area that is affected by isostatic uplift/subsidence grows at the expense of the maximum lithospheric deflection. Therefore, redistribution of mass from hillslopes into adjacent valleys or even to the margins of the orogen might not lead to any measurable isostatic response. In the European Alps, Quaternary glacial erosion created accommodation space in the form of glacial troughs and overdeepenings that had to be filled before sediments could effectively be exported out of the orogen. In contrast, meltwater could leave the system much more easily making the ice load disappear almost completely.

Effective elastic thickness. Estimates of the effective elastic thickness in the Alps range from 5 to 50 km (Karner and Watts, 1983; Sinclair et al., 1991; Royden, 1993; Steward and Watts, 1997) with generally lower values in the west than in the east. Using an EET of 14–24 km (average EET of 20 km) in the optimization procedure yields a best-fit viscosity of $\sim 1.8 \times 10^{20}$ Pa s (Fig. 3.7), but leads to residual uplift of the Swiss Plateau and the Jura Mountains with rates of up to 0.8 mm yr^{-1}. Yet, the low present-day, GPS-derived convergence rates across the Western and Central Alps (Fig. 3.3) preclude a tectonic origin of this excess uplift (Champagnac et al., 2009). On the other hand, mantle upwelling as proposed by Lyon-Caen and Molnar (1989) could be another potential cause for uplift in this region, particularly due to its proximity to the Upper Rhine Graben. However, the upper mantle structure as it is revealed by seismic tomography (Lippitsch et al., 2003) does not correlate with the pattern of uplift in that region. With an increasing EET the amount of excess uplift in the Swiss Molasse and the Jura Mountains decreases systematically and finally disappears when approaching an average EET of 50 km, which represents the upper limit of previously proposed values (see above).

Exported sediment volume. Another crucial point of Chapter 3 is the question of how much sediment has actually been exported since deglaciation. Hinderer et al. (2013) estimated the pre-industrial sediment flux out of the Alps to be 0.42 mm yr^{-1}, which is approximately six times the value (400 Gt) I adopted from Fig. 8 of Hinderer (2001). Nevertheless, if one assumed even a tenfold increase in exported material the removed mass of 4000 Gt would still be an order of magnitude lower than that by melting of the icecap (65×10^3 Gt), which does not change the conclusion that isostatic uplift of the European Alps is dominated by ice melting rather than erosion. However, deglaciation took place 21–17 ka while erosional unloading, though much smaller, is acting continuously. As shown in Chapter 3 the decay of a given deflection is mainly controlled by upper-mantle viscosity (Eq. 3.2), which generally varies over 3 orders of magnitude (10^{18}–10^{21} Pa s; e.g., Bürgmann and Dresen, 2008). At low upper-mantle viscosities ($<1 \times 10^{20}$ Pa s) the ice-load induced deflection would have certainly vanished by today. Yet, such low values are usually thought to be characteristic for tectonically active or volcanic regions like Iceland, the Andes or the Cascadia margin (see Table 3.1 for references). Therefore, the estimated viscosity range for the Alpine upper mantle of 1.5–3×10^{20} Pa s should be reasonable.

Uplift due to recent glacier shrinkage. Regarding the isostatic uplift caused by the present-day and the Little Ice Age (LIA) ice-volume loss, Barletta et al. (2006) claimed that an uplift rate of up to 0.8 mm yr^{-1}, which is about half of the measured maximum value, can be attributed to ice unloading since the end of the LIA approximately 1850 A.D. I adopted their value for the ice-volume loss since the end of the LIA of 155 km^3 (Barletta et al., 2006, and references therein), which is equivalent to a mass of ~142 Gt assuming an ice density of 917 kg m^{-3}. Using an EET of 50 km the equilibrium deflection due to the ice load would at maximum be 0.4 m only. With an upper mantle viscosity (μ) of 2.2×10^{20} Pa s, λ = 120 km as the wavelength of the load, and 166 years since unloading (see Equations 3.2 and 3.3) the present-day contribution to rock uplift would be at most 0.02 mm yr^{-1} (Fig. 6.1a). A stronger contribution, e.g., greater than 0.1 mm yr^{-1} would require the upper-mantle viscosity to be less than 4×10^{19} Pa s (Fig. 6.1b). However, due to the short LIA duration of only ~500–600 yr (e.g., Grove, 2001; Matthews and Briffa, 2005) full isostatic compensation of the ice load would imply a relaxation timescale on the order of 200–300 yr, which could only be achieved with unrealistically low upper-mantle viscosities $<3 \times 10^{18}$ Pa s (Fig. 6.1b). While Barletta et al. (2006) used a stratified viscoelastic Earth based on the preliminary reference earth model (PREM, Dziewonski and Anderson, 1981), the approach used here (Chapter 3) treats the problem as an elastic plate overlying a viscous substratum, hence direct comparison of both models might not be straightforward. Their upper mantle for example, extending down from 40 km depth, has a viscosity, which is twice as high (4.64×10^{20} Pa s) as the estimate used here, but at the same time they assumed a middle crust with low viscosity (2.15×10^{19} Pa s). Nevertheless, the pattern of modeled uplift that is due to ice loss since LIA does not resemble the pattern of the measured uplift. The maximum LIA-related uplift is located in the Central Alps and does not coincide with the maximum geodetically-determined uplift rates that are centered in the Eastern Alps. If the LIA signal would contribute substantially to the measured uplift rates one would expect a systematic residual uplift in my model over the Central Alps, which is not observed.

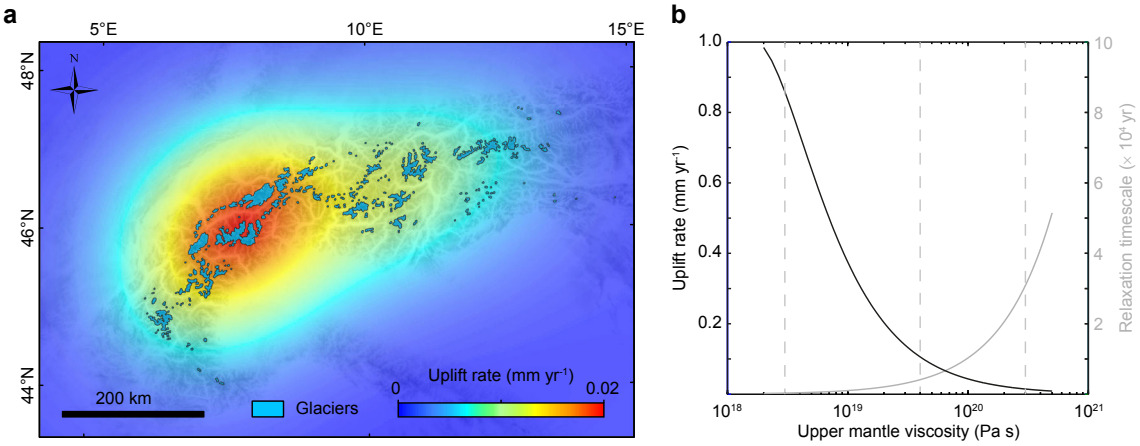

Figure 6.1: Isostatic rock uplift caused by post-LIA ice decay. (**a**) Approximate glacier cover during LIA and uplift-rate pattern caused by 155 km^3 ice-volume loss since 1850 A.D. assuming an EET of 50 km and an upper mantle viscosity of 2.2×10^{20} Pa s. (**b**) Relationship between maximum uplift rate, relaxation timescale and upper mantle viscosity. Dashed vertical lines show values referred to in the text.

Present-day uplift in the Western Alps. Recent data from precise leveling and GPS indicate a narrow zone of high uplift (2.5 mm yr^{-1}) in the Western Alps (Nocquet et al., 2016). With the absence of active crustal convergence across this region tectonics can be ruled out as a main driver of this vertical motion. However, glacial isostasy and erosional unloading only account for ~60% of the measured uplift rate and thus alternative processes have been proposed. Chéry et al. (2016) explain this discrepancy with a rheological anomaly below the central part of the Western Alps, involving low crustal (10^{21} Pa s) and upper mantle viscosities (10^{20} Pa s), the latter being consistent with the values proposed in Chapter 3. On the other hand, the region of unusually high uplift rates spatially coincides with a zone of low seismic velocity in the upper mantle (100–180 km depth), which was interpreted as an expression of asthenospheric upwelling, resulting from detachment of the European slab (Lippitsch et al., 2003). Nocquet et al. (2016) therefore point out that the excess uplift of ~1 mm yr^{-1} could entirely be attributed to such a deep-seated process. In light of

these new data it seems at least possible that the residual uplift in the upper Rhône Valley is a result of the same mantle anomaly Fig. 3.3). Future studies will likely benefit from an increase in the resolution of seismotomography (www.alparray.ethz.ch) and thus might be able to test this hypothesis.

Chapter 7

Conclusion & outlook

In this study, I investigated various aspects of landscape evolution that are associated with the formation of intermontane valley fills. The combination of field-based observations, remotely sensed data, topographic analysis and CRN dating has proven to be an efficient way to gain insight into the complex mechanisms and timescales that characterize the formation of transiently stored sediments within the interior of mountain belts. In particular, the chapter dealing with glacial isostasy in the Alps (Chapter 3) demonstrates how such knowledge can further be used in conjunction with numerical models to test hypotheses and to constrain fundamental properties of the Earth's interior. Regarding the three research questions outlined in Chapter 1 I draw the following conclusions:

1. In the European Alps, a large fraction of post-glacially eroded sediments has not been exported out of the orogen, but was stored in intermontane valleys. The total eroded mass (internally stored + exported) since the LGM ice retreat of ~4000–6000 Gt is one order of magnitude smaller than the mass loss due to deglaciation, which is ~65,000 Gt. This suggests a dominance of ice melting over erosional unloading in their relative contribution to the present-day rock uplift of the orogen. Accordingly, more than 90% of the long-wavelength uplift signal can be attributed to glacial isostatic adjustment. In contrast, the tectonic component is localized, but exceeds 50% in the Swiss Rhône Valley and parts of the Eastern Alps. However, due to the lack of crustal convergence across the Western Alps the excess uplift in that region might be due to a mantle anomaly, perhaps also influencing the uplift rates in the Rhône Valley (see Discussion above).

2. Valley-fill volumes can in principle be used to derive upstream erosion rates, if constraints on the timing of fill formation are available and the amount of lost material can be quantified. For the Alps a mean post-LGM erosion rate of 0.67–1.5 mm yr^{-1} can be deduced depending on the amount of exported material (400–4000 Gt, see Discussion) and the timing of ice retreat (16–18 ka BP).In case of the catchments of the Yarlung-Tsanpo and Nyang rivers upstream of the Namche Barwa massif, only a lower-bound erosion rate could potentially be specified due to the unknown amount of exported material and the fact that only the volume of the main alluvial plain was computed. However, the derived thickness distribution helped to reconstruct the former longitudinal river profile. Unlike in the European Alps, where the large sediment fills formed in glacially overdeepened valleys and thus were climatically controlled, the alluviated reaches of the Yarlung-Tsangpo and Nyang rivers were formed as a consequence of a rise of the fluvial baselevel at ~3 Ma that had a tectonic origin.

3. The >100-ka-old remnants of fluvio-lacustrine deposits in the Shyok Valley are due to prolonged river damming by the Siachen Glacier prior to the Eemian interglacial. Although subsequent glacier advances could also have blocked the Shyok River they did not reach the same extent as during the penultimate glaciation. Possible reasons for the occurrence of smaller glaciers could have been a progressive aridification of the region or the impact of glacial erosion on the mass balance. The contemporary valley fill of the Shyok and Nubra Rivers on the other hand is not related to river damming but reflects the back-filling of a glacially overdeepened valley segment. Since these overdeepenings can also be found were major Karakoram tributaries join the Indus or Shyok Rivers, glacial damming and associated outburst flooding were presumably frequent and widespread in the region during the Quaternary.

During the work on the individual chapters several new research questions emerged that could be addressed in future studies. The new constraints on ice extent and timing of glacier retreat in the Shyok and Nubra valleys presented in Chapter 5 could be the starting point for a numerical reconstruction of the former Karakoram ice cover. This could be used to test the hypothesis that many tributary glaciers were responsible for the formation of a cascade of glacier-dammed lakes along the margin of the mountain belt. In combination with an estimate of the stored and exported sediments the isostatic response to the varying surface loads could be derived, which may be an important component of the crustal deformation field.

A similar investigation could be undertaken at the Yarlung-Tsangpo Valley. Extrapolating the CRN-derived paleo-erosion rate of 0.1–0.2 mm yr^{-1} over the last 2–2.5 Ma results in an eroded volume that is equivalent to a 200 m rock column, when distributed evenly over the corresponding catchment. In contrast, the valley-fill volume upstream of the sampling site represents only ~2 m of catchment-wide erosion, thus ~99% of the eroded material since 2–2.5 Ma has been transported past the sampling site and most probably beyond the Tsangpo Gorge. The isostatic uplift due to this mass loss could be calculated and compared with the uplift rates estimated for the Namche Barwa and Gyala Peri massifs to decipher the relative contribution of tectonics and erosional unloading regarding regional uplift rates.

Bibliography

Airy, G.B., 1855. On the computation of the effect of the attraction of mountain-masses, as disturbing the apparent astronomical latitude of stations in geodetic surveys. Philosophical Transactions of the Royal Society of London 145, 101–104.

Aki, K., Richards, P.G., 2002. Quantitative seismology. volume 1. Univ. Science Books, Sausalito, Calif.

Allen, T.I., Wald, D.J., 2009. On the use of high-resolution topographic data as a proxy for seismic site conditions (VS30). Bulletin of the Seismological Society of America 99, 935–943. doi:10.1785/0120080255.

Amundson, J.M., Iverson, N.R., 2006. Testing a glacial erosion rule using hang heights of hanging valleys, Jasper National Park, Alberta, Canada. Journal of Geophysical Research 111, F01020. doi:10.1029/2005JF000359.

Anderson, B., Mackintosh, A., 2006. Temperature change is the major driver of late-glacial and Holocene glacier fluctuations in New Zealand. Geology 34, 121–124. doi:10.1130/G22151.1.

Anderson, R.S., Dühnforth, M., Colgan, W., Anderson, L., 2012. Far-flung moraines: Exploring the feedback of glacial erosion on the evolution of glacier length. Geomorphology 179, 269–285. doi:10.1016/j.geomorph.2012.08.018.

Arendt, A., T., B., Cogley, J., Gardner, A., Hagen, J.O., Hock, R., Kaser, G., Pfeffer, W.T., Moholdt, G., Paul, F., Radić, V., Andreassen, L., Bajracharya, S., Beedle, M., Berthier, E., Bhambri, R., Bliss, A., Brown, I., Burgess, E., Burgess, D., Cawkwell, F., Chinn, T., Copland, L., Davies, B., De Angelis, H., Dolgova, E., Filbert, K., Forester, R., Fountain, A., Frey, H., Giffen, B., Glasser, N., Gurney, S., Hagg, W., Hall, D., Haritashya, U., Hartmann, G., Helm, C., Herreid, S., Howat, I., Kapustin, G., Khromova, T., Kienholz, C., Koenig, M., Kohler, J., Kriegel, D., Kutuzov, S., Lavrentiev, I., LeBris, R., Lund, J., Manley, W., Mayer, C., Miles, E., Li, X., Menounos, B., Mercer, A., Moelg, N., Mool, P., Nosenko, G., Negrete, A., Nuth, C., Pettersson, R., Racoviteanu, A., Ranzi, R., Rastner, P., Rau, F., Raup, B.H., Rich, J., Rott, H., Schneider, C., Seliverstov, Y., Sharp, M., SigurÃ°sson, O., Stokes, C., Wheate, R., Winsvold, S., Wolken, G., Wyatt, F., Zheltyhina, N., 2012. Randolph Glacier Inventory: A Dataset of Global Glacier Outlines, version 2.0. Technical Report. Global Land Ice Measurement from Space. Boulder, Colorado. URL: http://www.glims.org/RGI/.

Argus, D.F., Peltier, W.R., Drummond, R., Moore, A.W., 2014. The Antarctica component of postglacial rebound model ICE-6G_C (VM5a) based on GPS positioning, exposure age dating of ice thicknesses, and relative sea level histories. Geophysical Journal International 198, 537–563. doi:10.1093/gji/ggu140.

Aric, K., Steinhauser, P., 1976. Geophysikalische Untersuchung des Inntal-Untergrundes bei Thaur, östlich von Innsbruck. Zeitschrift für Gletscherkunde und Glazialgeologie 12, 37–54.

Atwater, B.F., 1986. Pleistocene glacial-lake deposits of the Sanpoil River valley, northeastern Washington. U.S. Geological Survey Bulletin , 39.

Avouac, J.P., Burov, E.B., 1996. Erosion as a driving mechanism of intracontinental mountain growth. Journal of Geophysical Research-Solid Earth 101, 17747–17769. doi:10.1029/96jb01344.

Bagnold, R.A., 1966. An Approach to the Sediment Transport Problem from General Physics. USGS Professional Paper 422, 42. doi:10.1017/S0016756800049074.

Bahr, D.B., Meier, M.F., Peckham, S.D., 1997. The physical basis of glacier volume-area scaling. Journal of Geophysical Research 102, 20355. doi:10.1029/97JB01696.

Baker, V.R., 2002. High-energy megafloods: planetary settings and sedimentary dynamics. Flood and megaflood processes and deposits: recent and ancient examples: International Association of Sedimentologists Special Publication 32, 3–15.

Balco, G., Stone, J.O., Lifton, N.A., Dunai, T.J., 2008. A complete and easily accessible means of calculating surface exposure ages or erosion rates from 10Be and 26Al measurements. Quaternary Geochronology 3, 174–195. doi:10.1016/j.quageo.2007.12.001.

Balco, G.A., 2004. The sedimentary record of subglacial erosion beneath the Laurentide Ice Sheet. Ph.D. thesis. University of Washington.

Barber, D.C., Dyke, A., Hillaire-Marcel, C., Jennings, A.E., Andrews, J.T., Kerwin, M.W., Bilodeau, G., McNeely, R., Southon, J., Morehead, M.D., Gagnon, J.M., 1999. Forcing of the cold event of 8,200 years ago by catastrophic drainage of Laurentide lakes. Nature 400, 344–348.

Barletta, V.R., Ferrari, C., Diolaiuti, G., Carnielli, T., Sabadini, R., Smiraglia, C., 2006. Glacier shrinkage and modeled uplift of the Alps. Geophysical Research Letters 33, 3–7. doi:10.1029/2006GL026490.

Barnaba, C., Marello, L., Vuan, a., Palmieri, F., Romanelli, M., Priolo, E., Braitenberg, C., 2010. The buried shape of an alpine valley from gravity surveys, seismic and ambient noise analysis. Geophysical Journal International 180, 715–733. doi:10.1111/j.1365-246X.2009.04428.x.

Bassetti, M., Borsato, A., 2005. Evoluzione geomorfologica della Bassa Valle dell' Adige dall' Ultimo Massimo Glaciale: sintesi delle conoscenze e riferimenti ad aree limitrofe. Studi trentini di scienze naturali - Acta geologica 82, 31–42.

Bauder, A., Funk, M., Gudmundsson, G.H., 2003. The ice-thickness distribution of Unteraargletscher, Switzerland. Annals of Glaciology 37, 331–336. doi:doi:10.3189/172756403781815852.

Bauder, A., Funk, M., Huss, M., 2007. Ice-volume changes of selected glaciers in the Swiss Alps since the end of the 19th century. Annals of Glaciology 46, 145–149. doi:10.3189/172756407782871701.

Becker, T.W., Lowry, A.R., Faccenna, C., Schmandt, B., Borsa, A., Yu, C., 2015. Western US intermountain seismicity caused by changes in uppermantle flow. Nature 524, 458–461. doi:10.1038/nature14867.

van der Beek, P., Van Melle, J., Guillot, S., Pecher, A., Reiners, P.W., Nicolescu, S., Latif, M., 2009. Eocene Tibetan plateau remnants preserved in the northwest Himalaya. Nature Geosci 2, 364–368.

Benn, D., Bolch, T., Hands, K., Gulley, J., Luckman, A., Nicholson, L., Quincey, D., Thompson, S., Toumi, R., Wiseman, S., 2012. Response of debris-covered glaciers in the Mount Everest region to recent warming, and implications for outburst flood hazards. Earth-Science Reviews 114, 156–174. doi:10.1016/j.earscirev.2012.03.008.

Besson, O., Rouiller, J.D., Frei, W., Masson, H., 1991. Campagne de sismique-réflexion dans la vallée du Rhône (entre Sion et Martigny, Suisse), in: Bulletin de la Murithienne, pp. 45–64.

Bhutiyani, M.R., 2000. Sediment load characteristics of a proglacial stream of Siachen Glacier and the erosion rate in Nubra valley in the Karakoram Himalayas, India. Journal of Hydrology 227, 84–92. doi:10.1016/S0022-1694(99)00174-2.

Bills, B.G., Currey, D.R., Marshall, G.A., 1994a. Viscosity estimates for the crust and upper mantle from patterns of lacustrine shoreline deformation in the Eastern Great Basin. Journal of Geophysical Research 99, 22059–22086. doi:10.1029/95JB00014.

Bills, B.G., de Silva, S.L., Currey, D.R., Emenger, R.S., Lillquist, K.D., Donnellan, A., Worden, B., 1994b. Hydro-isostatic deflection and tectonic tilting in the central Andes: Initial results of a GPS survey of Lake Minchin shorelines. Geophysical Research Letters 21, 293–296. doi:10.1029/93GL03544.

Bishop, C.M., 1995. The multi-layer perceptron. Oxford University Press.

von Blanckenburg, F., 2004. Cosmogenic nuclide evidence for low weathering and denudation in the wet, tropical highlands of Sri Lanka. Journal of Geophysical Research 109, F03008. doi:10.1029/2003JF000049.

Bleibinhaus, F., Hilberg, S., Stiller, M., 2010. First results from a Seismic Survey in the Upper Salzach Valley, Austria. Austrian Journal of Earth Sciences 103, 28–32.

Blöthe, J.H., Korup, O., 2013. Millennial lag times in the Himalayan sediment routing system. Earth and Planetary Science Letters 382, 38–46. doi:10.1016/j.epsl.2013.08.044.

Bookhagen, B., Burbank, D.W., 2010. Toward a complete himalayan hydrological budget: Spatiotemporal distribution of snowmelt and rainfall and their impact on river discharge. Journal of Geophysical Research: Earth Surface 115, n/a–n/a. doi:10.1029/2009JF001426. f03019.

Bookhagen, B., Fleitmann, D., Nishiizumi, K., Strecker, M., Thiede, R., 2006. Holocene monsoonal dynamics and fluvial terrace formation in the northwest himalaya, india. Geology 34, 601–604.

Bookhagen, B., Thiede, R.C., Strecker, M.R., 2005. Late Quaternary intensified monsoon phases control landscape evolution in the northwest Himalaya. Geology 33, 149–152. doi:10.1130/G20982.1.

Booth, A.L., Zeitler, P.K., Kidd, W.S.F., Wooden, J., Liu, Y., Idleman, B., Hren, M., Chamberlain, C.P., 2004. U-Pb zircon constraints on the tectonic evolution of southeastern Tibet, Namche Barwa Area. American Journal of Science 304, 889–929. doi:10.2475/ajs.304.10.889.

Braucher, R., Brown, E., Bourlès, D., Colin, F., 2003. In situ produced 10Be measurements at great depths: implications for production rates by fast muons. Earth and Planetary Science Letters 211, 251–258. doi:10.1016/S0012-821X(03)00205-X.

Braucher, R., Del Castillo, P., Siame, L., Hidy, A., Bourlés, D., 2009. Determination of both exposure time and denudation rate from an in situ-produced 10Be depth profile: A mathematical proof of uniqueness. Model sensitivity and applications to natural cases. Quaternary Geochronology 4, 56–67. doi:10.1016/j.quageo.2008.06.001.

Bretz, J.H., 1969. The Lake Missoula Floods and the Channeled Scabland. The Journal of Geology 77, 505–543.

Brocard, G., van der Beek, P., Bourlès, D., Siame, L., Mugnier, J.L., 2003. Long-term fluvial incision rates and postglacial river relaxation time in the French Western Alps from 10Be dating of alluvial terraces with assessment of inheritance, soil development and wind ablation effects. Earth and Planetary Science Letters 209, 197–214. doi:10.1016/S0012-821X(03)00031-1.

Brocklehurst, S.H., Whipple, K.X., 2002. Glacial erosion and relief production in the Eastern Sierra Nevada, California. Geomorphology 42, 1–24. doi:10.1016/S0169-555X(01)00069-1.

Brocklehurst, S.H., Whipple, K.X., 2006. Assessing the relative efficiency of fluvial and glacial erosion through simulation of fluvial landscapes. Geomorphology 75, 283–299. doi:10.1016/j.geomorph.2005.07.028.

Brookfield, M., 1998. The evolution of the great river systems of southern Asia during the Cenozoic India-Asia collision: rivers draining southwards. Geomorphology 22, 285–312. doi:10.1016/S0169-555X(97)00082-2.

Brooks, G.R., 1992. Aspects of post-glacial sediment supply and its control upon the morphology of Squamish River, southwestern British Columbia. Ph.D. thesis. Univ. of British Columbia, Vancouver, B. C.

Brückl, E., Behm, M., Decker, K., Grad, M., Guterch, A., Keller, G.R., Thybo, H., 2010a. Crustal structure and active tectonics in the Eastern Alps. Tectonics 29, TC2011. doi:10.1029/2009TC002491.

Brückl, E., Brückl, J., Chwatal, W., Ullrich, C., 2010b. Deep alpine valleys: Examples of geophysical explorations in Austria. Swiss Journal of Geosciences 103, 329–344. doi:10.1007/s00015-010-0045-x.

Brummer, C.J., Montgomery, D.R., 2006. Influence of coarse lag formation on the mechanics of sediment pulse dispersion in a mountain stream, Squire Creek, North Cascades, Washington, United States. Water Resources Research 42, n/a–n/a. doi:10.1029/2005WR004776.

Bruyninx, C., 2004. The EUREF Permanent Network: a multi-disciplinary network serving surveyors as well as scientists. GeoInformatics 7, 32–35.

Büdel, J., 1981. Klima-Geomorphologie. Schweizerbart Science Publishers, Stuttgart, Germany. URL: http://www.schweizerbart.de//publications/detail/isbn/9783443010171/Budel_Klima_Geomorphologie_2_Auflage.

Bull, W.B., 1991. Geomorphic responses to climatic change. Oxford University Press.

Burbank, D.W., Derry, L.A., France-Lanord, C., 1993. Reduced Himalayan sediment production 8 Myr ago despite an intensified monsoon. Nature 364, 48–50. doi:10.1038/364048a0.

Burbank, D.W., Johnson, G.D., 1982. Intermontane-basin development in the past 4 Myr in the north-west Himalaya. Nature 298, 432–436. doi:10.1017/CBO9781107415324.004.

Burbank, D.W., Leland, J., Fielding, E., Anderson, R.S., Brozovic, N., Reid, M.R., Duncan, C., 1996. Bedrock incision, rock uplift and threshold hillslopes in the northwestern Himalayas. doi:10.1038/379505a0.

Burbank, D.W., Tahirkheli, R.A.K., 1985. The magnetostratigraphy, fission-track dating, and stratigraphic evolution of the Peshawar intermontane basin, northern Pakistan. Geological Society of America Bulletin 96, 539–552.

Burg, J.P., Nievergelt, P., Oberli, F., Seward, D., Davy, P., Maurin, J.C., Diao, Z., Meier, M., 1998. The Namche Barwa syntaxis: evidence for exhumation related to compressional crustal folding. Journal of Asian Earth Sciences 16, 239–252. doi:10.1016/S0743-9547(98)00002-6.

Burgisser, H.M., Gansser, A., Pika, J., 1982. Late Glacial lake sediments of the Indus valley area, northwestern Himalayas. Eclogae Geologicae Helvetiae 75, 51–63.

Bürgmann, R., Dresen, G., 2008. Rheology of the Lower Crust and Upper Mantle: Evidence from Rock Mechanics, Geodesy, and Field Observations. Annual Review of Earth and Planetary Sciences 36, 531–567. doi:10.1146/annurev.earth.36.031207.124326.

Burov, E.B., Diament, M., 1995. The effective elastic thickness (T e) of continental lithosphere: What does it really mean? Journal of Geophysical Research 100, 3905. doi:10.1029/94JB02770.

Caine, N., Swanson, F., 1989. Geomorphic coupling of hillslope and channel systems in two small mountain basins. Zeitschrift fuer Geomorphologie , 189–203.

Calais, E., Freed, a.M., Van Arsdale, R., Stein, S., 2010. Triggering of New Madrid seismicity by late-Pleistocene erosion. Nature 466, 608–611. doi:10.1038/nature09258.

Champagnac, J.D., Schlunegger, F., Norton, K., von Blanckenburg, F., Abbühl, L.M., Schwab, M., 2009. Erosion-driven uplift of the modern Central Alps. Tectonophysics 474, 236–249. doi:10.1016/j.tecto.2009.02.024.

Chéry, J., Genti, M., Vernant, P., 2016. Ice cap melting and low-viscosity crustal root explain the narrow geodetic uplift of the Western Alps. Geophysical Research Letters 43, 1–8. doi:10.1002/2016GL067821.

Chirouze, F., Huyghe, P., van der Beek, P., Chauvel, C., Chakraborty, T., Dupont-Nivet, G., Bernet, M., 2013. Tectonics, exhumation, and drainage evolution of the eastern Himalaya since 13 Ma from detrital geochemistry and thermochronology, Kameng River Section, Arunachal Pradesh. Geological Society of America Bulletin 125, 523–538. doi:10.1130/B30697.1.

Chmeleff, J., von Blanckenburg, F., Kossert, K., Jakob, D., 2010. Determination of the 10Be half-life by multicollector ICP-MS and liquid scintillation counting. Nuclear Instruments and Methods in Physics Research Section B: Beam Interactions with Materials and Atoms 268, 192–199. doi:10.1016/j.nimb.2009.09.012.

Cina, S.E., Yin, A., Grove, M., Dubey, C.S., Shukla, D.P., Lovera, O.M., Kelty, T.K., Gehrels, G.E., Foster, D.A., 2009. Gangdese arc detritus within the eastern Himalayan Neogene foreland basin: Implications for the Neogene evolution of the Yalu-Brahmaputra River system. Earth and Planetary Science Letters 285, 150–162. doi:10.1016/j.epsl.2009.06.005.

Clague, J., Evans, S.G., 2000. A review of catastrophic drainage of moraine-dammed lakes in British Columbia. Quaternary Science Reviews 19, 1763–1783. doi:10.1016/S0277-3791(00)00090-1.

Clague, J.J., Barendregt, R., Enkin, R.J., Foit, F.F., 2003. Paleomagnetic and tephra evidence for tens of Missoula floods in southern Washington. Geology 31, 247–250.

Clark, M.K., Schoenbohm, L.M., Royden, L.H., Whipple, K.X., Burchfiel, B.C., Zhang, X., Tang, W., Wang, E., Chen, L., 2004. Surface uplift, tectonics, and erosion of eastern Tibet from large-scale drainage patterns. Tectonics 23, n/a–n/a. doi:10.1029/2002TC001402.

Clarke, G., Leverington, D., Teller, J., Dyke, A., 2003. Superlakes, Megafloods, and Abrupt Climate Change. Science 301, 922–923. doi:10.1126/science.1085921.

Clarke, G.K.C., Anslow, F.S., Jarosch, A.H., Radić, V., Menounos, B., Bolch, T., Berthier, E., 2013. Ice volume and subglacial topography for western Canadian glaciers from mass balance fields, thinning rates, and a bed stress model. Journal of Climate 26, 4282–4303. doi:10.1175/JCLI-D-12-00513.1.

Clarke, G.K.C., Berthier, E., Schoof, C.G., Jarosch, A.H., 2009. Neural networks applied to estimating subglacial topography and glacier volume. Journal of Climate 22, 2146–2160. doi:10.1175/2008JCLI2572.1.

Cook, S.J., Swift, D.a., 2012. Subglacial basins: Their origin and importance in glacial systems and landscapes. Earth-Science Reviews 115, 332–372. doi:10.1016/j.earscirev.2012.09.009.

Copland, L., Sylvestre, T., Bishop, M.P., Shroder, J.F., Seong, Y.B., Owen, L.A., Bush, A., Kamp, U., 2011. Expanded and Recently Increased Glacier Surging in the Karakoram. Arctic, Antarctic, and Alpine Research 43, 503–516. doi:10.1657/1938-4246-43.4.503.

Cornwell, K., 1998. Quaternary break-out flood sediments in the Peshawar basin of northern Pakistan. Geomorphology 25, 225–248. doi:10.1016/S0169-555X(98)00061-0.

Cornwell, K., Hamidullah, S., 1992. Geomorphic evidence of catastrophic flooding along the middle Indus valley. Geol Bull Univ Peshawar 25, 113–121.

Costa, J.E., Schuster, R.L., 1988. The formation and failure of natural dams. Geological Society of America Bulletin 100, 1054–1068. doi:10.1130/0016-7606(1988)100<1054:TFAFON>2.3.CO;2.

Cronin, V.S., Johnson, W.P., Johnson, N.M., Johnson, G.D., 1989. Chronostratigraphy of the upper Cenozoic Bunthang sequence and possible mechanisms controlling base level in Skardu intermontane basin, Karkakoram Himalaya, Pakistan. Geological Society of America Special Papers 232, 295–309. doi:10.1130/SPE232-p295.

Crowley, J., Waters, D., Searle, M., Bowring, S., 2009. Pleistocene melting and rapid exhumation of the Nanga Parbat massif, Pakistan: Age and P–T conditions of accessory mineral growth in migmatite and leucogranite. Earth and Planetary Science Letters 288, 408–420. doi:10.1016/j.epsl.2009.09.044.

Cuffey, K.M., Paterson, W.S.B., 2010. The physics of glaciers. 4 ed., Elsevier.

Cunningham, A., 1854. Ladák, physical, statistical, and historical with notices of the surrounding countries. Allen, London.

Dahlen, F.A., 1984. Noncohesive critical Coulomb wedges: An exact solution. Journal of Geophysical Research 89, 10125. doi:10.1029/JB089iB12p10125.

Davies, J.H., von Blanckenburg, F., 1995. Slab breakoff: A model of lithosphere detachment and its test in the magmatism and deformation of collisional orogens. Earth and Planetary Science Letters 129, 85 – 102. doi:http://dx.doi.org/10.1016/0012-821X(94)00237-S.

Davis, W.M., 1902. Baselevel , Grade and Peneplain. The Journal of Geology 10, 77–111.

DeCelles, P.G., 2012. Foreland Basin Systems Revisited: Variations in Response to Tectonic Settings, in: Busby, C., Azor, A. (Eds.), Tectonics of Sedimentary Basins: Recent Advances. Wiley-Blackwell, Oxford, Calif.. chapter 20, pp. 405–426. doi:10.1002/9781444347166.ch20.

Derbyshire, E., Jijun, L., Perrott, F.A., Shuying, X., Waters, R.S., 1984. Quaternary glacial history of the Hunza Valley, Karakoram mountains, Pakistan. The International Karakoram Project 2, 456–495.

Dewald, A., Heinze, S., Jolie, J., Zilges, A., Dunai, T., Rethemeyer, J., Melles, M., Staubwasser, M., Kuczewski, B., Richter, J., Radtke, U., von Blanckenburg, F., Klein, M., 2013. CologneAMS, a dedicated center for accelerator mass spectrometry in Germany. Nuclear Instruments and Methods in Physics Research Section B: Beam Interactions with Materials and Atoms 294, 18–23. doi:10.1016/j.nimb.2012.04.030.

Dey, S., Thiede, R.C., Schildgen, T.F., Wittmann, H., Bookhagen, B., Scherler, D., Jain, V., Strecker, M.R., in revision. Climate-driven sediment aggradation and incision phases since the late pleistocene in the nw himalaya, india. Earth and Planetary Science Letters .

Ding, L., Zhong, D., Yin, A., Kapp, P., Harrison, T., 2001. Cenozoic structural and metamorphic evolution of the eastern Himalayan syntaxis (Namche Barwa). Earth and Planetary Science Letters 192, 423–438. doi:10.1016/S0012-821X(01)00463-0.

Dortch, J.M., Owen, L.a., Caffee, M.W., 2010. Quaternary glaciation in the Nubra and Shyok valley confluence, northernmost Ladakh, India. Quaternary Research 74, 132–144. doi:10.1016/j.yqres.2010.04.013.

Dortch, J.M., Owen, L.A., Caffee, M.W., Kamp, U., 2011a. Catastrophic partial drainage of Pangong Tso, northern India and Tibet. Geomorphology 125, 109–121. doi:10.1016/j.geomorph.2010.08.017.

Dortch, J.M., Owen, L.A., Schoenbohm, L.M., Caffee, M.W., 2011b. Asymmetrical erosion and morphological development of the central Ladakh Range, northern India. Geomorphology 135, 167–180. doi:10.1016/j.geomorph.2011.08.014.

Drew, F., 1873. Alluvial and Lacustrine Deposits and Glacial Records of the Upper-Indus Basin. Quarterly Journal of the Geological Society 29, 441–471. doi:10.1144/GSL.JGS.1873.029.01-02.39.

Duretz, T., Gerya, T.V., May, D.A., 2011. Numerical modelling of spontaneous slab breakoff and subsequent topographic response. Tectonophysics 502, 244–256.

Dürst Stucki, M., Reber, R., Schlunegger, F., 2010. Subglacial tunnel valleys in the Alpine foreland: An example from Bern, Switzerland. Swiss Journal of Geosciences 103, 363–374. doi:10.1007/s00015-010-0042-0.

Dürst Stucki, M., Schlunegger, F., 2013. Identification of erosional mechanisms during past glaciations based on a bedrock surface model of the central European Alps. Earth and Planetary Science Letters 384, 57–70. doi:10.1016/j.epsl.2013.10.009.

Duvall, A.R., Clark, M.K., Avdeev, B., Farley, K.A., Chen, Z., 2012. Widespread late Cenozoic increase in erosion rates across the interior of eastern Tibet constrained by detrital low-temperature thermochronometry. Tectonics 31, n/a–n/a. doi:10.1029/2011TC002969.

Dyurgerov, M., Meier, M., Armstrong, R., 2002. Glacier Mass Balance and Regime: Data of Measurements and Analysis. Institute of Arctic and Alpine Research Occasional Paper 55, 268.

Dziewonski, A.M., Anderson, D.L., 1981. Preliminary reference Earth model. Physics of the Earth and Planetary Interiors 25, 297–356. doi:10.1016/0031-9201(81)90046-7.

Eberle, M., 1987. Zur Lockergesteinsfüllung des St . Galler und Liechtensteiner Rheintales. Eclogae Geologicae Helvetiae 80, 193–206.

Egholm, D.L., Knudsen, M.F., Clark, C.D., Lesemann, J.E., 2011. Modeling the flow of glaciers in steep terrains: The integrated second-order shallow ice approximation (iSOSIA). Journal of Geophysical Research: Earth Surface 116, 1–16. doi:10.1029/2010JF001900.

Ehlers, J., Gibbard, P.L., 2004. Quaternary glaciations—extent and chronology, Part I Europe. Elsevier, Amsterdam.

Ekström, G., Nettles, M., Dziewoński, A., 2012. The global CMT project 2004–2010: Centroid-moment tensors for 13,017 earthquakes. Physics of the Earth and Planetary Interiors 200-201, 1–9. doi:10.1016/j.pepi.2012.04.002.

England, P., Molnar, P., 1990. Surface uplift, uplift of rocks, and exhumation of rocks. Geology 18, 1173–1177. doi:10.1130/0091-7613(1990)018<1173:SUUORA>2.3.CO.

Enkelmann, E., Ehlers, T., Zeitler, P., Hallet, B., 2011. Denudation of the Namche Barwa antiform, eastern Himalaya. Earth and Planetary Science Letters 307, 323–333. doi:10.1016/j.epsl.2011.05.004.

Evans, I.S., 2008. Glacial erosional processes and forms : mountain glaciation and glacier geography., in: Burt, T.P., Chorley, R.J., Brunsden, D., Cox, N.J., Goudie, A.S. (Eds.), The history of the study of landforms or the development of geomorphology : Quaternary and recent processes and forms (1890-1965) and the mid-century revolutions.. Geological Society, London. volume 4, p. 413.

Faccioli, E., Vanini, M., 2003. Complex seismic site effects in sediment-filled valleys and implications on design spectra. Progress in Structural Engineering and Materials 5, 223–238. doi:10.1002/pse.156.

Faran Ali, K., de Boer, D.H., 2008. Factors controlling specific sediment yield in the upper Indus River basin, northern Pakistan. Hydrological Processes 22, 3102–3114. doi:10.1002/hyp.6896.

Farinotti, D., Huss, M., Bauder, A., Funk, M., 2009. An estimate of the glacier ice volume in the Swiss Alps. Global and Planetary Change 68, 225–231. doi:10.1016/j.gloplacha.2009.05.004.

v. Ficker, H., Rickmers, W. (Eds.), 1932. Geologische Untersuchungen im Nordwestlichen Pamir-Gebiet und Mittleren Trans-Alai. D. Reimer, E. Vohsen, Berlin.

Finckh, A., Frei, P., 1991. Seismic reflection profiling in the Swiss Rhone valley. Part 1, Seismic reflection field work, seismic processing and seismic results of the Roche-Vouvry and Turtmann and Agarn lines. Eclogae Geologicae Helvetiae 84, 345–357.

Finnegan, N.J., Hallet, B., Montgomery, D.R., Zeitler, P.K., Stone, J.O., Anders, A.M., Yuping, L., 2008. Coupling of rock uplift and river incision in the Namche Barwa-Gyala Peri massif, Tibet. Bulletin of the Geological Society of America 120, 142–155. doi:10.1130/B26224.1.

Fischer, U.H., Porter, P.R., Schuler, T., Evans, A.J., Gudmundsson, G.H., 2001. Hydraulic and mechanical properties of glacial sediments beneath Unteraargletscher, Switzerland: Implications for glacier basal motion. Hydrological Processes 15, 3525–3540. doi:10.1002/hyp.349.

Florineth, D., 1998. Surface geometry of the Last Glacial Maximum (LGM) in the southeastern Swiss Alps (Graubünden) and its paleoclimatological significance. Eiszeitalter und Gegenwart 48, 23–27.

Florineth, D., Schlüchter, C., 1998. Reconstructing the Last Glacial Maximum (LGM) ice surface geometry and flowlines in the Central Swiss Alps. Eclogae Geologicae Helvetiae 91, 391–407.

Frank, H., 1979. Glazial übertiefte Täler im Bereich des Isar-Loisach-Gletschers. Eiszeitalter und Gegenwart 29, 77–99.

Fülöp, R.H., 2012. Quantifying the magnitude and timing of Holocene soil erosion events on parent materials of known age using in-situ cosmogenic C-14 and Be-10 depth-profiles. Ph.D. thesis. University of Glasgow.

Funk, M., Gudmundsson, G.H., Hermann, F., 1994. Geometry of the glacier bed of the Unteraarglacier, Bernese Alps, Switzerland. Zeitschrift für Gletscherkunde und Glazialgeologie 30, 187–194.

Funk, M., Rothlisberger, H., 1989. Forecasting the effects of a planned reservoir which will partially flood the tongue of Unteraargletscher in Switzerland. Annals of Glaciology 13, 76–81.

Gasse, F., Fontes, J., Van Campo, E., Wei, K., 1996. Holocene environmental changes in Bangong Co basin (Western Tibet). Part 4: Discussion and conclusions. Palaeogeography, Palaeoclimatology, Palaeoecology 120, 79–92. doi:10.1016/0031-0182(95)00035-6.

GEOSOND, 2014. GEOSOND: Geologische Sondierungen im Kanton Bern. URL: http://www.be.ch/geoportal.

Gilbert, G.K., 1877. Report on the Geology of the Henry Mountains. Technical Report. Department of the Interior. Washington, DC. doi:10.1038/031031a0.

Gilbert, G.K., Murphy, E.C., 1914. The transportation of debris by running water. 86, US Government Printing Office.

Godard, V., Tucker, G.E., Burch Fisher, G., Burbank, D.W., Bookhagen, B., 2013. Frequency-dependent landscape response to climatic forcing. Geophysical Research Letters 40, 859–863. doi:10.1002/grl.50253.

Göğüş, O.H., Pysklywec, R.N., 2008. Mantle lithosphere delamination driving plateau uplift and synconvergent extension in eastern anatolia. Geology 36, 723–726.

Golledge, N.R., Mackintosh, A.N., Anderson, B.M., Buckley, K.M., Doughty, A.M., Barrell, D.J.a., Denton, G.H., Vandergoes, M.J., Andersen, B.G., Schaefer, J.M., 2012. Last Glacial Maximum climate in New Zealand inferred from a modelled Southern Alps icefield. Quaternary Science Reviews 46, 30–45. doi:10.1016/j.quascirev.2012.05.004.

Gosse, J.C., Phillips, F.M., 2001. Terrestrial in situ cosmogenic nuclides: theory and application. Quaternary Science Reviews 20, 1475–1560. doi:10.1016/S0277-3791(00)00171-2.

Götz, J., Otto, J.C., Schrott, L., 2013. Postglacial sediment storage and rockwall retreat in a semi-closed inner-alpine sedimentary basin (Gradenmoos, Hohe Tauern, Austria). Geografia Fisica e Dinamica Quaternaria 36, 63–80. doi:10.4461/GFDQ.2013.36.5.

Granger, D.E., Kirchner, J.W., Finkel, R., 1996. Spatially Averaged Long-Term Erosion Rates Measured from in Situ-Produced Cosmogenic Nuclides in Alluvial Sediment. The Journal of Geology 104, 249–257. doi:10.1086/629823.

Granger, D.E., Muzikar, P.F., 2001. Dating sediment burial with in situ-produced cosmogenic nuclides: theory, techniques, and limitations. Earth and Planetary Science Letters 188, 269–281. doi:10.1016/S0012-821X(01)00309-0.

Granger, D.E., Riebe, C.S., 2007. Cosmogenic nuclides in weathering and erosion. Surface and Ground Water, Weathering and Soils: Treatise on Geochemistry 5, 1–43.

Granger, D.E., Smith, A.L., 2000. Dating buried sediments using radioactive decay and muogenic production of 26Al and 10Be. Nuclear Instruments and Methods in Physics Research Section B: Beam Interactions with Materials and Atoms 172, 822–826. doi:10.1016/S0168-583X(00)00087-2.

Grenerczy, G., 2005. Tectonic implications of the GPS velocity field in the northern Adriatic region. Geophysical Research Letters 32, 10–13. doi:10.1029/2005GL022947.

Grollimund, B., Zoback, M.D., 2001. Did deglaciation trigger intraplate seismicity in the New Madrid seismic zone? Geology 29, 175. doi:10.1130/0091-7613(2001)029<0175:DDTISI>2.0.CO;2.

Grove, J.M., 2001. The Iceberg in the Mist: Northern Research in pursuit of a "Little Ice Age". Springer Netherlands, Dordrecht. chapter The Initiation of the "Little Ice Age" in Regions Round the North Atlantic. pp. 53–82. doi:10.1007/978-94-017-3352-6{_}2.

Gudmundsson, G.H., 1994. An Order-of-Magnitude Estimate of the Current Uplift-Rates in Switzerland Caused by the Würm Alpine Deglaciation. Eclogae Geologicae Helvetica 87, 545—-557.

Gunn, J.P., Todd, H.J., Mason, K., 1930. The Shyok flood, 1929. Himalayan Journal 2, 35–47.

Gutenberg, B., Buwalda, J.P., Sharp, R.P., 1956. Seismic explorations on the floor of Yosemite Valley, California. Geological Society of America Bulletin 67, 1051–1078. doi:10.1130/0016-7606(1956)67[1051:SEOTFO]2.0.CO;2.

Haeberli, W., 1983. Frequency and characteristics of glacier floods in the Swiss Alps. Annals of Glaciology 4, 85–90.

Hain, M.P., Strecker, M.R., Bookhagen, B., Alonso, R.N., Pingel, H., Schmitt, a.K., 2011. Neogene to Quaternary broken foreland formation and sedimentation dynamics in the Andes of NW Argentina (25??S). Tectonics 30, 1–27. doi:10.1029/2010TC002703.

Haley, P.J., Soloway, D., 1992. Extrapolation limitations of multilayer feedforward neural networks, in: Proceeding of the International Joint Conference on Neural Networks, Baltimore, Md.. pp. 25–30.

Hancock, G.S., Anderson, R.S., Chadwick, O.A., Finkel, R.C., 1999. Dating fluvial terraces with and profiles: application to the Wind River, Wyoming. Geomorphology 27, 41–60. doi:10.1016/S0169-555X(98)00089-0.

Harbor, J.M., 1989. W.j. mcgee on glacial erosion laws and the development of glacial valleys. Journal of Glaciology 35, 419–425.

Hart, J.K., Rose, K.C., Martinez, K., 2011. Subglacial till behaviour derived from in situ wireless multi-sensor subglacial probes: Rheology, hydro-mechanical interactions and till formation. Quaternary Science Reviews 30, 234–247. doi:10.1016/j.quascirev.2010.11.001.

Hedrick, K.a., Seong, Y.B., Owen, L.a., Caffee, M.W., Dietsch, C., 2010. Towards defining the transition in style and timing of Quaternary glaciation between the monsoon-influenced Greater Himalaya and the semi-arid Transhimalaya of Northern India. Quaternary International 236, 21–33. doi:10.1016/j.quaint.2010.07.023.

Heinz, H., Walach, G., 1979. Ergebnisse refraktionsseismischer Messungen im Gebiet des Lurnfeldes (Drautal, Oberkärnten). Verh. Geol. B.-A. 2, 77–83.

Heisinger, B., Lal, D., Jull, A., Kubik, P., Ivy-Ochs, S., Knie, K., Nolte, E., 2002a. Production of selected cosmogenic radionuclides by muons: 2. Capture of negative muons. Earth and Planetary Science Letters 200, 357–369. doi:10.1016/S0012-821X(02)00641-6.

Heisinger, B., Lal, D., Jull, A., Kubik, P., Ivy-Ochs, S., Neumaier, S., Knie, K., Lazarev, V., Nolte, E., 2002b. Production of selected cosmogenic radionuclides by muons. Earth and Planetary Science Letters 200, 345–355. doi:10.1016/S0012-821X(02)00640-4.

Herman, F., Beaud, F., Champagnac, J.D., Lemieux, J.M., Sternai, P., 2011. Glacial hydrology and erosion patterns: A mechanism for carving glacial valleys. Earth and Planetary Science Letters 310, 498–508. doi:10.1016/j.epsl.2011.08.022.

Hewitt, K., 1982. Natural dams and outburst floods of the Karakoram Himalaya, in: Hydrological Aspects of Alpine and High Mountain Areas (Proceedings of the Exeter Symposium, Juiy 1982). IAHS, pp. 259–269.

Hewitt, K., 1998. Glaciers receive a surge of attention in the Karakoram Himalaya. Eos, Transactions American Geophysical Union 79, 104–105. doi:10.1029/98EO00071.

Hewitt, K., 1999. Quaternary Moraines vs Catastrophic Rock Avalanches in the Karakoram Himalaya, Northern Pakistan. Quaternary Research 51, 220–237. doi:10.1006/qres.1999.2033.

Hewitt, K., 2005. The Karakoram Anomaly? Glacier Expansion and the 'Elevation Effect', Karakoram Himalaya. Mountain Research and Development 25, 332–340. doi:10.1659/0276-4741(2005)025[0332:TKAGEA]2.0.CO;2.

Hewitt, K., 2009. Glacially conditioned rock-slope failures and disturbance-regime landscapes, Upper Indus Basin, northern Pakistan. Geological Society, London, Special Publications 320, 235–255. doi:10.1144/SP320.15.

Hewitt, K., Gosse, J., Clague, J.J., 2011. Rock avalanches and the pace of late Quaternary development of river valleys in the Karakoram Himalaya. Geological Society of America Bulletin 123, 1836–1850. doi:10.1130/B30341.1.

Hewitt, K., Liu, J., 2010. Ice-Dammed Lakes and Outburst Floods, Karakoram Himalaya: Historical Perspectives on Emerging Threats. Physical Geography .

Hilley, G.E., Strecker, M.R., 2005. Processes of oscillatory basin filling and excavation in a tectonically active orogen: Quebrada del Toro Basin, NW Argentina. Bulletin of the Geological Society of America 117, 887–901. doi:10.1130/B25602.1.

Hinderer, M., 2001. Late Quaternary denudation of the Alps. Geodinamica Acta 14, 231–263.

Hinderer, M., Kastowski, M., Kamelger, A., Bartolini, C., Schlunegger, F., 2013. River loads and modern denudation of the Alps - A review. Earth-Science Reviews 118, 11–44. doi:10.1016/j.earscirev.2013.01.001.

Hodges, K.V., Hurtado, J.M., Whipple, K.X., 2001. Southward extrusion of Tibetan crust and its effect on Himalayan tectonics. Tectonics 20, 799–809. doi:10.1029/2001TC001281.

Hoffmann, T., Schrott, L., 2002. Modelling sediment thickness and rockwall retreat in an Alpine valley using 2D-seismic refraction (Reintal, Bavarian Alps).

Hornik, K., Stinchcombe, M., White, H., 1989. Multilayer feedforward networks are universal approximators. Neural Networks 2, 359–366. doi:10.1016/0893-6080(89)90020-8.

Hu, D., Böning, P., Köhler, C.M., Hillier, S., Pressling, N., Wan, S., Brumsack, H.J., Clift, P.D., 2012. Deep sea records of the continental weathering and erosion response to East Asian monsoon intensification since 14ka in the South China Sea. Chemical Geology 326-327, 1–18. doi:10.1016/j.chemgeo.2012.07.024.

van Husen, D., 1979. Verbreitung, Ursachen und Füllung glazial übertiefter Talabschnitte an Beispielen in den Ostalpen. Eiszeitalter und Gegenwart 29, 9–22.

Huss, M., Farinotti, D., Bauder, A., Funk, M., 2008. Modelling runoff from highly glacierized alpine drainage basins in a changing climate. Hydrological Processes 22, 3888–3902. doi:10.1002/hyp.7055.

Hutter, K., 1983. Theoretical Glaciology. Kluwer Acad., Dordrecht.

Ingersoll, R.V., 2011. Tectonics of Sedimentary Basins, with Revised Nomenclature, in: C, B., Azor, A. (Eds.), Tectonics of Sedimentary Basins. John Wiley & Sons, Ltd, pp. 1–43. doi:10.1002/9781444347166.ch1.

IPCC, 2014. Climate Change 2014: Impacts, Adaptation , and Vulnerability. Part B: Regional Aspects. Contribution of Working Group II to the Fifth Assessment Report of the Intergovernmental Panel on Climate Change. Technical Report. IPPC. Cambridge.

Isotta, F.a., Frei, C., Weilguni, V., Perčec Tadić, M., Lassègues, P., Rudolf, B., Pavan, V., Cacciamani, C., Antolini, G., Ratto, S.M., Munari, M., Micheletti, S., Bonati, V., Lussana, C., Ronchi, C., Panettieri, E., Marigo, G., Vertačnik, G., 2014. The climate of daily precipitation in the Alps: Development and analysis of a high-resolution grid dataset from pan-Alpine rain-gauge data. International Journal of Climatology 34, 1657–1675. doi:10.1002/joc.3794.

Iverson, N.R., 2002. Processes of erosion, in: Menzies, J. (Ed.), Modern Glacial Environments, Processes, Dynamics and Environments. Elsevier, New York, pp. 131–145.

Ivy-Ochs, S., Kerschner, H., Reuther, A., Preusser, F., Heine, K., Maisch, M., Kubik, P.W., Schlüchter, C., 2008. Chronology of the last glacial cycle in the European Alps. Journal of Quaternary Science 23, 559–573. doi:10.1002/jqs.

Jaboyedoff, M., Derron, M.H., 2005. A new method to estimate the infilling of alluvial sediment of glacial valleys using a sloping local base level. Geogr. Fis. Din. Quat. 28, 37–46.

Jäckli, H., 1962. Die Vergletscherung der Schweiz im Würmmaximum. Eclogae Geologicae Helvetiae 55, 285–294. doi:10.5169/seals-162924.

James, T.S., Clague, J.J., Wang, K., Hutchinson, I., 2000. Postglacial rebound at the northern Cascadia subduction zone. Quaternary Science Reviews 19, 1527–1541. doi:10.1016/S0277-3791(00)00076-7.

Jongmans, D., Campillo, M., 1993. The response of the Ubaye Valley (France) for incident SH and SV waves: Comparison between measurements and modeling. Bulletin of the Seismological Society of America 83, 907–924.

Jordan, P., 2010. Analysis of overdeepened valleys using the digital elevation model of the bedrock surface of Northern Switzerland. Swiss Journal of Geosciences 103, 375–384. doi:10.1007/s00015-010-0043-z.

Kahle, H.G., Geiger, A., Bürki, B., Gubler, E., Marti, U., Wirth, B., Rothacher, M., Gurtner, W., Beutler, G., Bauersima, I., Pfiffner, O., 1997. Recent crustal movements, geoid and density distribution: contribution from integrated satellite and terrestrial measurements, in: Pfiffner, O.A., Lehner, P., Heitzmann, P., Mueller, S., Steck, A. (Eds.), NRP 20—Deep Structure of the Swiss Alps. Birkhäuser, Basel, pp. 251–259.

Kamb, B., 2001. Basal Zone of the West Antarctic Ice Streams and its Role in Lubrication of Their Rapid Motion, in: Alley, R., Bindschadler, R. (Eds.), The West Antarctic Ice Sheet: Behavior and Environment. antarctic ed.. American Geophysical Union, Washington, DC, pp. 157–199. doi:10.1029/AR077p0157.

Kaplan, M.R., Hein, A.S., Hubbard, A., Lax, S.M., 2009. Can glacial erosion limit the extent of glaciation? Geomorphology 103, 172–179. doi:10.1016/j.geomorph.2008.04.020.

Karner, G.D., Watts, A.B., 1983. Gravity anomalies and flexure of the lithosphere at mountain ranges. Journal of Geophysical Research 88, 10449—-10477. doi:10.1029/JB088iB12p10449.

Kavanaugh, J.L., Clarke, G.K.C., 2006. Discrimination of the flow law for subglacial sediment using in situ measurements and an interpretation model. Journal of Geophysical Research: Earth Surface 111, 1–20. doi:10.1029/2005JF000346.

Kelly, M.a., Buoncristiani, J.F., Schlüchter, C., 2004. A reconstruction of the last glacial maximum (LGM) ice-surface geometry in the western Swiss Alps and contiguous Alpine regions in Italy and France. Eclogae Geologicae Helvetiae 97, 57–75. doi:10.1007/s00015-004-1109-6.

Kohl, C., Nishiizumi, K., 1992. Chemical isolation of quartz for measurement of in-situ -produced cosmogenic nuclides. Geochimica et Cosmochimica Acta 56, 3583–3587. doi:10.1016/0016-7037(92)90401-4.

Koons, P.O., Zeitler, P.K., Hallet, B., 2013. Tectonic Aneurysms and Mountain Building, in: Shroder, J.F. (Ed.), Treatise on Geomorphology. Academic Press, San Diego, San Diego, pp. 318–349.

Korschinek, G., Bergmaier, A., Faestermann, T., Gerstmann, U., Knie, K., Rugel, G., Wallner, A., Dillmann, I., Dollinger, G., von Gostomski, C.L., Kossert, K., Maiti, M., Poutivtsev, M., Remmert, A., 2010. A new value for the half-life of 10Be by Heavy-Ion Elastic Recoil Detection and liquid scintillation counting. Nuclear Instruments and Methods in Physics Research Section B: Beam Interactions with Materials and Atoms 268, 187–191. doi:10.1016/j.nimb.2009.09.020.

Korup, O., 2004. Landslide-induced river channel avulsions in mountain catchments of southwest New Zealand. Geomorphology 63, 57–80. doi:10.1016/j.geomorph.2004.03.005.

Korup, O., Montgomery, D.R., 2008. Tibetan plateau river incision inhibited by glacial stabilization of the Tsangpo gorge. Nature 455, 786–789.

Korup, O., Montgomery, D.R., Hewitt, K., 2010. Glacier and landslide feedbacks to topographic relief in the Himalayan syntaxes. Proceedings of the National Academy of Sciences of the United States of America 107, 5317–5322. doi:10.1073/pnas.0907531107.

Korup, O., Schlunegger, F., 2007. Bedrock landsliding, river incision, and transience of geomorphic hillslope-channel coupling: Evidence from inner gorges in the Swiss Alps. Journal of Geophysical Research: Earth Surface 112. doi:10.1029/2006JF000710.

Korup, O., Schlunegger, F., 2009. Rock-type control on erosion-induced uplift, eastern Swiss Alps. Earth and Planetary Science Letters 278, 278–285. doi:10.1016/j.epsl.2008.12.012.

Korup, O., Tweed, F., 2007. Ice, moraine, and landslide dams in mountainous terrain. Quaternary Science Reviews 26, 3406–3422. doi:10.1016/j.quascirev.2007.10.012.

Koulakov, I., Kaban, M.K., Tesauro, M., Cloetingh, S., 2009. P- and S-velocity anomalies in the upper mantle beneath Europe from tomographic inversion of ISC data. Geophysical Journal International 179, 345–366. doi:10.1111/j.1365-246X.2009.04279.x.

Kuhlemann, J., Frisch, W., Székely, B., Dunkl, I., Kázmér, M., 2002. Post-collisional sediment budget history of the Alps: Tectonic versus climatic control. International Journal of Earth Sciences 91, 818–837. doi:10.1007/s00531-002-0266-y.

Kühni, A., Pfiffner, O., 2001. The relief of the Swiss Alps and adjacent areas and its relation to lithology and structure: topographic analysis from a 250-m DEM. Geomorphology 41, 285–307. doi:10.1016/S0169-555X(01)00060-5.

Lague, D., 2005. Discharge, discharge variability, and the bedrock channel profile. Journal of Geophysical Research 110, F04006. doi:10.1029/2004JF000259.

Lal, D., 1991. Cosmic ray labeling of erosion surfaces: in situ nuclide production rates and erosion models. Earth and Planetary Science Letters 104, 424–439. doi:10.1016/0012-821X(91)90220-C.

Lambeck, K., Smither, C., Johnston, P., 1998. Sea-level change, glacial rebound and mantle viscosity for northern Europe. Geophysical Journal International 134, 102–144. doi:10.1046/j.1365-246x.1998.00541.x.

Lane, E.W., 1955. Importance of fluvial morphology in hydraulic engineering. Proceedings (American Society of Civil Engineers); v. 81, paper no. 745 .

Lang, K.A., Huntington, K.W., 2014. Antecedence of the Yarlung–Siang–Brahmaputra River, eastern Himalaya. Earth and Planetary Science Letters 397, 145–158. doi:10.1016/j.epsl.2014.04.026.

Lang, K.A., Huntington, K.W., Montgomery, D.R., 2013. Erosion of the Tsangpo Gorge by megafloods, Eastern Himalaya. Geology 41, 1003–1006. doi:10.1130/G34693.1.

Langbein, W.B., Schumm, S.A., 1958. Yield of sediment in relation to mean annual precipitation. Transactions, American Geophysical Union 39, 1076. doi:10.1029/TR039i006p01076.

Larsen, I.J., Montgomery, D.R., 2012. Landslide erosion coupled to tectonics and river incision. Nature Geosci 5, 468–473.

Lavé, J., Avouac, J.P., 2001. Fluvial incision and tectonic uplift across the Himalayas of central Nepal. Journal of Geophysical Research 106, 26561–26591. doi:10.1029/2001JB000359.

LeCun, Y., Bottou, L., Orr, G.B., Müller, K.R., 1998. Efficient BackProp, in: Orr, G.B., Müller, K.R. (Eds.), Neural Networks: tricks of the trade. Springer, Berlin. chapter 1, pp. 9–50.

Li, H., Ng, F., Li, Z., Qin, D., Cheng, G., 2012. An extended "perfect-plasticity" method for estimating ice thickness along the flow line of mountain glaciers. Journal of Geophysical Research: Earth Surface 117, 1–11. doi:10.1029/2011JF002104.

Linsbauer, a., Paul, F., Haeberli, W., 2012. Modeling glacier thickness distribution and bed topography over entire mountain ranges with glabtop: Application of a fast and robust approach. Journal of Geophysical Research: Earth Surface 117, 1–17. doi:10.1029/2011JF002313.

Linton, D.L., 1963. The forms of glacial erosion. Transactions and Papers (Institute of British Geographers) , 1–28.

Lippitsch, R., Kissling, E., Ansorge, J., 2003. Upper mantle structure beneath the Alpine orogen from high-resolution teleseismic tomography. Journal of Geophysical Research 108, 2376. doi:10.1029/2002JB002016.

Liu-Zeng, J., Tapponnier, P., Gaudemer, Y., Ding, L., 2008. Quantifying landscape differences across the Tibetan plateau: Implications for topographic relief evolution. Journal of Geophysical Research 113, F04018. doi:10.1029/2007JF000897.

Lyon-Caen, H., Molnar, P., 1989. Constraints on the deep structure and dynamic processes beneath the Alps and adjacent regions from an analysis of gravity anomalies. Geophysical Journal International 99, 19–32. doi:10.1111/j.1365-246X.1989.tb02013.x.

Mackin, J., 1948. Concept of the graded river. Bulletin of the Geological Society of America 59, 463–512.

Malloy, M., 2004. Rapid erosion at the Tsangpo knickpoint and exhumation of southeastern Tibet. M.s. thesis. Lehigh University, PA.

Margat, J., der Gun, J., 2013. Groundwater around the world: a geographic synopsis. Taylor and Francis Ltd., London, U.K.

Mason, K., 1929. Indus floods and Shyok glaciers. Himalayan Journal 1, 10–29.

Matthews, J., Briffa, K., 2005. The ' Little Ice Age ': Re-Evaluation of an Evolving Concept. Geografiska Annaler: Series A, Physical Geography 87, 17–36. doi:10.1111/j.0435-3676.2005.00242.x.

McFadden, L.D., Wells, S.G., Jercinovich, M.J., 1987. Influences of eolian and pedogenic processes on the origin and evolution of desert pavements. Geology 15, 504–508. doi:10.1130/0091-7613(1987)15<504:IOEAPP>2.0.CO;2.

Meissner, R., Mooney, W., 1998. Weakness of the lower continental crust: a condition for delamination, uplift, and escape. Tectonophysics 296, 47 – 60. doi:http://dx.doi.org/10.1016/S0040-1951(98)00136-X.

Mey, J., Scherler, D., Zeilinger, G., Strecker, M.R., 2015. Estimating the fill thickness and bedrock topography in intermontane valleys using artificial neural networks. Journal of Geophysical Research : Earth Surface 120, 1–20. doi:10.1002/2014JF003270.

Mitrovica, J.X., 1996. Haskell [1935] revisited. Journal of Geophysical Research 101, 555–569.

Mitrovica, J.X., Forte, a.M., 2004. A new inference of mantle viscosity based upon joint inversion of convection and glacial isostatic adjustment data. Earth and Planetary Science Letters 225, 177–189. doi:10.1016/j.epsl.2004.06.005.

Møller, M.F., 1993. A scaled conjugate gradient algorithm for fast supervised learning. Neural Networks 6, 525–533. doi:10.1016/S0893-6080(05)80056-5.

Molnar, P., Boos, W.R., Battisti, D.S., 2010. Orographic Controls on Climate and Paleoclimate of Asia: Thermal and Mechanical Roles for the Tibetan Plateau. Annual Review of Earth and Planetary Sciences 38, 77–102. doi:10.1146/annurev-earth-040809-152456.

Montgomery, D.R., Brandon, M.T., 2002. Topographic controls on erosion rates in tectonically active mountain ranges. Earth and Planetary Science Letters 201, 481–489. doi:10.1016/S0012-821X(02)00725-2.

Montgomery, D.R., Hallet, B., Yuping, L., Finnegan, N., Anders, A., Gillespie, A., Greenberg, H.M., 2004. Evidence for Holocene megafloods down the Tsangpo River gorge, southeastern Tibet. Quaternary Research 62, 201–207. doi:10.1016/j.yqres.2004.06.008.

Mugnier, J.L., Gajurel, a., Huyghe, P., Jayangondaperumal, R., Jouanne, F., Upreti, B., 2013. Structural interpretation of the great earthquakes of the last millennium in the central Himalaya. Earth-Science Reviews 127, 30–47. doi:10.1016/j.earscirev.2013.09.003.

Nabney, I., 2002. NETLAB Algorithms for Pattern Recognition, Advances in Pattern Recognition. Springer, London.

Nakada, M., Lambeck, K., 1989. Late Pleistocene and Holocene sea-level change in the Australian region and mantle rheology. Geophysical Journal of the Royal Astronomical Society 96, 497–517. doi:10.1111/j.1365-246X.1989.tb06010.x.

Ng, F., Liu, S., 2009. Temporal dynamics of a jökulhlaup system. Journal of Glaciology 55, 651–665. doi:doi:10.3189/002214309789470897.

Nicoud, G., Royer, G., Corbin, J., Lemeille, F., Paillet, A., 2002. Creusement et remplissage de la vallée de l'Isère au Quaternaire récent. Apports nouveaux du forage GMB1 (1999) dans la région de Grenoble (France). Géologie de la France 4, 39–49.

Nocquet, J., Sue, C., Walpersdorf, A., Tran, T., Lenôtre, N., Vernant, P., Cushing, M., Jouanne, F., Masson, F., Baize, S., Chéry, J., van der Beek, P., 2016. Present-day uplift of the western Alps. Nature Sci. Report .

Nordman, M., Milne, G., Tarasov, L., 2015. Reappraisal of the Angerman River decay time estimate and its application to determine uncertainty in Earth viscosity structure. Geophysical Journal International 201, 811–822. doi:10.1093/gji/ggv051.

Norris, T.L., Gancarz, A.J., Rokop, D.J., Thomas, K.W., 1983. Half-life of 26 Al. Journal of Geophysical Research 88, B331. doi:10.1029/JB088iS01p0B331.

Norton, K.P., Abbühl, L.M., Schlunegger, F., 2010. Glacial conditioning as an erosional driving force in the Central Alps. Geology 38, 655–658. doi:10.1130/G31102.1.

Nye, J.F., 1976. Water flow in glaciers: jökulhlaups, tunnels and veins. Journal of Glaciology 17, 181–207.

O'Connor, J.E., Costa, J.E., 2004. The world's largest floods, past and present: their causes and magnitudes. volume 1254. US Geological Survey.

Oerlemans, J., 1984. Numerical experiments on large-scale glacial erosion.

Okuno, J., Nakada, M., 1998. Rheological structure of the upper- mantle inferred from the Holocene sea level change along the west coast of Kyushu, Japan, in: Wu, P. (Ed.), Dynamics of the Ice Age Earth: A Modern Perspective. Trans Tech Publications, Zurich, pp. 443–458.

Otto, J.C., Goetz, J., Schrott, L., 2008. Sediment storage in Alpine sedimentary systems-quantification and scaling issues, in: Sediment Dynamics in Changing Environments, International Association of Hydrological Sciences, Christchurch, New Zealand. pp. 258–265.

Otto, J.C., Schrott, L., Jaboyedoff, M., Dikau, R., 2009. Quantifying sediment storage in a high alpine valley (Turtmanntal, Switzerland). Earth Surface Processes and Landforms 34, 1726–1742. doi:10.1002/esp.1856.

Ouimet, W.B., Whipple, K.X., Royden, L.H., Sun, Z., Chen, Z., 2007. The influence of large landslides on river incision in a transient landscape: Eastern margin of the Tibetan Plateau (Sichuan, China). Geological Society of America Bulletin 119, 1462–1476. doi:10.1130/B26136.1.

Owen, L.a., Caffee, M.W., Bovard, K.R., Finkel, R.C., Sharma, M.C., 2006. Terrestrial cosmogenic nuclide surface exposure dating of the oldest glacial successions in the Himalayan orogen: Ladakh Range, northern India. Bulletin of the Geological Society of America 118, 383–392. doi:10.1130/B25750.1.

Owen, L.A., Kamp, U., Khattak, G.A., Harp, E.L., Keefer, D.K., Bauer, M.A., 2008. Landslides triggered by the 8 October 2005 Kashmir earthquake. Geomorphology 94, 1–9. doi:10.1016/j.geomorph.2007.04.007.

Pant, R.K., Phadtare, N.R., Chamyal, L.S., Juyal, N., 2005. Quaternary deposits in Ladakh and Karakoram Himalaya: A treasure trove of the palaeoclimate records. Current Science 88, 1789–1798.

Paterson, W.S.B., 1994. The Physics of Glaciers. 3rd ed., Butterworth-Heinemann, Oxford, U.K.

Pazzaglia, F.J., Gardner, T.W., Merritts, D.J., 1998. Bedrock Fluvial Incision and Longitudinal Profile Development Over Geologic Time Scales Determined by Fluvial Terraces, in: Tinkler, K.J., Wohl, E.E. (Eds.), Rivers Over Rock: Fluvial Processes in Bedrock Channels. American Geophysical Union, pp. 207–235. doi:10.1029/GM107p0207.

Penck, A., 1905. Glacial Features in the Surface of the Alps. The Journal of Geology 13, 1–19.

Persaud, M., Pfiffner, O.A., 2004. Active deformation in the eastern Swiss Alps: Post-glacial faults, seismicity and surface uplift. Tectonophysics 385, 59–84. doi:10.1016/j.tecto.2004.04.020.

Pfiffner, O.A., Heitzmann, P., Lehner, P., Frei, W., Pugin, A., Felber, M., 1997. Incision and backfilling of Alpine valleys: Pliocene, Pleistocene and Holocene processes, in: Pfiffner, O.A., Heitzmann, P., Lehner, P., Mueller, S., Steck, A. (Eds.), Deep Structure of the Swiss Alps: results of NRP 20. Birkhäuser, Basel, pp. 265–288.

Phartiyal, B., Sharma, A., 2009. Soft-sediment deformation structures in the Late Quaternary sediments of Ladakh: Evidence for multiple phases of seismic tremors in the North western Himalayan Region. Journal of Asian Earth Sciences 34, 761–770. doi:10.1016/j.jseaes.2008.11.008.

Phartiyal, B., Sharma, A., Upadhyay, R., Sinha, A.K., 2005. Quaternary geology, tectonics and distribution of palaeo- and present fluvio/glacio lacustrine deposits in Ladakh, NW Indian Himalaya–a study based on field observations. Geomorphology 65, 241–256. doi:10.1016/j.geomorph.2004.09.004.

Phillips, R.J., 2008. Geological map of the Karakoram fault zone, Eastern Karakoram, Ladakh, NW Himalaya. Journal of Maps 4, 21–37. doi:10.4113/jom.2008.98.

Phillips, W.M., Sloan, V.F., Shroder, J.F., Sharma, P., Clarke, M.L., Rendell, H.M., 2000. Asynchronous glaciation at Nanga Parbat, northwestern Himalaya Mountains, Pakistan. Geology 28, 431–434. doi:10.1130/0091-7613(2000)28<431:AGANPN>2.0.CO;2.

Pingel, H., Strecker, M.R., Alonso, R.N., Schmitt, A.K., 2013. Neotectonic basin and landscape evolution in the Eastern Cordillera of NW Argentina, Humahuaca Basin (˜24Â°S). Basin Research 25, 554–573. doi:10.1111/bre.12016.

Post, A., Mayo, L.R., 1971. Glacier dammed lakes and outburst floods in Alaska. US Geological Survey Washington.

Pratt, J.H., 1855. On the attraction of the himalaya mountains, and of the elevated regions beyond them, upon the plumb-line in india. Philosophical Transactions of the Royal Society of London 145, 53–100.

Pratt-Sitaula, B., Garde, M., Burbank, D.W., Oskin, M., Heimsath, A., Gabet, E., 2007. Bedload-to-suspended load ratio and rapid bedrock incision from Himalayan landslide-dam lake record. Quaternary Research 68, 111–120. doi:10.1016/j.yqres.2007.03.005.

Preusser, F., Reitner, J.M., Schlüchter, C., 2010. Distribution, geometry, age and origin of overdeepened valleys and basins in the Alps and their foreland. Swiss Journal of Geosciences 103, 407–426. doi:10.1007/s00015-010-0044-y.

Pugin, A., 1988. Carte des isohypses de la base des sédiments du Quaternaire en Suisse occidentale, avec quelques commentaires, Landeshydrologie und -geologie Bern (Switzerland). volume 3. Service hydrologique et g{é}ologique national.

Quanru, G., Guitang, P., Zheng, L., Chen, Z., Fisher, R.D., Sun, Z., Ou, C., Dong, H., Wang, X., Li, S., Lou, X., Fu, H., 2006. The Eastern Himalayan syntaxis: major tectonic domains, ophiolitic mélanges and geologic evolution. Journal of Asian Earth Sciences 27, 265–285. doi:10.1016/j.jseaes.2005.03.009.

Ratschbacher, L., Frisch, W., Linzer, H.G., Merle, O., 1991. Lateral extrusion in the eastern Alps, Part 2: Structural analysis. Tectonics 10, 257–271. doi:10.1029/90TC02623.

Reitner, J.M., 2007. Glacial dynamics at the beginning of Termination I in the Eastern Alps and their stratigraphic implications. Quaternary International 164-165, 64–84. doi:10.1016/j.quaint.2006.12.016.

Repka, J.L., Anderson, R.S., Finkel, R.C., 1997. Cosmogenic dating of fluvial terraces, fremont river, utah. Earth and Planetary Science Letters 152, 59 – 73. doi:http://dx.doi.org/10.1016/S0012-821X(97)00149-0.

Roberts, M.J., 2005. Jökulhlaups: A reassessment of floodwater flow through glaciers. Reviews of Geophysics 43, RG1002. doi:10.1029/2003RG000147.

Rolland, Y., Pêcher, A., Picard, C., 2000. Middle Cretaceous back-arc formation and arc evolution along the Asian margin: the Shyok Suture Zone in northern Ladakh (NW Himalaya). Tectonophysics 325, 145–173. doi:10.1016/S0040-1951(00)00135-9.

Rosgen, D.L., Silvey, H.L., 1996. Applied river morphology. volume 1481. Wildland Hydrology Pagosa Springs, Colorado.

Rosselli, A., Raymond, O., 2003. Mod{é}lisation gravim{é}trique 2.5 D et cartes des isohypses au 1: 100ï¿½000 du substratum rocheux de la vall{é}e du Rh{ê}ne entre Villeneuve et Brigue (Suisse). Eclogae geol. Helvet 96, 399–423. doi:10.1007/s00015-003-1088-z.

Röthlisberger, H., Vögtli, K., 1967. Recent D. C. resistivity soundings on Swiss glaciers. J. Glaciol. 6, 607–621.

Rowan, A.V., Brocklehurst, S.H., Schultz, D.M., Plummer, M.A., Anderson, L.S., Glasser, N.F., 2014. Late Quaternary glacier sensitivity to temperature and precipitation distribution in the Southern Alps of New Zealand. Journal of Geophysical Research 119, 1064–1081. doi:10.1002/2013JF003009.

Royden, L.H., 1993. The tectonic expression of slab pull at continental convergent boundaries. Tectonics 12, 303–325. doi:10.1029/92TC02248.

Ruess, D., Mitterschiffthaler, P., 2015. Rezente Höhenänderungen in Österreich abgeleitet aus geodätischen Wiederholungsmessungen, in: Hanke, K., Weinhold, T. (Eds.), 18. Internationale Geodätische Woche, Obergurgl, Wichmann, Berlin. pp. 111–123.

Schaller, M., von Blanckenburg, F., Veldkamp, A., Tebbens, L., Hovius, N., Kubik, P., 2002. A 30,000 yr record of erosion rates from cosmogenic in middle european river terraces. Earth and Planetary Science Letters 204, 307 – 320. doi:http://dx.doi.org/10.1016/S0012-821X(02)00951-2.

Scherler, D., 2014. Climatic limits to headwall retreat in the Khumbu Himalaya, eastern Nepal. Geology 42, 1019–1022. doi:10.1130/G35975.1.

Scherler, D., Bookhagen, B., Strecker, M.R., 2011a. Hillslope-glacier coupling: The interplay of topography and glacial dynamics in High Asia. Journal of Geophysical Research 116, F02019. doi:10.1029/2010JF001751.

Scherler, D., Bookhagen, B., Strecker, M.R., 2011b. Spatially variable response of Himalayan glaciers to climate change affected by debris cover. Nature Geoscience 4, 156–159. doi:10.1038/ngeo1068.

Scherler, D., Bookhagen, B., Wulf, H., Preusser, F., Strecker, M.R., 2015. Increased late Pleistocene erosion rates during fluvial aggradation in the Garhwal Himalaya, northern India. Earth and Planetary Science Letters 428, 255–266. doi:10.1016/j.epsl.2015.06.034.

Scherler, D., Lamb, M.P., Rhodes, E.J., Avouac, J.P., 2016. Climate-change versus landslide origin of fill terraces in a rapidly eroding bedrock landscape: San Gabriel River, California. Geological Society of America Bulletin , B31356.1doi:10.1130/B31356.1.

Scherler, D., Munack, H., Mey, J., Eugster, P., Wittmann, H., Codilean, A.T., Kubik, P., Strecker, M.R., 2014. Ice dams, outburst floods, and glacial incision at the western margin of the Tibetan Plateau: A >100 k.y. chronology from the Shyok Valley, Karakoram. Bulletin of the Geological Society of America 126, 738–758. doi:10.1130/B30942.1.

Schildgen, T., Dethier, D.P., Bierman, P., Caffee, M., 2002. 26Al and 10Be dating of Late Pleistocene and Holocene fill terraces: A record of fluvial deposition and incision, Colorado Front Range. Earth Surface Processes and Landforms 27, 773–787. doi:10.1002/esp.352.

Schildgen, T., Yildirim, C., Cosentino, D., Strecker, M., 2014. Linking slab break-off, Hellenic trench retreat, and uplift of the Central and Eastern Anatolian plateaus. Earth-Science Reviews 128, 147–168. doi:10.1016/j.earscirev.2013.11.006.

Schildgen, T.F., Robinson, R.A., Savi, S., Phillips, W.M., Spencer, J.Q., Bookhagen, B., Scherler, D., Tofelde, S., Alonso, R.N., Kubik, P.W., et al., 2016. Landscape response to late pleistocene climate change in nw argentina: Sediment flux modulated by basin geometry and connectivity. Journal of Geophysical Research: Earth Surface 121, 392–414.

Schlatter, A., Schneider, D., Geiger, A., Kahle, H.G., 2005. Recent vertical movements from precise levelling in the vicinity of the city of Basel, Switzerland. International Journal of Earth Sciences 94, 507–514. doi:10.1007/s00531-004-0449-9.

Schlüchter, C., 1988. The deglaciation of the Swiss-Alps : a paleoclimatic event with chronological problems. Bulletin de l'Association française pour l'étude du quaternaire 25, 141–145. doi:10.3406/quate.1988.1875.

Schmid, S.M., Pfiffner, O.a., Froitzheim, N., Schönborn, G., Kissling, E., 1996. Geophysical-geological transect and tectonic evolution of the Swiss-Italian Alps. Tectonics 15, 1036–1064. doi:10.1029/96TC00433.

Schrott, L., Adams, T., 2002. Quantifying sediment storage and Holocene denudation in an Alpine basin, Dolomites, Italy. Zeitschrift für Geomorphologie 128, 129–145.

Schrott, L., Hufschmidt, G., Hankammer, M., Hoffmann, T., Dikau, R., 2003. Spatial distribution of sediment storage types and quantification of valley fill deposits in an alpine basin, Reintal, Bavarian Alps, Germany. Geomorphology 55, 45–63. doi:10.1016/S0169-555X(03)00131-4.

Schwanghart, W., Scherler, D., 2014. TopoToolbox 2 – MATLAB-based software for topographic analysis and modeling in Earth surface sciences. Earth Surface Dynamics 2, 1–7. doi:10.5194/esurf-2-1-2014.

Seeber, L., Gornitz, V., 1983. River profiles along the Himalayan arc as indicators of active tectonics. Tectonophysics 92, 335–367. doi:10.1016/0040-1951(83)90201-9.

Seeber, L., Pêcher, A., 1998. Strain partitioning along the Himalayan arc and the Nanga Parbat antiform. Geology 26, 791–794. doi:10.1130/0091-7613(1998)026<0791:SPATHA>2.3.CO;2.

Seong, Y.B., Owen, L.A., Bishop, M.P., Bush, A., Clendon, P., Copland, L., Finkel, R., Kamp, U., Shroder, J.F., 2007. Quaternary glacial history of the Central Karakoram. Quaternary Science Reviews 26, 3384–3405. doi:10.1016/j.quascirev.2007.09.015.

Seward, D., Burg, J.P., 2008. Growth of the Namche Barwa Syntaxis and associated evolution of the Tsangpo Gorge: Constraints from structural and thermochronological data. Tectonophysics 451, 282–289. doi:10.1016/j.tecto.2007.11.057.

Shi, Y., Yu, G., Liu, X., Li, B., Yao, T., 2001. Reconstruction of the 30–40kabp enhanced Indian monsoon climate based on geological records from the Tibetan Plateau. Palaeogeography, Palaeoclimatology, Palaeoecology 169, 69–83. doi:10.1016/S0031-0182(01)00216-4.

Shreve, R.L., 1987. Blackhawk landslide, southwestern San Bernardino County, California, in: Hill, M. (Ed.), Cor- dilleran Section of the Geological Society of America (Centennial Field Guide), pp. 109–114.

Shroder, J.F., 1998. Slope failure and denudation in the western Himalaya. Geomorphology 26, 81–105. doi:10.1016/S0169-555X(98)00052-X.

Shroder, J.F., Khan, M.S., Lawrence, R.D., Madin, I.P., Higgins, S.M., 1989. Quaternary glacial chronology and neotectonics in the Himalaya of northern Pakistan. Geological Society of America Special Papers 232, 275–294. doi:10.1130/SPE232-p275.

Sigmundsson, F., Einarsson, P., 1992. Glacio-isostatic crustal movements caused by historical volume change of the Vatnajökull Ice Cap, Iceland. Geophysical Research Letters 19, 2123–2126. doi:10.1029/92GL02209.

Simpson, G., Castelltort, S., 2012. Model shows that rivers transmit high-frequency climate cycles to the sedimentary record. Geology 40, 1131–1134. doi:10.1130/G33451.1.

Sinclair, H.D., Coakley, B.J., Allen, P.A., Watts, A.B., 1991. Simulation of Foreland Basin Stratigraphy using a diffusion model of mountain belt uplift and erosion: An example from the central Alps, Switzerland. Tectonics 10, 599—-620. doi:10.1029/90TC02507.

Sklar, L., Dietrich, W.E., 1998. River Longitudinal Profiles and Bedrock Incision Models: Stream Power and the Influence of Sediment Supply, in: Rivers Over Rock: Fluvial Processes in Bedrock Channels. American Geophysical Union, pp. 237–260. doi:10.1029/GM107p0237.

Small, E.E., Anderson, R.S., 1995. Geomorphically Driven Late Cenozoic Rock Uplift in the Sierra Nevada, California. Science 270, 277–281. doi:10.1126/science.270.5234.277.

Smith, W.H.F., Wessel, P., 1990. Gridding with continuous curvature splines in tension. Geophysics 55, 293–305.

Snyder, N.P., 2003. Importance of a stochastic distribution of floods and erosion thresholds in the bedrock river incision problem. Journal of Geophysical Research 108, 2117. doi:10.1029/2001JB001655.

Sobel, E.R., Hilley, G.E., Strecker, M.R., 2003. Formation of internally drained contractional basins by aridity-limited bedrock incision. Journal of Geophysical Research 108. doi:10.1029/2002JB001883.

Steffen, D., Schlunegger, F., Preusser, F., 2010. Late pleistocene fans and terraces in the majes valley, southern peru, and their relation to climatic variations. International Journal of Earth Sciences 99, 1975–1989. doi:10.1007/s00531-009-0489-2.

Stein, S., Liu, M., Calais, E., Li, Q., 2009. Mid-Continent Earthquakes as a Complex System. Seismological Research Letters 80, 551–553. doi:10.1785/gssrl.80.4.551.

Steinbrener, J., 2011. Sedimentologische und geochemische Untersuchung der Tiefbohrung Wattens I (Tirol). Master. Universität Wien.

Stenni, B., Masson-Delmotte, V., Johnsen, S., Jouzel, J., Longinelli, A., Monnin, E., Röthlisberger, R., Selmo, E., 2001. An Oceanic Cold Reversal During the Last Deglaciation. Science 293, 2074–2077.

Steward, J., Watts, A.B., 1997. Gravity anomalies and spatial variations of flexural rigidity at mountain ranges. Journal of Geophysical Research 102, 5327—-5352.

Stewart, I.S., Sauber, J., Rose, J., 2000. Glacio-seismotectonics: Ice sheets, crustal deformation and seismicity. Quaternary Science Reviews 19, 1367–1389. doi:10.1016/S0277-3791(00)00094-9.

Stone, J.O., 2000. Air pressure and cosmogenic isotope production. Journal of Geophysical Research 105, 23753. doi:10.1029/2000JB900181.

Straumann, R.K., Korup, O., 2009. Quantifying postglacial sediment storage at the mountain-belt scale. Geology 37, 1079–1082. doi:10.1130/G30113A.1.

Straumann, R.K., Purves, R.S., 2008. Delineation of valleys and valley floors. Lecture Notes in Computer Science (including subseries Lecture Notes in Artificial Intelligence and Lecture Notes in Bioinformatics) 5266 LNCS, 320–336. doi:10.1007/978-3-540-87473-7-21.

Strecker, M.R., Alonso, R., Bookhagen, B., Carrapa, B., Coutand, I., Hain, M.P., Hilley, G.E., Mortimer, E., Schoenbohm, L., Sobel, E.R., 2009. Does the topographic distribution of the central Andean Puna Plateau result from climatic or geodynamic processes? Geology 37, 643–646. doi:10.1130/G25545A.1.

Strecker, M.R., Hilley, G.E., Arrowsmith, J.R., Coutand, I., 2003. Differential structural and geomorphic mountain-front evolution in an active continental collision zone: The northwest Pamir, southern Kyrgyzstan. Geological Society of America Bulletin 115, 166–181. doi:10.1130/0016-7606(2003)115<0166:DSAGMF>2.0.CO;2.

Sulebak, J., Hjelle, Ø., 2003. Multiresolution spline models and their applications in geomorphology. . . . and Modelling in Geomorphology: . . . , 221–237.

Suresh, N., Bagati, T.N., Kumar, R., Thakur, V.C., 2007. Evolution of quaternary alluvial fans and terraces in the intramontane pinjaur dun, sub-himalaya, nw india: Interaction between tectonics and climate change. Sedimentology 54, 809–833.

Swisstopo, 2005. Geological Map of Switzerland 1:500,000.

Tapponnier, P., Zhiqin, X., Roger, F., Meyer, B., Arnaud, N., Wittlinger, G., Jingsui, Y., 2001. Oblique Stepwise Rise and Growth of the Tibet Plateau. Science 294, 1671–1677.

Taylor, M., Yin, A., 2009. Active structures of the Himalayan-Tibetan orogen and their relationships to earthquake distribution, contemporary strain field, and Cenozoic volcanism. Geosphere 5, 199–214. doi:10.1130/GES00217.1.

Tesauro, M., Kaban, M.K., Cloetingh, S.A., 2013. Global model for the lithospheric strength and effective elastic thickness. Tectonophysics 602, 78–86. doi:10.1016/j.tecto.2013.01.006.

Tesauro, M., Kaban, M.K., Cloetingh, S.a.P.L., 2008. EuCRUST-07: A new reference model for the European crust. Geophysical Research Letters 35, 3–7. doi:10.1029/2007GL032244.

Tesauro, M., Kaban, M.K., Cloetingh, S.A.P.L., 2009. How rigid is Europe's lithosphere? Geophysical Research Letters 36, 1–6. doi:10.1029/2009GL039229.

Torres Acosta, V., Schildgen, T.F., Clarke, B.A., Scherler, D., Bookhagen, B., Wittmann, H., von Blanckenburg, F., Strecker, M.R., 2015. Effect of vegetation cover on millennial-scale landscape denudation rates in East Africa. Lithosphere 7, 408–420. doi:10.1130/L402.1.

Trauth, M.H., Alonso, R.A., Haselton, K.R., Hermanns, R.L., Strecker, M.R., 2000. Climate change and mass movements in the NW Argentine Andes. Earth and Planetary Science Letters 179, 243–256. doi:10.1016/S0012-821X(00)00127-8.

Tucker, G.E., 2004. Drainage basin sensitivity to tectonic and climatic forcing: implications of a stochastic model for the role of entrainment and erosion thresholds. Earth Surface Processes and Landforms 29, 185–205. doi:10.1002/esp.1020.

Tucker, G.E., Slingerland, R., 1997. Drainage basin responses to climate change. Water Resources Research 33, 2031–2047. doi:10.1029/97WR00409.

Turcotte, D.L., Schubert, G., 2002. Geodynamics. 2 ed., Cambridge University Press, Cambridge, U.K.

Tweed, F.S., Russell, A.J., 1999. Controls on the formation and sudden drainage of glacier-impounded lakes: implications for jökulhlaup characteristics. Progress in Physical Geography 23, 79–110. doi:10.1177/030913339902300104.

Van Der Beek, P., Bourbon, P., 2008. A quantification of the glacial imprint on relief development in the french western alps. Geomorphology 97, 52–72.

Van Husen, D., 1987. Die ostalpen in den eiszeiten. aus der geologischen geschichte /"Osterreichs. populärwiss. veröff. geol. b. A. Wien .

Vening Meinesz, F.A., 1931. Une nouvelle methode pour la reduction isostatique regionale de l'intensite de la pesanteur. Bulletin Géodésique (1922-1941) 29, 33–51.

Vernet, J.P., Horn, R., Badoux, H., 1974. Etude structurale du Léman par sismique réflexion continue. Eclogae Geologicae Helvetiae 67, 515–529.

Waitt, R.B., 1985. Case for periodic, colossal jökulhlaups from Pleistocene glacial Lake Missoula. Geological Society of America Bulletin 96, 1271–1286. doi:10.1130/0016-7606(1985)96<1271:CFPCJF>2.0.CO;2.

Wald, D.J., Allen, T.I., 2007. Topographic slope as a proxy for seismic site conditions and amplification. Bulletin of the Seismological Society of America 97, 1379–1395. doi:10.1785/0120060267.

Walder, J.S., Costa, J.E., 1996. Outburst floods from glacier-dammed lakes: The effect of mode of lake drainage on flood magnitude. Earth Surface Processes and Landforms 21, 701–723.

Wang, P., Scherler, D., Liu-Zeng, J., Mey, J., Avouac, J.P., Zhang, Y., Shi, D., 2014. Tectonic control of Yarlung Tsangpo Gorge revealed by a buried canyon in Southern Tibet. Science 346, 978–981. doi:10.1126/science.1259041.

Watts, A.B., 2001. Isostasy and Flexure of the Lithosphere. 1 ed., Cambridge University Press, Cambridge, U.K.

Weiss, S.M., Kulikowski, C.A., 1991. Computer systems that learn: classification and prediction methods from statistics. Neural Networks, Machine Learning, and Expert Systems .

Wells, S.G., McFadden, L.D., Poths, J., Olinger, C.T., 1995. Cosmogenic 3He surface-exposure dating of stone pavements. Implications for landscape evolution in deserts. Geology 23, 613–616. doi:10.1130/0091-7613(1995)023<0613:CHSEDO>2.3.CO;2.

Wickert, A.D., 2015. Open-source modular solutions for flexural isostasy: gFlex v1.0. Geoscientific Model Development Discussions 8, 4245–4292. doi:10.5194/gmdd-8-4245-2015.

Wickert, A.D., Mitrovica, J.X., Williams, C., Anderson, R.S., 2013. Gradual demise of a thin southern Laurentide ice sheet recorded by Mississippi drainage. Nature 502, 668–671. doi:10.1038/nature12609.

Wildi, W., 1984. Isohypsenkarte der quartären Felstäler in der Nord- und Ostschweiz mit kurzen Erläuterungen. Eclogae Geologicae Helvetiae 77, 541–551.

Willenbring, J.K., von Blanckenburg, F., 2010. Long-term stability of global erosion rates and weathering during late-Cenozoic cooling. Nature 465, 211–214. doi:10.1038/nature09044.

Willett, S.D., Schlunegger, F., Picotti, V., 2006. Messinian climate change and erosional destruction of the central European Alps. Geology 34, 613–616. doi:10.1130/G22280.1.

Wittmann, H., von Blanckenburg, F., Kruesmann, T., Norton, K.P., Kubik, P.W., 2007. Relation between rock uplift and denudation from cosmogenic nuclides in river sediment in the Central Alps of Switzerland. Journal of Geophysical Research: Earth Surface 112, 1–20. doi:10.1029/2006JF000729.

Wolman, M.G., Miller, J.P., 1960. Magnitude and Frequency of Forces in Geomorphic Processes. The Journal of Geology 68, 54–74.

Wolpert, D.H., 1994. The Mathematics of Generalization. Perseus Publishing, Santa Fe.

Wolpert, D.H., 1996a. The Existence of A Priori Distinctions Between Learning Algorithms. Neural Computation 8, 1391–1420. doi:10.1162/neco.1996.8.7.1391.

Wolpert, D.H., 1996b. The Lack of A Priori Distinctions Between Learning Algorithms. Neural Computation 8, 1341–1390. doi:10.1162/neco.1996.8.7.1341.

Wulf, H., Bookhagen, B., Scherler, D., 2010. Seasonal precipitation gradients and their impact on fluvial sediment flux in the Northwest Himalaya. Geomorphology 118, 13–21. doi:10.1016/j.geomorph.2009.12.003.

Zeitler, P.K., Malloy, M.A., Kutney, M.P., Idleman, B.D., Liu, Y., Kidd, W.S., Booth, A.L., 2006. Geochronological Evidence for the Tectonic and Topographic Evolution of SE Tibet. Eos 87.

Zeitler, P.K., Meltzer, A.S., Koons, P.O., Craw, D., Hallet, B., Chamberlain, C.P., Kidd, W.S.F., Park, S.K., Seeber, L., Bishop, M., Others, 2001. Erosion, Himalayan geodynamics, and the geomorphology of metamorphism. GSA Today 11, 4–9.

Appendix A

Supplementary data for Chapter 2

This data set contains 7 figures showing the validation and test error as a function of the number of sectors and hidden nodes for experiments involving natural landscapes with artificial fills (U1–U3,V1,V2) and natural landscapes with natural fills (Unteraar Glacier, Rhône Glacier, Rhône Valley). Stars indicate the respective minimum error configurations as listed in Tables 2.1 and 2.2. In addition a comparison between observed and estimated thickness distribution is provided in Figures A.1–A.5, whereas Figures A.6 and A.7 only show the estimated thickness distribution. The estimated thickness distribution results when the minimum error validation configuration is used for prediction.

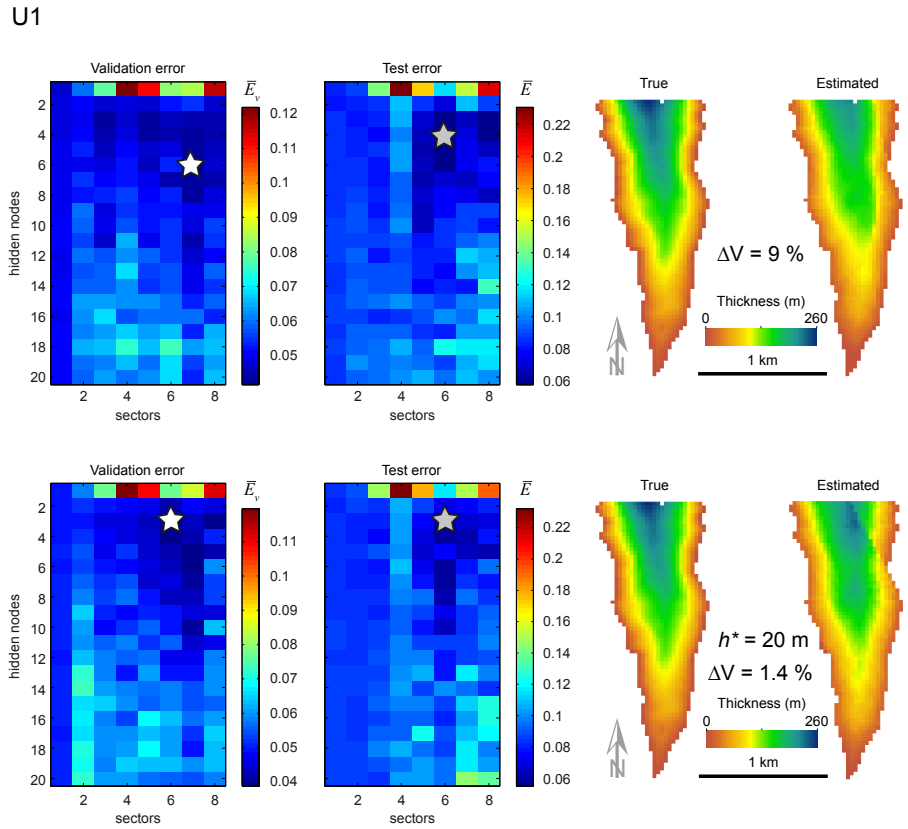

Figure A.1: Results for artificially filled glacial valley U1. Top row (bottom row) shows model outcome without (with) incorporation of prior knowledge.

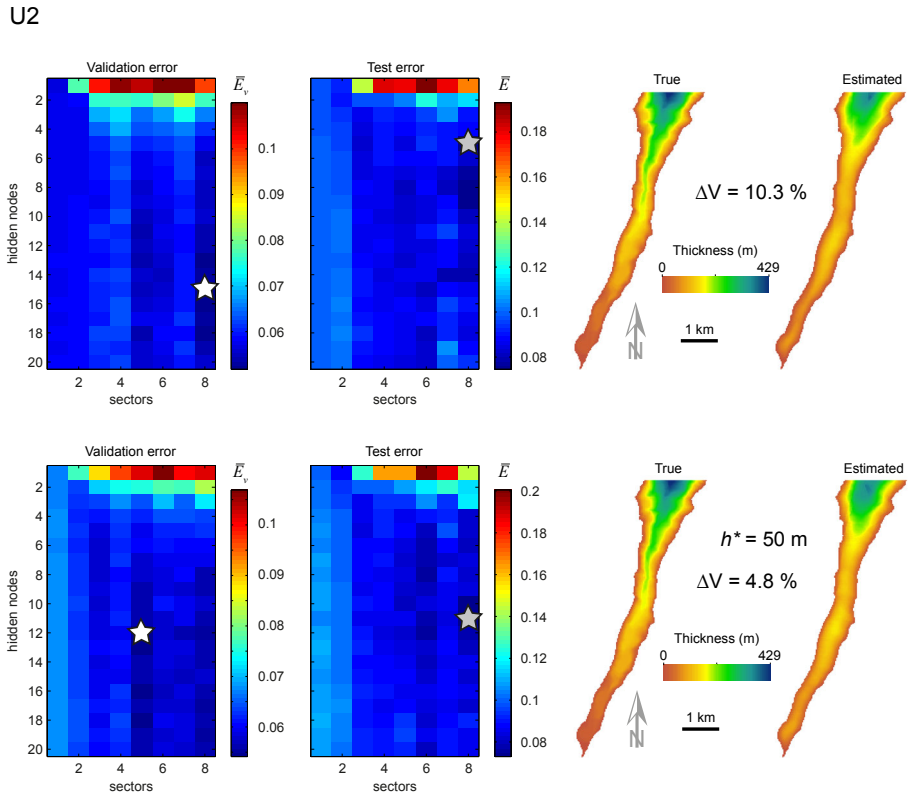

Figure A.2: Results for artificially filled glacial valley U2. Top row (bottom row) shows model outcome without (with) incorporation of prior knowledge.

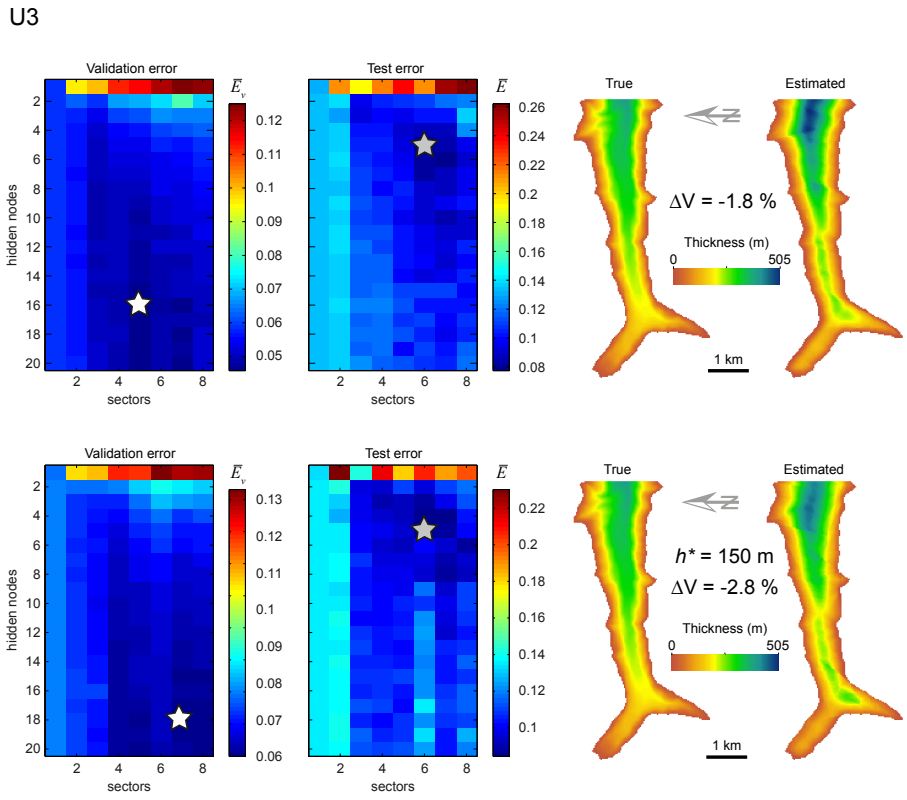

Figure A.3: Results for artificially filled glacial valley U3. Top row (bottom row) shows model outcome without (with) incorporation of prior knowledge.

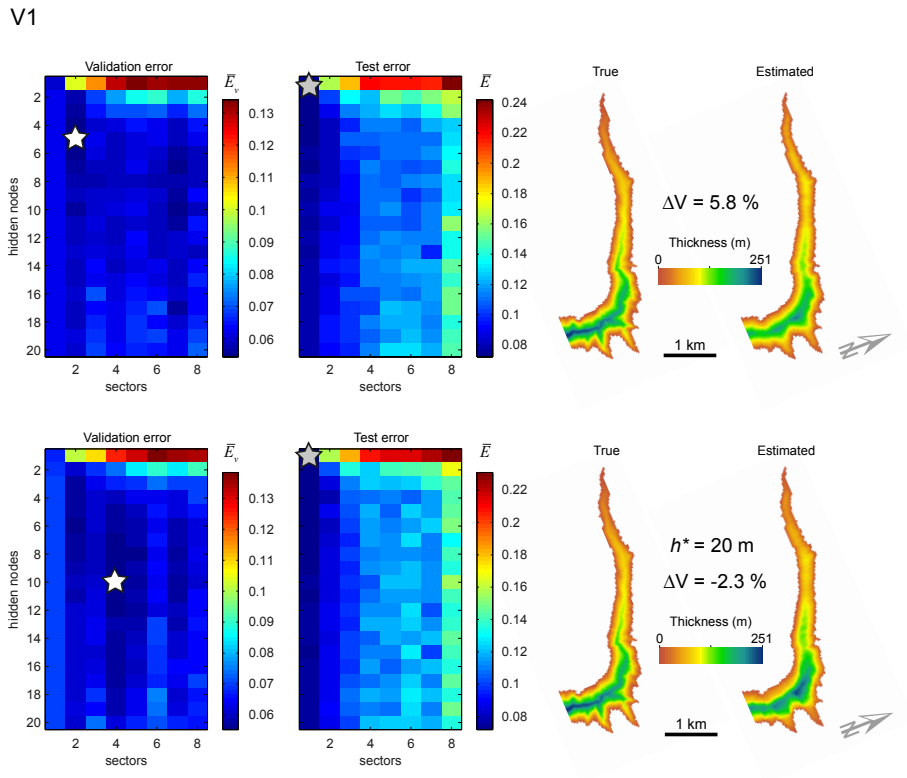

Figure A.4: Results for artificially filled fluvial valley V1. Top row (bottom row) shows model outcome without (with) incorporation of prior knowledge.

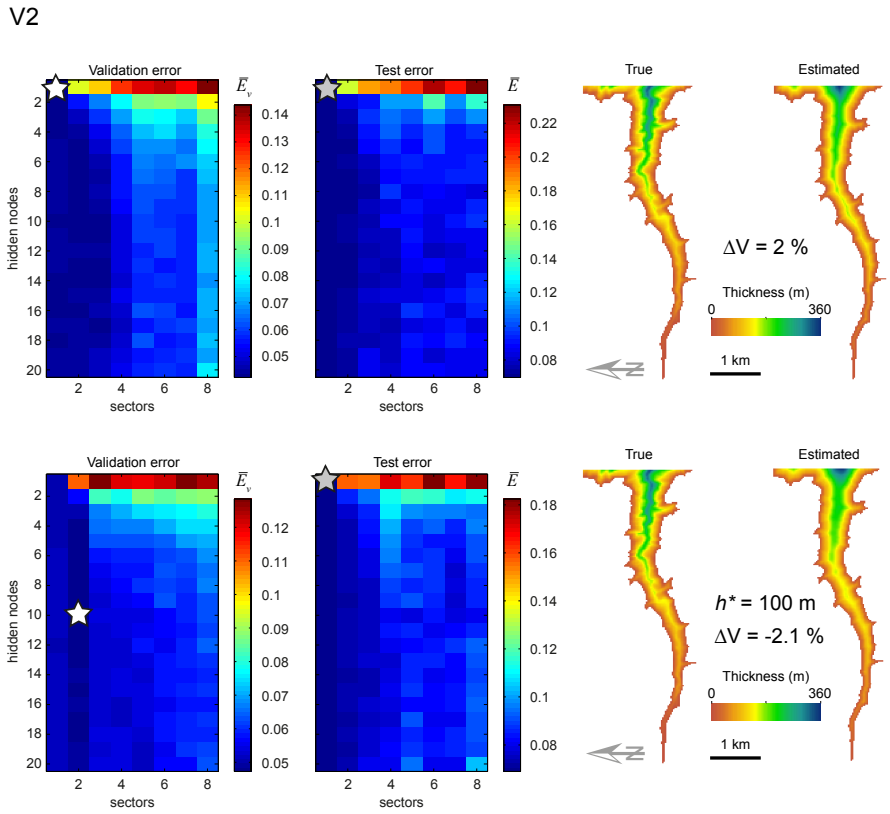

Figure A.5: Results for artificially filled fluvial valley V2. Top row (bottom row) shows model outcome without (with) incorporation of prior knowledge.

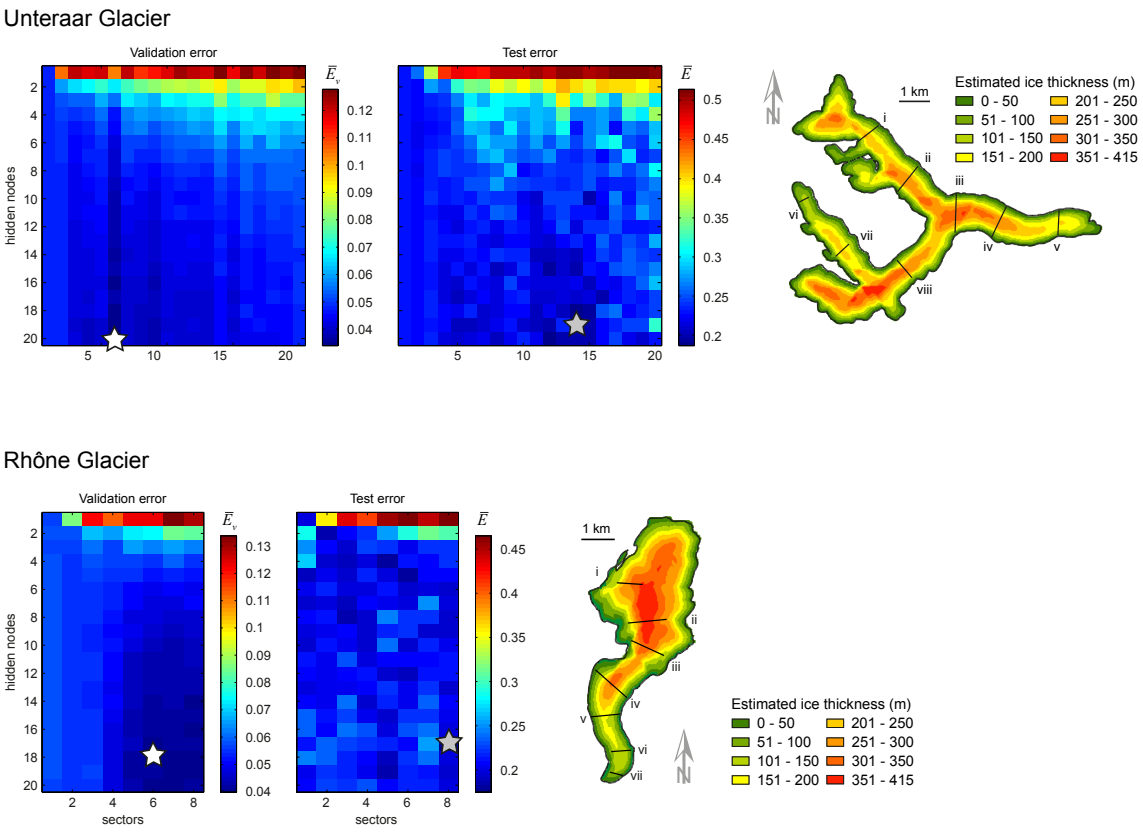

Figure A.6: Results for the Unteraar Glacier (top) and the Rhône Glacier (bottom).

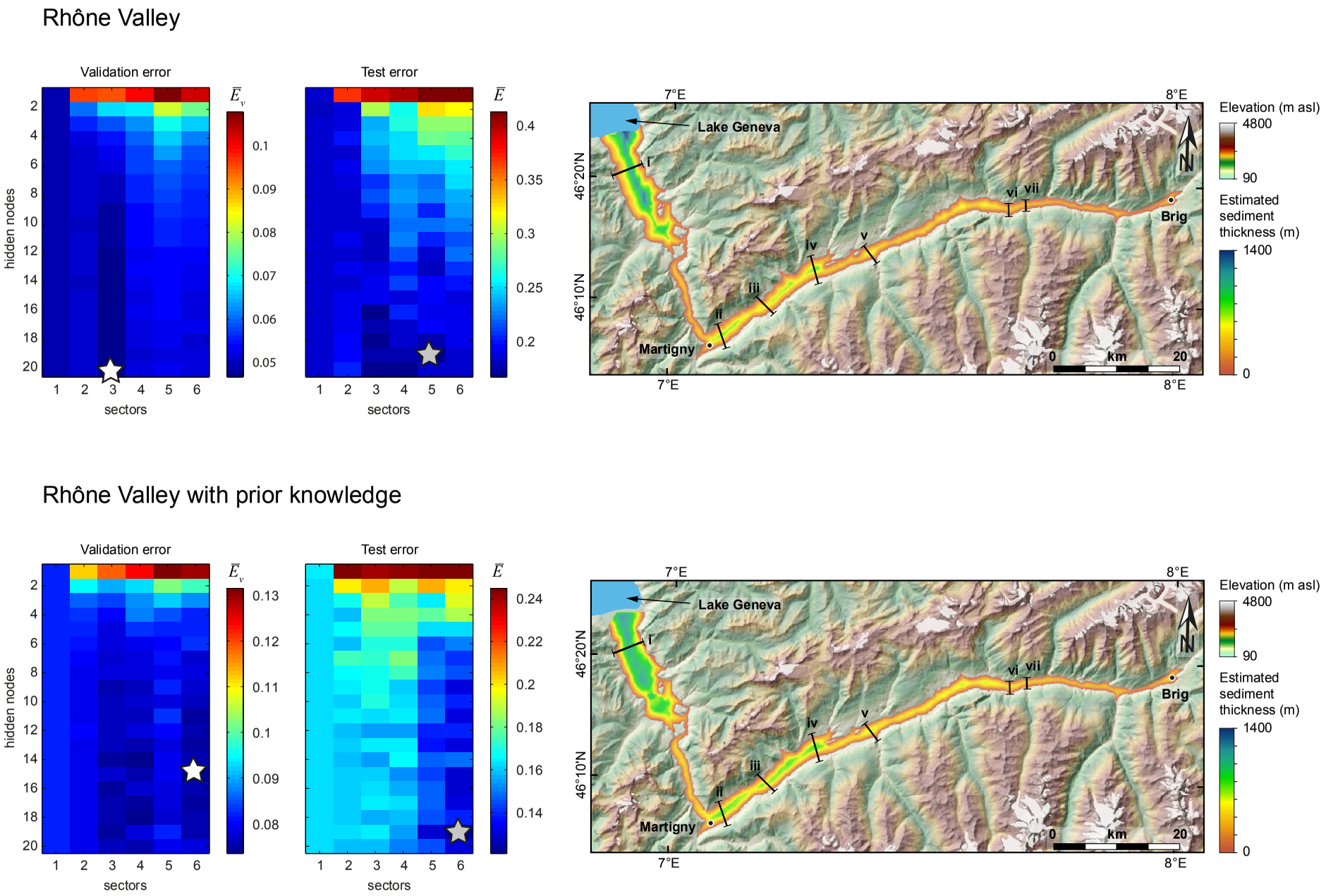

Figure A.7: Results for the Rhône Valley. Top row (bottom row) shows model outcome without (with) incorporation of prior knowledge.

Appendix B

Supplementary data for Chapter 5

This appendix provides additional details on the ^{10}Be depth profile modeling (Figures B.1–B.3), the recalculated ^{10}Be-exposure ages by Dortch et al. (2010) (Table B.1), and a data table with glacial striation measurements (Table B.2).

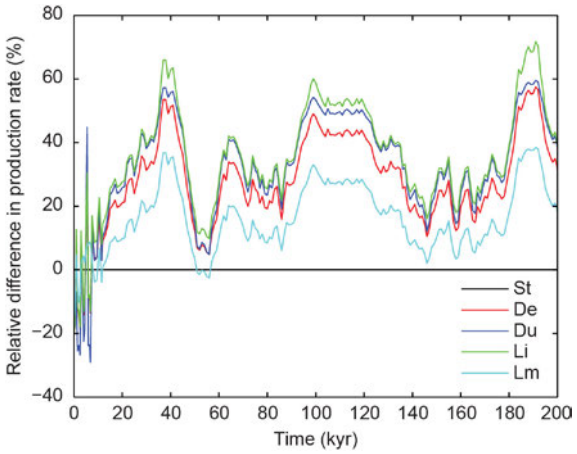

Figure B.1: Relative differences of instantaneous production rates during the past 200 kyr in the study area, according to the production rate scaling models available in the CRONUS online calculator (Balco et al., 2008). St=time-independent Lal/Stone scaling; De=time-dependent Desilets et al. scaling; Du=time-dependent Dunai scaling; Li=time-dependent Lifton et al. scaling; Lm=time-dependent form of the Lal/Stone scaling. See Balco et al. (2008) for details and references on the different scaling models.

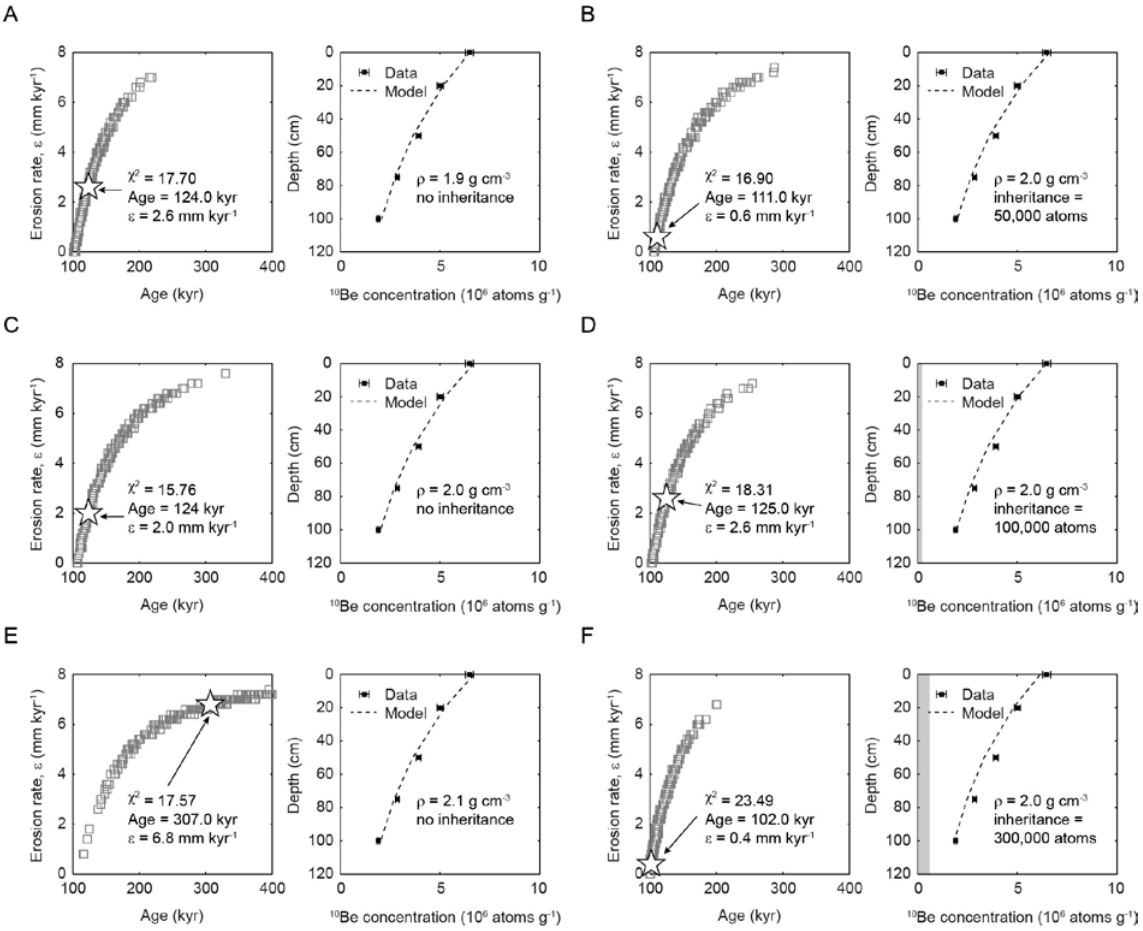

Figure B.2: Best-fit ^{10}Be depth-profile modeling results for the till plain at the Shyok-Nubra confluence, showing the effect of different densities, given no inheritance (A, C, E), and the effect of different inheritances for a fixed density of 2.0 g cm^{-3} (B, D, F). In each panel, the left plot shows the best-fit results from 200 Monte Carlo runs, the right plot shows modeled (dashed line) and measured (solid squares) ^{10}Be concentrations and their 2-σ total analytical uncertainties (error bars). Gray bars indicate the assumed inherited concentration. The ultimate best-fit solution is indicated with a star in the left plot of each panel and the corresponding modeled ^{10}Be-depth profile is shown in the right plot of each panel.

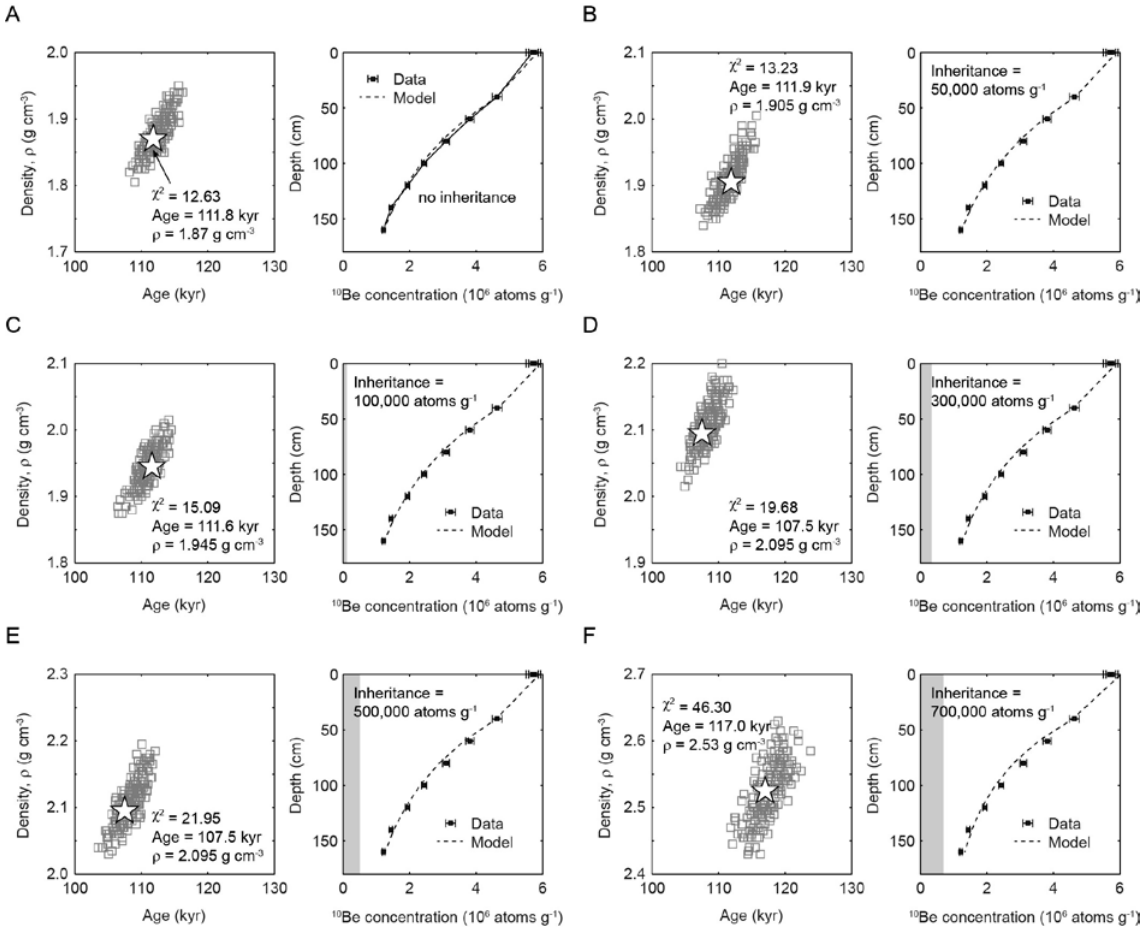

Figure B.3: ^{10}Be depth-profile modeling results for the terrace surface near Agham and different scenarios of inherited concentrations: (A) no inheritance, (B) 50,000 atoms g^{-1}, (C) 100,000 atoms g^{-1}, (D) 300,000 atoms g^{-1}, (E) 500,000 atoms g^{-1}, (F) 700,000 atoms g^{-1}. Symbols are as in Figure B.2. Reasonable fits can be achieved with each inheritance scenario, but the misfit (χ^2) between the modeled and measured data increases with increasing inheritances. Note the different scaling on the y-axis of the left plots.

Table B.1: Surface exposure ages, based on data published in Dortch et al. (2010), recalculated with the CRONUS online calculator (Balco et al., 2008). All uncertainties on model ages refer to the external errors; 'St', 'De', 'Du', 'Li', and 'Lm' refer to the different production rate scaling models (Balco et al., 2008). See Dortch et al. (2010) for further sample details. Ages from the last column ('Lm') were be used to compare with our new data.

	St	De	Du	Li	Lm
Sample Name	Age (kyr)	Age (kyr)	Age (kyr)	Age (kyr)	Age (kyr)
NU-1	85.1 ± 7.7	73.8 ± 8.9	72.0 ± 8.7	70.2 ± 7.1	75.9 ± 6.6
NU-2	66.8 ± 6.8	58.4 ± 7.6	57.2 ± 7.4	55.4 ± 6.2	60.0 ± 5.9
NU-3	47.6 ± 4.6	41.4 ± 5.2	40.8 ± 5.1	39.9 ± 4.3	42.2 ± 3.9
NU-4	80.5 ± 7.3	69.5 ± 8.5	68.0 ± 8.2	66.4 ± 6.8	71.8 ± 6.3
NU-5	48.1 ± 5.0	41.8 ± 5.5	41.2 ± 5.4	40.2 ± 4.6	42.6 ± 4.3
NU-6	43.0 ± 4.3	38.2 ± 4.9	37.6 ± 4.8	36.8 ± 4.1	38.7 ± 3.8
NU-7	61.8 ± 5.6	53.7 ± 6.5	52.4 ± 6.3	50.8 ± 5.2	55.1 ± 4.8
NU-8	47.0 ± 4.3	41.0 ± 5.0	40.4 ± 4.9	39.5 ± 4.1	41.7 ± 3.7
NU-9	25.5 ± 2.4	24.4 ± 3.1	24.3 ± 3.0	23.6 ± 2.5	24.3 ± 2.3
NU-10	48.0 ± 4.5	41.8 ± 5.1	41.2 ± 5.0	40.2 ± 4.2	42.5 ± 3.8
NU-11	28.7 ± 2.8	27.1 ± 3.4	26.9 ± 3.4	26.2 ± 2.8	27.1 ± 2.6
NU-12	32.2 ± 3.1	30.0 ± 3.7	29.7 ± 3.7	28.9 ± 3.1	30.1 ± 2.8
NU-13	118.6 ± 10.9	99.0 ± 12.2	96.6 ± 11.8	94.7 ± 9.8	103.9 ± 9.3
NU-14	112.8 ± 10.8	94.9 ± 11.9	92.6 ± 11.6	90.5 ± 9.7	99.5 ± 9.3
NU-15A	35.2 ± 3.3	31.7 ± 3.9	31.4 ± 3.9	30.6 ± 3.2	32.6 ± 3.0
NU-15B	37.8 ± 3.8	33.7 ± 4.3	33.3 ± 4.3	32.5 ± 3.6	34.7 ± 3.4
NU-16	163.9 ± 16.2	132.4 ± 17.0	128.3 ± 16.4	125.5 ± 13.7	140.8 ± 13.5
NU-17	147.3 ± 13.7	119.8 ± 14.8	116.5 ± 14.3	114.1 ± 11.9	126.6 ± 11.4
NU-18	111.3 ± 11.5	93.8 ± 12.3	91.4 ± 11.9	89.3 ± 10.1	98.3 ± 9.9
NU-19	155.7 ± 19.1	126.1 ± 18.6	122.4 ± 17.9	119.8 ± 15.7	133.6 ± 16.1
NU-20	70.5 ± 6.6	61.5 ± 7.6	60.4 ± 7.4	58.6 ± 6.1	63.2 ± 5.7
NU-21	86.3 ± 8.0	74.5 ± 9.2	72.8 ± 8.9	70.9 ± 7.4	76.9 ± 7.0
NU-23	87.0 ± 8.0	75.3 ± 9.3	73.6 ± 9.0	71.7 ± 7.4	77.6 ± 7.0
NU-24	112.0 ± 10.4	96.3 ± 11.9	94.0 ± 11.6	92.1 ± 9.6	99.1 ± 8.9
NU-25	46.6 ± 4.4	40.7 ± 5.0	40.1 ± 4.9	39.2 ± 4.1	41.4 ± 3.8
NU-26	50.6 ± 5.2	43.6 ± 5.7	42.9 ± 5.6	41.9 ± 4.7	44.6 ± 4.4
NU-27	124.8 ± 11.8	103.4 ± 12.9	100.8 ± 12.5	98.8 ± 10.4	108.8 ± 10.0
NU-28	121.1 ± 11.2	100.7 ± 12.4	98.3 ± 12.0	96.3 ± 10.0	105.8 ± 9.4
NU-29	142.6 ± 13.3	116.2 ± 14.4	113.1 ± 14.0	110.8 ± 11.6	122.7 ± 11.1
NU-30	132.4 ± 12.3	108.9 ± 13.4	106.1 ± 13.0	103.9 ± 10.8	114.7 ± 10.3

Table B.2: Glacial striation measurements. Note that the azimuth of the striation does usually not correspond to the flow direction of the glacier, because most striations were measured on the upglacier side of roches moutonnées, hence plunging in an up-valley direction. Readings refer to several measurements at one site, and relative ages are inferred from cross-cutting relationships.

			Reading 1		Reading 2		Reading 3		
Lat (°N)	Lon (°E)	Elevation (m a.s.l.)	Azimuth (°)	Plunge (°)	Azimuth (°)	Plunge (°)	Azimuth (°)	Plunge (°)	Relative age
34.543866	77.563636	3300	50	5					
34.543891	77.563746	3300	54	0					
34.543909	77.563746	3300	60	10					
34.543918	77.563725	3300	53	2					
34.544235	77.56368	3300	26	5					
34.544242	77.563746	3300	25	30					
34.544384	77.563572	3244	222	12					
34.544551	77.563607	3240	206	24					
34.568243	77.619189	3166	14	14	350	20			
34.569902	77.650878	3999	340	17					
34.570069	77.649412	3936	325	12	330	15	326	30	
34.574583	77.633295	3441	190	5					
34.574923	77.626045	3257	180	13					
34.575544	77.627373	3296	1	1					
34.57867	77.628127	3276	30	28	21	30	20	40	
34.672166	77.405306	3329	114	10					
34.672175	77.404764	3344	302	6	72	2			
34.67219	77.40498	3333	72	2					
34.672223	77.405177	3329	104	9					
34.672229	77.405185	3340	104	9	114	10			
34.67224	77.404741	3329	302	6					
34.695559	77.308948	3490	16	10	198	7	4	12	
34.695812	77.308889	3499	5	1					
34.71681	77.242239	3255	145	7					
34.71681	77.242239	3255	154	12					
34.71681	77.242239	3255	136	3					
34.717598	77.242533	3286	155	10					old
			184	23					interm.
			210	36					young
34.72522	77.569422	3198	340	2					